Semiconductors, Vol. 39, No. 2, 2005, pp. 161–173. From Fizika i Tekhnika Poluprovodnikov, Vol. 39, No. 2, 2005, pp. 177–188.

ELECTRONIC AND OPTICAL PROPERTIES OF SEMICONDUCTORS

Ab initio Studies of the Band Parameters of III–V and II–VI Zinc-Blende Semiconductors[1]

S. Zh. Karazhanov and L. C. Lew Yan Voon^

Department of Physics, Worcester Polytechnic Institute, Worcester, Massachusetts 01609-2280, USA

^e-mail: llew@wpi.edu

Submitted November 5, 2003; accepted for publication May 17, 2004

Abstract—Electronic band-structure calculations are performed for zinc-blende III–V (AlP, AlAs, AlSb, GaP, GaAs, GaP, InP, InAs, and InSb) and II–VI (ZnS, ZnSe, ZnTe, CdS, CdSe, and CdTe) semiconductors using an ab initio pseudopotential method within a local-density approximation (LDA). Lattice parameters, band gaps, Luttinger parameters, momentum matrix elements and effective masses are studied in detail. It is shown that LDA calculations cannot systematically give accurate band parameters. It is found that LDA band parameters calculated using experimentally determined lattice constants are more accurate than those using LDA lattice constants. We found that inclusion of the *d* electrons of Group-II atoms in the core gives more accurate band parameters. © *2005 Pleiades Publishing, Inc.*

1. INTRODUCTION

Density-functional theory (DFT) is a powerful tool for studying the electronic structure of solids. It is well known that the band gaps of bulk solids calculated within the theory are systematically underestimated compared to experimentally determined ones [1] because of the theory's failure to describe excited-state properties. Moreover, the problem rests with more than the local-density approximation (LDA). Following $\mathbf{k}\cdot\mathbf{p}$ theory (see, e.g., [2]), however, one can say that if fundamental excitation gaps are incorrect, then band dispersions should be as well. This realization has been used by Cardona *et al.* [3–6] in generating corrected band parameters (Luttinger parameters and spin splittings) for a number of semiconductors. Nevertheless, there remains some dispute regarding this issue [7]. For instance, in 1992, Fiorentini and Baldereshi [8, 9], using pseudopotential plane waves within the LDA, found that conduction-band masses (m_c) at point Γ were very close to experimental values for GaAs, AlAs, and Ge. However, the values of m_c found in [10] differ significantly from those determined experimentally for GaAs, GaSb, InP, and InAs. Similarly, the conduction-band effective masses calculated by Wang and Zunger [11] within the LDA agree well with experimental data for Si, while for CdSe the masses were not very accurate and a semiempirical modification led to somewhat better agreement. Kane [12], however, found that it was not possible to attain correct band gap and cyclotron masses in Si with a local static potential such as the LDA. Fairly good agreement with the experiment was obtained by Wang and Klein [13] for the conduction and valence band effective masses of GaP, GaAs, ZnS, and ZnSe using a linear combination of Gaussian orbitals within the LDA. A systematic study by Huang and Ching [14] of the effective masses for 32 semiconductors using a semi–ab initio technique shows much better agreement. Therefore, despite the importance of effective masses, the question of whether calculations within the LDA give correct effective masses is still open.

There is even less explicit research on the correctness of momentum matrix elements (E_p) calculated within the LDA, which are often claimed to be accurate. However, the validity of the statement has been less directly verified. The standard argument is that, in a pseudopotential approach, the pseudo–wave function has a very high overlap with the true wave function [11]. The value of E_p for GaAs calculated by Winkler [15], and Kageshima and Shiraishi [16] within the LDA is about ~1.7 times smaller than that determined experimentally [17, 18]. Kageshima and Shiraishi [16] concluded that wave functions calculated by the pseudopotential method lack a precise description around the atomic core regions. Furthermore, they suggested that momentum matrix elements cannot be directly estimated from these wave functions because the functions are smoother around the atomic cores, while the actual wave functions oscillate greatly. To fix the error, a core-repair term was added. By including the correction, significant improvement was indeed achieved for zinc-blende and wurtzite GaN. However, momentum matrix elements for polysilane, siloxene, and GaAs calculated with the correction and without it differ from each other by only 5.43, 3.0, and 1.8%, respectively. Wang and Zunger [11], however, had previously found a larger increase in the momentum matrix elements. To complicate matters further, Levine and Allan [19] found that, even within a scissors approximation, the velocity operator becomes renormalized.

[1]This article was submitted by the authors in English.

It should be noted that the correctness of the calculated and experimentally determined values of E_p is also being debated. Efros and Rosen [20], for example, concluded that Fu, Wang, and Zunger's calculation result of $E_p = 14.98$ eV for bulk InP using a direct diagonalization method [21] is smaller than the measured value 20.6 eV, which indicates an underestimation of the coupling between the conduction and valence bands and an overestimation of the influence of the remote bands. However, even the values of E_p extracted from the experiments have an intrinsic scatter. For bulk InP, for example, experimental values of E_p vary from 16.6 [22] to 20.7 eV [23]. Therefore, the question of whether the momentum matrix elements calculated by the LDA are correct is still open.

It should also be noted that the above-mentioned problems are relatively less studied in II–VI semiconductors, which have a cation *d* band inside the main valence band playing a significant role in their electronic structures [24–29]. In III–V semiconductors the *d* levels are several eV lower in their energy than the lowest *sp* valence band states [30]. So the effect of the *d* states on the electronic structure of III–V compounds can be disregarded. In earlier research, the strong *p*–*d* coupling in II–VI semiconductors has usually been taken into account by including the *d* electrons (i) in the core, but also including nonlinear core corrections for exchange and correlation, and (ii) in the valence complex [24–26], but keeping the *s* and *p* semicore electrons in the core. Currently, the description of *p*–*d* coupling is still being improved. Despite numerous studies, the question as to which of the approaches related to *p*–*d* coupling is correct and consistent with $\mathbf{k} \cdot \mathbf{p}$ band parameters is still open.

In this paper we provide the first systematic study of eigenvalues at Γ, *X*, and *L*; the Kane momentum matrix elements E_p and E_p' (defined as $2P^2/m_0$ in eV) corresponding to the fundamental direct *p*–*s* energy gap E_g and the *p*–*p* gap E_g' at point Γ; the conduction-band effective masses m_c^{001}, m_c^{011}, and m_c^{111}; the heavy-hole effective masses m_{hh}^{001}, m_{hh}^{011}, and m_{hh}^{111}; the light-hole effective masses m_{lh}^{001}, m_{lh}^{011}, and m_{lh}^{111}; and the Luttinger parameters γ_1^L, γ_2^L, and γ_3^L. Furthermore, we answer the question as to whether band parameters calculated within the framework of the LDA are correct.

2. COMPUTATIONAL DETAILS

2.1. Local-Density Approximation

Ab initio calculations were performed for III–V (AlP, AlAs, AlSb, GaP, GaAs, GaP, InP, InAs, and InSb) and some II–VI (ZnS, ZnSe, ZnTe, CdS, CdSe, and CdTe) semiconductors with a zinc-blende structure. We did not study the II–VI compounds HgS, HgSe, and HgTe, because it is well known that spin–orbit coupling (which is not accounted for in this work) plays a significant role [24]. The unit cell considered consists of two atoms of Group-III (II) at (0, 0, 0) and an atom of Group-V (VI) at (a/4, a/4, a/4), where a is the lattice constant.

Ab initio pseudopotentials were generated using the Trouillier–Martins method [31]. We have considered *s*, *p* and *d* as valence states in order to build the pseudopotential for the atoms of Group-III and V using the *p* potential as the local potential, while *s* and *d* are taken as the nonlocal parts. We determined E_{cut} by requiring convergence of the total energy E_{tot}. For all the III–V semiconductors considered, $E_{\text{cut}} = 60$ Ry was used.

To study the II–VI compounds, *s*, *p*, and *d* states were considered as valence states. Pseudopotentials for Group-II atoms were generated in two ways: (i) including the *d* electrons, which are inside the valence shell, in the valence complex while keeping the semicore *s* and *p* states in the core, and (ii) including the *d* electrons in the core. For the latter case, we used $E_{\text{cut}} = 30$ Ry, and a nonlinear exchange correlation was added, which is known to give better agreement with experimental data [25]. For the former case, convergent results were obtained for $E_{\text{cut}} = 70$ Ry. The semicore *d* electrons of the III–V compounds were included in the core because, as discussed in Section 1, the energy level of the electrons arc far below the outermost *sp* levels [30] and the electrons are not expected to signifcantly affect the band structure of the compounds.

Band-structure calculations were performed using the PEtot code developed by L.-W. Wang [32], which uses the ab initio pseudopotential method within the LDA and neglects spin–orbit coupling. The Pulay–Kerker scheme was used for self-consistent potential mixing. In addition, *g*-space Kleinman–Bylander nonlocal pseudopotential implementations were used with a mask function scheme, without the need for preprocessing the pseudopotentials. The LDA exchange-correlation contribution was accounted for by means of Perdew and Zunger's parametrization [33] of the calculations by Ceperley and Alder [34]. The self-consistent solution of the one-electron Kohn–Sham equation was performed using a planewave pseudopotential algorithm [35].

The potential for the unit cell under consideration was found by performing self-consistent calculations using 10 special *k* points in the Brillouin zone. Then, using this potential, eigenenergies at the special *k* points were found by nonconsistent calculations.

2.2. Band Parameters

Carrier effective masses are defined as

$$\frac{1}{m_c(\mathbf{k}_0)} = \frac{1}{\hbar^2}\frac{\partial^2 E(\mathbf{k})}{\partial k^2}\bigg|_{\mathbf{k}=\mathbf{k}_0} \quad (1)$$

Table 1. Experimental [37–40] and LDA (a_0, ad_0) lattice constants (Å) for the zinc-blende III–V and II–VI semiconductors with *d* electrons of Group-II atoms included in the core (a_0) and in the valence complex (ad_0)

	AlP	AlAs	AlSb	GaP	GaAs	GaSb	InP	InAs	InSb
a_0	5.4131	5.6246	6.0788	5.2836	5.5073	5.9380	5.6591	5.8564	6.2863
Experiment [39]	5.4670	5.6600	6.1355	5.4512	5.6533	6.0959	5.8687	6.0583	6.4794
	ZnS	ZnSe	ZnTe	CdS	CdSe	CdTe			
a_0	4.8674	5.1706	5.6730	5.3038	5.5639	6.0517			
ad_0	5.3404	5.6202	6.0072	5.8064	6.0572	6.4174			
Experiment [37]	5.4102	5.6676	6.1037	5.8180	6.0520	6.4860			
Experiment [38]	5.4110	5.6690	6.0890	5.8300	6.0840	6.4800			
Experiment [40]	5.4100	5.6680	6.1000	5.8250	6.0520	6.4820			

for a direction **k** about some point $\mathbf{k}_0$ in the Brillouin zone. We studied effective masses along [001], [011] and [111] directions in the vicinity of $\mathbf{k}_0 \equiv \Gamma(0, 0, 0)$ point. The masses can, in principle, be calculated by the $\mathbf{k} \cdot \mathbf{p}$ theory equation (see, e.g., [2]). In this study, we calculated the band energies at a sequence of *k* points around Γ and calculated m_c directly from Eq. (1).

We considered the conduction-band effective masses m_c^{001}, m_c^{011}, and m_c^{111}; the heavy-hole effective masses m_{hh}^{001}, m_{hh}^{011}, and m_{hh}^{111}; and the light-hole effective masses m_{lh}^{001}, m_{lh}^{011}, and m_{lh}^{111}. To calculate the effective masses, 11 *k* points were used in the ranges from $(2\pi/a)/(0, 0, -1/20)$ to $(2\pi/a)/(0, 0, 1/20)$ for the direction [001], from $(2\pi/a)/(0, -1/20, -1/20)$ to $(2\pi/a)/(0, 1/20, 1/20)$ for the direction [011], and from $(2\pi/a)/(-1/20, -1/20, -1/20)$ to $(2\pi/a)/(1/20, 1/20, 1/20)$ for the direction [111]. The momentum matrix elements were determined at the Γ point.

Following [36] and using the calculated effective-mass values, the Luttinger valence-band parameters γ_1^L, γ_2^L, and γ_3^L were calculated as

$$\gamma_1^L = \frac{1}{2}\left(\frac{1}{m_{lh}^{001}} + \frac{1}{m_{hh}^{001}}\right), \quad (2)$$

$$\gamma_2^L = \frac{1}{4}\left(\frac{1}{m_{lh}^{001}} - \frac{1}{m_{hh}^{001}}\right), \quad (3)$$

$$\gamma_3^L = \frac{1}{4}\left(\frac{1}{m_{lh}^{001}} + \frac{1}{m_{hh}^{001}} - \frac{2}{m_{hh}^{111}}\right). \quad (4)$$

Energies and momentum matrix elements are given in eV, and effective masses are given in units of the electron rest mass m_0 throughout the paper. All the calculations were performed for two values of the lattice constants: (i) determined experimentally (to be called the experimental lattice constant hereafter) and (ii) determined by a search of the total energy minimum (to be called the theoretical lattice constant hereafter).

3. RESULTS

3.1. Lattice Constants

It will become clear that band structure depends critically upon such parameters as the lattice constant (among others). By a search of the total-energy minimum, lattice constants were found (Table 1) that, for the III–V compounds and II–VI semiconductors with *d* electrons included in the valence complex, differ from those determined experimentally by <3 and <1.5%, respectively. However, if the *d* electrons of Group-II atoms are included in the core, then calculated lattice constants for the II–VI compounds differ significantly from experimentally determined ones (>7%). It should be noted that experimentally determined lattice constants for II–VI compounds given in handbooks differ somewhat from each other. For example, in [37], the lattice constant for CdSe is $a = 6.052$ Å while in another handbook, [38], $a = 6.084$ Å. Our calculated lattice constant is between the two experimental values. Since, for all the other semiconductors considered in this study, the calculated lattice constant is always smaller than the experimentally determined one, we used $a = 6.084$ Å for CdSe from [38] for band-structure calculations using the experimental lattice constant. For other II–VI compounds, we used the experimental lattice constants given in [37].

3.2. Eigenvalues

Self-consistent and nonconsistent band-structure calculations were performed using both calculated and experimentally determined lattice constants. As we disregarded spin–orbit coupling, the valence band maximum at point Γ is triple degenerated for all the compounds considered. For III–V and II–VI compounds, eigenvalues at Γ, *X*, and *L* are given in Table 2, and they are in general agreement with previous calculations [9, 13, 14, 24–26, 29, 41–43]. Band gaps (E_g) for AlP, AlAs, AlSb, and GaP are indirect, with the valence band maximum at point Γ and conduction band minimum at point *X*, while those for other III–V compounds are direct. As expected, band gaps for AlP, AlAs, AlSb,

Table 2. Eigenvalues (eV) at Γ, *X*, and *L* for the zinc-blende III–V and II–VI compounds calculated using the theoretical (a_0, ad_0) and experimental (a_e, ad_e) lattice constants including the *d* electrons of Group-II atoms in the core (a_0, a_e) and in valence complex (ad_0, ad_e). The results are compared to experimental data [39, 40] and theoretical calculations within **k** · **p** theory [2], LDA, and GW [25]

		AlP	AlAs	AlSb	GaP	GaAs	GaSb	InP	InAs	InSb
Γ_1^c	a_0	3.3457	2.1517	1.6488	2.5982	1.1885	0.5885	1.3831	0.4131	0.2986
	a_e	3.0929	1.9979	1.4354	1.7736	0.5337	0.0000	0.7205	0.0000	0.0000
X_1^c	a_0	1.4194	1.3127	1.1291	1.4058	1.2861	0.8275	1.5522	1.3821	1.2050
	a_e	1.4739	1.3437	1.1766	1.5872	1.4245	0.9086	1.7198	1.5340	1.3487
L_1^c	a_0	2.7809	2.1399	1.3611	1.9424	1.2413	0.5738	1.8019	1.2331	0.7186
	a_e	2.6692	2.0680	1.2806	1.6262	0.9888	0.3868	1.4918	0.9624	0.5300
Experiment [39]		3.6200	3.1400	2.2190	2.7800	1.4240	0.7500	1.3400	0.4180	0.1800
k · **p** [2]		5.1200	3.0600		2.8700	1.5200	0.8100	1.4200	0.4200	0.2370

		ZnS	ZnSe	ZnTe	CdS	CdSe	CdTe
Γ_1^c	a_0	5.325	3.908	2.971	3.646	2.780	2.186
	a_e	2.933	1.968	1.587	2.155	1.513	1.217
	ad_0	2.004	1.180	1.077	0.913	0.394	0.499
	ad_e	1.868	1.076	0.901	0.901	0.371	0.420
X_1^c	a_0	2.953	2.594	1.971	3.379	2.932	2.329
	a_e	3.618	3.171	2.451	3.757	3.322	–1.263
	ad_0	3.132	2.764	2.125	3.301	2.923	2.364
	ad_e	3.242	2.820	2.167	3.311	2.943	2.427
L_1^c	a_0	5.159	4.073	2.621	–0.487	4.003	2.750
	a_e	3.985	3.107	2.117	3.908	3.186	–0.462
	ad_0	3.128	2.395	1.610	2.770	2.193	1.605
	ad_e	3.084	2.351	1.563	2.761	2.179	1.581
Experiment [40]		3.680	2.700	2.280	2.500	1.900	1.490
k · **p** [2]		3.800	2.820	2.390	2.560	1.840	1.600
LDA [25]		2.370	1.450	1.330	1.370	0.760	0.800
GW [25]		3.980	2.840	2.570	2.830	2.010	1.760

GaP, GaAs, and GaSb calculated using both of the lattice constants are underestimated, while those for InP, InAs, and InSb are overestimated for the calculated lattice constant and underestimated for the experimentally determined lattice constant. The overestimate can be related to the small gap and the disregarding of the spin–orbit coupling; similar results were obtained by Huang and Ching [14]. One can also see that the LDA calculations of different authors vary significantly. For example, the direct band gap of GaAs, GaSb, InAs, and InSb calculated by Geller *et al.* [10] within the LDA using the full-potential linearized augmented plane-wave (FLAPW) method was 0.25, –0.3, –0.53, and –0.57 eV, respectively, while that of AlAs, GaAs, and GaSb calculated by Wei and Zunger [41] within the LDA was 1.84, 0.15, and –0.165 eV, respectively. The band gaps of III–V compounds that we calculated are similar to those of [8, 9, 15].

It should also be noted that the direct band gaps calculated in this study using the calculated lattice constant are larger than those found using the experimentally determined lattice constants. This can be attributed, in part, to the direct-gap increase with compression (equivalent to small *a*). In the latter case, band gaps can even be zero for GaSb, InAs, and InSb. Moreover, the band gaps for AlP, GaP, GaAs, GaSb, InP, InAs, and InSb calculated using the calculated lattice constants are much closer to the experimental band gaps.

For the II–VI compounds, the calculated eigenenergies are in general agreement with previous calculations [24–26]. If the *d* electrons of the atoms of Group-II are included in the core with nonlinear core corrections,

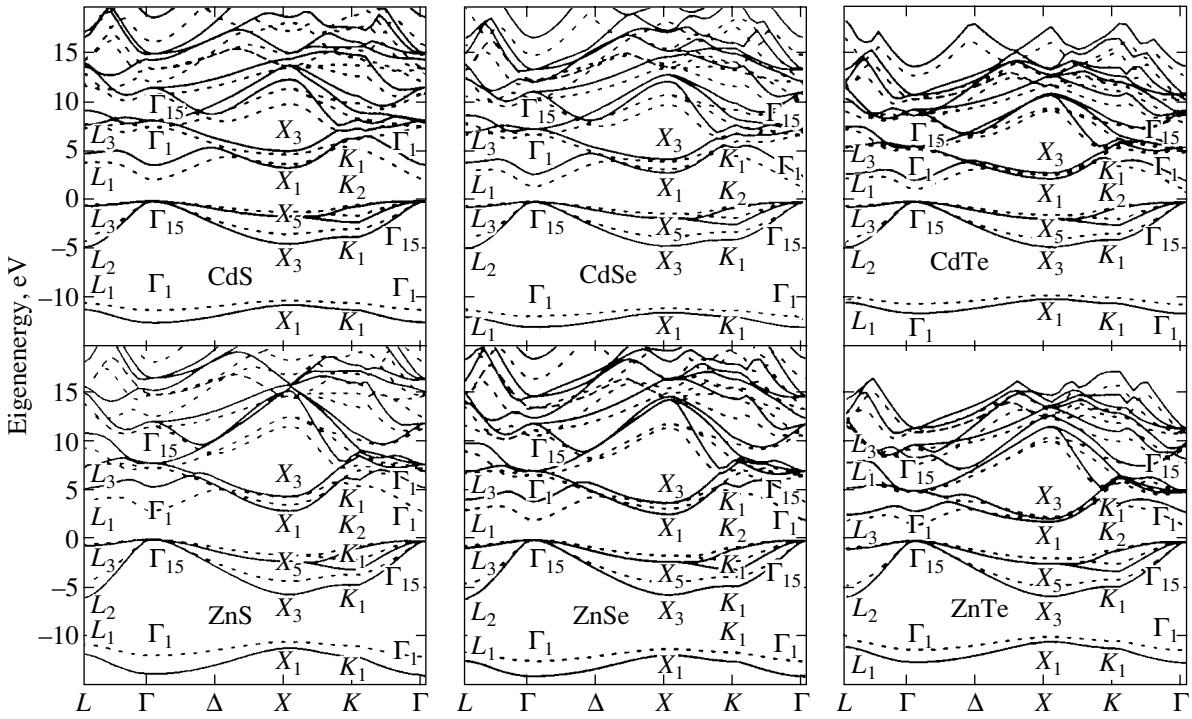

Fig. 1. Results of the band-structure calculations. Solid curves are calculated with theoretical lattice constants (a_0) and dashed curves with experimental ones (a_e).

and theoretical lattice constants are used in band-structure calculations, then the band gaps of all the II–VI compounds (except CdSe and CdTe) become indirect, with the valence-band maximum at point Γ and the conduction-band minimum at point *X* (see Table 2 and Fig. 1), which contradicts the experimental data [37, 38, 40]. This error is because of the big difference between the LDA lattice constants and the experimentally determined ones (see Table 1). If the experimental lattice constants are used in band-structure calculations, then eigenenergies (Table 2 and Fig. 1) are much more consistent with the LDA [25, 26] and GW [25] calculations.

It is well known that the inclusion of the *d* electrons of the atoms of Group-II in the valence complex causes strong *p*–*d* coupling of the upper valence band with *d* states, which results in a repulsion of the former upward and reduces the band gap [24–26, 29]. Our results in Table 2 and Fig. 2 are consistent with this statement. Furthermore, the energy levels of the *d* electrons (Γ_{12}^d and Γ_{15}^d) fall between the *s* and *p* valence bands, which is in good agreement with the calculations of Wang and Klein [13] for ZnS and ZnSe using a linear combination of Gaussian orbitals method with the LDA. However, the energies of the bands are much higher than the experimentally determined ones [30], which indicates an overestimation of the *p*–*d* coupling by the LDA, in agreement with the calculations in [13, 24–26, 29]. The Γ_{12}^d and Γ_{15}^d bands are almost dispersionless and very narrow. It indicates that these states are well localized. Therefore, the above-mentioned overestimation is consistent with Wang and Klen's statement [13]: "…the more these lower states are localized (narrower bands), the larger the disagreement is…." Comparing Fig. 1 with Fig. 2, one can see that, due to the involvement of *d* electrons in the valence shell, the band gaps are significantly reduced for the II–VI compounds considered. Note that the difference between the eigenenergies calculated using the theoretical and the experimental lattice constants in Fig. 2 is smaller than that in Fig. 1. The small difference of the former is because the LDA and experimental lattice constants are close to each other.

Analysis of Table 2 (also, Fig. 1 and Fig. 2) shows that the band gaps calculated in this work using the experimental lattice constant and including the *d* electrons in the core are much bigger than those of previous ones calculated using the LDA [25] and smaller than those determined by the GW [25] approach using experimental lattice constants. Our calculated band gap for ZnS is also smaller than 3.55 eV [26]. However, our calculated band gaps, obtained with the *d* electrons included in the valence complex, are in good agreement with 1.02 eV for ZnTe, 0.47 eV for CdTe [24], and 1.84 eV for ZnS [26], which are much smaller than the experimental values.

The eigenvalues at some of the special *k* points for a number of the compounds considered is in general agreement with other LDA calculations (e.g., those by Huang and Ching [14] using a minimal basis semi–ab

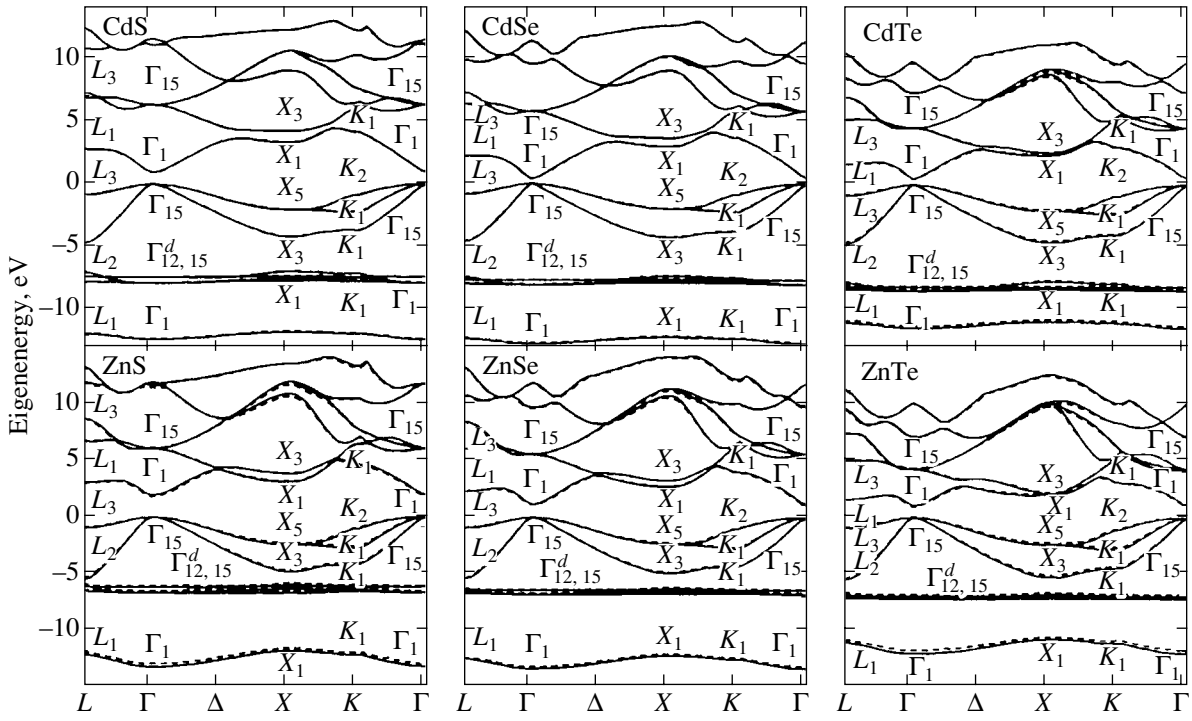

Fig. 2. Results of the band-structure calculations with the inclusion of the *d* electrons of Group-II atoms in the valence complex. Solid curves are calculated with theoretical lattice constants (ad_0) and dashed curves with experimental ones (ad_e).

initio approach and by Wang and Klein [13] using the LDA). However, the agreement is not systematic. Note that the discrepancies between the theoretical band gaps of different authors can be related to the accuracy of the LDA calculations; different parameters used to generate the pseudopotentials of the atoms of Group-II, III, V and VI; and different values of the E_{cut} and lattice constant.

The other important conclusions that can be derived from this comparative analysis is that, systematically, the band gaps (E_g) are underestimated and the energies of the semicore states are overestimated. However, this error, as discussed in Section 1, is not an artifact of numerical band-structure approximations, rather it is a failure of DFT.

3.3. Momentum Matrix Elements and Luttinger Parameters

Momentum matrix elements are the key parameters when discussing the optical properties of semiconductors. Therefore, to study the problem using ab initio band structure calculations is an important step. Our calculated results for E_p and E_p', and the Luttinger parameters γ_1^L, γ_2^L, and γ_3^L are given in Table 3 and Table 4 for the III–V and II–VI compounds, respectively.

Analysis of Tables 3 and 4 shows that the momentum matrix elements calculated in this study are much smaller than those found from $\mathbf{k}\cdot\mathbf{p}$ theory for all the semiconductors considered except AlP, ZnS and ZnSe for which good agreement was achieved. The small values of E_p can be related to the underestimation of the coupling of the valence-band maximum [20]. For InP our result agrees well with that of Fu, Wang, and Zunger [21, 44] calculated by the direct diagonalization method. In addition, $E_p' < E_p$ for all the semiconductors apart from GaSb, InAs, and InSb that have zero band gaps in the LDA calculations using experimentally determined lattice constants.

Momentum matrix elements calculated when the *d* electrons of Group-II atoms are kept in the core are larger than those found for the *d* electrons included in the valence complex. This indicates that the *d* electrons result in the underestimation of the coupling between the conduction band minimum and valence band maximum. The former approach gives better agreement with tight-binding and LMTO calculations [5] for ZnS, ZnSe, and ZnTe, and also with $\mathbf{k}\cdot\mathbf{p}$ calculations [2] for ZnS. However, for all the II–VI compounds considered other than ZnTe, the value of E_p' is much smaller than that calculated in [5], where it was found that the value of E_p' is comparable to that of E_p. Note that the momentum matrix element between the semicore Γ_{15}^d states and conduction band minimum (not shown in Table 4) is between 1 and 3 eV, which is smaller than E_p but

Table 3. Momentum matrix elements (eV) and Luttinger parameters for zinc-blende III–V compounds using the theoretical (a_0) and experimental (a_e) lattice constants

		E_p	E'_p	γ_1^L	γ_2^L	γ_3^L
AlP	a_0	17.183	0.015	3.696	0.826	1.454
	a_e	16.807	0.036	3.750	0.893	1.494
	k · **p** [2]	17.700		3.470	0.060	1.150
AlAs	a_0	15.678	0.144	5.203	1.526	2.179
	a_e	15.437	0.172	5.355	1.628	2.263
	[39]	21.100		3.45, 3.25	0.68, 0.64	1.29, 1.21
	k · **p** [2]	21.100		4.040	0.780	1.570
AlSb	a_0	14.548	0.592	5.810	1.659	2.401
	a_e	14.206	0.634	6.180	1.898	2.604
	k · **p** [2]	18.700		4.150	1.010	1.750
GaP	a_0	18.758	0.150	5.729	1.222	2.289
	a_e	17.496	0.366	6.517	1.872	2.672
	[39]	22.200		4.050	0.490	1.250
	k · **p** [2]	22.200		4.200	0.980	1.660
GaAs	a_0	17.189	0.440	10.336	3.526	4.479
	a_e	16.136	0.634	18.198	7.674	8.493
	[39]	25.700		6.80–7.20	2.10–2.50	1.00–2.90
	k · **p** [2]	25.700		7.650	2.410	3.280
	k · **p** [2], TB [45]	22.500	0.025	7.070	2.400	3.050
	Experiment [17]	22.53–28.9	3.55–6.0	5.64–7.21	1.35–2.49	2.49–3.09
	Experiment [18]	27.860	2.36	4.80–8.56	1.22–2.90	1.85–3.74
	LDA [15]	15.820	2.27	9.270	3.120	4.010
GaSb	a_0	15.726	0.997	16.291	6.305	7.371
	a_e	0.000	8.540	115.200	56.033	56.933
	k · **p** [2]	22.400		11.800	4.030	5.260
	[39]	25.00, 26.1		13.10, 13.30	4.40, 4.50	5.70, 6.00
InP	a_0	15.456	0.048	6.638	3.033	2.760
	a_e	14.314	0.205	9.768	3.836	4.423
	[39]	17.000		4.95–5.15	0.94–1.65	1.62–2.35
	k · **p** [2]	20.400		6.280	2.080	2.760
InAs	a_0	14.427	0.169	19.481	8.428	9.171
	a_e	0.000	7.132	33.807	15.819	16.427
	k · **p** [2]	22.200		19.670	8.370	9.290
InSb	a_0	13.866	0.454	24.259	10.681	11.504
	a_e	0.000	7.152	23.493	10.545	11.220
	[39]	21.200		33.50, 40.10	14.50, 18.10	15.70, 19.20
	k · **p** [2], TB [45]	23.100		35.080	15.640	16.910

about 10 times bigger than those between the other remote bands for all the II–VI compounds considered. This factor can be related to the LDA overestimation of the influence of the valence band semicore *d* states. Matrix elements between the lowest conduction band Γ_1^c and valence band Γ_{12}^d, and the remote conduction band states Γ_1^c and Γ_{12}^c is zero, which is related to the symmetry properties of the crystal.

Luttinger parameters calculated in this study for the III–V compounds in Table 3 are much smaller than those found by **k** · **p** theory or experiments, though the order of magnitude is the same. For II–VI semiconduc-

Table 4. Momentum matrix elements (eV) and Luttinger parameters for II–VI semiconductors with *d* electrons of Group-II atoms included in the core (a_0, a_e) and in the valence complex (ad_0, ad_e) using the theoretical (a_0, ad_0) and experimental (a_e, ad_e) lattice constants. The results are compared to calculations within other methods, such as TBLMTO [5] and $\mathbf{k}\cdot\mathbf{p}$ [2, 23]

		E_p	E'_p	γ_1^L	γ_2^L	γ_3^L
ZnS	a_0	19.649	0.008	3.158	0.746	1.262
	a_e	14.735	0.279	2.981	0.973	1.278
	ad_0	12.262	0.232	4.113	1.160	1.641
	ad_e	12.013	0.301	4.143	1.241	1.686
	TBLMTO [5]	24.882	20.998	2.120	0.510	1.560
	TBLMTO [5]	15.295	6.708	1.280	0.090	1.140
	$\mathbf{k}\cdot\mathbf{p}$ [2]	20.400		2.540	0.750	1.090
ZnSe	a_0	16.961	0.048	3.954	1.079	1.635
	a_e	12.843	0.545	4.238	1.542	1.882
	ad_0	11.358	0.484	6.465	2.371	2.831
	ad_e	11.146	0.544	6.817	2.530	3.008
	[37]			4.300	1.140	1.840
	$\mathbf{k}\cdot\mathbf{p}$ [23]	23.000				
	TBLMTO [5]	16.230	9.835	3.210	0.750	2.000
	$\mathbf{k}\cdot\mathbf{p}$ [2]	24.200		3.770	1.240	1.670
ZnTe	a_0	16.075	0.507	4.327	1.132	1.759
	a_e	12.758	1.062	4.835	1.721	2.131
	ad_0	12.272	0.907	7.215	2.511	3.123
	ad_e	11.820	1.020	7.790	2.897	3.451
	TBLMTO [5]	19.667		3.440	0.590	2.030
	[37]			3.900	0.600	0.900
	[37]			3.900	0.830	1.300
	[37]			4.000	0.830	1.300
	[37]				0.800	1.700
	$\mathbf{k}\cdot\mathbf{p}$ [2]	19.100		3.740	1.070	1.640
CdS	a_0	15.356	0.000	2.721	0.841	1.152
	a_e	11.631	0.195	2.647	0.975	1.181
	ad_0	9.301	0.219	5.101	1.880	2.224
	ad_e	9.273	0.228	5.121	1.897	2.238
	TBLMTO [5]			3.440	0.970	2.150
	TBLMTO [5]			2.200	0.350	1.530
	$\mathbf{k}\cdot\mathbf{p}$ [23]	21.000				
CdSe	a_0	13.563	0.036	3.265	1.162	1.443
	a_e	10.125	0.374	3.806	1.515	1.735
	ad_0	8.670	0.384	11.694	5.144	5.511
	ad_e	8.600	0.405	12.160	5.394	5.752
	TBLMTO [5]			4.40	1.600	2.680
	$\mathbf{k}\cdot\mathbf{p}$ [23]	20.000				
CdTe	a_0	13.600	0.256	3.862	1.258	1.664
	a_e	10.732	0.663	4.353	1.709	1.982
	ad_0	9.735	0.628	10.072	4.207	4.652
	ad_e	9.488	0.697	11.208	4.831	5.245
	TBLMTO [5]	21.066	5.098	4.340	1.600	2.660
	[37]			5.300	1.700	2.000
	[37]			4.110	1.080	1.950
	$\mathbf{k}\cdot\mathbf{p}$ [23]	18.500				
	$\mathbf{k}\cdot\mathbf{p}$ [2]	20.700		5.290	1.890	2.460

Table 5. Effective masses (in units of the free-electron mass m_0) for zinc-blende III–V compounds calculated using the theoretical (a_0) and experimentally determined (a_e) lattice constants. The results have been compared to those calculated within pseudopotential [46], $\mathbf{k}\cdot\mathbf{p}$ [17, 18, 45] and semi–ab initio [14] theories, and to experimental data [17, 18, 45, 46]

		m_c^{001}	m_c^{011}	m_c^{111}	m_{hh}^{001}	m_{hh}^{011}	m_{hh}^{111}	m_{lh}^{001}	m_{lh}^{011}	m_{lh}^{111}
AlP	a_0	0.176	0.176	0.176	0.489	6.272, 0.490	1.270	0.187	0.139	0.128
	a_e	0.170	0.170	0.170	0.509	6.138, 0.509	1.310	0.181	0.137	0.126
	[14]				0.513		1.372	0.211		0.145
AlAs	a_0	0.115	0.115	0.115	0.465	5.199, 0.465	1.183	0.121	0.098	0.092
	a_e	0.110	0.110	0.110	0.476	5.142, 0.476	1.206	0.116	0.095	0.090
	[14]				0.409		1.022	0.153		0.109
	[46]	0.152			0.457		1.087	0.200		0.161
	Experiment [46]	0.150			0.478		1.149	0.208		0.166
	LDA [9]		0.122			0.480			0.129	
	Experiment [9]		0.124			0.491			0.153	
AlSb	a_0	0.110	0.110	0.110	0.401	3.746, 0.401	0.992	0.110	0.088	0.083
	a_e	0.100	0.100	0.100	0.419	3.769, 0.419	1.029	0.100	0.083	0.078
	[14]				0.336		0.872	0.123		0.091
GaP	a_0	0.128	0.128	0.128	0.305	2.444, 0.305	0.731	0.122	0.090	0.083
	a_e	0.100	0.100	0.100	0.361	2.687, 0.361	0.853	0.097	0.079	0.074
	[14]				0.419		0.997	0.160		0.113
GaAs	a_0	0.058	0.057	0.058	0.304	2.353, 0.305	0.726	0.058	0.049	0.047
	a_e	0.030	0.030	0.030	0.351	2.551, 0.351	0.826	0.030	0.028	0.027
	[14]				0.395		0.934	0.089		0.072
	[15]	0.067			0.460		0.950	0.085		0.077
	Experiment [17]				0.340–0.475		0.450–1.030	0.082–0.120		0.070–0.082
	$\mathbf{k}\cdot\mathbf{p}$ [18]				0.340–0.800		0.520–4.000	0.082–0.142		0.075–0.120
GaSb	a_0	0.035	0.035	0.036	0.272	2.074, 0.272	0.646	0.035	0.031	0.030
	a_e	0.004	0.006	0.008	0.219	2.274, 0.319	0.747	0.004	0.006	0.008
	[14]				0.231		0.551	0.052		0.047
InP	a_0	0.095	0.095	0.095	0.389	2.570, 0.389	0.895	0.093	0.078	0.074
	a_e	0.058	0.058	0.058	0.477	2.979, 0.477	1.084	0.057	0.052	0.051
	LDA [42]	0.570			0.430		0.970	0.057		
	SLDA [42]	0.060			0.400		0.900	0.057		
	SEPM [42]	0.095			0.470		1.030	0.097		
	Experiment [42]	0.079, 0.081			0.520, 0.610		0.630, 0.950	0.104, 0.118		
InAs	a_0	0.028	0.028	0.028	0.381	2.524, 0.381	0.878	0.028	0.026	0.026
	a_e	0.015	0.017	0.018	0.461	2.885, 0.461	1.048	0.015	0.016	0.017
	EPM [47]				0.480			0.040		
	LDA [10]	0.094		0.112	0.353			0.046		
	sX [10]	0.022		0.021	0.388			0.025		
	Experiment [10]	0.023			0.410			0.026		
	$\mathbf{k}\cdot\mathbf{p}$ [2]	0.023			0.410			0.026		
	Experiment [2]	0.024			0.410			0.026		
InSb	a_0	0.022	0.023	0.023	0.345	2.333, 0.345	0.799	0.022	0.021	0.021
	a_e	0.023	0.024	0.025	0.416	2.638, 0.416	0.949	0.022	0.023	0.024

Table 6. Effective masses (in units of the free-electron mass m_0) for II–VI semiconductors including the *d* electrons of atoms of Group-II in the core (a_0, a_e) and in the valence complex (ad_0, ad_e), and using the LDS (a_0, ad_0) and experimentally determined (a_e, ad_e) lattice constants. In [2, 37] all the effective masses (except CdTe and m_c^{011} for ZnS, [37]) are given without specific directions and are determined experimentally [37]

		m_c^{001}	m_c^{011}	m_c^{111}	m_{hh}^{001}	m_{hh}^{011}	m_{hh}^{111}	m_{lh}^{001}	m_{lh}^{011}	m_{lh}^{111}
ZnS	a_0	0.193	0.193	0.193	0.601	8.463, 0.601	1.578	0.215	0.161	0.149
	a_e	0.183	0.183	0.183	0.966	8.938, 0.961	2.350	0.203	0.171	0.162
	ad_0	0.145	0.145	0.145	0.557	2.884, 0.556	1.203	0.155	0.127	0.119
	ad_e	0.142	0.141	0.141	0.602	3.071, 0.602	1.297	0.151	0.126	0.119
	Experiment [37]	0.340	0.184			1.760, 1.121			0.230	0.169
	k · **p** [2]		0.280							
ZnSe	a_0	0.146	0.146	0.146	0.557	7.505, 0.561	1.462	0.164	0.129	0.120
	a_e	0.126	0.126	0.126	0.866	7.550, 0.867	2.113	0.137	0.120	0.115
	ad_0	0.083	0.084	0.084	0.581	3.651, 0.559	1.246	0.089	0.078	0.075
	ad_e	0.081	0.081	0.081	0.569	3.078, 0.571	1.248	0.084	0.075	0.073
	Experiment [37]	0.142	0.147	0.160						
	Experiment [40]	0.130	0.170	0.570	0.750					
	k · **p** [2]		0.140							
	[14]				1.814		0.784	0.191		0.147
ZnTe	a_0	0.146	0.147	0.147	0.485	5.501, 0.484	1.236	0.152	0.118	0.110
	a_e	0.118	0.118	0.118	0.717	5.975, 0.719	1.742	0.121	0.105	0.101
	ad_0	0.081	0.081	0.081	0.456	2.800, 0.456	1.032	0.082	0.071	0.068
	ad_e	0.073	0.073	0.073	0.501	2.988, 0.501	1.126	0.074	0.066	0.063
	Experiment [37]	0.122	0.128	0.130						
	Experiment [40]	0.130			0.600					
	k · **p** [2]		0.180							
	[14]				0.541		1.354	0.155		0.119
CdS	a_0	0.196	0.197	0.197	0.962	12.800, 0.953	2.400	0.227	0.184	0.173
	a_e	0.191	0.190	0.190	1.433	12.621, 1.433	3.499	0.218	0.192	0.184
	ad_0	0.108	0.108	0.108	0.745	3.249, 0.745	1.532	0.113	0.101	0.097
	ad_e	0.107	0.107	0.107	0.754	3.285, 0.754	1.551	0.112	0.101	0.097
	Experiment [40]		0.140		0.510					
	[14]				0.929		1.935	0.201		0.161
CdSe	a_0	0.079	0.104	0.116	1.063	46.105, 0.943	2.643	0.179	0.147	0.139
	a_e	0.134	0.133	0.133	1.289	8.295, 1.309	2.982	0.146	0.133	0.129
	ad_0	0.045	0.045	0.045	0.711	3.282, 0.712	1.491	0.045	0.043	0.043
	ad_e	0.043	0.043	0.043	0.729	3.355, 0.729	1.524	0.044	0.042	0.041
	Experiment [37]	0.11								
	Experiment [40]		0.110		0.44					
CdTe	a_0	0.145	0.146	0.146	0.743	7.910, 0.742	1.874	0.157	0.132	0.125
	a_e	0.122	0.122	0.122	1.070	8.542, 1.070	2.567	0.129	0.117	0.113
	ad_0	0.054	0.054	0.054	0.603	3.110, 0.603	1.304	0.054	0.051	0.050
	ad_e	0.047	0.048	0.048	0.647	3.292, 0.647	1.393	0.048	0.045	0.045
	Experiment [37]	0.094	0.096	0.095	0.720	0.810	0.840	0.130	0.120	0.120
	Experiment [37]	0.099								
	Experiment [40]		0.90		0.720	0.840	0.120			
	k · **p** [2]		0.096							
	[14]				0.478		1.114	0.125		0.095

tors, we found that the involvement of *d* electrons in the core significantly reduces the Luttinger parameters compared to those with *d* electrons in the valence complex (see Table 4). However, the former approach gives better agreement with $\mathbf{k} \cdot \mathbf{p}$ theory [2], and with tight-binding and linear muffin-tin-orbital (TBLMTO) calculations [5]. This analysis indicates that, from LDA calculations, one can sometimes attain the correct momentum matrix elements and Luttinger parameters; however, this can not be achieved systematically.

3.4. Effective Masses

Carrier effective masses are one of the important parameters in any discussion of transport phenomena, exciton effects, electron–hole liquids, and so on in semiconductors. They are usually determined by cyclotron resonance, electroreflectance measurements or from analysis of transport data. In this section we present the results of our calculations of electron effective masses at the conduction band minimum and hole effective masses at the valence band maximum. The results for III–V and II–VI compounds are given in Table 5 and Table 6, respectively. For the indirect gap semiconductors AlP, AlAs, AlSb, and GaP, m_c is usually discussed for the conduction band minimum at Γ and points other than Γ (say *X* or *L*). In this study, we consider all effective masses only for point Γ.

Analysis of Tables 5 and 6 shows that the effective masses of conduction band electrons are isotropic, while those of the holes are anisotropic. The effective masses for heavy-holes (m_{hh}) and light-holes (m_{lh}) correspond to the splitting of the Γ_{15}^{v} state into double and single degenerate bands, respectively. Since we have disregarded spin–orbit coupling, the split-off mass band is not discussed. Analysis of Table 5 shows that conduction-band effective masses for AlP, AlSb, GaP, GaSb, and InSb are much smaller than the m_c = 0.25, 0.18, 0.17, 0.22, and 0.13 calculated by $\mathbf{k} \cdot \mathbf{p}$ theory [2]. One can also see that conduction-band effective masses calculated using the LDA lattice constant are closer to experimental data than those calculated using the experimental lattice constant. Note that all the effective masses for AlP, AlAs, AlSb, and InSb using the theoretical and experimentally determined lattice constants do not differ from each other very much, while the difference is significant for the other III–V semiconductors studied.

Analysis of Table 5 shows that the values of m_{hh}^{001} and m_{hh}^{111} for AlAs, GaAs, InP, and InAs calculated in this study agree well with previous calculations and experimental data, while such an agreement was not achieved for m_{lh}^{001} and m_{lh}^{111}. Due to the lack of experimental or calculated data, we could not make such a comparison for other semiconductors and for effective masses in other directions. For InP, InAs, and InSb, note that not only the band gaps but also conduction-band effective masses are overestimated. This indicates that there is a correlation between changes in the band gap and the conduction-band effective mass, which is qualitatively consistent with the $\mathbf{k} \cdot \mathbf{p}$ theory (see, e.g., [2]). Moreover, distinct from Fiorentini and Baldereschi [8, 9], none of the conduction-band effective masses for III–V compounds apart from AlAs agree with the experimental data.

Analysis of Table 6 shows that the effective masses of all the II–VI compounds calculated when the *d* electrons are kept in the core is bigger than those found when including the *d* electrons in the valence complex. It indicates that the semicore *d* electrons result not only in an underestimation of the band and coupling between the valence band maximum and conduction band minimum, but also change the dispersion around point Γ. Our calculated values of the light-hole effective masses (m_{lh}) are in good agreement with experimental data for ZnS and CdTe. Due to the lack of theoretical or experimental data we could not make such a comparison for the other II–VI compounds. Calculated heavy-hole effective masses (m_{hh}) differ significantly from those of [2, 37, 40] for all the II–VI compounds considered other than CdTe. For the latter, good agreement is achieved if the theoretical lattice constant is used.

The effective masses for all the compounds considered agree somewhat with those calculated by Huang and Ching [14] using a minimal basis semi–ab initio approach and by Wang and Klein [13] using the LDA, but the agreement is not systematic. Based on the above analysis, one can say that LDA calculations can sometimes provide the correct values of conduction or valence-band effective masses in some of the specific directions. However, it is not systematic.

4. CONCLUSION

In summary, band-structure calculations were performed for III–V and II–VI semiconductors with a zinc-blende structure. By a search of the total energy minimum, lattice constants were found that differ from the experimentally determined ones by <3% for III–V compounds, and by 1.5 and 7% for the II–VI semiconductors with the *d* electrons of Group-II atoms included into the valence shell and into the core, respectively.

Band parameters calculated within the LDA correctly have a tendency to be smaller than those determined experimentally or calculated theoretically within the $\mathbf{k} \cdot \mathbf{p}$, tight-binding, or semi-empirical methods. From this point of view, our results are in general agreement with those obtained using the other ab initio codes.

The difference of the calculated direct band gaps for III–V compounds are in the range from 6.5 to 66% for theoretical lattice constants and from 15 to 100% for experimental lattice constants. The difference for the II–VI semiconductors with the *d* electrons of Group-II atoms included in the core is in the range from 30 to

47% for theoretical lattice constant and from 14 to 28% for experimental lattice constant. If the *d* electrons are included in the valence complex, then the error in the calculation of the band gap becomes significant due to *p*–*d* repulsion.

The momentum matrix elements E_p calculated in this study are smaller than those obtained within the $\mathbf{k} \cdot \mathbf{p}$ theory [2], since the latter is known to be closer to experimental data. For III–V compounds, the difference between the values of E_p obtained within the two theories is in the range from 2.9 to 35% for the theoretical lattice constant and from 21 to 38% for experimentally determined lattice constants. For II–VI compounds with the *d* electrons of Group-II atoms included in the core, the difference is in the range from 3.7 to 34.3% for the theoretical lattice constant and from 27.8 to 48.1% for the experimentally determined lattice constant. Involvement of the *d* electrons in the valence complex increases the error in the calculation of E_p.

The effective masses of conduction band electrons were found to be isotropic, while those of holes were anisotropic. Calculated m_c for the III–V semiconductors differed from experimentally determined m_c by 13 to 23% for the theoretical lattice constant and from 26 to 55% for the experimental lattice constant. For II–VI compounds with the *d* electrons of Group-II atoms included in the core, the difference of the calculated m_c from experimentally determined m_c is in the range from 8 to 54% for the theoretical lattice constant, while that for the experimental lattice constant is in the range from 2 to 46%. We found that the effective masses of all the $A^{II}B^{VI}$ compounds calculated when the *d* electrons are kept in the core are larger than those found when including the *d* electrons in the valence complex. This indicates that the semicore *d* electrons not only result in an underestimation of band gaps and coupling between the valence band maximum and conduction band minimum, but also change the dispersion around point Γ. Furthermore, conduction-band effective masses calculated using the LDA lattice constant are closer to experimental data than those calculated using the experimental lattice constant. The effective masses for all the compounds considered partially agree with those calculated by Huang and Ching [14] using a minimal basis semi–ab initio approach and by Wang and Klein [13], but the agreement is not systematic.

We found that the correctness of the LDA band parameters for all the compounds considered is not systematic. Comparing the LDA band parameters calculated using the LDA and using experimental lattice constants, we conclude that the latter is more preferable to use for LDA band-structure calculation. We showed that consideration of the *d* electrons of Group-II atoms in the core can give more correct band parameters for II–VI compounds. We found that involvement of the *d* electrons of Group-II atoms in the valence shell in the LDA band-structure calculations results in a decrease of band gaps; a increase of lattice constants; a decrease of momentum matrix elements; an increase of Luttinger parameters; and a decrease of electron, heavy-hole and light-hole effective masses in all directions. In this case, only the equilibrium lattice constant can be determined with a high accuracy, while all the other band parameters are inaccurate.

ACKNOWLEDGMENTS

This work was supported by an NSF CAREER award (NSF grant no. 9984059). We thank Dr. Julia Mullen (Worcester Polytechnic Institute) and Dr. L.-W. Wang (NERSC, Lawrence Berkeley National Laboratory) for help with the computations. Band-structure calculations were performed using the PEtot code [32] developed by the U.S. Department of Energy and can be downloaded from http://www.nersc.gov/~linwang/PEtot/PEtot.html.

REFERENCES

1. L. J. Sham and M. Schlüter, Phys. Rev. Lett. **51**, 1888 (1983).
2. P. Lawaetz, Phys. Rev. B **4**, 3460 (1971).
3. M. Willatzen, M. Cardona, and N. E. Christensen, Phys. Rev. B **50**, 18054 (1994).
4. M. Willatzen, M. Cardona, and N. E. Christensen, Phys. Rev. B **51**, 13150 (1995).
5. M. Willatzen, M. Cardona, and N. E. Christensen, Phys. Rev. B **51**, 17992 (1995).
6. L. C. Lew Yan Voon, M. Willatzen, and M. Cardona, Phys. Rev. B **53**, 10703 (1996).
7. L. C. Lew Yan Voon, S. Karazhanov, and W. A. Harrison, Phys. Rev. B **66**, 235211 (2002).
8. V. Fiorentini and A. Baldereschi, J. Phys.: Condens. Matter **4**, 5967 (1992).
9. V. Fiorentini, Phys. Rev. B **46**, 2086 (1992).
10. C. B. Geller, W. Wolf, S. Picozzi, *et al.*, Appl. Phys. Lett. **79**, 368 (2001).
11. L.-W. Wang and A. Zunger, Phys. Rev. B **51**, 17398 (1995).
12. E. O. Kane, Phys. Rev. B **4**, 1910 (1971).
13. C. S. Wang and B. M. Klein, Phys. Rev. B **24**, 3393 (1981).
14. M.-Z. Huang and W. Y. Ching, J. Phys. Chem. Solids **46**, 977 (1985).
15. R. Winkler, in *Proceedings of 24th International Conference on the Physics of Semiconductors*, Ed. by D. Gershoni (World Sci., Jerusalem, 1998).
16. H. Kageshima and K. Shiraishi, Phys. Rev. B **56**, 14985 (1997).
17. T. E. Ostromek, Phys. Rev. B **54**, 14467 (1996).
18. P. Pfeffer and W. Zawadzki, Phys. Rev. B **53**, 12813 (1996).
19. Z. H. Levine and D. C. Allan, Phys. Rev. Lett. **63**, 1719 (1989).
20. A. L. Efros and M. Rosen, Appl. Phys. Lett. **73**, 1155 (1998).

21. H. Fu, L.-W. Wang, and A. Zunger, Appl. Phys. Lett. **71**, 3433 (1997).
22. T. Nakashima, C. Hamaguchi, J. Komeno, and M. Ozeki, J. Phys. Soc. Jpn. **54**, 725 (1985).
23. C. Hermann and C. Weisbuch, Phys. Rev. B **15**, 823 (1977).
24. S.-H. Wei and A. Zunger, Phys. Rev. B **37**, 8958 (1988).
25. O. Zakharov, A. Rubio, X. Blase, *et al.*, Phys. Rev. B **50**, 10780 (1994).
26. P. Schröer, P. Krüger, and J. Pollman, Phys. Rev. B **47**, 6971 (1993).
27. M. Rohlfing, P. Krüger, and J. Pollman, Phys. Rev. B **56**, R7065 (1997).
28. M. Rohlfing, P. Krüger, and J. Pollman, Phys. Rev. B **57**, 6485 (1998).
29. W. Luo, S. Ismail-Beigi, M. L. Cohen, and S. G. Louie, Phys. Rev. B **66**, 195215 (2002).
30. L. Ley, R. A. Pollak, F. R. McFeely, *et al.*, Phys. Rev. B **9**, 600 (1974).
31. N. Trouillier and J. L. Martins, Phys. Rev. B **43**, 1993 (1991).
32. L.-W. Wang, *Planewave Total Energy Code (PEtot)*, http://www.nersc.gov/~linwang/PEtot/PEtot.html (2001).
33. J. P. Perdew and A. Zunger, Phys. Rev. B **23**, 5048 (1981).
34. D. M. Ceperley and B. J. Alder, Phys. Rev. Lett. **45**, 566 (1980).
35. M. C. Payne, M. P. Teter, D. C. Allan, *et al.*, Rev. Mod. Phys. **64**, 1045 (1992).
36. S. K. Pugh, D. J. Dugdale, S. Brand, and R. A. Abram, Semicond. Sci. Technol. **14**, 23 (1999).
37. *Numerical Data and Functional Relationships in Science and Technology. New Series. Group III: Crystal and Solid State Physics. Semiconductors*, Suppl. and Extens., Vol. III/17. *Intrinsic Properties of Group IV Elements and III–V, II–VI and I–VII Compounds*, Ed. by O. Madelung and M. Schulz (Springer, Berlin, 1982), Vol. 22a.
38. N. K. Abrikosov, V. B. Bankina, L. V. Portskaya, L. E. Shelimova, and E. V. Skudnova, *Semiconducting II–VI, IV–VI, and V–VI Compounds* (Plenum, New York, 1969).
39. *Numerical Data and Functional Relationships in Science and Technology. New Series. Group III: Crystal and Solid State Physics. Semiconductors. Physics of Group IV Elements and III–V Compounds*, Ed. by O. Madelung, M. Schulz, and H. Weiss (Springer, Berlin, 1982), Vol. 17a.
40. *Data in Science and Technology. Semiconductors: Other than Group IV Elements and III–V Compounds*, Ed. by O. Madelung (Springer, Berlin, 1992).
41. S.-H. Wei and A. Zunger, Phys. Rev. B **39**, 3279 (1989).
42. H. Fu and A. Zunger, Phys. Rev. B **55**, 1642 (1997).
43. M. L. Cohen and J. R. Chelikowsky, *Electronic Structure and Optical Properties of Semiconductors* (Springer, Berlin, 1988).
44. H. Fu, L.-W. Wang, and A. Zunger, Appl. Phys. Lett. **73**, 1157 (1998).
45. N. Cavassilas, F. Aniel, K. Boujdaria, and G. Fishman, Phys. Rev. B **64**, 115207 (2001).
46. D. M. Wood and A. Zunger, Phys. Rev. B **53**, 7949 (1996).
47. L.-W. Wang, J. Kim, and A. Zunger, Phys. Rev. B **59**, 5678 (1999).

Semiconductors, Vol. 39, No. 2, 2005, pp. 174–176. Translated from Fizika i Tekhnika Poluprovodnikov, Vol. 39, No. 2, 2005, pp. 189–191.

ELECTRONIC AND OPTICAL PROPERTIES OF SEMICONDUCTORS

Photoreflection Studies of the Dopant Activation in InP Implanted with Be^+ Ions

L. P. Avakyants^, P. Yu. Bokov, and A. V. Chervyakov

Moscow State University, Vorob'evy gory, Moscow, 119992 Russia

^e-mail: avakants@genphys.phys.msu.ru

Submitted May 17, 2004; accepted for publication May 24, 2004

Abstract—Photoreflection spectroscopy is used to study the activation of impurity in InP crystals implanted with 100-keV Be^+ ions at a dose of 10^{13} cm^{-2} and then subjected to thermal annealing for 10 s. After annealing at temperatures no higher than 400°C, lines characteristic of crystalline InP are not observed in the photoreflection spectrum, which indicates that the crystal lattice has become disordered as a result of the ion implantation. If the annealing temperature is in the range from 400 to 700°C, the lines related to the fundamental transition in InP (1.34 eV) and the transition between the conduction band and the subband, which has split off from the valence band owing to a spin–orbit interaction (1.44 eV), are observed in the spectrum, which indicates that the InP crystal structure is restored. The dopant is activated in samples annealed at 800°C, as indicated by the Franz–Keldysh oscillations observed in the corresponding photoreflection spectra. Free-carrier concentration is determined from the oscillation period and is found to be equal to 2.2×10^{16} cm^{-3}. © *2005 Pleiades Publishing, Inc.*

1. INTRODUCTION

Indium phosphide (InP) is an important semiconductor material used in the fabrication of high-frequency field-effect transistors. It is valuable due to its high charge-carrier mobility and comparatively wide band gap (~1.35 eV at 300 K). Ion implantation and subsequent annealing is an efficient method of forming semiconductor layers with a specified dopant profile. The implantation of high-energy impurity ions into a crystal is accompanied by a disordering of the crystal lattice. In order to remove radiation defects and attain the electrical activation of impurities, one uses various types of annealing (conventional thermal, laser-related, and rapid thermal). Therefore, it is important to study the characteristics of ion-implanted layers before and after annealing with the aim of choosing annealing conditions that ensure the optimal activation of the impurity.

In a number of studies (see, for example, [1]), the aforementioned characteristics have been studied using the spectroscopy of Raman scattering. This method provides data on both structural and electrical properties, since a longitudinal optical phonon is related to plasma oscillations in polar semiconductors. However, it is difficult to determine such an important parameter as the charge-carrier concentration from Raman scattering data on *p*-type semiconductors that include, in particular, InP doped with Be. This difficulty is caused by the weak dependence of the frequency of coupled phonon–plasmon modes on the charge-carrier concentration [2]. In this study, we use a contactless method of photoreflection spectroscopy to obtain data on the carrier concentration. This method provides a high sensitivity in studies of both the special features of the energy-band structure of a semiconductor and the built-in electric fields whose magnitudes are controlled by the impurity distribution and concentration.

2. EXPERIMENTAL

We studied samples of undoped *n*-InP ($n \approx 10^{16}$ cm^{-3}) with a (100) surface orientation. After mechanical polishing and chemical etching, the semiconductor wafers were implanted with 100-keV beryllium ions at a dose of 10^{13} cm^{-2}. The samples were then subjected to thermal annealing for 10 s at temperatures ranging from 300 to 800°C. The photoreflection spectra were measured using the system described previously in [3]. The spectral width of the monochromator slits amounted to 1 meV. The reflection was modulated using an He–Ne laser (the power was 10 mW and the wavelength, 632.8 nm) with a modulation frequency of 370 Hz. The spectra were measured at room temperature.

3. RESULTS AND DISCUSSION

In Fig. 1, we show the photoreflection spectra of InP samples subjected to postimplantation thermal annealing at various temperatures. After annealing at temperatures from 400 to 700°C, the spectra included lines related to the fundamental transition in InP (E_g = 1.34 eV) and to the transition between the conduction band and the subband, which is split off from the valence band ($E_g + \Delta_{so}$ = 1.44 eV) as a result of the spin–orbit interaction (see Fig. 2). As can be seen from Fig. 1, when the annealing temperature increases, the intensities of the observed lines also increase; simultaneously, the widths of the lines decrease. In addition, the line E_g shifts to lower energies. This effect can be related to restoration of the InP crystal structure.

1063-7826/05/3902-0174$26.00 © 2005 Pleiades Publishing, Inc.

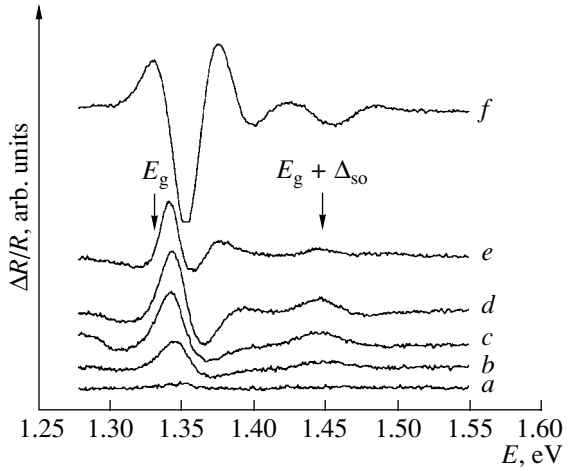

Fig. 1. The photoreflection spectra of InP ion-implanted with Be^+ at a dose of 10^{13} cm^{-2} after subsequent 10-s thermal annealing at temperatures of (*a*) 300, (*b*) 400, (*c*) 500, (*d*) 600, (*e*) 700, and (*f*) 800°C.

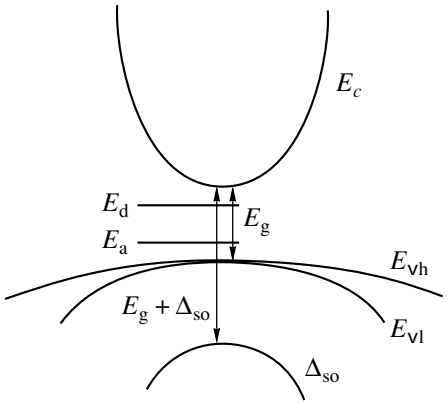

Fig. 2. A schematic representation of the InP energy-band structure in the vicinity of the Γ point: E_c stands for the conduction band; E_{vh}, for the heavy-hole subband of the valence band; E_{vl}, for the light-hole subband of the valence band; Δ_{so}, for the subband split off from the valence band owing to the spin–orbit interaction; and E_a and E_d are the acceptor and donor levels, respectively.

The photoreflection spectra of the samples annealed at temperatures from 400 to 700°C have a shape characteristic of a low-field case and can be described using the Aspnes formula [4]

$$\frac{\Delta R}{R}(E) = \mathrm{Re}[Ae^{i\varphi}(E - E_i + \Gamma)^{-m}], \qquad (1)$$

where A and φ are the amplitude and phase parameters, respectively; E is the photon-energy of the probe radiation; E_i is the energy position of the ith spectral feature; Γ is the phenomenological broadening parameter; and m is the parameter defined by the type of critical point and by the order of the derivative of the dielectric constant $\varepsilon(E)$ with respect to energy. In the case under consideration, we have $m = 2$ [4]. We determined the main parameters of the spectral lines by approximating the low-field spectra with the sum of two expressions (1) for the lines E_g and $E_g + \Delta_{so}$, respectively.

In Fig. 3, we show the position of the E_g line as a function of the annealing temperature. As can be seen, this line shifts to lower energies as the annealing temperature increases. Such shifts were previously observed [5] when studying the compensation of *n*-GaAs conductivity using an implantation of B^+ ions. The observed shift of the E_g line cannot be related to either the dimensional effects or the stresses since each of the mentioned factors would make a corresponding contribution to the shift of the line $E_g + \Delta_{so}$ (see Fig. 2). However, as the annealing temperature increases, a shift of the line $E_g + \Delta_{so}$ is not observed. Apparently, the observed shift of the E_g line is caused by the appearance of acceptor levels near the valence-band top (E_a in Fig. 2) and to donor levels near the conduction-band bottom. In this case, the energy of the E_g transition should decrease by the acceptor-activation energy E_a as a result of the appearance of the acceptor levels. At the same time, the appearance of these levels should not affect the energy of the transition $E_g + \Delta_{so}$.

The Franz–Keldysh oscillations are observed near the fundamental-absorption edge in the photoreflection spectra of the sample annealed at a temperature of 800°C; i.e., the spectrum acquires a shape characteristic of the so-called midfield conditions and is abruptly shifted to lower energies (see Fig. 3), which indicates that the impurity is activated.

In order to describe the midfield spectra using the Franz–Keldysh oscillations, we used the approximation [4]

$$\frac{\Delta R}{R} \propto \cos\left[\frac{2}{3}\left(\frac{\hbar\omega - E_g}{\hbar\Omega}\right)^{3/2} + \frac{\pi(d-1)}{4}\right], \qquad (2)$$

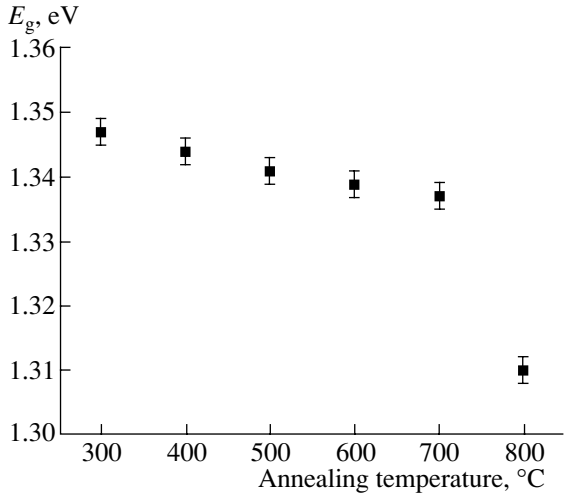

Fig. 3. The annealing-temperature dependence of the position of the spectral line that corresponds to the fundamental transition in InP (E_g).

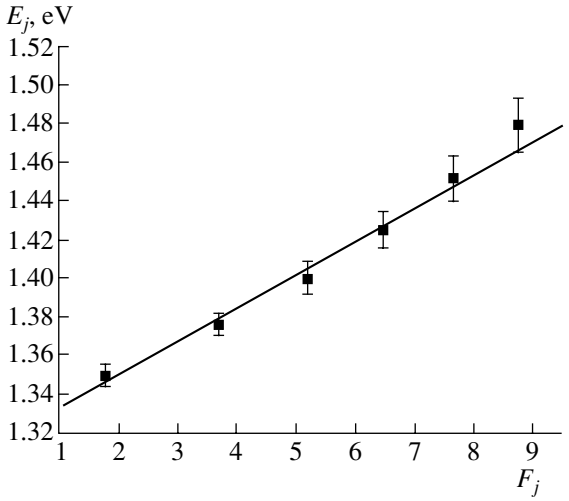

Fig. 4. The dependence of the positions of extrema E_j in the Franz–Keldysh oscillations on F_j (6) for a sample annealed at a temperature of 800°C. The circles represent the extrema of the Franz–Keldysh oscillations and the solid line corresponds to the result of processing using the least-squares method.

where $\hbar\omega$ is the energy of the probe-radiation photons, E_g is the fundamental-transition energy, and $\hbar\Omega$ is the electrooptical energy equal to

$$\hbar\Omega = \left(\frac{e^2E_s^2\hbar^2}{8\mu}\right)^{1/3}. \quad (3)$$

Here, μ is the reduced interband effective mass

$$\frac{1}{\mu} = \frac{1}{m_e^*} + \frac{1}{m_h^*}, \quad (4)$$

where m_e^* and m_h^* are the effective masses of the electron in the conduction band and hole in the valence band, respectively; E_s is the electric field built into the semiconductor; and d is the dimensionality of the critical point. We have $d = 3$ for direct band-to-band transitions in InP. In this situation, the positions of the extrema in the oscillations $(\hbar\omega)_j$ are given by

$$(\hbar\omega)_j = \hbar\Omega(F_j) + E_g, \quad j = 1, 2, 3, \quad (5)$$

where

$$F_j = \left[3\pi\frac{j - 1/2}{2}\right]^{2/3}. \quad (6)$$

In Fig. 4, we show the positions of the extrema of the Franz–Keldysh oscillations F_j in relation to F_j (6). It can be seen from Fig. 4 that the dependence $E_j(F_j)$ is adequately approximated using a straight line, which is in good agreement with (5) and (6). By assuming that the interband effective mass μ is equal to $0.071m_e$ [6] for transitions between the conduction band and the heavy-hole subband of the valence band, we were able to determine the values of the built-in field E_s and the fundamental-transition energy E_g for the sample under consideration. We thus found that E_s = 50 kV/cm and E_g = 1.310 eV.

It is well known [7] that the magnitude of the built-in electric field is controlled by the surface region of the space charge and depends on the charge-carrier concentration n and the surface potential V_s; i.e.,

$$E_s = \left[\frac{2en(V_s - kT/e)}{\varepsilon\varepsilon_0}\right]^{1/2}, \quad (7)$$

where $\varepsilon\varepsilon_0 = 12.4 \times 8.85 \times 10^{-14}$ F/cm, V_s = 0.64 V is the surface potential, and $\varepsilon = 12.4$ is the relative static dielectric constant of InP (001) (the values of ε and V_s are taken from [6]). In this case, the value of the built-in electric field calculated using formula (7) corresponds to a charge-carrier concentration of 2.2×10^{16} cm^{-3}.

4. CONCLUSION

We used photoreflection spectroscopy to study the activation of impurity in InP implanted with 100-keV Be^+ ions at a dose of 10^{13} cm^{-2}.

The observed variations in the photoreflection spectra (an increase in the intensity of the lines and a decrease in their width) can be related to the restoration of the InP crystal structure. The appearance of the Franz–Keldysh oscillations in the photoreflection spectra indicates that the impurity activation occurs as a result of annealing at a temperature of 800°C. The charge-carrier concentration determined from the period of the Franz–Keldysh oscillations was found to be equal to 2.2×10^{16} cm^{-3} for a dose of the ion-implanted beryllium ions equal to 10^{13} cm^{-2}.

The results obtained show that photoreflection spectroscopy can be used to estimate the charge-carrier concentration and optimize the conditions of annealing ion-implanted InP.

REFERENCES

1. L. P. Avakyants, V. S. Gorelik, and E. D. Obraztsova, J. Mol. Struct. **219**, 141 (1991).
2. M. Gargouri, B. Prevot, and C. Schwab, J. Appl. Phys. **62**, 3902 (1987).
3. L. P. Avakyants, P. Yu. Bokov, I. P. Kazakov, and A. V. Chervyakov, Vestn. Mosk. Univ., Ser. 3: Fiz. Astron. **4**, 48 (2002).
4. D. E. Aspnes, Surf. Sci. **37**, 418 (1973).
5. L. P. Avakyants, V. S. Gorelik, A. B. Korshunov, *et al.*, Kratk. Soobshch. Fiz., No. 2, 17 (1999).
6. P. J. Hughes, B. L. Weiss, and T. J. S. Hosea, J. Appl. Phys. **77**, 6472 (1995).
7. R. N. Bhattacharya, H. Shen, P. Parayanthal, *et al.*, Phys. Rev. B **37**, 4044 (1988).

Translated by A. Spitsyn

Semiconductors, Vol. 39, No. 2, 2005, pp. 177–181. Translated from Fizika i Tekhnika Poluprovodnikov, Vol. 39, No. 2, 2005, pp. 192–196.

ELECTRONIC AND OPTICAL PROPERTIES OF SEMICONDUCTORS

The Effect of Current Pulse Annealing on the Electrical Properties of Polycrystalline *p*-Si

V. A. Gridchin and V. M. Lubimskiĭ^

Novosibirsk State Technical University, Novosibirsk, 630092 Russia

^e-mail: lubvlm@ngs.ru

Submitted June 7, 2004; accepted for publication June 21, 2004

Abstract—The effect of current pulse annealing on the conductivity, hole density and mobility, and piezoresistance of polycrystalline Si is studied. Series of current pulses were used during annealing, which made it possible to reduce the threshold current density. After the pulse annealing, the hole density remained unchanged but the mobility increased. Furthermore, the magnitudes of longitudinal and transverse strain sensitivity decreased. The decrease in strain sensitivity after pulse annealing cannot be explained in terms of the existing model of current annealing. © *2005 Pleiades Publishing, Inc.*

1. INTRODUCTION

The effect of current pulse annealing (CPA) on the conductance of polysilicon resistors was first observed in [1], and then studied in [2–8]. It was found that the resistance of a resistor made of polycrystalline Si with a carrier density of approximately 10^{20}–10^{21} cm^{-3} decreases after a pulse of current exceeding some threshold value is passed through it [1]. A similar change of resistance was observed in polycrystalline Si–Ge doped with boron possessing the impurity concentration 6×10^{19} cm^{-3} [9]. The physical model explaining this effect in polysilicon [2] is as follows: as the current pulse flows through a polysilicon resistor, the Joule heat is mainly released in amorphous layers at the interfaces between crystallites, which melts these layers. The impurity is accumulated in the melted region, and, upon cooling, a channel is formed that has a resistance lower than that before the annealing. As a result, the total resistance of the resistor decreases, whereas the carrier density determined from the Hall measurements remains constant [1, 2].

The effect of CPA on the piezoresistance and conductivity of polycrystalline silicon was studied in [5–7]. The longitudinal S_l and transverse S_t strain sensitivities of *p*-type polycrystalline Si were determined in [5, 6], where it was found that the absolute values of strain sensitivities increase after CPA; however, their variation was less than the relative variation of resistances. Based on the CPA data, the strain sensitivities of crystallites and barriers were then determined [5, 6]. A model describing the piezoresistance of polycrystalline Si using the strain sensitivities of crystallites and barriers was offered in [10], but the authors of [11] found this approach unconvincing.

A single-pulse mode of annealing was used in [1–6]. The threshold current density, necessary for the start of the decrease in resistance after the current pulse, was ~10^6 A/cm^2 [1, 3–6, 8, 9]. To reach this current density, the resistors used in [1, 3–6, 8] were approximately 0.5 μm thick and no more than 20 μm wide.

In regard to practical applications, the CPA effect opens the way for variation in the resistance of polysilicon resistors after the fabrication of integrated circuits, which is important, for example, for operational amplifiers or tensoresistive bridges. To improve the reliability and control over the CPA process, it is desirable to reduce the threshold current. One might expect that the threshold current density can be reduced if the polysilicon layer is heated to the annealing temperature by passing, for example, a series of current pulses through it.

The goal of this study was to investigate the effect of CPA with a train of current pulses on the conductivity, Hall factor, and piezoresistance of polycrystalline silicon.

2. EXPERIMENTAL RESULTS

Polycrystalline silicon films were produced on (100) Si wafers in a low-pressure reactor at 610 and 625°C. The thickness of the oxide was 0.43 μm and the thickness of the polysilicon films was 0.5 μm. The films were doped by implantation with 50-keV boron ions at a dose of ~4×10^{15} ion/cm^2. They were then annealed at 1000–1150°C for 40 min. The parameters of these films are listed in Table 1. It should be noted that the films had no texture (i.e., they are isotropic).

For the experimental determination of the electrical characteristics of the films, test structures (Fig. 1) were formed by photolithography, which made it possible to measure the resistance, longitudinal and transverse

1063-7826/05/3902-0177$26.00

Table 1. The parameters of samples before CPA

Sample no.	ρ_s, Ω/□, 24°C	ρ_v, 10^{-3} Ω cm, 24°C	p, 10^{19} cm^{-3}, 24°C	μ, cm^2 V^{-1} s^{-1}, 24°C	TKρ_s, 10^{-4} K^{-1}, 24°C	T_{gr}, °C	T_{ann}, °C	Si* layer thickness, μm	d, μm*	ρ_v, 10^{-3} Ω cm [12]
1	84	4.62	6.5	21	1.83	610	1000	0.55	6.52	≈2
4	51	2.8	6.75	33	7.9		1150	0.55	14.7	≈1.8
5, 5–1	65	3.4	7	26.5	5	625	1000	0.525	10.3	≈1.7

Note: * d is the average size of a crystallite in the film; T_{gr} is the growth temperature; and T_{ann} is the annealing temperature.

strain sensitivity (also called the gauge factor), and the Hall effect. Resistors R_1 and R_2 were 50 μm in width and 500 μm in length.

The wafers were cut into samples in the form of rectangular parallelepipeds, with the long axis parallel to the [110] direction of a Si substrate (Fig. 1).

The Hall effect was studied in the dc mode in a static magnetic field of 1.56 T. A current was passed through contacts *4* and *8*, and the Hall voltage was measured across contacts *5* and *6*.

The strain sensitivity was determined under the deformation of samples in the shape of rigidly fixed cantilever bars. The strain sensitivity and resistance were measured using the four-probe method: the current from a current source passed through contacts *1* and *4* or *4* and *8*, and the voltage was measured across contacts *2* and *3* or *6* and *7*.

The longitudinal, S_l, and transverse, S_t, strain sensitivities were determined from the relations [13]

$$\frac{\Delta U_l}{U_l} = S_l\varepsilon_l + S_t\varepsilon_t, \quad \frac{\Delta U_t}{U_t} = S_l\varepsilon_t + S_t\varepsilon_l,$$

where U_l and U_t are the voltages across contacts *6* and *7* or *2* and *3*, respectively; ΔU_l and ΔU_t are the changes in the respective voltages under deformation; and ε_l and ε_t are the strains along and across the resistor R_1.

It was assumed that the strain is completely transferred from the substrate to the polysilicon resistors.

The procedural order for the experiment was as follows. First, the temperature dependences of the conductivity and Hall factor were measured. Next, the temperature dependences of the longitudinal and transverse strain sensitivities were determined. Then, CPA was performed on the samples, which were placed in a machine for the mechanical loading of bars. To stabilize the sample parameters, thermal cycling in the temperature range 20–100°C was performed. Then the strain sensitivity after CPA was determined, and, finally, the Hall factor and conductivity were measured.

CPA was performed by passing a train of 80–100-mA current pulses with a width of 150–250 μs and duty factor of 0.3–0.5 through contacts *1* and *4* or *4* and *8* for 1–2 s. After the current pulses had passed through the contacts, resistances R_{1-4} or R_{4-8} were measured. As expected, the threshold current decreased to (3–4) × 10^5 A/cm^2.

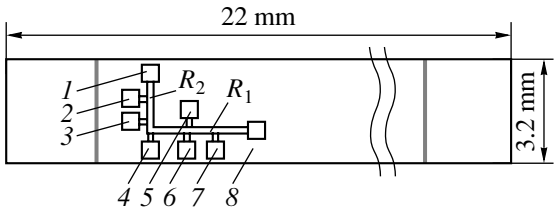

Fig. 1. A cantilever bar with longitudinal and transverse resistors.

3. DISCUSSION OF THE RESULTS

After the pulse annealing, the resistance of the resistors decreased to a different extent, from several percent to several tens of percent, dependently on the duration of the pulse train. Figure 2 shows the typical temperature dependences of the resistance for the three samples under study. Similarly to [1, 3–7], the hole

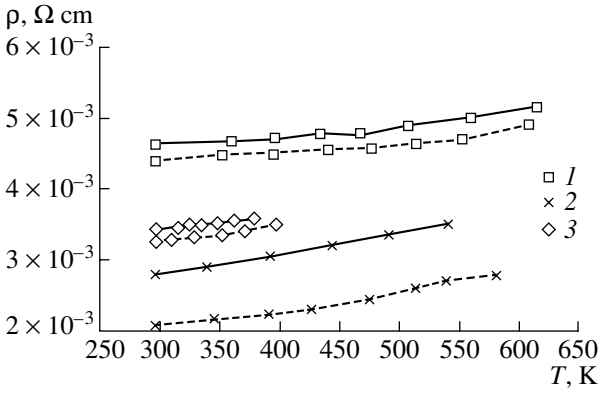

Fig. 2. Temperature dependences of the resistivity of the samples before (solid lines) and after (dashed lines) CPA for sample nos. (*1*) 1, (*2*) 4, and (*3*) 5.

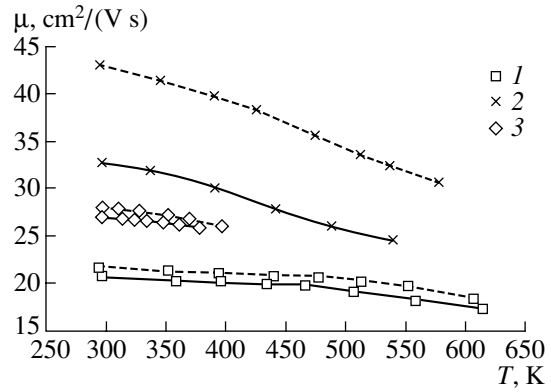

Fig. 3. Temperature dependences of the hole mobility before (solid lines) and after (dashed lines) CPA for sample nos. (*1*) 1, (*2*) 4, and (*3*) 5.

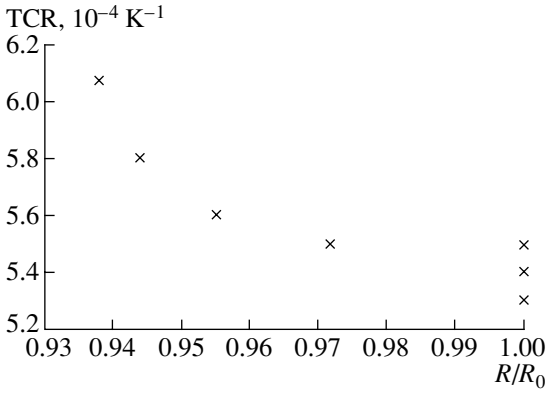

Fig. 4. The temperature coefficient of the resistance (TCR) as a function of the ratio of resistances before and after CPA.

density remained unchanged within the limits of the experimental error after CPA, and the changes in the resistivity were related to changes in the hole mobility. Figure 3 shows the temperature dependences of the hole mobility before and after CPA. As can be seen from a comparison of Figs. 2 and 3, the temperature dependences of resistivity and mobility are similar.

As is well known, for the majority of scattering mechanisms, the temperature dependences of carrier mobility can be represented as

$$\mu = AT^r,$$

where A and r are constants.

It was found that annealing does not change the character of the mobility temperature dependence. This fact indicates that the mechanism of hole scattering remains virtually unchanged after CPA.

Figure 4 shows, for samples cut from wafer no. 5, the dependences of the temperature coefficient of the resistance on the ratio of resistances before (R_0) and after (R) CPA. It can be seen that the temperature coefficient of the resistance increases as the ratio R/R_0 increases, similarly to what was observed in the boron-doped sample [3].

The values of the room-temperature surface resistance, carrier density and mobility, and resistance across contacts *5* and *6* for the two samples under study are listed in Table 2.

$R_{5,6}$ is constituted by the transverse resistance of resistor R_1 and the resistance of leads to the potential contact pads. The number of contact pads is 8. About 60–70% of the value of $R_{5,6}$ is determined by the resistance of the leads. As can be seen from Table 2, the resistance $R_{5,6}$ remains virtually unchanged upon annealing, whereas the resistance of the transverse resistors changes by 26 and 40%.

Figures 5 and 6 show the typical temperature dependences of the strain sensitivity before and after CPA for several of the samples under study. The resistance of the longitudinal resistors in sample nos. 1, 4, and 5 decreased after CPA by 5, 35, and 3.8%, respectively, and the resistance of the transverse resistors in sample nos. 1, 4, 5-1, and 5 decreased by 14, 15, 30, and 3.8%, respectively. As can be seen in the figures, both the longitudinal and transverse strain sensitivity of sample nos. 1 and 4 decrease after CPA. The change in longitudinal strain sensitivity is always less than the change in resistivity; in addition, the slopes of temperature dependences of the strain sensitivity before and after CPA are similar. In the case of the small change in the resistance of sample no. 5 after CPA, the changes in S_l and S_t are comparable with the experimental error (Figs. 5, 6).

Only the increase of the strain sensitivity magnitude after CPA can be explained in terms of the model of current annealing offered in [2, 3] and the existing model of conduction in polycrystalline silicon, and only on the qualitative level. According to the presently existing model of conduction, the resistivity of polysilicon is defined by the resistivities of crystallites ρ_c and barriers ρ_b, for example, [11]

$$\rho = \frac{2w}{L}\rho_b + \left(1 - \frac{2w}{L}\right)\rho_c,$$

where L is the average size of a crystallite and w is the half-width of the charged layer.

Table 2

Sample no.	Annealing	ρ_s, Ω/□	p, 10^{19} cm^{-3}	μ, cm^2 V^{-1} s^{-1}	$R_{5,6}$, Ω
4	No	51.2	6.8	33	630
4	Yes	37.8	6.9	46	622
2	No	101.7	7.25	17.2	1022
2	Yes	59.5	10	20.6	1026

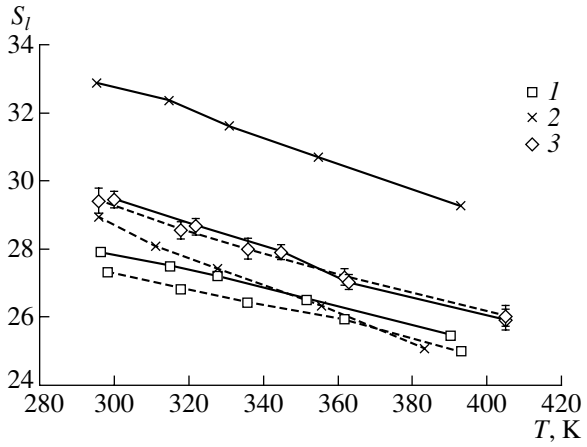

Fig. 5. Temperature dependences of the longitudinal strain sensitivity before (solid lines) and after (dashed lines) CPA for sample nos. (*1*) 1, (*2*) 4, and (*3*) 5.

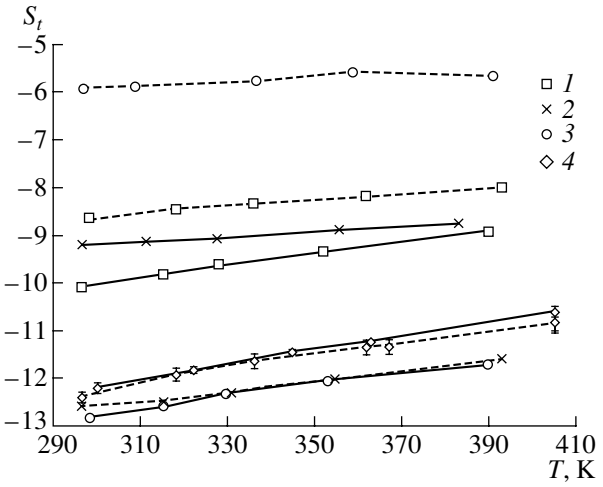

Fig. 6. Temperature dependences of the transverse strain sensitivity before (solid lines) and after (dashed lines) CPA for sample nos. (*1*) 1, (*2*) 4, (*3*) 5-1, and (*4*) 5.

In polysilicon with a carrier density of (6–7) × 10^{19} cm^{-3}, the piezoresistance is mainly defined by grains, and the contribution of barriers is insignificant [11, 13, 14]. The expressions for estimation of strain sensitivity can be simplified if, as in our case, the axis of the bar coincides with the [110] direction, because then $\varepsilon_t \approx 0.06\varepsilon_l$. Therefore, if the strain sensitivities before and after CPA, respectively, are

$$S_{l,t} = \frac{\Delta\rho_{l,t}}{\rho\varepsilon_l} = \left(1 - \frac{2w}{L}\right)\frac{\Delta(\rho_c)_{l,t}}{\rho\varepsilon_l}$$

and

$$S^*_{l,t} = \frac{\Delta\rho_{l,t}}{\rho^*\varepsilon_l} = \left(1 - \frac{2w}{L}\right)\frac{\Delta(\rho_c)_{l,t}}{\rho^*\varepsilon_l},$$

then

$$\frac{S^*_{l,t}}{S_{l,t}} = \frac{\rho}{\rho^*},$$

and, as the resistance of the resistor decreases, the strain sensitivity must increase in the same proportion.

Two facts found in the CPA study were unexpected: First, the magnitude of the decrease in the transverse strain sensitivity is stronger than that in the longitudinal sensitivity, whereas the change in resistivities after CPA is the same. Second, even at large changes in the resistivity after annealing, the temperature dependences of the mobility and strain sensitivity change insignificantly, if at all. These facts are unexpected because potential barriers exist on the interfaces between the crystallites and these barriers reduce the temperature coefficient of the resistivity of polycrystalline silicon [11]. Therefore, one might expect that the temperature dependences of the mobility and strain sensitivity would change after CPA.

The existing models of conduction and CPA proceed from the assumption of carrier motion along a single coordinate. However, the change in conductivity after CPA can modify the spreading of a current in crystallites. The piezoresistance in silicon is strongly angle-dependent, which can cause a decrease in strain sensitivity when the angular distributions of current in the adjacent crystallites are changed.

CONCLUSIONS

(1) After CPA, the resistance is mainly changed along the resistors.

(2) The change in the resistivity of *p*-polysilicon is related to the change in the hole mobility.

(3) The temperature dependences of the strain sensitivity are not changed, or change only slightly, and the hole mobility is slightly changed by CPA.

(4) The decrease in strain sensitivity as a result of CPA cannot be explained in terms of the existing model of CPA and the model of carrier motion along a single coordinate.

REFERENCES

1. Y. Amemiya, T. Ono, and K. Kato, IEEE Trans. Electron Devices **26**, 1738 (1979).
2. K. Kato, T. Ono, and Y. Amemiya, IEEE Trans. Electron Devices **29**, 1156 (1982).
3. K. Kato and T. Ono, Jpn. J. Appl. Phys. **35**, 4209 (1996).
4. S. V. Sputaĭ, in *Proceedings of All-Union Conference on Topical Problems in Electron Instrument Making. Sensor Electronics* (Novosibirsk, Russia, 1991), p. 33.
5. V. A. Gridchin and S. V. Sputay, in *Proceedings of 11th International Conference on High Vacuum, Interface and Thin Films, HVITF-94* (1994), p. 606.

6. V. Sputaĭ, in *Abstracts of 1st International Conference on Sensors of Electrical and Nonelectrical Quantities* (Barnaul, Russia, 1993), Part 1, p. 95.
7. V. V. Grishchenko, A. M. Loganikhin, and V. M. Lyubimskiĭ, in *Proceedings of V International Conference on Topical Problems in Electron Instrument Making* (Novosibirsk, Russia, 2000), Vol. 4, p. 8.
8. D. W. Feldbaumer, J. A. Babcock, V. M. Mercier, and C. K. Y. Chun, IEEE Trans. Electron Devices **42**, 689 (1995).
9. J. F. Babcock, P. Francis, R. Bashir, *et al.*, IEEE Electron Device Lett. **21**, 283 (2000).
10. P. H. French and A. G. R. Evans, Solid-State Electron. **32**, 1 (1989).
11. V. Mosser, J. Suski, J. Goss, and E. Obermeir, Sens. Actuators A **28**, 113 (1991).
12. S. M. Sze and J. C. Irvin, Solid-State Electron. **11**, 599 (1968).
13. D. Schubert, W. Jenschke, T. Uhlig, and F. M. Schmidt, Sens. Actuators **11**, 145 (1987).
14. V. A. Gridchin and V. M. Lyubimskiĭ, Mikroélektronika **32**, 261 (2003) [Russ. Microelectronics **32**, 205 (2003)].

Translated by D. Mashovets

Semiconductors, Vol. 39, No. 2, 2005, pp. 182–188. Translated from Fizika i Tekhnika Poluprovodnikov, Vol. 39, No. 2, 2005, pp. 197–203.

ELECTRONIC AND OPTICAL PROPERTIES OF SEMICONDUCTORS

Spectroscopic Study of Ga-Doped Ge under Uniaxial Pressure

Ya. E. Pokrovskiĭ^ and N. A. Khval'kovskiĭ

Institute of Radio Engineering and Electronics, Russian Academy of Sciences, Moscow, 125009 Russia

^e-mail: yaep@mal.cplire.ru

Submitted July 27, 2004; accepted for publication August 12, 2004

Abstract—To identify the optical transitions responsible for the excitation of long-wavelength stimulated emission in uniaxially compressed Ga-doped Ge, the optical absorption and photoconductivity spectra of the material were investigated at a wide range of pressures in directions [111] and [001]. The dependence of the valence band splitting between the light- and heavy-hole subbands in Ge as a function of the applied pressure was found. As determined from this dependence, the deformation potential constants for the valence band appeared to be less than the presently accepted values. It is shown that, as pressure increases, some of the excited states of the Ga impurity levels reach the light-hole band, enter it, and remain close to its edge (the resonant states). It is possible that a population inversion of these resonant states gives rise to the excitation of stimulated emission at a photon energy of about 10 meV. No specific features confirming the existence of resonant impurity states near the edge of the heavy-hole band were found in the spectra. © *2005 Pleiades Publishing, Inc.*

1. INTRODUCTION

Long-wavelength stimulated emission from Ge crystals doped with Ga at a concentration of $N \approx 10^{14}$ cm^{-3} was first observed in [1] and further investigated in [2–5]. The emission arose at low (4.2 K) temperature in a high (2–4 kV/cm) electric field in samples fabricated in the form of total-internal-reflection cavities, under the uniaxial compression of crystals at a pressure of P = 4–10 kbar. It was suggested in [3–5] that the effect is related to the accumulation of hot holes in the resonant states of the impurity, whose energy, under deformation, is shifted into the continuous spectrum and to the edge of the heavy-hole band. Calculations [6–8] have supported the feasibility of this explanation. However, no direct experiments confirming this mechanism of population inversion have come to our notice.

The existence of impurity states against the background of the continuous spectrum of carriers is related to the complex band structure of a semiconductor. For example, the absorption [9] and photoconductivity spectra of Si demonstrate peaks corresponding to transitions from the ground state of the Group-III acceptor impurity, $1S_{3/2}$, to states $2P_{1/2}$ and $3P_{1/2}$, which are associated with the valence subband split off due to the spin–orbit interaction. These peaks are blue-shifted in respect to the peaks of the principal series $P_{3/2}$ by an energy close to spin–orbit splitting (44 meV) and broadened (≈0.5 meV) due to their short lifetime. Optical transitions between *S*-type states are forbidden, and they are observed only in the Raman spectra. For example, for boron impurity, it was found that the $1S_{1/2}$ state is localized in the band gap at 23 meV above the valence band edge [10]. The calculation in [11] yielded a closer position to this level for the shallow acceptor in Si.

The resonant states of impurities in Ge can be observed under the uniaxial deformation of crystals. The absorption spectra of Group-III acceptors in uniaxially compressed Ge have only been studied at low pressures: $P < 0.5$ kbar (see [12] and the references therein). The photoconductivity related to the impurity in Ga-doped Ge was studied at high pressure applied in the [001] direction [13, 14]. In [14], the positions of resonant states near the edge of the heavy-hole band, calculated in [8], are shown in the photoconductivity spectra. However, no specific features that could be attributed to these states are manifested in these spectra. In this study, we have investigated the absorption and photoconductivity spectra of Ge:Ga in a wide range of compressive deformations, and the resulting analysis of their evolution allowed us to reveal several resonant states of the impurity.

2. EXPERIMENTAL

Under study were samples of Ge doped with Ga at a concentration N of 1.5×10^{15} to 5×10^{13} cm^{-3}, with dimensions of $1 \times 1 \times 10$ or $2 \times 2 \times 10$ mm^3, cut along the [111] or [001] direction. Several samples were fabricated in the form of total-internal-reflection cavities. Samples were compressed in an insert constituted by two coaxial stainless steel tubes. The outer tube ended with a brass cylinder that had a channel and window and accommodated a sample. The stress produced by a certified dynamometer and (1 : 3) lever was transferred to the sample via the internal tube and a brass plug sliding within the channel of the cylinder. The second insulating caprolon plug was firmly fixed in the channel. The sample was precisely centered in the channel with the use of a lift-off jig, and compressed by the plugs between electrodes made of annealed copper. At this

stage, the end faces of the sample made imprints on the electrodes, and these imprints fixed the sample. In most cases, the GaInSn alloy contacts, which are in a liquid state at room temperature, were deposited on the edges of the sample. During the compression of the sample, any excess amount of alloy was squeezed out from under the contacts. For samples with this type of contacts, the noise of the photoconductivity was determined by background room-temperature fluctuations. To study the absorption and normalize the photoconductivity spectra, a Ge:Sb photoresistor ($N_{Sb} \approx 10^{15}$ cm^{-3}) was placed behind the sample. The aperture of the photodetector was limited by a short tube of 0.8×8 mm^2 in area, situated in close vicinity to the sample. As a result, the light that did not pass through the sample was prevented from reaching the photodetector. The insert was immersed in a liquid-helium bath in a cryostat (4.2 K). The windows of the bath, made of fused silica or crystalline quartz (for ranges of 7–12 and 10–30 meV, respectively), limited the intensity of the background radiation. This configuration allowed us to significantly raise the threshold sensitivity of both the detector and the samples under study. The spectra were recorded using an LAFS-1000 Fourier spectrometer with Lavsan (Dacron) beam-splitters of 12 and 6 μm in thickness, with a resolution of 0.08 and 0.3 meV, respectively.

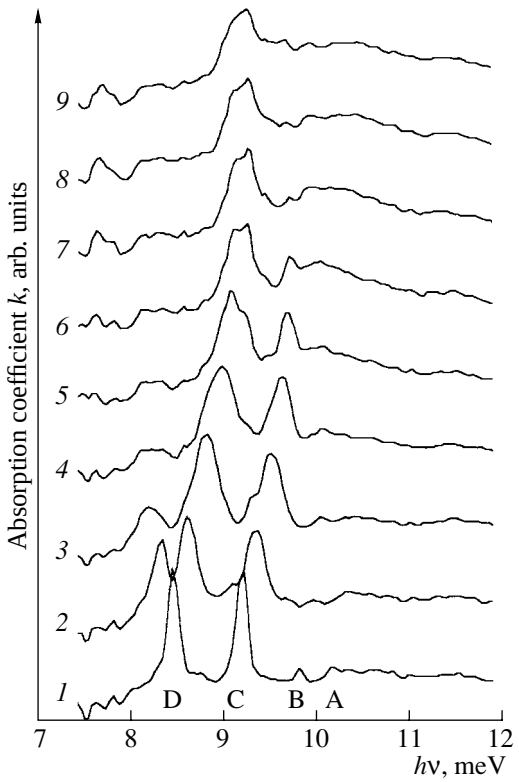

Fig. 1. Absorption spectra of a Ge sample of $2 \times 2 \times 10$ mm^3 in size, doped with Ga (Ga concentration $N = 1.4 \times 10^{14}$ cm^{-3}), under uniaxial compression in the [111] direction. Pressure P at (*1*) 0, (*2*) 0.23, (*3*) 0.47, (*4*) 0.7, (*5*) 0.93, (*6*) 1.16, (*7*) 1.4, (*8*) 1.6, and (*9*) 1.86 kbar.

3. RESULTS

Only allowed optical transitions from the occupied states are observed in the impurity absorption and photoconductivity spectra. At low temperatures in Ge doped with Group-III acceptors, these are the transitions from the lower branch of 1*S* state to *P*-type states and to the valence band. Studies of absorption spectra can provide information on the energy spectrum within these limits. However, the samples for this analysis must have sufficient optical thickness; i.e., either a high concentration of impurities or large size is demanded. For a photoconductivity study, a small absorption in the samples is sufficient. However, in the photoelectric study, the photoconductivity arises only at the excitation of holes into the valence band or shallow local states close to this band, via the photothermal ionization of these states. Furthermore, as the pressure increased, the threshold electric field in the samples strongly decreased, and at high pressure it did not exceed 1 V/cm. Therefore, the photoconductivity study was reasonable only for bias voltages of no higher than 0.1–0.5 V, which posed additional problems. Below, we present only the data obtained by the methods that appeared to be the most efficient.

Figure 1 shows the absorption spectra for Ge:Ga in the range of small energies at low pressure P in the [111] direction. At $P = 0$, the spectrum demonstrates lines with the energies $h\nu$: A (10.17), B (9.84), C (9.2), and D (8.44) meV. Weak long-wavelength lines E (8 meV) and F (6.74 meV) are not seen in this picture. Taking into account that these lines arise in the excitation of holes from the ground state, we shall denote the corresponding final states by the same letters. The energy of the ground state of the Ga impurity in Ge is usually accepted as 11.32 meV [9]. However, the valence band edge is not clearly defined, because a quasi-continuous spectrum of high excited states is adjacent to it. The binding energy of a high excited state can be calculated with reasonable precision in the effective mass approximation. Then, we can take the energy of the ground state to be the sum of this calculated energy and the energy of the line, during excitation of the corresponding optical transition. The theory of optical absorption and photoionization of Group-III acceptors in Ge was derived in [15].

As the crystal is compressed, the impurity ground state 1*S* is split into lower $1S_{1/2}$ and upper $1S_{3/2}$ branches. State C is not split, and state D is weakly split under compression in the [111] direction. The splitting of line D, related to the splitting of the 1*S* ground state, is observed up to $P < 1$ kbar. As P increases, the thermal population of the upper branch decreases, and this component disappears. A weak component is split from line C. It then shifts to lower energies, whereas line C comes close to the valence band ($P \approx 1$ kbar), reaches

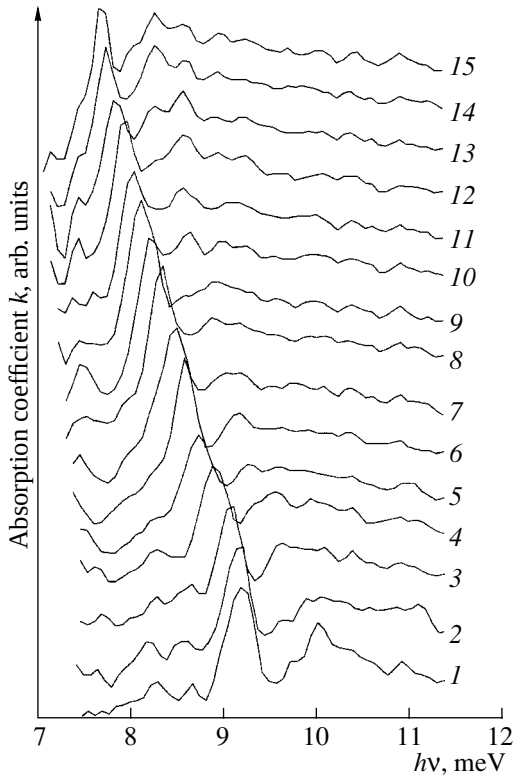

Fig. 2. Absorption spectra of a Ge:Ga sample ($1 \times 1 \times 10$ mm^3, 1.8×10^{14} cm^{-3}). [111] ‖ **P** at (*1*) 0.93, (*2*) 1.4, (*3*) 1.86, (*4*) 2.3, (*5*) 2.8, (*6*) 3.3, (*7*) 3.7, (*8*) 4.2, (*9*) 4.6, (*10*) 5.1, (*11*) 5.6, (*12*) 6, (*13*) 6.5, (*14*) 7, and (*15*) 7.4 kbar.

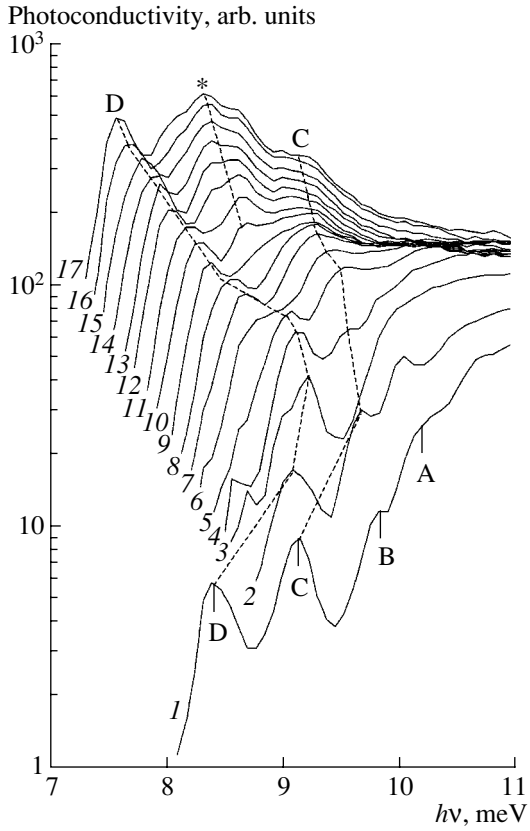

Fig. 3. Photoconductivity spectra of a Ge:Ga sample (cavity $1 \times 1 \times 10$ mm^3, 1.8×10^{14} cm^{-3}). [111] ‖ **P** at (*1*) 0, (*2*) 0.47, (*3*) 0.93, (*4*) 1.4, (*5*) 1.86, (*6*) 2.3, (*7*) 2.8, (*8*) 3.3, (*9*) 3.7, (*10*) 4.2, (*11*) 4.6, (*12*) 5.1, (*13*) 5.6, (*14*) 6, (*15*) 6.5, (*16*) 7, and (*17*) 7.4 kbar. The dotted lines indicate the energies of states C and D, and the energies of an unidentified state (asterisk).

its edge ($P \approx 1.2$ kbar), and enters the band of allowed energies ($P \approx 1.5$ kbar). It can be seen that, along with the decrease in line C intensity, the absorption increases at the edge of the light-hole band. Then, line C turns into a broad (≈1 meV) band in the range of the continuous spectrum, and its magnitude decreases as pressure increases.

As pressure increases further (Fig. 2), line D is localized near the edge of the light-hole band, at a distance of about 0.3 meV, and is shifted to lower energies along with the band edge owing to a decrease in the binding energy of the ground state $1S_{1/2}$. However, at $P \approx 5$ kbar, a spectral peak appears again between line D and the band edge; furthermore, it enters the band and broadens. This effect can be related to the splitting of the deeper excited states E and F, whose upper energy levels reach the edge of the light-hole band. Wide spectral peaks near the edge of the light-hole band are also clearly visible in the photoconductivity spectra (Fig. 3). The dotted lines in Fig. 3 mark the energies of states C and D and the broad peak that arises at high pressures (marked by an asterisk). It can be seen that, as pressure increases, these peaks are shifted slightly, deeper into the light-hole band.

The splitting of the valence band into light- and heavy-hole subbands is easily observed in both the absorption and the photoconductivity spectra. In the samples with the Ga concentration $N \approx 10^{14}$ cm^{-3}, the absorption in the high-energy range is weak; therefore, we present the photoconductivity spectra (Fig. 4). It can be seen that, as pressure increases, the spectra in the energy range 10–30 meV successively reach a common dependence of the response on the photon energy, which is defined by light holes. At energies sufficient for the excitation of carriers into the heavy-hole band, portions with an increasing photoconductivity branch off from this steadily decreasing curve. The branching points, which correspond to the minimum photoconductivity, shift to higher energies in proportion to the applied pressure. The branches then coincide with a common dependence corresponding to photoconductivity at $P = 0$. No specific features indicating the presence of resonant states were found in this spectral range. Similar results were obtained in the study of absorption in a sample with a higher (1.5×10^{15} cm^{-3}) concentration of Ga. In this sample, the absorption lines were considerably broadened, meaning that the dips between line D and the continuous spectrum range

were not so distinct. Nevertheless, a fair correlation was obtained between the specific features of these absorption spectra and the photoconductivity spectra in lightly doped samples.

In the experiments with [001] compression, samples with $N \approx 5 \times 10^{13}$ cm^{-3} and small absorption in the entire range of the continuous spectrum were studied. Figure 5 shows the photoconductivity spectra. They are similar to the spectra presented in Fig. 4, but they change more strongly as pressure P increases. It can be seen that, as P increases, the spectra successively reach a common dependence defined by light holes. This is followed by the branching range, which corresponds to the onset of transitions to the heavy-hole band. Furthermore, the branches coincide with the general dependence for photoconductivity at $P = 0$. No local specific features were found in this spectral range. In the vicinity of the photoconductivity edge, the spectra are similar to those shown in Fig. 3. As in the case of [111] compression, peaks of photothermal ionization for states B, C, and D are observed. Then, as pressure increases, states B and C enter the light-hole band, where they are transformed into broad peaks near its edge. State D approaches the band edge, but does not enter it; rather, it shifts to lower energies owing to the decrease in the energy of the lowest impurity state $1S_{1/2}$.

It is necessary to note that the position of the branching points did not depend on the orientation of the electric field or the quality of the treatment for the sample surface. Nevertheless, these factors exerted a strong influence on the shape of the branches. The inset in Fig. 5 shows a portion of the photoconductivity spectrum for one of the crystals. In the first case, the crystal was fabricated in the form of a high-precision total-internal-reflection cavity. In the second case, a polished sample was studied. In the third case, current contacts were deposited onto the side faces of the cavity after they had undergone treatment with a thin abrasive, and the electric field was applied in the [100] direction, normal to the [001] deformation. It can be seen that the shapes of the branches in the transition of photoconductivity from the range of light to heavy holes are different in each case. A minor difference related to the orientations of electric and deformation fields can be attributed to anisotropy of a uniaxially compressed crystal. However, the strong effect obtained from the surface treatment was unexpected. A similar strong difference between the good and spoiled cavities was observed in the range of the branching of photoconductivity spectra for crystals compressed in the [111] direction.

4. DISCUSSION

The analysis of absorption and photoconductivity spectra shown in Figs. 1–5 allows us to reconstruct the energy spectrum of the holes in Ga-doped Ge under uniaxial compression and identify several important specific features within it.

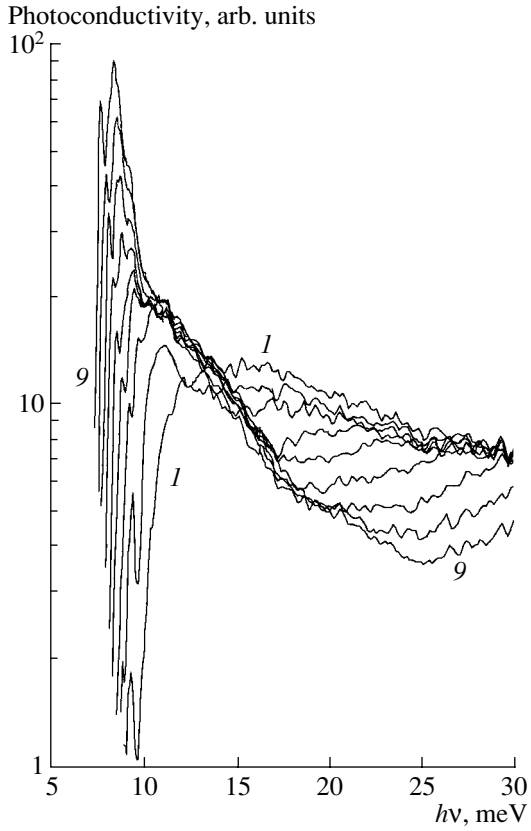

Fig. 4. Photoconductivity spectra of a Ge:Ga sample (cavity $1 \times 1 \times 10$ mm^3, 1.8×10^{14} cm^{-3}). [111] || **P** for (*1*–*9*) from 0 to 7.4 kbar. The step was 0.93 kbar.

The energy is measured from the edge of the valence band at $P = 0$. The reconstruction of the energy diagram consists in the determination of the positions of specific features in the experimental spectra in respect to the new zero point. The pressure symmetrically splits the valence band into light- ($VB_{1/2}$) and heavy-hole ($VB_{3/2}$) subbands by $\Delta \propto P$ [16]. Since the precise position of the valence band edge is unknown, it is natural to measure it from the dip nearest to the low-wavelength edge of the continuous spectrum. A single dip of this kind is clearly seen after line D in the photoconductivity spectra at [111] || **P** > 2 and [001] || **P** > 1.5 kbar. Then, Δ can be determined as the energy spacing between this dip and that at the branching point. The dips at the branching points are better seen in the photoconductivity spectra of the polished samples (see the inset in Fig. 5). Therefore, these spectra were also used for the determination of the energies at the dips.

Figure 6 shows the spectrum of hole states in Ge:Ga under uniaxial compression in the [111] and [001] directions (reconstructed in the aforementioned approximations). Since the energies of light- and heavy-hole subbands can be determined only at a considerable pressure, the experimental values were linearly extrapolated into

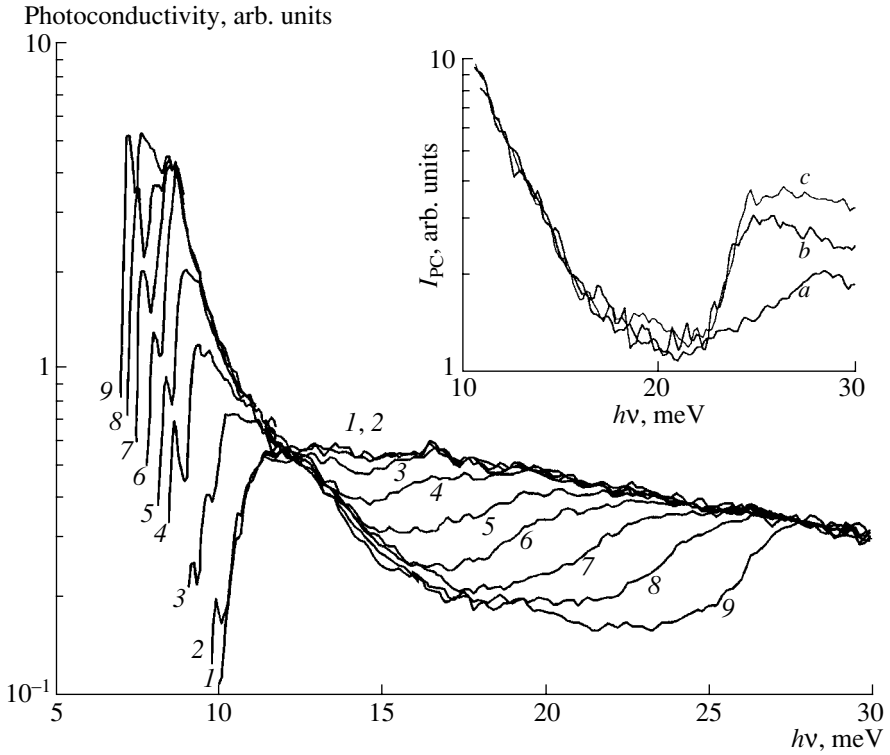

Fig. 5. Photoconductivity spectra of a Ge:Ga sample (cavity $1 \times 1 \times 10$ mm^3, 5×10^{13} cm^{-3}). [001] ‖ **P** at (*1*) 0, (*2*) 0.93, (*3*) 1.4, (*4*) 1.86, (*5*) 2.3, (*6*) 2.8, (*7*) 3.3, (*8*) 3.7, and (*9*) 4.2 kbar. In the inset, photoconductivity spectra of the same sample at $P = 4.2$ kbar are shown for (*a*) the cavity, electric field **E** ‖ **P**; (*b*) the polished sample, **E** ‖ **P**; and (*c*) the sample with contacts on the side facets, **E** ⊥ **P**.

the range of low pressures (the dashed straight lines in Fig. 6). The intersection of these straight lines at $P = 0$ confirms the validity of this extrapolation. As follows from Fig. 6, the splitting of the Ge valence band is directly proportional to the pressure:

$$\begin{aligned} \Delta_{111} &= 2.5P[\text{meV/kbar}] = d0.58S_{44}P, \\ \Delta_{001} &= 3.65P[\text{meV/kbar}] = 2b(S_{11} - S_{12})P. \end{aligned} \quad (1)$$

Here, b and d are the deformation potential constants, and S_{44}, S_{11}, and S_{12} are the compliance coefficients of Ge [16, 17]. As follows from (1), $d = 2.9$ eV and $b = 1.45$ eV. The obtained values of the deformation potential constants are at least 30–40% lower than those previously published [12, 16, 17]. However, in this study these values are determined from direct experiments on the splitting of the valence subbands at a wide range of external pressures. The reproducibility of data is good, and we do not see any source of systematic bias that could be responsible for this discrepancy.

The energies of states 1*S*, C, and D at $P = 0$ shown in Fig. 6 are taken from [9]. As the pressure P in directions [111] or [001] increases, the evolution of the excited states is not quite the same. States C and D do eventually approach the edge of the light-hole band, but C enters the range of the continuous spectrum, while D remains outside. As for the state marked by asterisks in Figs. 3 and 6, we cannot attribute it to some specific deep impurity state. Once again, we stress that all the states entering the range of the continuous energy spectrum are slightly shifted downwards into the light-hole band as deformation increases. Special attention must be drawn to the splitting of the ground state 1*S*. Its dependence on pressure can be monitored by the splitting of the singlet line D, as long as the upper branch $1S_{3/2}$ is occupied. At 4.2 K this is possible up to $P \approx 1$ kbar (points in Fig. 6). Assuming that the splitting of the 1*S* state is proportional to *P*, we can extrapolate its upper branch to higher pressures. This procedure is, to a great extent, arbitrary; particularly as the determination of the proportionality constant cannot be precise in the range of low *P*. As follows from Fig. 6, this coefficient is close to 1.3 meV/kbar. It is noteworthy that the ratio between the splitting of the 1*S* state and the valence subbands (0.53) is very close to that calculated in [18]. As can be seen from the extrapolation of the shift of the level in accordance with the coefficient found (dashed line in Fig. 6), the $1S_{3/2}$ state approaches the light-hole band at $P \approx 5$–6 kbar. It would be hardly expected that, upon a further moderate increase in pressure to 7–8 kbar, the energy of this state would come close to the edge of the heavy-hole band $VB_{3/2}$.

As is mentioned above, no specific features related to resonant states of the Ga impurity were found in the

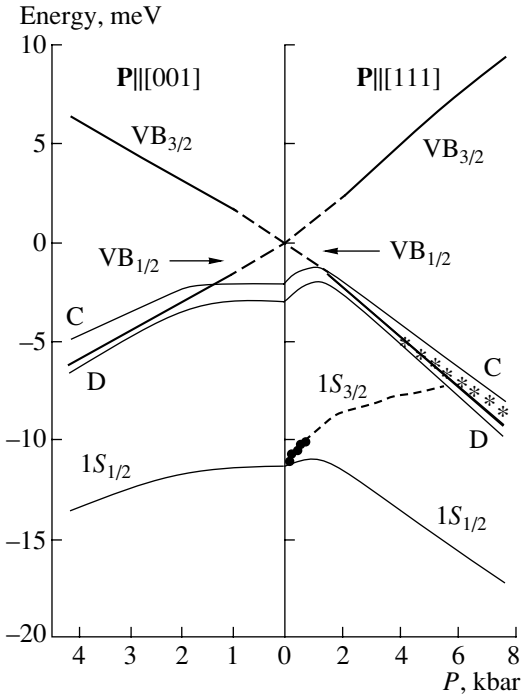

Fig. 6. Evolution of the energy spectrum of Ge:Ga under the uniaxial [111] or [001] compression of a crystal with a pressure P. $VB_{1/2}$ and $VB_{3/2}$ are the light- and heavy-hole subbands; and $1S_{1/2}$, D and C are the energy levels of the ground and excited states of impurity levels. The points show the $1S_{3/2}$ level from Fig. 1, and the asterisks, an unidentified resonant state. The Dashed lines are the extrapolations of the experimental data to low and high pressures.

energy range 10–30 meV. Moreover, the resonant states observed in our experiment lay in the range of the continuous spectrum near the edge of the light-hole band. This experimental result is inconsistent with the results of the calculations in [5–7], where the resonant acceptor states lay close to the edge of the heavy-hole band. However, resonant states near the edge of the light-hole band are also of interest. For example, the accumulation of holes in these states can be responsible for the excitation of a stimulated emission at P = 3.9 kbar in the [001] direction at $h\nu \approx 10$ meV immediately after the breakdown of the Ga impurity [19]. This energy is close to the energy spacing between the ground $1S_{1/2}$ and resonant C states at the same P (Fig. 6).

5. CONCLUSIONS

To reveal the possible role played by the resonant states of a Ga impurity in the excitation of stimulated emission in Ge, the impurity absorption and photoconductivity spectra of the material were studied under uniaxial compression. Based on an analysis of the spectra's evolution, the pressure dependence of the splitting between the light- and heavy-hole bands is determined in the range 0–7.5 kbar for [111] and 0–4.2 kbar for the [001] direction. The deformation potential constants of the valence band, b = 1.45 eV and d = 2.9 eV, determined from these experiments, appeared to be less than the currently accepted values. It is shown that, as pressure increases, some of the local levels of Ga impurity approach the light-hole band, then enter it and remain near its edge, where they form broad (≈1 meV) spectral peaks. It is possible that, at the breakdown of the Ga impurity, the population inversion in these states gives rise to stimulated emission in the 10 meV range. No evidence of resonant states of impurity near the edge of the heavy-hole band, which were predicted in several calculations, was found. We believe that the problem concerning the possible role of resonant states can be resolved by studying spectra of photoconductivity and the absorption of spontaneous and stimulated emission under identical conditions.

ACKNOWLEDGMENTS

The authors are grateful to V.P. Sinis for his assistance during the experiment and to I.V. Altukhov, M.S. Kagan, and A.F. Polupanov for their participation in discussions of the results.

This study was supported by the Russian Foundation for Basic Research, project no. 04-02-16891, and by the European Office of Aerospace Research and Development (EOARD), International Science & Technology Center (ISTC) grant no. 2206p.

REFERENCES

1. I. V. Altukhov, M. S. Kagan, and V. P. Sinis, Pis'ma Zh. Éksp. Teor. Fiz. **47**, 136 (1988) [JETP Lett. **47**, 164 (1988)].
2. I. V. Altukhov, M. S. Kagan, K. A. Korolev, *et al.*, Zh. Éksp. Teor. Fiz. **101**, 756 (1992) [Sov. Phys. JETP **74**, 404 (1992)].
3. I. V. Altukhov, M. S. Kagan, K. A. Korolev, *et al.*, Pis'ma Zh. Éksp. Teor. Fiz. **59**, 455 (1994) [JETP Lett. **59**, 476 (1994)].
4. I. V. Altukhov, M. S. Kagan, K. A. Korolev, *et al.*, Fiz. Tekh. Poluprovodn. (St. Petersburg) **30**, 1091 (1996) [Semiconductors **30**, 578 (1996)].
5. I. V. Altukhov, M. S. Kagan, K. A. Korolev, *et al.*, Zh. Éksp. Teor. Fiz. **115**, 89 (1999) [JETP **88**, 51 (1999)].
6. M. A. Odnoblyudov, A. A. Pakhomov, V. M. Chistyakov, *et al.*, Fiz. Tekh. Poluprovodn. (St. Petersburg) **31**, 1180 (1997) [Semiconductors **31**, 1014 (1997)].
7. M. A. Odnoblyudov, A. A. Prokof'ev, and I. N. Yassievich, Zh. Éksp. Teor. Fiz. **121**, 692 (2002) [JETP **94**, 593 (2002)].
8. V. Ya. Aleshkin, V. I. Gavrilenko, and D. V. Kozlov, Zh. Éksp. Teor. Fiz. **120**, 1495 (2001) [JETP **93**, 1296 (2001)].
9. A. K. Ramdas and S. Rodrigues, Rep. Prog. Phys. **44**, 1287 (1981).
10. G. B. Wright and A. Mooradian, Phys. Rev. Lett. **18**, 608 (1967).

11. O. L. Lipari and A. Baldareschi, Solid State Commun. **25**, 665 (1978).
12. R. L. Jones and P. Fiser, Phys. Rev. B **2**, 2016 (1970).
13. A. G. Kazanskii, P. L. Richards, and E. E. Haller, Appl. Phys. Lett. **31**, 496 (1977).
14. V. Y. Aleshkin, A. V. Gavrilenko, V. I. Gavrilenko, *et al.*, Phys. Status Solidi C **0**, 680 (2003).
15. Sh. M. Kogan and A. F. Polupanov, Zh. Éksp. Teor. Fiz. **80**, 394 (1981) [Sov. Phys. JETP **53**, 201 (1981)].
16. G. L. Bir and G. E. Pikus, *Symmetry and Stain-Induced Effects in Semiconductors* (Nauka, Moscow, 1972; Wiley, New York, 1975).
17. P. I. Baranskiĭ, V. P. Klochkov, and I. V. Potykevich, *Semiconductor Electronics* (Naukova Dumka, Kiev, 1975), pp. 8, 129 [in Russian].
18. A. F. Polupanov and R. Taksinbaev, Fiz. Tekh. Poluprovodn. (Leningrad) **18**, 279 (1984) [Sov. Phys. Semicond. **18**, 173 (1984)].
19. Yu. P. Gousev, I. V. Altukhov, E. G. Chirkova, *et al.*, Appl. Phys. Lett. **75**, 757 (1999).

Translated by D. Mashovets

Semiconductors, Vol. 39, No. 2, 2005, pp. 189–191. Translated from Fizika i Tekhnika Poluprovodnikov, Vol. 39, No. 2, 2005, pp. 204–207.

SEMICONDUCTOR STRUCTURES, INTERFACES, AND SURFACES

The Effect of Laser Radiation on the Formation of Oriented Cadmium Sulfide Layers under Highly Nonequilibrium Conditions

A. P. Belyaev^, V. P. Rubets, and V. V. Antipov

St. Petersburg State Technological Institute (Technical University), St. Petersburg, 190013 Russia

^e-mail: Belyaev@tu.spb.ru

Submitted February 16, 2004; accepted for publication April 14, 2004

Abstract—The effect of low-power laser radiation on the formation of oriented cadmium sulfide layers from a vapor phase on a substrate cooled with liquid nitrogen (highly nonequilibrium conditions) is studied. The results of technological experiments, the results of a study of electron diffraction (electron diffraction patterns), and condensation diagram data are reported. It is found that, depending on the substrate temperature, laser radiation can both improve and worsen the crystal quality of films. It is shown that a condensation diagram of cadmium sulfide layers formed on a substrate exposed to low-power laser radiation is shifted to higher temperatures relative to a condensation diagram obtained without laser radiation. The experimental results are interpreted in the context of a solitonic heteroepitaxy model. © *2005 Pleiades Publishing, Inc.*

1. INTRODUCTION

Studies of the formation of layers of binary II–VI compounds by the vacuum condensation from a vapor phase onto a substrate cooled with liquid nitrogen (highly nonequilibrium conditions) have been reported previously [1–9]. The results of these studies for the first time allowed researchers to carry out a low-temperature synthesis of semiconductor epitaxial films on an oriented substrate and oriented films on an amorphous substrate as well as to fabricate structures with unconventional properties. In this context, we report below the results of studying the effect of low-power laser radiation on the formation of cadmium sulfide layers under highly nonequilibrium conditions.

2. EXPERIMENTAL

The samples under study were synthesized at a residual pressure of 10^{-3} Pa on a muscovite-mica substrate cooled with liquid nitrogen, using a previously described procedure [2, 3]. Open evaporation was used for the synthesis. In this case, an evaporator reactor containing cadmium sulfide powder was arranged above the substrate at a distance of about 50 mm. The evaporator temperature was 900 K. The temperatures of the evaporator and the substrate were measured using copper–Constantan thermocouples. The possible overheating of the substrate was monitored by the above-mentioned procedure [2, 3]. The integrated growth rates were calculated using experimental data on the film's thickness and its formation time.

The thickness was measured using a MII-4 interferometer, and the structure was studied using an ÉMR-100 diffractometer. The layers under study were ~0.2 μm thick.

For the synthesis under laser radiation, we used an ILGI-503 gas laser with a power of 3 mW and a repetition frequency of pulses of 100 Hz at the wavelength $\lambda = 337$ nm. The laser radiation, using a special optical system, was incident at an angle to the substrate and had a spotlike shape ~2 mm in diameter.

3. RESULTS

We studied the formation of the cadmium sulfide films under highly nonequilibrium conditions, i.e., on a substrate cooled with liquid nitrogen. The studies carried out included technological experiments; recording of condensation diagrams, i.e., dependences of the growth rate on the substrate temperature; and study of electron diffraction.

The condensation diagram of the system under investigation was qualitatively similar to the condensation diagram of cadmium telluride layers [9]. It included regions with an anomalously low condensation rate, in which the integrated growth rate of the films decreased by several orders of magnitude. Thus, synthesized films were of a high structural quality. This fact is confirmed by Fig. 1a, which shows the electron diffraction pattern of a sample grown at the optimal substrate temperature for oriented growth: $T_s^{opt} = 200$ K. The structure of the films grown in the same technological mode on the laser-irradiated substrate degraded (Fig. 1b), while the growth rate increased by ~10%. As the substrate temperature rose somewhat above T_s^{opt}, the situation became reversed. The laser radiation

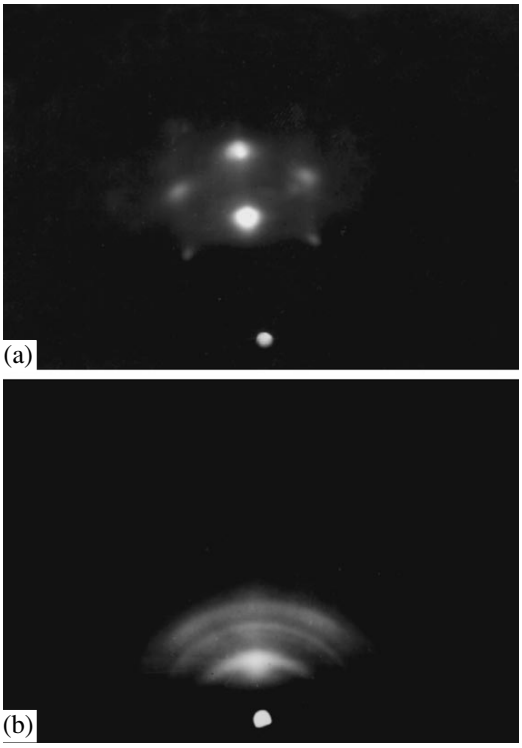

Fig. 1. The electron diffraction patterns of cadmium sulfide films grown at the substrate temperature T_s = 200 K (a) without laser radiation and (b) under the effect of laser radiation.

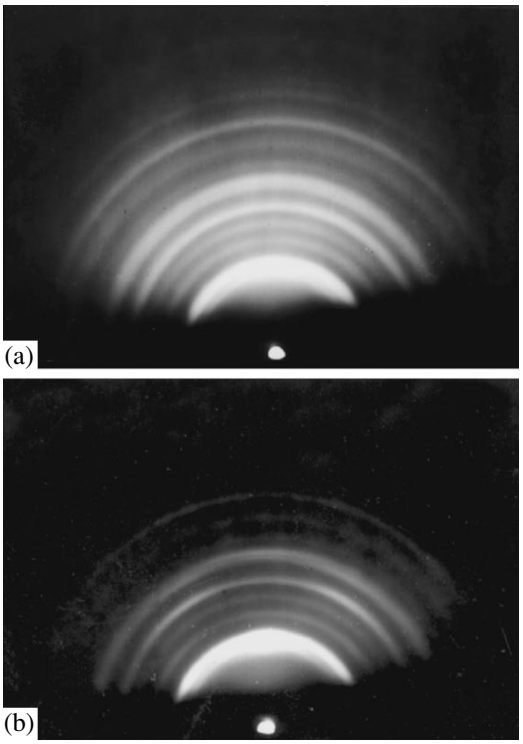

Fig. 2. The electron diffraction patterns of cadmium sulfide films grown at the substrate temperature T_s = 220 K (a) without laser radiation and (b) under the effect of laser radiation.

improved the film's crystal quality, while the growth rate decreased by ~10%. This fact is illustrated in Figs. 2 and 3, which show the typical electron diffraction patterns of films grown at T_s = 220 K and T_s = 230 K (a) without laser radiation and (b) on the laser-irradiated substrate.

4. DISCUSSION

It is known [2, 3, 5, 6, 9] that the formation of the oriented layer on an oriented substrate under highly nonequilibrium conditions includes nucleation, condensation (the formation of dispersed particles (DPs) on the substrate), incorporation, and coalescence into the continuous layer. The specific features of this formation under highly nonequilibrium conditions are nucleation and incorporation. The nucleation at very high supersaturation proceeds in the vapor phase, while the incorporation of DPs into the crystal lattice at extremely low temperatures is performed in a diffusionless way owing to the soliton mechanism of mass transfer. The joint effect of these specific features leads to a correlated orientation of the DPs and a low growth rate of the layer.

The soliton mechanism of mass transfer consists in the motion of the DPs, which is due to the motion of misfit dislocations between the DPs and the substrate. This motion occurs specifically in the form of particle-like waves (solitons). In this motion mode, the atoms move sequentially in the DP-substrate plane. At each instant, almost all the DP atoms remain immobile relative to the substrate, and only a very small group of atoms move. The atoms ahead of the wave front are immobile since the wave still has not reached them, and the atoms behind the front are immobile since the wave has already propagated through them. Only atoms that constitute the wave front at that instant contribute to the motion. On the passing of such a wave (one soliton), the DP shifts by one lattice constant. At low temperatures, when the atomic diffusivity is very low, this diffusionless soliton mechanism is more favorable than other mass transfer mechanisms by virtue of the ability of solitons to propagate with a low energy loss.

The emergence of solitons is caused by a certain relation between the lattice constants of the DP $a(T_r)$ and the substrate $b(T_s)$. This relation ensues from the following condition, whose fulfillment is necessary for the emergence of solitons and was obtained theoretically in [10]:

$$\frac{a(T_r) - b(T_s)}{b(T_s)} > (2/\pi)^{3/2}\sqrt{f/\lambda a(T_r)}\ldots. \qquad (1)$$

Here, f and λ are parameters characterizing the interaction forces between the DP atoms and the substrate, and the interaction between the substrate atoms, respectively.

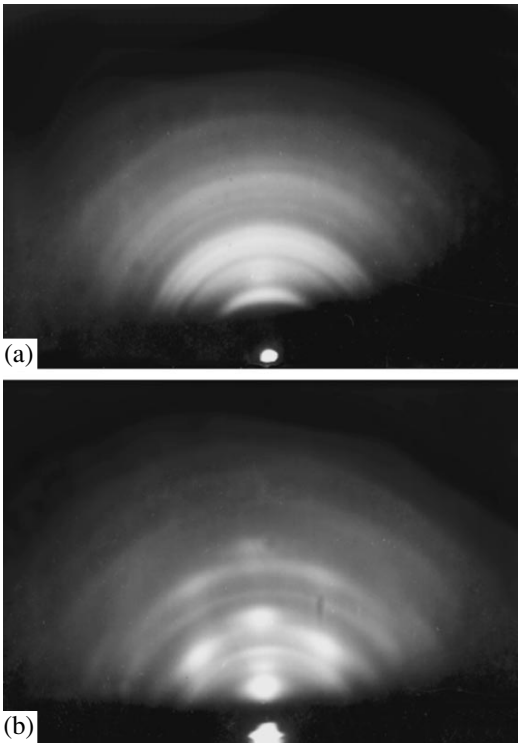

Fig. 3. The electron diffraction patterns of cadmium sulfide films grown at the substrate temperature T_s = 230 K (a) without laser radiation and (b) under the effect of laser radiation.

If the value of $a(T_r)$ is close to that of $b(T_s)$, the necessary relation between them can be attained by varying the substrate temperature T_s and the DP temperature T_r.

In previous studies devoted to layer growth under highly nonequilibrium conditions [2–9], the fulfillment of condition (1) was provided by varying the substrate temperature T_s. In the experiment discussed, an additional degree of freedom is added, specifically laser radiation. The radiation mainly affects the DP temperature T_r. This fact can be perceived even without estimation calculations, since the DP surface, which absorbs the radiation, exceeds the surface contacting the substrate and serving as a heat sink by a factor of several times. The inverse relation is valid for the substrate since the surface exposed to radiation is partially occupied by DPs.

The substrate and the DPs can become lattice-matched, which is necessary for the emergence of solitons, due to the temperature difference between the substrate and the DP. Therefore, an increase in the DP temperature T_r under the effect of laser radiation should cause condition (1) to be satisfied at a higher substrate temperature T_s.

The suggested model is completely consistent with the experimental results. Indeed, compared with the structure of films grown under the same conditions without radiation, the crystal structure under the effect of laser radiation at substrate temperatures higher than T_s^{opt} improves (compare Figs. 2a, 3a, and Figs. 2b, 3b). Conversely, at the optimal substrate temperature T_s^{opt}, laser radiation deteriorated the crystal quality of the films (compare Figs. 1a and 1b). A decrease in the growth rate in the first case, naturally, is attributed to increased reevaporation, which is caused by a higher DP temperature, while an increase in the growth rate at T_s^{opt} is attributed to violation of condition (1). By virtue of this fact, the energy dissipation is stronger than at the optimal temperature and, consequently, the DP temperature is lower. Laser radiation appears to shift the condensation diagram to higher temperatures.

5. CONCLUSIONS

(i) During the growth of cadmium sulfide layers under highly nonequilibrium conditions, low-power laser radiation shifts the optimal substrate temperature for oriented growth to higher temperatures.

(ii) The growth features of cadmium sulfide layers in highly nonequilibrium conditions under low-power laser radiation are consistently explained in the context of the soliton heteroepitaxy model.

ACKNOWLEDGMENTS

This study was supported by the Russian Foundation for Basic Research, project no. 02-03-40432.

REFERENCES

1. A. P. Belyaev, V. P. Rubets, and I. P. Kalinkin, Fiz. Tekh. Poluprovodn. (St. Petersburg) **31**, 966 (1997) [Semiconductors **31**, 823 (1997)].
2. A. P. Belyaev, V. P. Rubets, and I. P. Kalinkin, Fiz. Tverd. Tela (St. Petersburg) **39**, 382 (1997) [Phys. Solid State **39**, 333 (1997)].
3. A. P. Belyaev, V. P. Rubets, and I. P. Kalinkin, Neorg. Mater. **34** (3), 238 (1998).
4. A. P. Belyaev, V. P. Rubets, and M. Yu. Nuzhdin, Fiz. Tekh. Poluprovodn. (St. Petersburg) **34**, 1208 (2000) [Semiconductors **34**, 1157 (2000)].
5. A. P. Belyaev and V. P. Rubets, Fiz. Tekh. Poluprovodn. (St. Petersburg) **35**, 294 (2001) [Semiconductors **35**, 279 (2001)].
6. A. P. Belyaev, V. P. Rubets, and I. P. Kalinkin, Zh. Tekh. Fiz. **71** (4), 133 (2001) [Tech. Phys. **46**, 495 (2001)].
7. A. P. Belyaev and V. P. Rubets, Fiz. Tekh. Poluprovodn. (St. Petersburg) **36**, 843 (2002) [Semiconductors **36**, 789 (2002)].
8. A. P. Belyaev, V. P. Rubets, M. Yu. Nuzhdin, and I. P. Kalinkin, Fiz. Tekh. Poluprovodn. (St. Petersburg) **37**, 641 (2003) [Semiconductors **37**, 617 (2003)].
9. A. P. Belyaev, V. P. Rubets, I. P. Kalinkin, and M. Yu. Nuzhdin, Zh. Fiz. Khim. **77**, 1883 (2003).
10. S. A. Kukushkin and A. V. Osipov, Fiz. Tverd. Tela (St. Petersburg) **36**, 1461 (1994) [Phys. Solid State **36**, 799 (1994)].

Translated by N. Korovin

Semiconductors, Vol. 39, No. 2, 2005, pp. 192–197. Translated from Fizika i Tekhnika Poluprovodnikov, Vol. 39, No. 2, 2005, pp. 208–213.

SEMICONDUCTOR STRUCTURES, INTERFACES, AND SURFACES

Scattering of Charge Carriers at the Boundaries of Crystallites in Films of Polycrystalline Silicon

V. A. Gridchin, V. M. Lyubimskiĭ^, and A. G. Moiseev

Novosibirsk State Technical University, Novosibirsk, 630092 Russia

^e-mail: lubvlm@ngs.ru

Submitted March 4, 2004; accepted for publication April 15, 2004

Abstract—Scattering of charge carriers by the potential barriers at grain boundaries in films of polycrystalline silicon is considered. The influence of this scattering mechanism on charge-carrier mobility is analyzed. Satisfactory agreement between the calculated and experimental values of mobility is observed. The model developed in this study can be used to gain insight into other kinetic phenomena. *© 2005 Pleiades Publishing, Inc.*

1. INTRODUCTION

Electrical conductivity is the most comprehensively studied kinetic phenomenon in polycrystalline silicon [1–4]. According to existing one-dimensional models, the resistivity of polycrystalline silicon is controlled by the resistivity of crystallites (grains) and of grain boundaries. Due to the effect of the grain boundaries, the resistivity of polycrystalline silicon is higher than that of single-crystal silicon at the same level of doping. Conductivity models make it possible to give a qualitative and, if two artificial factors are introduced, quantitative explanation of the concentration and temperature dependences of electrical conductivity and also the presence of a minimum in the charge-carrier mobility in relation to the impurity concentration. These models also serve as a basis for the development of new models [5] and interpretation of new experimental data concerned with polycrystalline silicon [6–9] and other materials [10, 11].

All the existing models of electrical conductivity in polycrystalline silicon are based on the following assumptions: (i) electrical conductivity inside crystallites is the same as in single crystals at a corresponding charge-carrier concentration and (ii) transport of charge carriers through a potential barrier is described in terms of thermal electron emission. In these models, the fact that the sizes of crystallites in the film can vary several times and can be comparable to the de Broglie wavelength is disregarded. For example, the de Broglie wavelength for holes and electrons at room temperature is equal to about 200 Å (see, e.g., [12]). In addition, the application range of the models [1–4] is restricted only to electrical conductivity and is not extended to other kinetic phenomena.

In this paper, we suggest a quantum-mechanical model of charge-carrier scattering at the potentials of the grain boundaries in polycrystalline silicon that takes into account a spread in the grain sizes; furthermore, we analyze the effect of this scattering mechanism on charge-carrier mobility and the solution of the Boltzmann equation in this model. Such an approach makes it possible to describe not only the electrical conductivity but also other kinetic phenomena.

2. THEORY

Scattering of electrons at the grain boundaries in polycrystalline metal films has been considered previously [13]. It was assumed in that study that the potential at the grain boundaries had the form of the Dirac delta function, whereas the multiparticle distribution function $g(z_1, z_2, \ldots, z_N)$ of potential barriers was a known Gaussian function. The representation of the potential barriers at crystallite boundaries in metals as the delta function is quite justified; however, this representation does not hold for semiconductors due to the lower concentration of charge carriers in these materials.

A solution to the problem of charge-carrier scattering in polycrystalline films involves some difficulties if the crystallites have an arbitrary size, shape, and orientation. Therefore, we suggest a model in which the crystallites have the shape of rectangular parallelepipeds with one of the axes perpendicular to the film, while the other two axes are parallel and perpendicular to the applied external field E_z. Potential barriers with a finite height are assumed to exist at the crystallite boundaries; distances between these barriers correspond to the sizes of the crystallites. The latter are not correlated; therefore, the coordinates z_n of potential-barrier centers are shifted by a random quantity δz_n with respect to the mean values of these coordinates. The charge-carrier scattering occurs at potential barriers, impurities, phonons, and so on. The scattering mechanisms are independent of each other. It is important that the variation in the potential-barrier energy, resulting from the application of an external electric field, is much smaller than the mean energy of the charge carriers.

A model of potential barriers is illustrated in Fig. 1.

1063-7826/05/3902-0192$26.00 © 2005 Pleiades Publishing, Inc.

Potential barriers at the grain boundaries are described by the function

$$u = \sum_n^N U_0(z - z_n), \quad z_n = nd + \delta z_n, \quad N = \frac{L_z}{d},$$

where L_z is the sample length along the z axis.

The Boltzmann equation for the model under consideration, which has an electric field E_z applied along the z axis, and for other scattering mechanisms with the relaxation time τ taken into account can be written as [13]

$$eE v_z \frac{\partial f_0(k)}{\partial \varepsilon} = \int P(k, k')(\Phi(k) - \Phi(k'))dk' + \frac{\Phi(k)}{\tau}.$$

Here, $\Phi(k) = f(k) - f_0(k)$, where $f(k)$ and $f_0(k)$ are nonequilibrium and equilibrium Fermi distribution functions; $P(k, k')$ is the probability of a charge-carrier transition from state k to state k' due to scattering at unordered potential barriers; e is the elementary charge; and ε and v_z are the energy of the charge carriers and the component of their velocity along the z axis.

In order to determine $P(k, k')$, we assume that $u(z)$ is a weak perturbation of the Hamiltonian operator, whereas the unperturbed states are described by the wave function

$$\psi_k = \Omega^{-1/2}\exp(ikr),$$

where $\Omega = L_x L_y L_z$ is the volume of a polycrystal.

The probability of the transition from state k to state k' is defined by the squared modulus of the corresponding matrix element. Thus, we have

$$|\langle k|u|k'\rangle|^2 = |S|^2|U|^2,$$

$$S = \frac{1}{N}\sum_n \exp(-i\Delta k_z z_n),$$

$$U = \frac{1}{d}\int U_0(z')\exp(-i\Delta k_z z')dz', \quad z' = z - z_n.$$

If we assume that the shifts δz_n of the potential barriers are random quantities, we introduce a distribution function $g(\delta z)$ that describes these shifts with respect to their mean positions. Assuming that the shift of each potential barrier is independent of the shift of another potential barrier, we obtain the expression

$$|S|^2 = \frac{1}{N}(1 - |g(\Delta k_z)|^2) + |g(\Delta k_z)|^2|S_M(\Delta k_z)|^2,$$

where $g(\Delta k_z) = \int g(\delta z)\exp(-i\Delta k_z \delta z)d(\delta z)$ and $S_M(\Delta k_z) = \frac{1}{N}\sum_n \exp(-i\Delta k_z dn)$ is the structure factor.

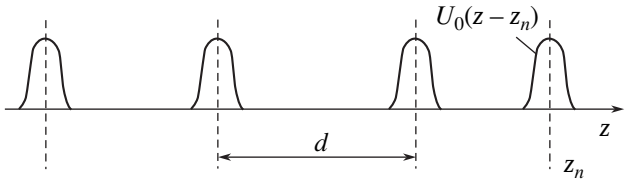

Fig. 1. A model of potential barriers.

By further assuming that these shifts obey the Gaussian distribution law

$$g(\delta z) = \frac{1}{s\sqrt{2\pi}}\exp\left(-\frac{\delta z^2}{2s^2}\right)$$

with the standard deviation s, we obtain

$$P(k, k') = A(|\Delta k_z|)\delta(k'_x - k_x)\delta(k'_y - k_y)\delta(k'_z + k_z),$$

$$A(|\Delta k_z|) = \begin{cases} \dfrac{|U|^2 m^* d}{\hbar^3 |k_z|}(1 - \exp(-2k_z^2 s^2)), & \Delta k_z \neq \dfrac{2\pi n}{d} \\ \infty, & \Delta k_z = \dfrac{2\pi n}{d}. \end{cases}$$

As a result of solving the Boltzmann equation, the function $\Phi(k)$ can be written as

$$\Phi(k) = \tau^* eE v_z \frac{\partial f_0}{\partial \varepsilon}, \tag{1}$$

where $\tau^{*-1} = \tau^{-1} + 2A(|k_z|)$.

It follows from expression (1) that a spread in the sizes of the crystallites in the case of scattering at potential barriers leads to an additional scattering with the relaxation time

$$\tau_b = \frac{1}{2A(|k_z|)}.$$

The current density can be calculated using the well-known formula

$$\mathbf{j} = -\frac{e}{4\pi^3}\int \mathbf{v}\Phi(k)dk.$$

The mean relaxation time in the case of scattering at potential barriers can be determined if we assume that there are no other scattering mechanisms ($\tau = \infty$ and $\tau^* = \tau_b$).

In the case of degenerate statistics, the electrical conductivity can be represented as

$$\sigma = -\frac{2e^2(m_d^*)^{\frac{3}{2}}}{\sqrt{2}\pi^2 m^* \hbar^3}\int_0^{\infty}\int_0^{\pi} \frac{\partial f_0}{\partial \varepsilon}\tau_b(\varepsilon, \theta)\varepsilon^{\frac{3}{2}}\cos^2\theta \sin\theta d\theta d\varepsilon, \tag{2}$$

where m_d^* is the effective density-of-states mass.

Parameters of the studied samples

Sample no.	ρ_s, Ω/□ (24°C)	p, 10^{19} cm^{-3} (24°C)	μ, cm^2 V^{-1} s^{-1} (24°C)	$T K\rho_s$, 10^{-4} K^{-1} (24°C)	T_{gr}, °C	T_{ann}, °C	The Si* layer thickness, μm	d, 10^{-6} cm	s, 10^{-6} cm
1	84	6.5	21	1.83	610	1000	0.55	6.52	3.4
2	76	6.45	23	2.8		1050	0.55	9.63	4.2
3	58	6.7	28	5		1100	0.55	13.2	5.4
4	51	6.75	33	7.9		1150	0.55	14.7	5.3
5	65	7	26.5	5	625	1000	0.525	10.3	3.8
6	61	7.25	28	6.6		1050	0.505	10.5	4.3
7	53	7.9	31	9		1100	0.480	15.6	5.6
8	56	7.75	32	10		1150	0.46	17.3	7.0

In this case, the relaxation time is given by

$$\langle\tau_b\rangle = -\frac{\int_0^\infty\int_0^\pi \frac{\partial f_0}{\partial\varepsilon}\tau_b(\varepsilon,\theta)\varepsilon^{\frac{3}{2}}\cos^2\theta\sin\theta d\theta d\varepsilon}{\int_0^\infty f_0\varepsilon^{\frac{1}{2}}d\varepsilon}. \quad (3)$$

If there is no degeneracy, the electrical conductivity can be written as

$$\sigma = \frac{\sqrt{2}e^2\hbar^3 p}{\sqrt{\pi}(m^*)^{5/2}(k_0T)^{3/2}} \times\int_0^\infty \tau_b(k_z)k_z^2\exp\left(-\frac{k_z^2\hbar^2}{2m^*k_0T}\right)dk_z, \quad (4)$$

where p is the hole concentration.

It follows from formula (4) that

$$\langle\tau_b\rangle = \frac{\sqrt{2}\hbar^3}{\sqrt{\pi}(m^*)^{3/2}(k_0T)^{3/2}} \times\int_0^\infty \tau_b(k_z)k_z^2\exp\left(-\frac{k_z^2\hbar^2}{2m^*k_0T}\right)dk_z. \quad (5)$$

The condition for applying perturbation theory to the model under consideration consists in the fulfillment of the relation $\tau > \frac{\hbar}{k_0T}$ when there is no degeneracy and the relation $\tau > \frac{\hbar}{\eta}$ for a completely degenerate electron gas (η is the Fermi energy). These relations are based on the fact that successive scattering events are disregarded in the first approximation of perturbation theory [14]. In addition, the same relations represent the criterion for the applicability of the kinetic equation and, as is well known, correspond to the charge-carrier mobility on the order of 10 cm^2/(V s).

The expression for the relaxation time can be simplified in the case of scattering at potential barriers. This simplification is based on the fact that the standard deviation between the sizes of the crystallites and the mean values $s \approx 0.3$–$0.5d$ according to the experimental data (see table) [15]. An analysis of the integrands in expressions (4) and (5) shows that they have a maximum at $k \approx 7\times10^6$–10^7 cm^{-1} at temperatures higher than 100 K; as a result, the major contribution to the integrals comes from the range 10^6 cm$^{-1} < k < 3\times10^7$ cm^{-1}. Therefore, we may assume that $k_z^2 s^2 \gg 1$ for polycrystalline films with crystallite mean sizes of $d \geq 2\times10^{-6}$ cm; consequently, the formula for the relaxation time $\tau_b = \frac{1}{2A(|k_z|)}$ is simplified and can be written as

$$\tau_b = \frac{\hbar^3|k_z|}{2m^*d|U|^2}. \quad (6)$$

A comparison of expression (6) with the expression for relaxation time [13] shows that these expressions coincide when the electron wavelength is smaller than the standard deviation of the sizes of the crystallites ($k_z^2 s^2 \gg 1$).

3. COMPARISON OF THEORETICAL AND EXPERIMENTAL RESULTS

Before discussing the results of the calculations and experimental data, the following points should be noted. It is well known that it is impossible to adequately describe the temperature dependences of charge-carrier mobility in single-crystal p-Si if generally accepted mechanisms of scattering are used. Therefore, it would seem erroneous to expect that one can attain agreement between experimental and theoretical dependences for polycrystalline p-Si by varying some of the parameters. In this context, we gave partic-

ular attention to the following issues when assessing the results obtained using the suggested model:

(i) whether an increase in the charge-carrier mobility is observed as the temperature is increased at low levels of doping; and

(ii) whether the mobility increases as the grain size increases.

At an impurity concentration higher than 10^{17}–10^{18} cm^{-3}, the potential at the grain boundaries in polycrystalline *p*-Si has the shape shown in Fig. 2 at and corresponds to a mobility minimum [2, 3]; analytically, this potential is given by

$$U_0 = \begin{cases} V_b\left(1 + \dfrac{\delta - 2|x|}{2w}\right)^2, & \dfrac{\delta}{2} < |x| < \dfrac{\delta}{2} + w \\ V_0, & |x| < \dfrac{\delta}{2}. \end{cases}$$

In polycrystalline *p*-Si, we have

$$V_b = \frac{e^2 N w^2}{2\varepsilon\varepsilon_0};$$

therefore, the half-width of the depletion region w can be estimated using the formula [1]

$$w = \frac{Q_t}{2N},$$

where N is the impurity concentration and Q_t is the density of the trap states.

As was mentioned above, perturbation theory can be used if the potential is such that the relaxation time satisfies the inequalities $\tau_b > \dfrac{\hbar}{k_0 T}$ for a nondegenerate semiconductor and $\tau_b > \dfrac{\hbar}{\eta}$ for a completely degenerate semiconductor. This circumstance imposes a restriction both on the value of the potential and the range of the potential definition (on the width of the potential region in a one-dimensional case). For example, for the density of the trap states $Q_t = (1.9–3.7) \times 10^{12}$ cm^{-2} [1, 2] and the charge-carrier mobility of 20–30 cm^2/(V s) at room temperature, the charge-carrier concentration should exceed 10^{19} cm^{-3} according to calculations of the relaxation time in the case of scattering at potential barriers. In this situation, $w < 10$–20 Å, which is smaller than the Broglie wavelength by an order of magnitude. The charge carriers are degenerate at such a high concentration, which means that formulas (2) and (3) must be used.

In the majority of the previous publications concerned with electrical conductivity of polycrystalline silicon, the values of charge-carrier mobility at room temperature and the temperature coefficients of resistivity have been reported. Therefore, when comparing

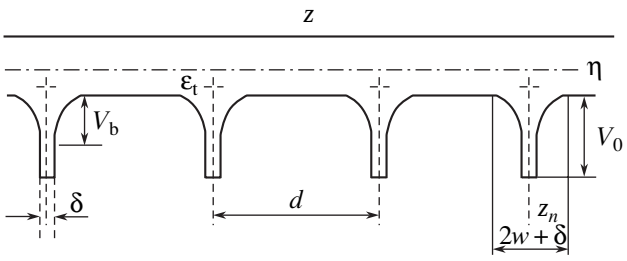

Fig. 2. A model of the potential barriers in polycrystalline *p*-Si.

the theoretical and experimental data, we used our own results and published experimental data [1] for the hole concentrations of 10^{19} and 5×10^{19} cm^{-3}. The mean sizes of the grains were equal to 230 Å in the films of polycrystalline silicon studied by Seto [1].

The films of polycrystalline silicon studied by us were formed in a low-pressure reactor at temperatures of 610 and 625°C on oxidized silicon wafers oriented in the (100) plane. The oxide thickness was 0.43 μm. The thickness of the polysilicon film was approximately 0.5 μm. The film was doped using implantation of boron ions with an energy of 50 keV and a dose of 4×10^{15} cm^{-2}, with subsequent annealing for 40 min at 1000–1150°C. The parameters of the studied films are listed in the table. The films were isotropic. As can be seen from the table, the mean grain sizes in the films varied from 650 to 1730 Å for a hole concentration ranging from 6.5×10^{19} to 8×10^{19} cm^{-3}. In this case, the potential-barrier width is on the order of 10 Å and is much smaller than the mean free path of the holes.

The Fermi energy appearing in formulas (2) and (3) is obtained by solving an electroneutrality equation for the nondepleted (middle) portion of the grain

$$N_v \int_0^\infty \frac{\varepsilon^{\frac{1}{2}} d\varepsilon}{\exp\left(\dfrac{\varepsilon - \eta}{k_0 T}\right) + 1} = N_a^-,$$

where N_v is the effective density of the states and N_a is the concentration of ionized acceptors.

We have $N_a^- \approx N_a$ if the impurity concentration is 10^{19} cm^{-3} or higher.

The value of w is determined as a result of solving the following electroneutrality equation for the depletion region:

$$\frac{1}{w}\int_0^w p(x)dx + \frac{Q_t^+}{2w} = N_a^- \approx N_a,$$

$$Q_t^+ = \frac{Q_t}{2\exp\left(\dfrac{\eta - \varepsilon_t + V_b}{k_0 T}\right) + 1}.$$

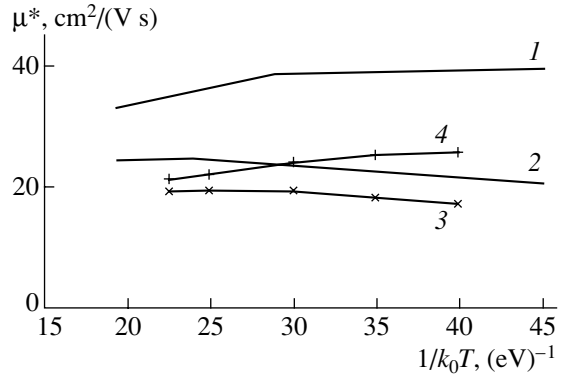

Fig. 3. Temperature dependences of the charge-carrier mobility in polycrystalline *p*-Si. The hole concentration p = (*1*) 1.0×10^{19}, (*2*) 5.0×10^{19}, (*3*) 1.0×10^{19}, and (*4*) 5.0×10^{19} cm^{-3}. Curves *1* and *2* correspond to the calculation and curves *3* and *4* represent the experimental data.

Here, ε_t is the energy of the trap states, Q_t is the density of the trap states, and Q_t^+ is the density of the charged trap states.

The first term on the left-hand of the above equation is much smaller than the second and third terms. Therefore,

$$w = \frac{Q_t^+}{2N_a}.$$

If the amorphous layer is disregarded, the mean hole concentration is given by

$$\langle p \rangle = \frac{1}{d}\left(2N_v \int_0^w \int_{\frac{V_b}{k_0T}\left(1-\frac{x}{w}\right)^2}^{\infty} \frac{\varepsilon^{\frac{1}{2}} d\varepsilon dx}{\exp\left(\frac{\varepsilon-\eta}{k_0T}\right)+1} + (d-2w)N_v \int_0^{\infty} \frac{\varepsilon^{\frac{1}{2}} d\varepsilon}{\exp\left(\frac{\varepsilon-\eta}{k_0T}\right)+1}\right). \quad (7)$$

At $\langle p \rangle > 10^{19}$ cm^{-3}, the first term on the right-hand side of Eq. (7) amounts to less than 3%.

In Figs. 3–5, we show the temperature dependences of the hole mobility μ* calculated using the suggested model; experimental hole mobilities reported by Seto [1] and our own experimental data are also shown. In Figs. 4 and 5, we also show the hole mobilities in single-crystal silicon. We calculated this mobility using the formula

$$\frac{1}{\mu^*} = \frac{1}{\mu} + \frac{1}{\langle \mu_b \rangle}, \quad (8)$$

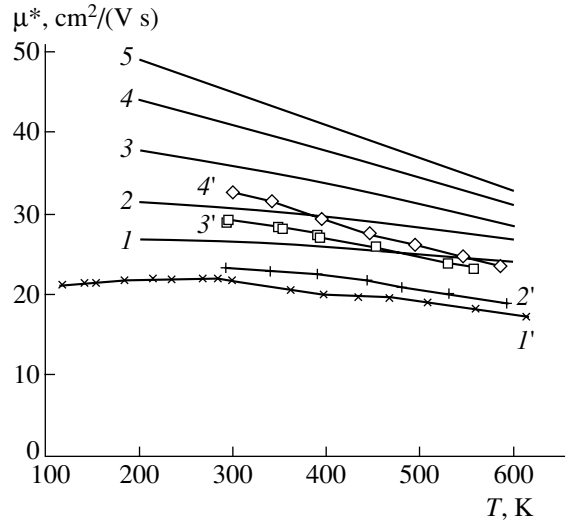

Fig. 4. Temperature dependences of the charge-carrier mobility in polycrystalline and single-crystal *p*-Si. Curves *1*–*4* represent the results of the calculations and curves *1*'–*4*' represent the experimental data. Curves *1* and *1*' are for sample 1; curves *2* and *2*', for sample 2; curves *3* and *3*', for sample 3; curves *4* and *4*', for sample 4; and curve *5*, for single-crystal *p*-Si with a hole concentration of 7×10^{19} cm^{-3}.

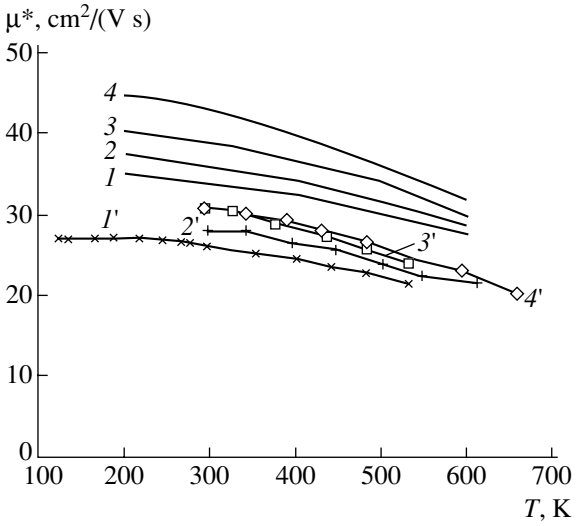

Fig. 5. Temperature dependences of the charge-carrier mobility in polycrystalline and single-crystal *p*-Si. Curves *1*–*3* correspond to the results of the calculations; squares, crosses, and curves *1*'–*4*' represent the experimental data. Curves *1* and *1*' are for sample 5; curves *2* and *2*', for sample 6; curves *3* and *3*', for sample 7; curves *3* and *4*', for sample 8; and curve *4*, for single-crystal *p*-Si with a hole concentration of 8×10^{19} cm^{-3}.

where μ is the experimental value of mobility in single-crystal silicon and $\langle \mu_b \rangle = \frac{e\langle \tau_b \rangle}{m^*}$ is the mobility in polycrystalline silicon in the case of scattering at the potential barriers.

Quantity $\langle \tau_b \rangle$ was calculated using formula (3).

Calculation of the mobility with formula (8), rather than with formulas (1) and (3), leads to underestimation of that mobility [16]. However, the necessity of using formula (8) in calculations stems from the fact that there are several mechanisms of charge-carrier scattering in single-crystal silicon at temperatures of 200–600 K; consequently, it is rather difficult to take into account the contribution of each mechanism to the mobility.

When calculating the mobility, we analyzed the effects of Q_t, w, δ, and V_0 on the relaxation time. It was found that the relaxation is most profoundly affected by the rectangular portion of the intercrystallite potential; at the same time, the variation in the temperature dependence of the mobility as the impurity concentration is changed is related to the quadratic coordinate dependence of the potentials.

When calculating the mobilities shown in Figs. 3–5, we used the following parameter values: $Q_t = (1.9–3.7) \times 10^{12}$ cm^{-2}, $V_0 = 0.65$ eV, and $\delta = 2.5–9$ Å.

According to estimations, $Q_t = 2.5 \times 10^{12}$ cm^{-2} and $\delta = 6.4–8.5$ Å for polycrystalline *n*-Si [4], whereas $Q_t = 3.7 \times 10^{12}$ cm^{-2} [1] and $Q_t = 1.9 \times 10^{12}$ cm^{-2} [2] for polycrystalline *p*-Si.

It can be seen from Fig. 3 that an increase in both the experimental and calculated mobility is observed as the temperature increases if the impurity concentration is equal to 10^{19} cm^{-3}. It can be also seen from Figs. 3–5 and the table that the charge-carrier mobility increases as the mean grain size increases.

The dependences shown in Figs. 3–5 indicate that the calculated mobilities exceed the experimental values. The larger values of the calculated mobilities can be caused by the following factors: (i) The shape of the actual intercrystallite potential differs from that shown in Fig. 2 (the shape of the potential profoundly affects its scattering properties). (ii) Crystallites in the film of polycrystalline silicon have a complex shape. Moreover, the area of contact with neighboring crystallites is apparently smaller that the side-surface area, which leads to an overestimated value of experimentally determined resistivity and an underestimated value of mobility. (iii) Finally, an arbitrary orientation of crystallites with respect to each other is disregarded in the suggested model; this random orientation should give rise to additional scattering.

4. CONCLUSION

We suggested a model of charge-carrier scattering by potential barriers at the boundaries of crystallites. We derived an expression for the relaxation time of this type of scattering. It follows from this expression that the scattering becomes more intense as the sizes of the crystallites decrease. Comparison of the results of the calculations with experimental data shows that the model adequately describes charge-carrier scattering by potential barriers and that it is necessary to take into account this scattering in calculations of the value and temperature dependence of the charge-carrier mobility in polycrystalline *p*-Si. The results obtained can be used to describe other kinetic phenomena.

REFERENCES

1. J. Y. W. Seto, J. Appl. Phys. **46**, 5247 (1975).
2. N. C. C. Lu, C. Y. Gerberg, C. Y. Lu, and J. D. Meidl, IEEE Trans. Electron Devices **28**, 818 (1981).
3. M. M. Manddurah, K. C. Saraswat, and T. I. Kamins, IEEE Trans. Electron Devices **28**, 1163 (1981).
4. M. M. Manddurah, K. C. Saraswat, and T. I. Kamins, IEEE Trans. Electron Devices **28**, 1171 (1981).
5. K. M. Doshchanov, Fiz. Tekh. Poluprovodn. (St. Petersburg) **32**, 690 (1998) [Semiconductors **32**, 619 (1998)].
6. K. M. Doshchanov, Fiz. Tekh. Poluprovodn. (St. Petersburg) **31**, 954 (1997) [Semiconductors **31**, 813 (1997)].
7. D. V. Shengurov, D. A. Pavlov, V. N. Shabanov, *et al.*, Fiz. Tekh. Poluprovodn. (St. Petersburg) **32**, 627 (1998) [Semiconductors **32**, 562 (1998)].
8. Chung-Hui Cheu, Yean-Kuen Fang, Chin-Wei Yang, *et al.*, IEEE Electron Device Lett. **22**, 524 (2001).
9. Hang-Ming Chuang, Kong-Beng Thei, Sheng-Fu Tsai, and Wen-Chau Liu, IEEE Trans. Electron Devices **50**, 1413 (2003).
10. S. A. Kolosov, Yu. V. Klevkov, and A. F. Plotnikov, Fiz. Tekh. Poluprovodn. (St. Petersburg) **38**, 305 (2004) [Semiconductors **38**, 293 (2004)].
11. S. A. Kolosov, Yu. V. Klevkov, and A. F. Plotnikov, Fiz. Tekh. Poluprovodn. (St. Petersburg) **38**, 473 (2004) [Semiconductors **38**, 455 (2004)].
12. A. I. Anselm, *Introduction to Semiconductor Theory* (Nauka, Moscow, 1978; Prentice Hall, Englewood Cliffs, N.J., 1981), Chap. 7.
13. A. F. Mayadas and M. Shatzkes, Phys. Rev. B **1**, 1382 (1970).
14. V. L. Bonch-Bruevich and S. G. Kalashnikov, *Physics of Semiconductors* (Nauka, Moscow, 1977), Chap. 14 [in Russian].
15. D. Maier-Schneider, A. Koprululu, S. Ballhausen Holm, and E. Obermeier, J. Micromech. Microeng. **6**, 436 (1996).
16. A. I. Anselm and V. I. Klyachkin, Zh. Éksp. Teor. Fiz. **22**, 297 (1952).

Translated by A. Spitsyn

Semiconductors, Vol. 39, No. 2, 2005, pp. 198–201. Translated from Fizika i Tekhnika Poluprovodnikov, Vol. 39, No. 2, 2005, pp. 214–217.

SEMICONDUCTOR STRUCTURES, INTERFACES, AND SURFACES

The Influence of a Nonlinear Electromagnetic Wave on Electric Current Density in a Surface Superlattice in a Strong Electric Field

D. V. Zav'yalov, S. V. Kryuchkov^, and N. E. Meshcheryakova

Volgograd State Pedagogical University, 400131 Volgograd, Russia

^e-mail: sed@fizmat.vspu.ru

Submitted April 14, 2004; accepted for publication April 23, 2004

Abstract—The current density in a combination of a 2D electron gas and a superlattice subjected to a strong electric field under exposure to a cnoidal electromagnetic wave is studied, with electron–phonon coupling explicitly taken into account. A dc electric quantizing field is directed along the superstructure axis, with the vector of the field strength of the nonlinear wave being perpendicular to this axis. It is found that the constant component of the current density along the superlattice axis is oscillatory and depends on the electric field strength. © *2005 Pleiades Publishing, Inc.*

Recently, special attention has been paid to transport in two-dimensional (2D) systems combined with a superstructure [1–5]. For example, Shubnikov–de Haas oscillations of an electron gas in a 2D system of antidots were considered in [6], and the electrical properties of superlattices grown in inversion layers on high-index silicon surfaces were considered in detail in [7]. The periodic potential described in [7] generates a superlattice (SL) with narrow forbidden minibands, which are described by a band spectrum in the weak-binding approximation. Methods for producing SLs, in 2D electron gas, that have a spectra satisfactorily described by the tight-binding approximation were suggested in [8]. The possibility of electromagnetic soliton propagation in such structures was studied in [9]. It is known [10] that linear electromagnetic waves are transformed into nonlinear (cnoidal) waves in materials with nonparabolic spectra. In this context, the influence of the field of a cnoidal wave polarized along the SL axis on the SL conductivity in a strong electric field was considered in [11]. A number of features distinguishing this problem from a similar problem regarding a linear wave field were also indicated. The calculations in [11] were carried out using the classical Boltzmann equation for the approximation of constant relaxation time τ.

In this paper, we report the results of studying the density of the electric current along the SL axis in 2D electron gas subject to the field of a cnoidal electromagnetic wave, while explicitly taking into account electron–phonon coupling. The x axis, which is parallel to the SL axis, has a dc electric field $\mathbf{E}$ applied along it. The cnoidal electromagnetic wave propagates in the same direction, such that the vector $\mathbf{E}_1$ of the wave's electric field is perpendicular to the x axis (in contrast to [11], where vector $\mathbf{E}_1$ is parallel to the x axis). Let the dc field be strong enough to satisfy the condition $\Omega\tau \gg 1$, where $\Omega = eEd/\hbar$ is the Stark frequency, $\mathbf{E}$ is the dc electric field strength, d is the SL period, and τ is the relaxation time. If, in addition, $\hbar\Omega \ll Eg$ and $\hbar\omega \ll E_g$ (E_g is the miniband gap and ω is the electromagnetic wave frequency), we can use a one-miniband approximation and express the electron energy spectrum as

$$\varepsilon(\mathbf{p}_\perp, \nu) = \frac{p_\perp^2}{2m} + \nu\hbar\Omega, \tag{1}$$

where m is the effective mass of charge carriers in the direction perpendicular to the SL axis, $p_\perp$ is the electron quasi-momentum component along the y axis, and ν is an integer. In (1), the fact that the application of a strong electric field along the SL axis gives rise to the Stark quantization effect is taken into account [12]; as a result, the energy spectrum becomes quasi-discrete.

Let the electric field of the cnoidal wave

$$\mathbf{E}_1 = \mathbf{E}_0 \mathrm{cn}[ut, k], \quad 0 < k < 1, \tag{2a}$$

$$\mathbf{E}_1 = \mathbf{E}_0 \mathrm{dn}[ut, k^{-1}], \quad k > 1, \tag{2b}$$

also be applied to the SL. Here $\mathbf{E}_0 \perp x$, E_0 is the nonlinear wave amplitude, u is the frequency dimensionality constant, $cn(x, k)$ and $dn(x, k)$ are the Jacobi elliptic functions, and k is the magnitude of the elliptic functions (wave nonlinearity magnitude). A distinctive feature of cnoidal waves is the dependence of the frequency $\omega(k) = 2\pi/T_{cw}(k)$ ($T_{cw}(k)$ is the wave period) on the nonlinearity modulus k; i.e.,

$$\omega(k) = \frac{\pi u}{2\mathrm{K}(k)}, \quad 0 < k < 1, \tag{3a}$$

$$\omega(k) = \frac{\pi u}{2\mathrm{K}(k^{-1})k}, \quad k > 1, \tag{3b}$$

where K(k) is a total elliptic integral of the first kind.

In expressions (2a) and (2b), spatial dispersion is disregarded, which is justified if the electromagnetic wavelength is long in comparison with the mean free path of the electrons.

Due to additivity of the electron-energy spectrum, the electron wave function in the above-described situation, without external influences, is a product of two functions: $\Psi = \Psi_1 \cdot \Psi_2$. Here, Ψ_1 corresponds to the Stark ladder state [12], and Ψ_2 to the state exactly accounting for the effect of the cnoidal wave field [13],

$$\Psi_1(p_\perp, \nu) = d^{-1/2} J_{\nu - x/d}\left(\frac{\Delta}{\hbar\Omega}\right), \tag{4a}$$

$$\Psi_2(p_\perp, \nu) = \sqrt{\frac{1}{L_y}} \exp\left[\frac{i}{\hbar}\left(p_\perp y - \frac{p_\perp^2}{2m}t + \frac{p_\perp \hbar}{md(k)}\int_0^t \varphi(t')dt' - \frac{\hbar^2}{2m(d(k))^2}\int_0^t \varphi^2(t')dt' - \nu\hbar\Omega t\right)\right], \tag{4b}$$

where Δ is the conduction miniband half-width; L_y is the size of the normalizing area S along the y axis; $J_n(x)$ is the nth-order Bessel function;

$$d(k) = \frac{2u\hbar k}{eE_0}, \quad k < 1; \tag{5a}$$

$$d(k) = \frac{2u\hbar}{eE_0}, \quad k > 1; \tag{5b}$$

and $\varphi(t)$ is the dimensionless component of the vector potential of the cnoidal wave, which is expressed as

$$\varphi(t) = 2\arcsin[ksn(ut, k)], \quad k < 1, \tag{6a}$$

$$\varphi(t) = 2\arcsin[sn(ut, k^{-1})], \quad k > 1. \tag{6b}$$

To calculate the current density, we use the general theory of semiconductor conductivity in quantizing electric fields developed in [14]. In polar crystals, carriers are scattered by optical phonons. Let these phonons be dispersionless and their frequency ω_0 be constant. In accordance with [15], let us write the expression for the electric current density along the SL axis as

$$j = 2\pi ed \sum_{\nu, \nu', \mathbf{p}_\perp, \mathbf{p}'_\perp} (\nu - \nu') f(\mathbf{p}_\perp) W_{\nu - \nu'}(\mathbf{p}_\perp, \mathbf{p}'_\perp), \tag{7}$$

where e is the elementary charge; $f(\mathbf{p}_\perp)$ is the electron distribution over perpendicular components of the quasi-momentum; $W_{\nu - \nu'}(\mathbf{p}_\perp, \mathbf{p}'_\perp)$ is the scattering probability, which includes two parts corresponding to phonon emission and absorption. This scattering probability is defined by the formulas

$$W_{\nu - \nu'}(\mathbf{p}_\perp, \mathbf{p}'_\perp) = W^+_{\nu - \nu'}(\mathbf{p}_\perp, \mathbf{p}'_\perp) + W^-_{\nu - \nu'}(\mathbf{p}_\perp, \mathbf{p}'_\perp), \tag{8}$$

$$W^\pm_{\nu - \nu'}(\mathbf{p}_\perp, \mathbf{p}'_\perp) = \sum_{\mathbf{q}, s} \frac{4\pi^2 C_q^2 \hbar}{2\omega_0 \rho \delta S L_y} |C_s|^2 J^2_{\nu - \nu'}\left(\frac{2\Delta}{\Omega}\sin\frac{q_x d}{2}\right) \times \left(N_0 + \frac{1}{2} \pm \frac{1}{2}\right)\delta(\varepsilon' - \varepsilon \pm \hbar\omega_0 - (\nu - \nu')\hbar\Omega + s\hbar\omega(k)) \times \delta(p'_\perp - p_\perp \pm q_\perp), \tag{9}$$

where C_q is the electron–phonon coupling constant, ρ is the crystal density, δ is the layer thickness, q_x and $q_\perp$ are the phonon quasi-momentum components along the coordinate axes, and $\varepsilon = p_\perp^2/2m$. The coefficient C_s appeared due to the following expansion in the Fourier series:

$$\exp\left(i\frac{p_\perp - p'_\perp}{md(k)}\int_0^t \varphi(t')dt'\right) = \sum_{s=-\infty}^{\infty} C_s \exp(s\omega(k)t), \tag{10}$$

where

$$|C_s|^2 = \frac{1}{\pi^2} \times \int_0^\pi\int_0^\pi \cos\left[\frac{q_\perp}{d(k)m\omega(k)}(\Phi(y) - \Phi(y')) - s(y - y')\right]dy\,dy', \tag{11}$$

$$\Phi(y) = 2y\arcsin\left[ksn\left(\frac{2K(k)y}{\pi}, k\right)\right] - 8\sum_{n=1}^{\infty}\frac{q^{n-1/2}}{1 + q^{2n-1}}\left(\frac{y}{2n-1}\sin(2n-1)y + \frac{1}{(2n-1)^2}\cos(2n-1)y - \frac{1}{(2n-1)^2}\right), \quad 0 < k \le 1, \tag{12a}$$

$$\Phi(y) = 2y\arcsin\left[sn\left(\frac{2K(k^{-1})ky}{\pi}, k^{-1}\right)\right] - 4ky^2 - \sum_{n=1}^{\infty}\frac{q^n}{1 + q^{2n}}\left(\frac{4y}{n}\sin(2n-1)y + \frac{2}{kn^2}\cos(2nky) - \frac{2}{kn^2}\right), \quad k > 1, \tag{12b}$$

$$q = \exp(-\pi K(k')/K(k)), \quad k' = \sqrt{1 - k^2} \text{ at } 0 < k < 1, \tag{13a}$$

$$q = \exp(-\pi K(k')/K(k^{-1})), \quad k' = \sqrt{1 - k^2} \text{ at } k > 1. \tag{13b}$$

Let us assume that the cnoidal wave frequency $\omega(k)$ is much higher than the Stark frequency Ω and that $\hbar\omega(k) \gg \hbar\Omega, \acute{\varepsilon}$ ($\acute{\varepsilon}$ is the mean energy of the electrons' transverse motion). This condition is satisfied at $\omega(k) \ge 10^{14}$ s^{-1}. Then the absorption and emission of HF field

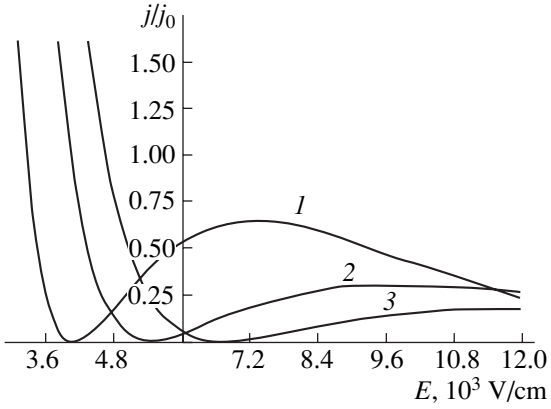

The dependence of the constant component of the current density along the SL axis on the dc electric field strength at $\Delta = 10^{-2}$ eV; $u \approx 10^{14}$ s^{-1}; $E_0 \approx 3 \times 10^5$ V/cm; $d \approx 10^{-6}$ cm; and k = (*1*) 0.7, (*2*) 0.5, and (*3*) 0.2.

photons can be disregarded. Under such circumstances, there is no zero-phonon component of the electric current (which, taking into account the HF field effect, can be nonzero). The cnoidal field has a dynamic effect on carriers, and the heating of the electron-gas is controlled only by the effect of the dc electric field. In view of the above, only the term with $s = 0$ can be retained in expression (10) in the sum over s. In this case, the distribution function $f(\mathbf{p}_\perp)$ can be defined as (see [16])

$$f(\mathbf{p}_\perp) = \sqrt{\frac{2\pi}{m\theta}}\frac{d\hbar}{S}n_0\exp\left(-\frac{p_\perp^2}{2m\theta}\right), \quad (14)$$

where n_0 is the surface electron concentration, $\theta = \Delta^2(2N_0 + 1)/2\omega_0\hbar$, and N_0 is the Plank distribution function for phonons.

Taking into account formulas (8)–(14) and performing a summation over $p_\perp$ and $p'_\perp$ in Eq. (7), we derive the expression for the current

$$j = j_1 + j_2, \quad (15)$$

$$j_{1,2} = j_{01,2}\sum_\nu \nu D_\nu\left(\frac{2\Delta}{\Omega\hbar}\right)\exp\left(\frac{\nu\hbar\Omega \pm \hbar\omega_0}{2\theta}\right)B_\nu, \quad (16)$$

$$j_{01,2} = \frac{en_0\sqrt{m}C_q^2}{2\omega_0\rho\delta\sqrt{2\pi\theta}\pi^2\hbar}\left(N_0 + \frac{1}{2} \pm \frac{1}{2}\right), \quad (17)$$

$$D_\nu\left(\frac{2\Delta}{eEd}\right) = \int_0^\pi J_\nu^2\left(\frac{2\Delta}{\Omega\hbar}\sin\alpha\right)d\alpha, \quad (18)$$

$$B_\nu = \int_0^\infty\int_0^\pi\int_0^\pi \cos\left[\frac{2\sqrt{2\theta\xi}}{d(k)\sqrt{m}\omega(k)}(\Phi(y) - \Phi(y'))\right]\frac{1}{\sqrt{\xi}} \times \exp\left(-\xi - \frac{\beta}{\xi}\right)d\xi dy dy', \quad (19)$$

$$\beta = \frac{(\hbar\nu\Omega \mp \hbar\omega_0)^2}{16\theta^2}. \quad (20)$$

The derived expressions are valid under the condition $\Omega \ll \theta$. In a case where $\Omega \gg \theta$, θ should be substituted with k_BT (k_B is the Boltzmann constant and T is the temperature). At low temperatures, N_0 and j_2 both vanish (as follows from expressions (17) and (18)).

In the limiting case ($\Omega \gg \theta$, $\beta \gg 1$), the integral in expression (19) can be calculated using the saddle-point method; as a result, we obtain

$$j = j_0\left(\frac{\Omega\hbar}{\Delta}\right)^{-\frac{5}{2}} \times \int_0^\pi\int_0^\pi \cos\left(\frac{\sqrt{2\Omega\hbar}}{d(k)\omega(k)\sqrt{m}}(\Phi(y) - \Phi(y'))\right)dy dy', \quad (21)$$

where

$$j_0 = \frac{en_0C_q^2\sqrt{m}}{2\omega_0\rho\delta\pi\hbar\sqrt{2\Delta}}(2N_0 + 1).$$

In a general case, it is impossible to analytically calculate the integrals appearing in expression (21); therefore, further analysis was carried out using numerical methods.

The results of the numerical analysis were used to plot the dependences of the current density along the SL axis on the dc electric field strength at various values of the nonlinearity parameter k (see figure).

The dependence of the current density on the dc electric field is highly nonmonotonic. The curves include regions of negative differential conductivity, which are caused by Bragg reflections. It is noteworthy that the current density is subject to large-amplitude oscillations, which are unrelated to the carrier transitions between Stark sublevels and are attributed to the phenomenon of "electrical–geometrical" resonance. Indeed, in the quantizing electric field in the absence of carrier scattering, the current is zero [14]. In this study, the current arises as a result of scattering by phonons. Under the condition $\Omega \gg \theta$, it is mainly phonons with momenta on the order of $\sqrt{2\Omega\hbar m}$ that contribute to scattering. The deformation potential of these phonons is averaged over the electron-oscillation period in the HF field. In fields where the double carrier oscillation amplitude $2eE_0/m(\omega(k))^2$ becomes commensurable with the wavelength of the significant phonons $2\pi\sqrt{\hbar}/\sqrt{2\Omega m}$, the effective constant of electron–phonon coupling vanishes.

As the wave nonlinearity parameter k decreases (and, hence, the wave frequency $\omega(k)$ increases), the falloff of the current to zero and its subsequent increase are more gradual, and the height of the local maxima decreases.

We should emphasize a significant difference between the results of this study and the results of [11]. In [11], it was shown that the steady-state *I–V* characteristic included a region of absolute negative conductivity at the cnoidal wave fields E_1 on the order of 10^3 V/cm. However, we did not observe this effect.

When the nonlinearity magnitude k tends to zero, the cnoidal wave degenerates into a harmonic wave, and expression (21) features a passage to the limit, i.e., to the results previously obtained in [17] in a study of the influence of a high-frequency linear wave on the SL conductivity in a quantizing electric field.

Let us perform numerical estimations. At the concentration $n_0 \approx 10^{10}$ cm^{-2}, $\delta \approx 2 \times 10^{-6}$ cm [6], $\Delta \approx 10^{-2}$ eV [8], $\omega_0 \approx 2 \times 10^{12}$ s^{-1}, and $m \approx 10^{-29}$ g, we have $j_0 \approx 0.4$ A/mm^2, which seems to be quite feasible for experimental detection. At the chosen numerical values, the applicability conditions for the single-miniband approximation, Stark quantization, and the absence of carrier heating in the HF field are satisfied.

ACKNOWLEDGMENTS

This study was supported by the regional competition "Volga Region-2004" of the Russian Foundation for Basic Research, project no. 04-02-96505.

REFERENCES

1. K. Klitzing, G. Dorda, and M. Pepper, Phys. Rev. Lett. **45**, 494 (1980).
2. T. Ando, A. B. Fowler, and F. Stern, *Electronic Properties of Two-Dimensional Systems* (Am. Phys. Soc., New York, 1982; Mir, Moscow, 1985).
3. A. A. Bykov, G. M. Gusev, Z. D. Kvon, *et al.*, Pis'ma Zh. Éksp. Teor. Fiz. **53**, 407 (1991) [JETP Lett. **53**, 427 (1991)].
4. Y. H. Xie, E. A. Fitzgerald, D. Monroe, *et al.*, J. Appl. Phys. **73**, 8364 (1993).
5. V. Umansky, R. De-Piccolotto, and M. Heiblum, Appl. Phys. Lett. **71**, 683 (1997).
6. G. M. Gusev, Z. D. Kvon, V. B. Besman, *et al.*, Fiz. Tekh. Poluprovodn. (St. Petersburg) **26**, 539 (1992) [Sov. Phys. Semicond. **26**, 304 (1992)].
7. V. A. Volkov, V. A. Petrov, and V. B. Sandomirskiĭ, Usp. Fiz. Nauk **131**, 423 (1980) [Sov. Phys. Usp. **23**, 375 (1980)].
8. D. Ferry, L. Akers, and E. Greeneich, *Ultra Large Scale Integrated Microelectronics* (Prentice Hall, Englewood Cliffs, 1988; Mir, Moscow, 1991).
9. S. V. Kryuchkov and A. I. Shapovalov, Fiz. Tverd. Tela (St. Petersburg) **39**, 1470 (1997) [Phys. Solid State **39**, 1305 (1997)].
10. F. G. Bass, A. A. Bulgakov, and A. P. Tetervov, *High-Frequency Properties of Semiconductors with Superlattices* (Nauka, Moscow, 1989) [in Russian].
11. D. V. Zav'yalov and S. V. Kryuchkov, Fiz. Tekh. Poluprovodn. (St. Petersburg) **35**, 575 (2001) [Semiconductors **35**, 554 (2001)].
12. J. Callaway, *Energy Band Theory* (Academic, New York, 1964; Mir, Moscow, 1969).
13. V. A. Pazdzerskiĭ, Fiz. Tekh. Poluprovodn. (Leningrad) **6**, 758 (1972) [Sov. Phys. Semicond. **6**, 658 (1972)].
14. V. V. Bryksin and Yu. A. Firsov, Zh. Éksp. Teor. Fiz. **61**, 2373 (1971) [Sov. Phys. JETP **34**, 1272 (1972)].
15. S. V. Kryuchkov and V. A. Yakovlev, Fiz. Tekh. Poluprovodn. (Leningrad) **10**, 171 (1976) [Sov. Phys. Semicond. **10**, 101 (1976)].
16. I. B. Levinson and Ya. Yasevichyute, Zh. Éksp. Teor. Fiz. **62**, 1902 (1972) [Sov. Phys. JETP **35**, 991 (1972)].
17. S. V. Kryuchkov and N. P. Mikheev, Fiz. Tekh. Poluprovodn. (Leningrad) **18**, 1296 (1984) [Sov. Phys. Semicond. **18**, 809 (1984)].

Translated by A. Kazantsev

Semiconductors, Vol. 39, No. 2, 2005, pp. 202–205. Translated from Fizika i Tekhnika Poluprovodnikov, Vol. 39, No. 2, 2005, pp. 218–221.

SEMICONDUCTOR STRUCTURES, INTERFACES, AND SURFACES

Fabrication and Photoelectric Properties of the ZnO–Cu(In,Ga)Se_2 Heterojunctions

V. F. Gremenok[1], G. A. Il'chuk[2], S. E. Nikitin[3], V. Yu. Rud'[4]^, and Yu. V. Rud'[3]

[1]*Institute of Solid-State and Semiconductor Physics, Belarussian Academy of Sciences, ul. Brovki 17, Minsk, 220072 Belarus*

[2]*Lviv Polytechnic National University, Lviv, 79013 Ukraine*

[3]*Ioffe Physicotechnical Institute, Russian Academy of Sciences, Politekhnicheskaya ul. 26, St. Petersburg, 194021 Russia*

[4]*St. Petersburg State Polytechnical University, St. Petersburg, 195251 Russia*

^e-mail: rudvas@spbstu.ru

Submitted April 14, 2004; accepted for publication April 28, 2004

Abstract—Thin-film *n*-ZnO:Al/*p*-Cu(In,Ga)Se_2 heterojunctions are fabricated by magnetron sputtering of an ZnO target, leading to a deposition of Cu(In,Ga)Se_2 films on the surface. The photoelectric properties of the fabricated heterojunctions are studied under exposure to natural and linearly polarized light. It is concluded that the resulting cadmium-free environmentally safe heterostructures can be used as high-efficiency broad-band photoconverters of natural and linearly polarized light. *© 2005 Pleiades Publishing, Inc.*

1. INTRODUCTION

Earlier applied physical studies of compound diamond-like chalcogenides with a lattice of chalcopyrite Cu(In,Ga)Se_2 led to the fabrication of solar cells that had, for thin-film photoconverters, an unprecedentedly high quantum efficiency ($\eta \approx 19.2\%$) and an extraordinary radiation resistance [1–3]. As a rule, the active region of these structures included Cu(In,Ga)Se_2/CdS heterojunctions [4, 5]. Nowadays, making allowance for modern ecological standards, it is necessary to exclude cadmium, which is highly toxic, from the composition of solar cells. However, the abandonment of CdS provides an opportunity to increase the optical transmission of the short-wavelength radiation into the active region of the structure. Therefore, we are of the opinion that it is interesting to exclude the Cu(In,Ga)Se_2/CdS barrier from widely used thin-film Cu(In,Ga)Se_2/CdS/ZnO solar cells retaining Cu(In,Ga)Se_2/ZnO as a converter. This study is aimed at solving the above problem and is concerned with photoelectric phenomena in the *n*-ZnO:Al/*p*-Cu(In,Ga)Se_2 heterojunctions fabricated by magnetron-sputtering deposition of thin ZnO:Al films on the surface of Cu(In,Ga)Se_2 alloy films.

2. EXPERIMENTAL

To fabricate thin-film heterojunctions, we used mirror-smooth molybdenum films 1 μm thick deposited onto substrates made of sodium-containing glass. We grew the films of the Cu(In,Ga)Se_2 alloy to a thickness of 2 μm using molecular beams of each constituent element (Cu, In, Ga, and Se). During the deposition, we controlled the beam density for each element, the substrate temperature was kept in the range 540–550°C, and the total vapor pressure in a reactor volume was $\sim(5–10) \times 10^{-6}$ mbar.

The microprobe X-ray spectral analysis of the grown Cu(In,Ga)Se_2 films showed that each element was distributed with a high uniformity over the surface and in the bulk. Typical experimental film compositions are given in the table. The X-ray studies showed that the

The elemental composition of the Cu(In,Ga)Se_2 films and the photoelectric properties of the *n*-ZnO:Al/*p*-Cu(In,Ga)Se_2 heterojunctions at $T = 300$ K

Structure no.	Concentration, at %				R_0, Ω	S_U^m, V/W	S_I^m, mA/W	$\Delta\hbar\omega$, eV	δ, eV	E_G, eV	P_I, % ($\theta \approx 70°$)
	Cu	In	Ga	Se							
B1	18.26	23.34	9.94	48.05	10^3–10^5	30	0.04	1.6–1.9	1.17	1.17	5
B2	25.64	20.73	7.68	49.95	25–60	–	–	–	–	–	–
B3	12.03	32.55	4.81	50.61	10^4–10^5	200	3	1.55	1.23	1.23	8
B4	19.27	21.61	10.50	42.60	10^4	50	0.15	1.60	1.17	1.17	10

Note: All films have *p*-type conductivity.

1063-7826/05/3902-0202$26.00 © 2005 Pleiades Publishing, Inc.

resulting fine-grained Cu(In,Ga)Se_2 films are single-phase, have a chalcopyrite structure, and are textured in the crystallographic direction [112]. In the X-ray diffraction patterns of these films, the reflections of the superstructure 101, 113, and 211, along with a series of lines (112, 220/204, 312/116, etc.) are resolved. Tetragonal splitting of the doublet 116/312 usually corresponds to the formation of an ordered chalcopyrite structure. Microscopic studies of the Cu(In,Ga)Se_2 films, using a Stereoscan-360 scanning electron microscope, showed that their surface is mirror-smooth and the structure closely packed. The latter fact indicates that the obtained substance is single-phase, which is consistent with the X-ray diffraction data. The table shows that the concentrations of alloy-forming elements in various films grown from molecular beams, are, in fact, different. This circumstance indicates that it is possible to control the atomic composition with the four elements used in the described method of growing Cu(In,Ga)Se_2 films. All grown Cu(In,Ga)Se_2 films are of *p*-type conductivity.

The ZnO:Al/*p*-Cu(In,Ga)Se_2 heterojunctions were fabricated in argon using magnetron sputtering of a pressed ZnO target with an additive of pure Al at 2.5% [6]. The substrate temperature during the deposition of the ZnO:Al films was no higher than ~50°C at a system pressure of ~0.5 Pa. The duration of the ZnO:Al films' deposition onto the surface of the *p*-Cu(In,Ga)Se_2 substrate usually took 2–4 h. Owing to a change in the argon pressure during the deposition of the *n*-ZnO films, we controlled the concentration of free carriers, which increased as the argon pressure increased. The highest concentration was ~10^{20} cm^{-3} at $T = 300$ K. The ZnO films generally adhered well to the Cu(In,Ga)Se_2 surface, had a mirror-smooth outer surface, and were homogeneous in their interference-related color.

3. RESULTS

3.1. Current–Voltage Characteristics

According to measurements of the steady-state current–voltage (*I–V*) characteristics, all the fabricated *n*-ZnO:Al/*p*-Cu(In,Ga)Se_2 heterojunctions exhibited rectification. Figure 1 shows the typical *I–V* characteristics of one of the fabricated heterojunctions, and the table shows some of their photoelectric parameters. The forward direction of the fabricated heterojunctions corresponds to the positive polarity of the external bias applied to the *p*-Cu(In,Ga)Se_2 film, which is consistent with the approximate energy-band model of the heterojunction. At voltages of $U \approx 5$ V, for the most satisfactory heterojunctions, the forward current exceeds the reverse current by a factor of 40–50 at $T = 300$ K.

At forward biases of $U \lesssim 0.5$ V, the dark current of the heterojunctions obeys the known diode equation [7]

$$I = I_s(eU/e^{\beta kT} - 1), \quad (1)$$

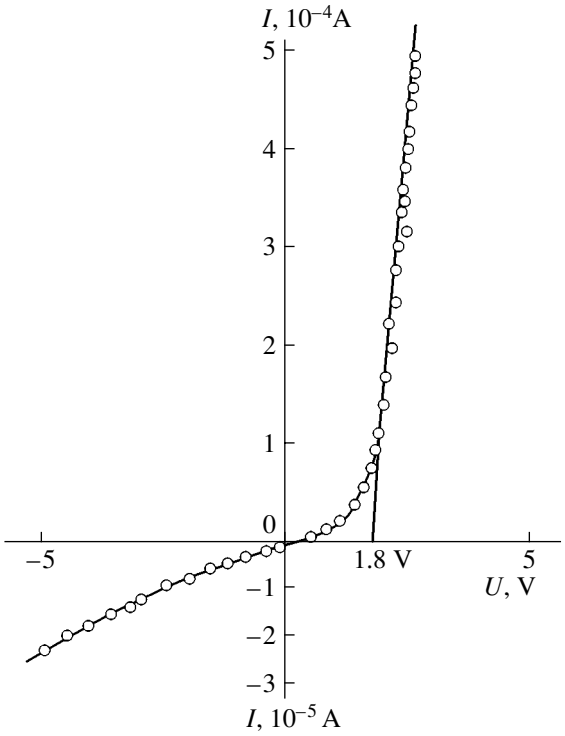

Fig. 1. The steady-state current–voltage characteristic of the *n*-ZnO:Al/*p*-Cu(In,Ga)Se_2 heterojunction at $T = 300$ K for sample B1. The conducting direction corresponds to the positive polarity of the external bias applied to the *p*-Cu(In,Ga)Se_2 film.

where the saturation current $I_s \approx 5 \times 10^{-7}$ A at $T = 300$ K, while the diode coefficient $\beta \approx 6$–10, which allows us to assume that the forward current has a tunneling–recombination origin.

As the forward-bias voltage increases, $U > 2$ V, the dark current at the forward bias starts to follow the linear law

$$I = \frac{U - U_0}{R_0}, \quad (2)$$

where the cutoff voltage $U_0 \approx 1.8$ V, while the residual resistance R_0, as one can see from the table, varies in the rather wide range 25–10^5 Ω. This fact should presumably be attributed to changes in the composition of the Cu(In,Ga)Se_2 films. It is noteworthy that the smallest values of R_0 correspond to an excess of Cu in the Cu(In,Ga)Se_2 films (sample B2 in the table), while the highest resistance $R_0 \approx 10^5$ Ω is observed for the heterojunctions with a high In content (samples B1 and B3 in the table).

For reverse biases ranging from 0.1 to 0.5 V, the reverse current of the heterojunctions under study is described by the power-law dependence $I \propto U^m$, where the exponent $m \approx 0.84$ in the voltage range 0.1–0.5 V, while at $U > 0.5$ V it increases somewhat to $m \approx 1.2$. The closeness of the exponent to unity may correspond

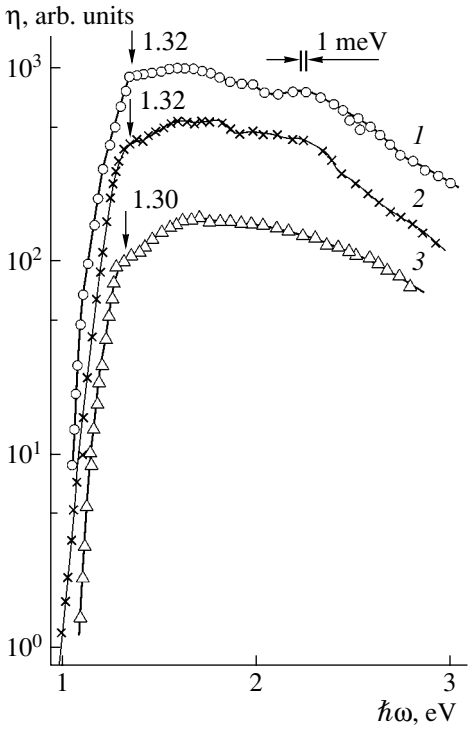

Fig. 2. Spectral dependences of the relative quantum efficiency of photoconversion for the *n*-ZnO:Al/*p*-Cu(In,Ga)Se_2 heterojunctions at $T = 300$ K in nonpolarized light. The illumination of the *n*-ZnO:Al film's side. Sample numbers: (*1*) B3, (*2*) B4, and (*3*) B1. To exclude the overlap, the spectra are shifted along the axis η.

to carrier tunneling or to the manifestation of currents limited by the space charge in the velocity saturation mode [8, 9].

3.2. Photoelectric Characteristics

Illumination of the fabricated heterojunctions leads to the emergence of photovoltage. The sign of this photovoltage is always negative at the *n*-ZnO:Al film, which coincides with the rectification direction. Furthermore, it is independent of the energy of incident photons, the coordinate of the light probe (diameter 0.2 mm) on the surface, and the radiation intensity. The above-mentioned properties allow us to attribute the observed photoelectric effect to the only active region, which emerges due to the contact of the ZnO and Cu(In,Ga)Se_2 films. The highest voltage (S_U^m) and current (S_i^m) photosensitivities of the fabricated heterojunctions are given in the table. They are always realized under illumination of the *n*-ZnO film's side. The observed variations in the highest photosensitivity of the heterojunctions, it seems, should primarily be attributed to the properties of the Cu(In,Ga)Se_2 films, which are determined by deviations from the stoichiometry and, consequently, by the growth parameters.

Figure 2 shows the spectral dependences of the relative quantum efficiency of the photoconversion η for the ZnO:Al/Cu(In,Ga)Se_2 heterojunctions, which is determined as the ratio of the short-circuit current to the number of incident photons. In particular, Fig. 2 shows that the η spectra are very similar for the fabricated heterojunctions if the ZnO:Al film's side is illuminated. Indeed, an abrupt long-wavelength increase in photosensitivity for all the heterojunctions sets in at photon energies of $\hbar\omega \geq 1$ eV. At the coordinates $(\eta\hbar\omega)^2$–$\hbar\omega$, the long-wavelength increase in photosensitivity becomes linear. According to the theory of fundamental absorption in semiconductors [7], this circumstance allows us to conclude that band-to-band optical transitions in the Cu(In,Ga)Se_2 alloys occur, which is consistent with an analysis of the optical absorption spectra for these materials [10]. By extrapolating the dependences $(\eta\hbar\omega)^2 \longrightarrow 0$ for the fabricated heterojunctions, we determined the values of the band gap E_G for the Cu(In,Ga)Se_2 films, (these values are given in the table). An increase in the band gap of the quaternary-alloy films relative to the $CuInSe_2$ ternary compound [10, 11] is attributed to an increase in the concentration of Ga atoms. In contrast, the observed variations in E_G in various Cu(In,Ga)Se_2 films (see table) can be associated with oscillations of the deviation of the quaternary-phase composition from stoichiometry. These oscillations represent the effect of the growth parameters on the physical properties of quaternary alloys.

It follows from Fig. 2 that the high photosensitivity of the fabricated heterojunctions manifests itself in the depth of the fundamental absorption for Cu(In,Ga)Se_2. The table gives the spectral range of high photosensitivity $\Delta\hbar\omega$ for several structures under illumination of the ZnO side. One can see that certain heterojunctions are highly photosensitive in an extended region of photon energies, for example, sample B1 (see table). Sometimes, the photosensitivity peaks at a certain photon energy for a specific heterojunction. Such a feature is observed in the photosensitivity spectra of heterojunctions B3 and B4 (see table).

The broad-band character of the spectra $\eta(\hbar\omega)$ for the fabricated thin-film heterojunctions indicates that they possess a high-quality heterointerface. One can also see from the table that the full width at a half-maximum of the photosensitivity spectra (δ) for the *n*-ZnO:Al/*p*-Cu(In,Ga)Se_2 heterojunctions attains large values, 1.15–1.47 eV, which are required for the development of highly efficient photoconverters.

The exposure of the heterojunctions to linearly polarized light along the normal to the *n*-ZnO:Al active surface showed that the variations in the spatial orientation of the vector of the light wave's electric field do not affect the photosensitivity of the *n*-ZnO:Al/*p*-Cu(In,Ga)Se_2 heterojunctions. This fact indicates that natural photopleochroism is absent, partly because of the isotropic photoactive absorption in the structural components, but primarily because of the fine-grained structure of

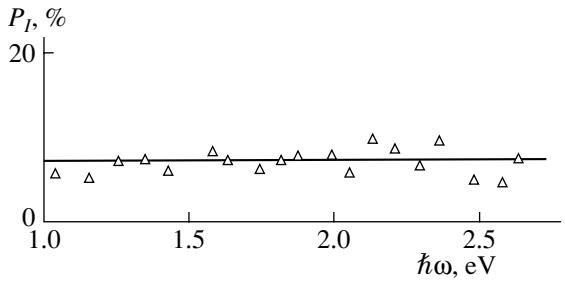

Fig. 3. The spectral dependence of the coefficient of the induced photopleochroism for the *n*-ZnO:Al/*p*-Cu(In,Ga)Se_2 heterojunction at $T = 300$ K for sample B3. $\theta = 70°$, the illumination of the ZnO film's side.

the Cu(In,Ga)Se_2 and ZnO thin films. Photopleochroism in such objects usually emerges under the oblique incidence of the linearly polarized light on their receiving surfaces [12]. Figure 3 shows a typical spectral dependence of the coefficient of the induced photopleochroism P_I for one of the fabricated heterojunctions under illumination of the ZnO:Al film's side at the angle of incidence $\theta = 70°$. One can see that the coefficient of the induced photopleochroism is almost constant over the entire range of photosensitivity for the heterojunction. The magnitude of the photopleochroism was found to be substantially smaller than the theoretical estimate ($P_I \approx 30\%$ at $\theta = 70°$ [12]), which was determined using the refractive index for ZnO taken from [11]. The fact that there is a considerable decrease in the coefficient P_I with respect to the theoretical value over the entire photosensitive region indicates that a high antireflection level, which is necessary to provide highly efficient photoconversion, is attained for the fabricated *n*-ZnO:Al/*p*-Cu(In,Ga)Se_2 heterojunctions.

4. CONCLUSIONS

Thus, we fabricated ZnO/Cu(In,Ga)Se_2 cadmium-free photosensitive heterojunctions in which the ZnO film simultaneously serves as a barrier and antireflection coating. This is of interest for the development of environmentally safe thin-film photoconverters based on I–III–VI chalcopyrite materials.

ACKNOWLEDGMENTS

This study was supported by INTAS, project 2001-283; and by a Program of Basic Research of the Department of Physics of the Russian Academy of Sciences "New Concepts of Energy Conversion in Semiconductor Structures."

REFERENCES

1. V. Nadenau, D. Braunder, D. Hariskos, *et al.*, Prog. Photovoltaics **3**, 363 (1995).
2. U. Rau and H. W. Schock, Renewable Sustainable Energy Rev. **1**, 277 (2001).
3. A. Jasenek and U. Rau, J. Appl. Phys. **90**, 650 (2001).
4. D. Hariscos, M. Ruckh, U. Ruhle, *et al.*, Sol. Energy Mater. Sol. Cells **41–42**, 345 (1996).
5. D. Braunder, D. Hariskos, T. Walter, and H. W. Schock, Sol. Energy Mater. Sol. Cells **40**, 97 (1996).
6. S. E. Nikitin, Yu. A. Nikolaev, I. K. Polushina, *et al.*, Fiz. Tekh. Poluprovodn. (St. Petersburg) **37**, 1329 (2003) [Semiconductors **37**, 1291 (2003)].
7. S. Sze, *Physics of Semiconductor Devices*, 2nd ed. (Wiley, New York, 1981; Mir, Moscow, 1984).
8. E. Hermandez, Cryst. Res. Technol. **13**, 385 (1998).
9. M. A. Lampert and P. Mark, *Current Injection in Solids* (Academic, New York, 1970; Mir, Moscow, 1973).
10. T. J. Coutts, L. L. Kazmerski, and S. Wagner, *Copper Indium Diselenide for Photovoltaic Applications* (Pergamon, Amsterdam, 1986).
11. *Physicochemical Properties of Semiconductor Materials: A Handbook*, Ed. by A. V. Novoselova and V. B. Lazarev (Nauka, Moscow, 1979) [in Russian].
12. F. P. Kesamanly, V. Yu. Rud', and Yu. V. Rud', Fiz. Tekh. Poluprovodn. (St. Petersburg) **33**, 513 (1999) [Semiconductors **33**, 483 (1999)].

Translated by N. Korovin

Semiconductors, Vol. 39, No. 2, 2005, pp. 206–213. Translated from Fizika i Tekhnika Poluprovodnikov, Vol. 39, No. 2, 2005, pp. 222–229.

SEMICONDUCTOR STRUCTURES, INTERFACES, AND SURFACES

The Qualitative Difference between Mechanisms of Electroforming in Si–SiO_2–W Structures Based on *n*-Si and *p*-Si

V. M. Mordvintsev^, S. E. Kudryavtsev, and V. L. Levin

Institute of Microelectronics and Information Science, Russian Academy of Sciences, ul. Universitetskaya 21, Yaroslavl, 150007 Russia

^e-mail: mvm@imras.yar.ru

Submitted April 26, 2004; accepted for publication May 17, 2004

Abstract—The experimental results of studying electroforming in open Si–SiO_2–W sandwich structures that have an SiO_2 layer approximately 20 nm thick are reported. It is noted that these processes are radically different for *p*-Si and *n*-Si. In the former case, the current–voltage characteristic is *N*-shaped, which is typical of electroforming. In the latter case, the dependence is *S*-shaped, which is typical of an electrical breakdown with thermal instability. The mechanisms of the above processes are discussed. The noted distinction can be associated with the fact that it is not the hole flow but only the electron flow across the structure that leads to the decomposition of molecules on the surface of the insulating gap and to the formation of conducting-phase particles from these molecules. © *2005 Pleiades Publishing, Inc.*

1. INTRODUCTION

The phenomenon of electroforming in the metal–insulator–metal (MIM) structures was actively studied at the end of the last century [1, 2]. The initial stage of this phenomenon is the formation of a conducting medium consisting of the molecules located at the surface of the insulating gap of the MIM structure. When a current flows through the structure, the conducting medium is formed due to the decomposition of the molecules under electron impact [3], which leads to an irreversible increase in the conductivity of the structure. A fundamental feature of electroforming is the self-formation (self-organization) of the insulating nanometer-width gap in the forming conducting medium [4]. This circumstance accounts for the main manifestations of this phenomenon, particularly the *N*-shaped current–voltage (*I–V*) characteristic of the electroformed MIM structures. The starting materials for the decomposition can be either molecules introduced from outside, for example, organic molecules of vacuum-pump oils [2] or photoresist [5], or the dielectric material itself, which forms the surface of the insulating gap.

In order to study the process of electroforming and its application-related purposes, the use of a construction in the form of an open sandwich MDM (metal–dielectric–metal) structure with a dielectric film of approximately 10 nm thick was suggested in [6]. In this structure, the insulating gap free for the access and removal of molecules, which participate in the formation of the conducting medium, is formed as the end of the dielectric film during local etching of the two upper layers of a conventional sandwich MDM structure. When considering the practical application of nanosized MIM diodes, which have an active conducting medium serving as the element of nonvolatile electrically reprogrammable memory [6], the most convenient design is the open Si–SiO_2–W sandwich structure [5]. In order to attain the rectifying *I–V* characteristic of a memory cell with the required polarity, *p*-Si is necessary. The main features of electroforming in such structures have already been described [5, 7]. However, experiments showed that similar structures with *n*-Si behave very differently under the same conditions, which reveals a deep physical distinction between the *p*- and *n*-Si materials. In this article, we report and discuss the relevant experimental results and clarify the mechanism of electroforming, which occurs in structures in which a semiconductor is one of the electrodes.

2. EXPERIMENTAL

In a simplified form, the preparation procedure for the open Si–SiO_2–W sandwich structures (see inset in Fig. 1) involved the following operations: chemical etching of Si wafers; thermal oxidation of Si until an SiO_2 layer with a thickness of d = 15–30 nm was formed on the wafer surface; deposition of a W film of approximately 0.15 μm thick by magnetron sputtering; photolithography on the W film in order to form the pattern of the upper conducting buses; and a second photolithography in order to form the photoresist mask, through which the W film and then SiO_2 were initially etched. The last operation was monitored in situ using the procedure described previously in [8], which provided the accuracy needed to determine the final instant of etching and, consequently, the nanometer-scale reproducibility of the structure profile. This operation opened the end of the SiO_2 film, which served as an insulating gap between the electrodes, namely, the film

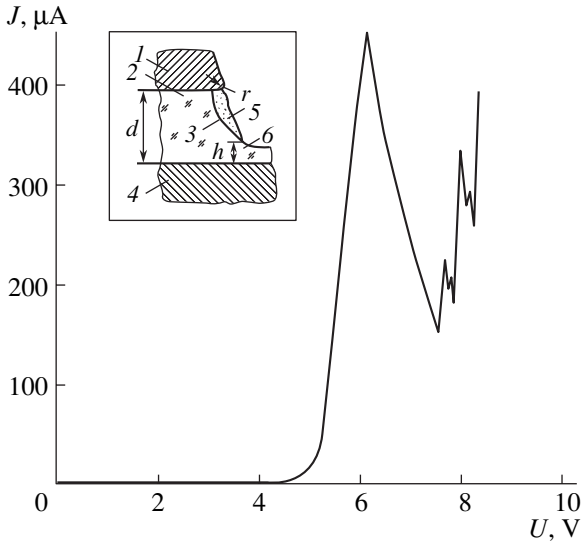

Fig. 1. The current–voltage characteristic of the open *p*-Si–SiO_2–W sandwich structure under the photoresist layer. This characteristic illustrates the process of electroforming. For *p*-Si, ρ = 10 Ω cm and *d* = 16 nm. The open end length is 64 μm. The rate of voltage rise is 0.02 V/s. The ballast resistance R_b = 0. A schematic representation of the open Si–SiO_2–W sandwich structure after electroforming is shown in the inset: (*1*) W film, (*2*) SiO_2 film, (*3*) open end of the SiO_2 film (insulating gap), (*4*) Si, (*5*) conducting medium, and (*6*) residual oxide with the thickness *h*.

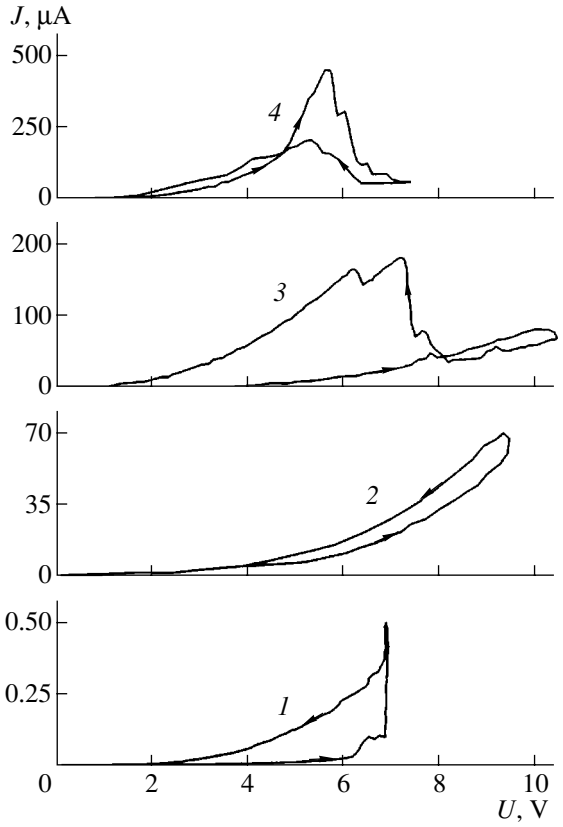

Fig. 2. Current–voltage characteristics of the open *p*-Si–SiO_2–W sandwich structure, which reflect the process of electroforming in high (10^{-5} Pa) oil-free vacuum. For *p*-Si, ρ = 0.1 Ω cm and *d* = 29 nm. The open end length is 64 μm. The rate of voltage scanning is 1.6 V/s. The ballast resistance R_b = 0. The run numbers are (*1*) third, (*2*) seventh, (*3*) eighth, and (*4*) twelfth (the steady state).

end and the Si substrate. Even though the thermally grown SiO_2 was etched off completely, a natural oxide layer with a thickness of approximately 1 nm was formed at the Si surface. Therefore, a certain residual oxide with the thickness *h* always existed. This oxide separated the Si and the conducting medium produced by electroforming. For the substrate, we used *p*-Si:B wafers with the resistivity ρ = 10 or 0.1 Ω cm as well as *n*-Si:P with ρ = 4.5 Ω cm. Local *p*-type regions were formed on some *n*-Si wafers via the diffusion of B, which allowed us to carry out certain experiments (see below). The technology and topology of the used open Si–SiO_2–W sandwich structures was described in more detail in [5]. Chips with the fabricated structures were welded into glass–metal cases, which could then be placed into a vacuum chamber so that electroforming could be performed. Electroforming was also carried out in air for the structures coated with photoresist film (FP-9120-1 positive photoresist). In this case, the film effectively protected the insulating gaps from atmospheric oxygen, which is known to suppress electroforming, while the source of the conducting medium was the carbon-containing photoresist material itself.

Figures 1 and 2 show typical *I–V* characteristics, which illustrate the results of electroforming in the open *p*-Si–SiO_2–W sandwich structures. The forward-polarity voltage was applied with a minus at the W electrode. Naturally, a large increase in the current and conductivity was not observed at the reverse polarity since the larger part of the applied voltage dropped across a wide depleted semiconductor layer. If the structure is coated with the photoresist layer (Fig. 1), well-developed electroforming can already be observed in the first cycle of a slow voltage rise. This process is characterized by a considerable and irreversible increase in conductivity and by the *N*-shaped *I–V* characteristic, which is the most clear attribute of this process. The rising portion of the curve is associated with the accumulation of a carbonaceous medium, which is formed during the decomposition of the organic molecules of a photoresist under the electron impact. This impact is attained by the effect of electron flow due to the presence of low initial conductivity across the insulating gap. The descending portion is caused by a partial burn-out of the emerging conducting medium and by a widening of the forming nanometer insulating gap [5] at somewhat higher voltages. The series ballast resistance was not used during electroforming in this case (R_b = 0), and the relatively high current *J*, in combination with the *N*-shaped *I–V* characteristic, indicates that the conducting medium accumulates over the entire perimeter of the open end of the structure rather than at one of its

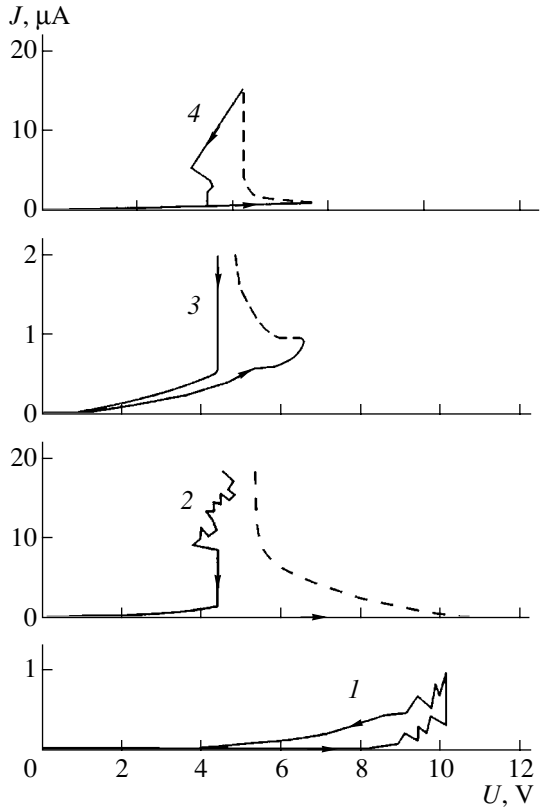

Fig. 3. The current–voltage characteristic of the open *n*-Si–SiO_2–W sandwich structure under the photoresist layer. For *n*-Si, ρ = 4.5 Ω cm and *d* = 24 nm. The open end length is 64 μm. The rate of voltage scanning is 0.5 V/s. The ballast resistance R_b = 140 Ω. The run numbers are (*1*) second, (*2*) third, (*3*) fifth, and (*4*) sixth.

points [5, 7]. The jumplike rise in current at high voltages is associated with the same processes that form the conducting medium, which start to develop in new regions of the photoresist arranged directly as well as indirectly on the surface of the insulating gap.

In circumstances where the photoresist layer is removed and the *p*-Si–SiO_2–W structures are kept under high vacuum, electroforming proceeds a substantially different manner (Fig. 2). It is necessary to keep the structures at noticeably higher voltages for a prolonged period in order to bring the currents up to the values shown in Fig. 1 and to form the *N*-shaped *I–V* characteristic. In Figs. 1 and 2, the values of resistivity for Si and the widths of the insulating gaps (thickness *d* of the SiO_2 film) are quite different. However, the experiments showed that the above conclusion is valid for various resistivity and thickness values of Si. It is noteworthy that in these experiments, as before, R_b = 0. Since electroforming was carried out in oil-free vacuum, the only source for the conducting medium is the decomposition of the dielectric of the insulating gap itself, i.e., SiO_2. Processes similar to ours in their mechanism and results, in which a surface of dielectrics was irradiated by low-energy (5–100 eV) electrons, were previously studied in [9]. In experiments carried out in diffusion-pump vacuum, which contained the vapor of the organic vacuum oils typical in electroforming, this process was developed somewhat more rapidly, but the results were qualitatively similar [5]. In this case, it is reasonable to assume that the role of the vacuum-pump oil's organic molecules, which are adsorbed on the surface of the insulating gap, is important, at least at the initial stages of the process. However, the rate of this process was much lower than it was under the photoresist. At low voltages (about 6 V) it was possible to attain a developed electroforming state with the emergence of the *N*-shaped *I–V* characteristic only for exposure times longer by one-and-a-half to two orders of magnitude.

Despite the distinctions mentioned, the final result of the electroforming, which was carried out at R_b = 0, was similar for the open *p*-Si–SiO_2–W sandwich structures in all the cases under consideration. The *N*-shaped *I–V* characteristic had a peak in the range 5–7 V at almost the same current values. The memory effect shown in Fig. 2 is typical in this case. This effect manifests itself as a gradual variation in the *I–V* characteristics of the structure, which increases its conductivity. Similar curves were observed for the structures in which both electrodes were made of metal [1, 2, 4]; i.e., the fabrication of one of the electrodes from a semiconductor does not affect the electroforming in this respect. This circumstance is quite understandable, since a thick enriched layer is formed at the Si surface for the used polarity and applied voltage, and the semiconductor simply serves as a conducting electrode. In this case, a decrease in the resistance of the structure is associated with the continuous accumulation of the conducting medium in the insulating gap. However, the presence of the semiconductor electrode can lead to other electroforming features.

The experiments showed that the behavior of similar photoresist-coated *n*-Si–SiO_2–W structures was radically different. Figure 3 shows their typical *I–V* characteristics in a case where the same linearly varying forward voltage is applied. It is natural that the forward voltage in this case has the opposite polarity compared to that for the structures based on *p*-Si, namely, the plus is at the W electrode. One can see that the conductivity of the structure also increases. However, no electroforming leading to the emergence of the *N*-shaped *I–V* characteristic is developed. At a certain voltage close to the voltage necessary for rapid electroforming on *p*-Si, a highly-conducting state with a reversible *S*-shaped *I–V* characteristic is formed. Such a characteristic is typical of the electrical breakdown accompanying thermal instability [10]. It is known that a conducting channel emerges locally in the material bulk in such cases. In this channel, heating the dielectric and semiconductor leads to an increase in the carrier density and an anomalous rise in conductivity (current pinching) [11]. In the experiments, a small ballast resistance (R_b = 140 Ω), which restricted the current, was connected in series to

the Si–SiO_2–W structure. In Fig. 3, the portions of the curves that have dashed lines represent an almost instantaneous (not detected by a recorder) decrease in the voltage U across the structure owing to the voltage drop across R_b. For the structures based on p-Si, no S-shaped I–V characteristics were observed under any of the experimental conditions set.

However, the use of the large ballast resistance $R_b \approx 10$ MΩ during voltage application allowed us to obtain N-shaped I–V characteristics with currents in the range of several microamperes. Such characteristics correspond to the formation of single nanometer-sized conducting elements at the surface of the insulating gap. This phenomenon occurred both for the Al–Al_2O_3–W MIM structures [12] and for the structures based on p-Si [5]. This circumstance confirms the fact that the formation of the conducting medium in the insulating gap, which corresponds to electroforming, also takes place in the n-Si–SiO_2–W structures.

3. DISCUSSION

The revealed distinction in the behavior of the open Si–SiO_2–W sandwich structures based on n- and p-Si means that the developing process for the formation of the conducting medium, in the first case, causes a rapid (explosion-like) rise in conductivity and an increase in the dissipated power. These phenomena are most probably local, but eventually develop in the bulk of Si and SiO_2, and lead to thermal instability, i.e., to the electrical breakdown of the structure and the formation of the reversible S-shaped I–V characteristic. In the case of p-Si, a certain factor exists that retards the accumulation of the conducting medium on the surface of the insulating gap; consequently, it is possible that the nanometer-sized insulating gap, which restricts the current across the structure, is formed prior to the breakdown. This circumstance manifests itself in the emergence of the N-shaped I–V characteristic as well as preventing the thermal instability from developing, which would lead to the S-shaped I–V characteristic.

From the most general considerations, we can note two basic distinctions between the open Si–SiO_2–W sandwich structures based on n-Si and p-Si. The first distinction lies in the opposite directions of the currents, which can be essential for asymmetric electrodes. In both cases, the W electrode is a small-curvature tip (see inset in Fig. 1), while the Si electrode is planar. The second distinction is that the current in each structure can be transported by different types of carriers, namely, electrons or holes. It will be shown below that both factors can be important.

The mechanism used to form the conducting medium during electroforming was mentioned for the first time in [13] and described in detail in [7]. It includes the decomposition of the molecules in an initially dielectric material, which are arranged on the surface of the insulating gap, under electron impact. In the case of adsorbed organic molecules, this decomposition leads to the removal of hydrogen and surface enrichment with carbon, i.e., with conducting-phase particles, and also to the formation of a carbonaceous conducting medium. The decomposition of the molecules under electron impact is the limiting stage of this process. Under such conditions, the rate of accumulation for the conducting medium should be proportional to the flowing current. If the material forming the conducting medium is SiO_2, its decomposition is accompanied by oxygen desorption and by surface enrichment with Si, which forms the conducting phase.

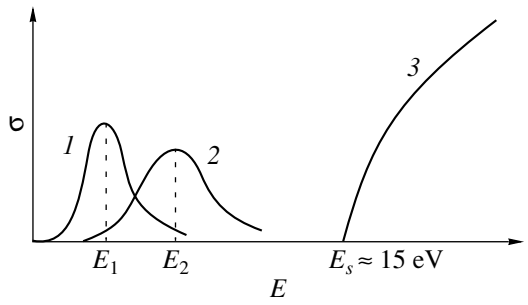

Fig. 4. Qualitative dependences of the effective cross section of the dissociation of molecules σ under electron impact as a function of the electron energy E: (*1*, *2*) dissociative attachment and (*3*) dissociation through the excited states. Curve *1* corresponds to the photoresist molecules and curve *2*, to SiO_2. E_1 and E_2 are the peak energies for σ(E).

Taking into account the low energies of electrons that can exist under electroforming conditions (lower than 10 eV), only a process similar to the dissociative adhesion of an electron to a molecule can be effective under electron impact [14]. The dependence of the cross section of the dissociative adhesion on the electron energy E has a resonance character (Fig. 4), with the highest E ranging from fractions of to several electronvolts. Another decomposition mechanism occurring under electron impact is a dissociation via the excited states [15]. This is a threshold process, and the threshold electron energy is approximately 15 eV (Fig. 4). Therefore, this process cannot noticeably affect electroforming.

The current passing through the open Si–SiO_2–W sandwich structure can lead to the dissociative attachment of electrons to molecules on the surface of the insulating gap. This is followed by the formation of the conducting medium if the voltage drop across the SiO_2 layer is larger than the potential barrier height at the interface between the conducting electrode and SiO_2 [7]. Figure 5 shows the energy-band diagrams of the Si–SiO_2–W structures for n- and p-Si at the voltage U = 5 V and a thickness of SiO_2 $d \approx 10$ nm. Here, we disregard the fact that all the processes occur at the open end of the dielectric film and, instead, consider the diagram for a conventional sandwich structure. In addition, we disregard the possible effect of the surface states at the Si–SiO_2 interface, which can lead to a certain additional

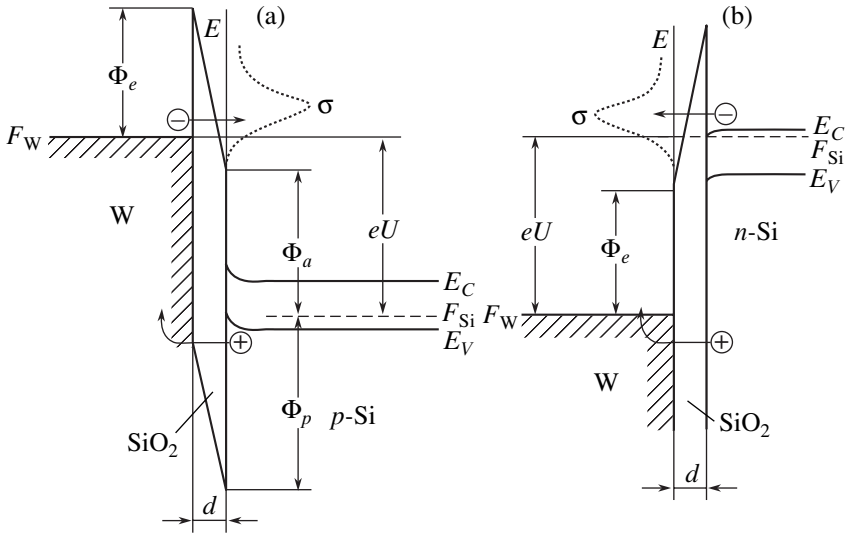

Fig. 5. Energy-band diagrams of the (a) *p*-Si–SiO_2–W structures and (b) *n*-Si–SiO_2–W structures for the forward voltage $U = 5$ V. Dotted curves represent the distribution of the cross section of the dissociative attachment by electron energy E for a molecule adsorbed at the SiO_2 surface. F_W and F_{Si} are the Fermi levels for W and Si. Other notation is explained in the text (Section 3).

band bending in Si. We consider this effect to be considerably less profound than electroforming and electrical breakdown, which proceed at voltages that are an order of magnitude larger than possible band bending. We also disregarded any distortion of the diagram owing to image forces. The quantities along the ordinate, namely, the potential barrier heights and the Si band gap E_C–E_V, are plotted on a scale according to the actual values taken from [10]. The work function for W is assumed to be equal to 4.54 eV. We qualitatively showed the distribution of the cross section of the dissociative attachment σ by electron energies E for a molecule adsorbed on the surface of the insulating gap, which is related to the energy-band diagram. In the case of *p*-Si (Fig. 5a), an electron should tunnel from the metal, through the dielectric layer, to a molecule with a corresponding energy level in order to be trapped by this molecule. As a result, the molecule is transferred to the self-decay repulsive term of the negative ion, which constitutes the mechanism of dissociative attachment. Such tunneling is possible only if the position of aforementioned level coincides with the Fermi level in the metal F_W, i.e., the condition $eU > \Phi_a$ should be satisfied. Here, Φ_a is the energy gap between the Fermi level in Si F_{Si} and the conduction band bottom for SiO_2. For *n*-Si, a similar condition is expressed as $eU > \Phi_e = (\phi_M - \chi)$, where ϕ_M is the work function for the metal electrode (W) and χ is the electron affinity for SiO_2 (0.9 eV [10]). These relations account for the threshold character of electroforming and the voltage-induced switching in electroformed structures [5]. The experimental values of this threshold voltage are approximately 3–4 V, which is satisfactorily consistent with the height of the corresponding barriers.

From the standpoint of the mechanism suggested, the above-mentioned distinction between electroforming for the *p*-Si–SiO_2–W structures under the photoresist and in vacuum may be attributed to the different positions of the peak of the effective cross section for the dissociative attachment of electrons $\sigma(E)$ on the electron energy axis. For the photoresist's organic molecules, the $\sigma(E)$ dependence is peaked at E_1, while for the surface SiO_2 molecules, which are the molecules decomposing in oil-free vacuum, the peak occurs at E_2 (Fig. 4): $E_1 < E_2$. If the dependence $\sigma(E)$ for SiO_2 is shifted to higher values of E, the following experimentally found effects should be observed: lower rates of electroforming in vacuum than under the photoresist, at relatively low voltages, as well as a considerable increase in these rates when there is an increase of several volts in the voltage U.

Referring to the difference between the behavior of the structures based on *p*-Si and *n*-Si, the following should be noted. For the *n*-Si–SiO_2–W structures, the relatively low currents at moderately high voltages (see curve *2* in Fig. 2 and curve *1* in Fig. 3) can be explained by the fact that the electrons are emitted from *n*-Si in this case, i.e., from the planar electrode. In contrast, in the *p*-Si–SiO_2–W structure, the electrons are emitted from the W electrode tip, which has a small curvature radius r (Fig. 1). This circumstance leads to a local increase in the electric field strength, which is inversely proportional to r [16], and to a corresponding decrease in the transparency of the surface potential barrier for electron escape from W. Therefore, in the case of *p*-Si, the conducting medium is accumulated at lower voltages, and the rise of the current across the structure initially surpasses the corresponding process for *n*-Si.

However, the aforementioned feature is not the main difference between electroforming for *n*-Si and *p*-Si. Rather, at a certain voltage across the *n*-Si–SiO_2–W structure, the conductivity increases so rapidly that a local electrical breakdown develops and the *S*-shaped *I–V* characteristic emerges. This is not the case at the same voltages for the *p*-Si–SiO_2–W structures. The important question is what the factor restricting the breakdown development in *p*-Si is. Particularly as it occurs even in the absence of the external ballast resistance and high measured currents. It was assumed that the most important of these factors is the spreading resistance in Si because it has high resistivity compared with metals in MIM structures [7]. In this model, electroforming develops in the following way [7]. As the voltage is applied, the current starts to pass locally from one nanospike to the cathode surface, which leads to a local formation of the conducting medium in the form of a separate nanostructure. The local spreading resistance in Si is connected in series to this structure, and the voltage drop across Si decreases the voltage across the insulating gap itself. This provides softer electroforming and excludes local breakdowns. The same mechanism is responsible for the fact that the conducting medium is accumulated over the entire perimeter of the insulating gap. The voltage applied to the structure drops completely across the fragments of the insulating gap, where the conducting medium has not yet started to form, thus stimulating the onset of the current flowing through them, and, consequently, the formation of the particles of the conducting phase. These circumstances lead to high total currents across the structure, although the local current densities are not high; in fact, they are insufficient for the electrical breakdown. Such a pattern of electroforming is confirmed by experiments for *p*-Si with various values of conductivity [7]. However, the data on *n*-Si show that this mechanism is insufficient to prevent the electrical breakdown. In the *n*-Si–SiO_2–W structures, the effect of local spreading resistance should also be pronounced; in particular, the values of the resistivity ρ of the substrates for *p*-Si and *n*-Si (ρ = 10 and 4.5 Ω cm, respectively) should be large and close to each other. However, the electrical breakdown with the *S*-shaped *I–V* characteristic is developed for *n*-Si (Fig. 3). Furthermore, a decrease in the resistivity for *p*-Si by even two orders of magnitude (Fig. 2), when the effect of local spreading resistance should be abruptly reduced, does not lead to electrical breakdown in the *p*-Si–SiO_2–W structure, which also points to another prevention mechanism for *p*-Si.

The above-mentioned geometric factor can be considered as one of the more probable causes of the electrical breakdown in the *n*-Si–SiO_2–W structures. This factor leads to the fact that the electron emission from the surface of the planar Si electrode should be less localized than that from the W tip. Therefore, the region of current flow in the structures based on *n*-Si, which are coated with the photoresist, can occupy a larger volume of the photoresist. Thus, a channel, which is more stable regarding burnout of the forming carbonaceous conducting medium, is formed in the photoresist. This channel cannot restrict the current efficiently, and the thermal instability region occupies the semiconductor bulk.

However, there is another more fundamental mechanism. The considerations given below and the experimental data indicate that the radically different character of electroforming for *n*-Si and *p*-Si can be caused by the different types of charge carriers (electrons and holes) in the structures. After electroforming, the open Si–SiO_2–W sandwich structures are similar to Schottky barriers in both their design and conduction mechanism. A very thin SiO_2 layer with the thickness $h \approx 1$ nm is located between the conducting medium formed in the insulating gap and Si (Fig. 1), which is typical of conventional Schottky diodes [17]. The special features of this Schottky diode are an unconventional material for the conducting contact (the formed conducting medium), the varying thickness *h* of the tunneling-transparent dielectric at the semiconductor surface [5], and a very small area of conducting contact (only over the end of the dielectric film). It is known that the Schottky-barrier current is mainly transported by minority carriers and that the injection factor, i.e., the ratio of the minority-carrier current to the total current, ranges from 0.01 to 0.15 for the forward polarity [17]. Consequently, the current should mainly be transported by holes in the *p*-Si–SiO_2–W electroformed structures, and by electrons in the *n*-Si–SiO_2–W structures. This assumption was then confirmed experimentally (see below).

Taking into account the mechanism by which the conducting medium is formed via the dissociative attachment of electrons, we can suggest that the hole flux cannot lead to the decomposition of the starting molecules on the surface of the insulating gap. The energy positions of the holes (Fig. 5) prevents them from tunneling through the SiO_2 layer to cause electron trapping, in which a molecule is adsorbed on the surface and subsequently dissociated. This means that only a small fraction of the current (several percent) can contribute to the formation of the conducting-phase particles in the *p*-Si–SiO_2–W electroformed structure, while, for the *n*-Si–SiO_2–W structure, this percentage is larger by one to two orders of magnitude and is always close to unity. The accumulation rates of the conducting phase should be related by the corresponding ratio. Therefore, if a high current starts to flow locally across *n*-Si, conductivity increases very rapidly, and the system is abruptly transferred into a state of electrical breakdown.

A more detailed consideration of the features of the *p*-Si–SiO_2–W structure shows that the situation should be somewhat more complex during electroforming. The energy-band diagram in Fig. 5a shows that in the initial state, where the conducting medium is still absent in the insulating gap ($d \approx 20$ nm), the potential barrier height for holes ($\Phi_p \approx 5$ eV) is noticeably larger than it is for electrons ($\Phi_e \approx 3.5$ eV). Therefore, the

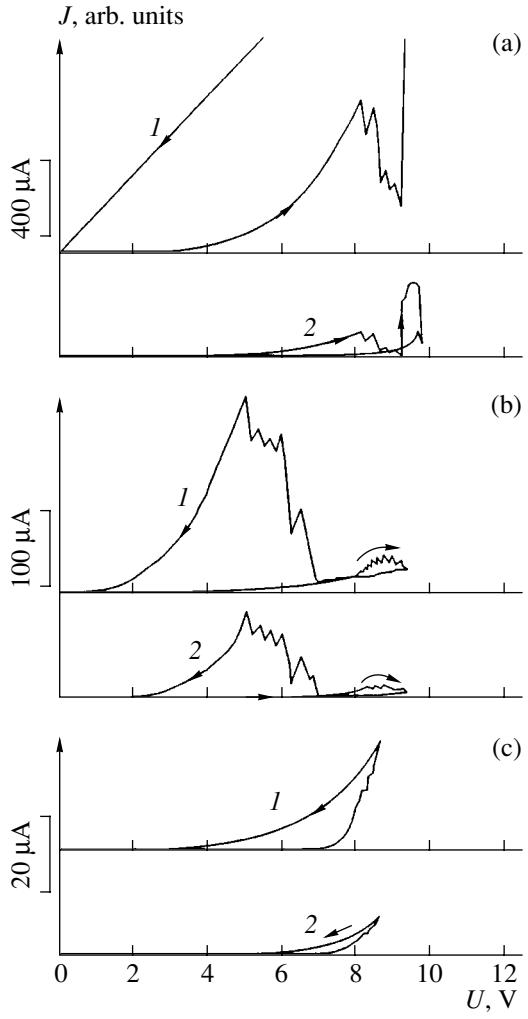

Fig. 6. Current–voltage characteristics of the *p*-Si–SiO_2–W sandwich structure based on the *p*-Si diffusion layer, which illustrate the process of electroforming in high (10^{-3} Pa) diffusion-pump vacuum (d = 18 nm). The open end length is 64 μm. (*1*) is the total current and (*2*) is the electron component of the total current. The ballast resistance R_b = 0. The run numbers are (a) first, (b) second, and (c) third. The rates of voltage rise are (a) 0.01 V/s (forward run) and 0.5 V/s (reverse run), and (b, c) 0.5 V/s.

electron current can exceed the hole current at the initial stage of electroforming, and, only once the conducting medium is formed should this relation reverse itself, so that a situation characteristic of the Schottky barriers is almost attained.

To verify all this reasoning, we carried out certain experiments that allowed us to measure the fractions of the electron and hole currents during the electroforming of the *p*-Si–SiO_2–W structures. We formed the *p*-type regions on the *n*-Si substrate (ρ = 4.5 Ω cm) by B diffusion. The depth of the *p–n* junction was approximately 1 μm, and the sheet resistance, 1000 Ω/□. A thin SiO_2 layer was formed above only the *p*-type regions, and a thick (0.5 μm) SiO_2 film was formed above the *n*-Si, which excluded the formation of spontaneous inversion layers during the measurements. The insulating gap of the open *p*-Si–SiO_2–W sandwich structure was fabricated in a conventional way. During the electroforming and measurements, a positive voltage U was applied to the *p*-type region, the W electrode was grounded, and a constant reverse voltage of 2 V was kept across the *p–n* junction. We simultaneously measured the currents in the circuits of the W electrode (the total current) and of the *n*-type substrate. The current across the reverse-biased *p–n* junction is the current of the electrons injected from W after the low intrinsic reverse current has been subtracted. The remaining part of the total current across the Si–SiO_2–W structure was transported by holes and was fed into the circuit of the *p*-type region. Since the diffusion layer was no thicker than 1 μm, the recombination of the injected electrons in *p*-Si could be disregarded in the first approximation.

Figure 6 shows the *I–V* characteristics of electroforming in the structures under study for the total current and for its electron component. It can be seen that at the initial stage of the process, when the conductivity abruptly increases during the reverse voltage run (Fig. 6b), the electron current represents a considerable fraction of the total current. In the final stage of this process (at low voltages), the formation of the conducting medium ceases and the fraction of the electron current is much smaller. During the next cycle (Fig. 6c), the electron component is already insignificant, i.e., as was assumed, the current across the *p*-Si–SiO_2–W structure in the electroformed state is mainly transported by holes. There is another special feature of this sample, specifically, an abrupt increase in the conductivity occurred at the peak voltage (Fig. 6c, curve *1*) and, as result, the structure transformed into a state with a very high current. This state apparently corresponds to a complete overgrowth of the insulating gap with the conducting medium. In this case, the structure is very similar to the Schottky diode, and the electron current practically vanishes (the reverse run of curve *2* in Fig. 6c). Despite the current in such a state being comparable with the current of the structures based on *n*-Si (Fig. 3), no current instability emerges. This behavior is caused by the fact that the conducting medium is uniformly distributed over the perimeter of the insulating gap (64 μm) and that local current densities are not high. The structure can be transformed into a conventional high-resistance state; however, the voltage applied should be somewhat higher than usual.

Thus, the results of these experiments completely confirmed the assumption made about the mechanism and character of conductivity in open *p*-Si–SiO_2–W electroformed sandwich structures. This mechanism, in turn, can explain why there is no electrical breakdown when the thermal instability emerges, in contrast with the structures based on *n*-Si. In the structures based on *n*-Si, the current is transported by electrons at all the stages of electroforming development. A small hole

component, even if present, exerts a negligibly weak effect. The fraction of the electron component in the current across the structures based on *p*-Si drops by more than an order of magnitude after the onset of the formation of the conducting-phase particles and as the conducting medium is accumulated. Consequently, the rate of formation for the conducting medium decreases, since holes, in contrast to electrons, cannot lead to the decomposition of molecules. This mechanism operates locally at each point of the insulating gap and without any delay. Therefore, the development of the thermal instability is effectively blocked due to the restriction of the rate of the rise in current, which makes it possible for the insulating gap to form according to a conventional electroforming model.

4. CONCLUSIONS

The results of experiments with electroforming in open Si–SiO_2–W structures based on *n*-Si and *p*-Si revealed a basic distinction in their behavior. In the case of the *p*-Si–SiO_2–W structures, the *I–V* characteristic is *N*-shaped, which is conventional for electroforming. For the *n*-Si–SiO_2–W structures under a photoresist layer, the *I–V* characteristic is *S*-shaped, which is typical of an electrical breakdown accompanied by thermal instability. An analysis of the conductivity mechanisms in these systems, which was confirmed by additional experiments, showed that this distinction can be associated with different current carriers (electrons and holes) as well as with the different role of electrons and holes in the formation of the conducting medium. Due to their dissociative adhesion, only the electrons can lead to the formation of conducting-phase particles from the starting molecules on the insulating gap surface.

The obtained experimental data as well as the deeper insight provided into the mechanisms of electroforming in Si-based structures can be used to develop the elements of a nonvolatile electrically reprogrammable memory based on self-forming conducting nanostructures.

REFERENCES

1. G. Dearnaley, A. M. Stoneham, and D. V. Morgan, Usp. Fiz. Nauk **112**, 8 (1974).
2. H. Pagnia and N. Sotnik, Phys. Status Solidi A **108** (11), 11 (1988).
3. V. M. Mordvintsev and V. L. Levin, Phys. Low-Dimens. Semicond. Struct. **12**, 243 (1995).
4. K. A. Valiev, V. L. Levin, and V. M. Mordvintsev, Zh. Tekh. Fiz. **67** (11), 39 (1997) [Tech. Phys. **42**, 1275 (1997)].
5. V. M. Mordvintsev and S. E. Kudryavtsev, Mikroélektronika **30**, 353 (2001) [Russ. Microelectronics **30**, 303 (2001)].
6. K. A. Valiev, S. E. Kudryavtsev, V. L. Levin, *et al.*, Mikroélektronika **26**, 3 (1997) [Russ. Microelectronics **26**, 1 (1997)].
7. V. M. Mordvintsev and S. E. Kudryavtsev, Zh. Tekh. Fiz. **72** (4), 53 (2002) [Tech. Phys. **47**, 426 (2002)].
8. V. M. Mordvintsev and T. K. Shumilova, Mikroélektronika **28**, 122 (1999) [Russ. Microelectronics **28**, 114 (1999)].
9. P. Townsend, in *Sputtering by Particle Bombardment*, Ed. by R. Behrisch (Springer, New York, 1983; Mir, Moscow, 1986), Vol. 2.
10. S. Sze, *Physics of Semiconductor Devices*, 2nd ed. (Wiley, New York, 1981; Mir, Moscow, 1984).
11. A. F. Volkov and Sh. M. Kogan, Usp. Fiz. Nauk **96**, 633 (1968) [Sov. Phys. Usp. **11**, 881 (1968)].
12. V. M. Mordvintsev, S. E. Kudryavtsev, and V. L. Levin, Mikroélektronika **27**, 49 (1998) [Russ. Microelectronics **27**, 40 (1998)].
13. V. M. Mordvintsev and V. L. Levin, Zh. Tekh. Fiz. **64** (12), 88 (1994) [Tech. Phys. **39**, 1249 (1994)].
14. A. V. Eletskiĭ and B. M. Smirnov, Usp. Fiz. Nauk **147**, 459 (1985) [Sov. Phys. Usp. **28**, 956 (1985)].
15. G. F. Drukarev, *Collisions of Electrons with Atoms and Molecules* (Nauka, Moscow, 1978; Plenum, New York, 1987).
16. A. Modinos, *Field, Thermionic, and Secondary Electron Emission Spectroscopy* (Plenum, New York, 1984; Nauka, Moscow, 1990).
17. V. I. Strikha, E. V. Buzaneva, and I. A. Radzievskiĭ, *Semiconductor Devices with the Schottky Barrier: Physics, Technology, and Applications* (Radio i Svyaz', Moscow, 1974) [in Russian].

Translated by N. Korovin

Semiconductors, Vol. 39, No. 2, 2005, pp. 214–217. Translated from Fizika i Tekhnika Poluprovodnikov, Vol. 39, No. 2, 2005, pp. 230–233.

SEMICONDUCTOR STRUCTURES, INTERFACES, AND SURFACES

Luminescence of Multilayer Structures Based on InAsSb at λ = 6–9 μm

N. V. Zotova, S. A. Karandashev, B. A. Matveev^, M. A. Remennyĭ, N. M. Stus', and N. G. Tarakanova

Ioffe Physicotechnical Institute, Russian Academy of Sciences, Politekhnicheskaya ul. 26, St. Petersburg, 194021 Russia
^e-mail: bmat@iropt3.ioffe.rssi.ru

Submitted May 31, 2004; accepted for publication June 7, 2004

Abstract—Multilayer gradient $InAs_{1-x}Sb_x$/…/$InAs_{1-x-y}Sb_xP_y$/*n*-InAs structures emitting in a wavelength range of 6 to 9 μm during injection, extraction, and optical pumping were studied. © *2005 Pleiades Publishing, Inc.*

1. INTRODUCTION

The presence of fundamental absorption bands developed from hydrocarbons, nitrogen oxides, and other commercial and natural gases in the mid-IR spectral region (3–14 μm) is promising for the development and application of optical sensors based on IR light-emitting diodes (LEDs) as well as the photodiodes (PDs) in gas-analysis devices used for environmental and technological monitoring. Two advantages of optical sensors are their selectivity in relation to the possibility of matching the spectral characteristics of LEDs, PDs, and the detected gases, and a high operating speed due to the absence of chemical interaction with the medium under analysis (as it is limited by the lifetime of the minority charge carriers in the semiconductor). Another application of IR LEDs is the testing of thermovision systems, which are generally adapted to one of the atmospheric transmission windows (3–5 or 8–14 μm). In a reversely biased *p–n* junction, an extraction of minority charge carriers decreases the emissive ability of the LED surface in comparison with its equilibrium (thermal) value; i.e., it leads to the appearance of negative luminescence [1], which makes it possible to imitate the emission of cold objects. In this case, the optical temperature drop (*dt*) is from 8 [2] to 53 K [3], depending on how it is determined and on the structural features of the diodes.

The basic material used in the fabrication of LEDs operating at interband transitions in the wavelength range 5–8 μm is indium antimonide. At room temperature, electroluminescence at $\lambda \approx 5.5$ μm was obtained in LEDs based on an InSb/InAlSb heterostructure [4] and at $\lambda \approx 5$ and ≈8 μm in LEDs based on an InAs/InAsSb quantum well [5]. Immersion InSb LEDs and PDs operating at room temperature were used to detect NO_2 [6]. A further advance of LEDs operating at interband transitions to the long-wavelength region can be obtained using an InAsSb solid solution, the band gap of which has a characteristic minimum at 95 meV for compositions similar to $InAs_{0.4}Sb_{0.6}$ at room temperature. Previously, we studied the fabrication of a LED with a *p–n* junction in a gradient InAsSbP layer with maximum emission at λ = 5.3 μm at room temperature [7].

In this paper, we study the fabrication of multilayer gradient structures based on InAsSb emitting in a wavelength ranging from 6 to 9 μm during injection, extraction, and optical pumping. In addition, the current–voltage, power–current, and spectral characteristics for these methods of excitation are presented.

2. EXPERIMENTAL

Samples were grown by liquid-phase epitaxy at temperatures of 650–720°C on *n*-InAs(111) substrates. In order to improve the structural quality of the active layers, a stepwise growth of the buffer layers was performed, with a gradual increase in the antimony content from layer to layer [8] (Fig. 1). Figure 1 shows the distributions for the components of the $InAs_{1-x-y}Sb_xP_y$ composition, measured on a CAMEBAX X-ray microanalyzer, and the depth distribution of the band gap, calculated using the relations from [9] (starting with the InAs substrate). An image of a cleaved surface etched in a color etchant is shown above Fig. 1. A sharp change in the brightness indicates one of the stepwise changes in the composition from layer to layer. We investigated the electroluminescence of the *p–n* structure, in which a *p–n* junction was obtained by Zn doping a $InAs_{1-x}Sb_x$ layer of approximately 5 μm thick, most distant from the substrate, to a hole density of $\sim 5 \times 10^{17}$ cm^{-3} and by the luminescence at the optical excitation of undoped isotypic structures. (The electron density in the upper $InAs_{1-x}Sb_x$ layer was $\sim 10^{17}$ cm^{-3}.)

The electroluminescence was measured on triangular samples with an area of 0.01 cm^{-2} and edges formed by cleaved $(1\bar{1}0)$ faces. The *p*-type side of the samples was soldered to a TO-18 housing, and a point cathode contact ~100 μm in diameter was formed at the center of the triangular surface of *n*-InAs, similarly to the sam-

1063-7826/05/3902-0214$26.00

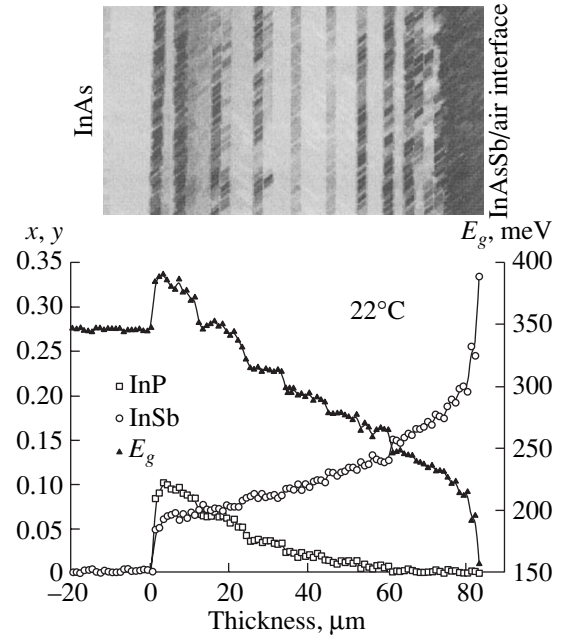

Fig. 1. Depth distribution of the $InAs_{1-x-y}Sb_xP_y$ composition (left scale) and the band gap width (right scale) starting with the substrate and the micrograph of the $(1\bar{1}0)$ cleaved surface decorated in a color etchant (above).

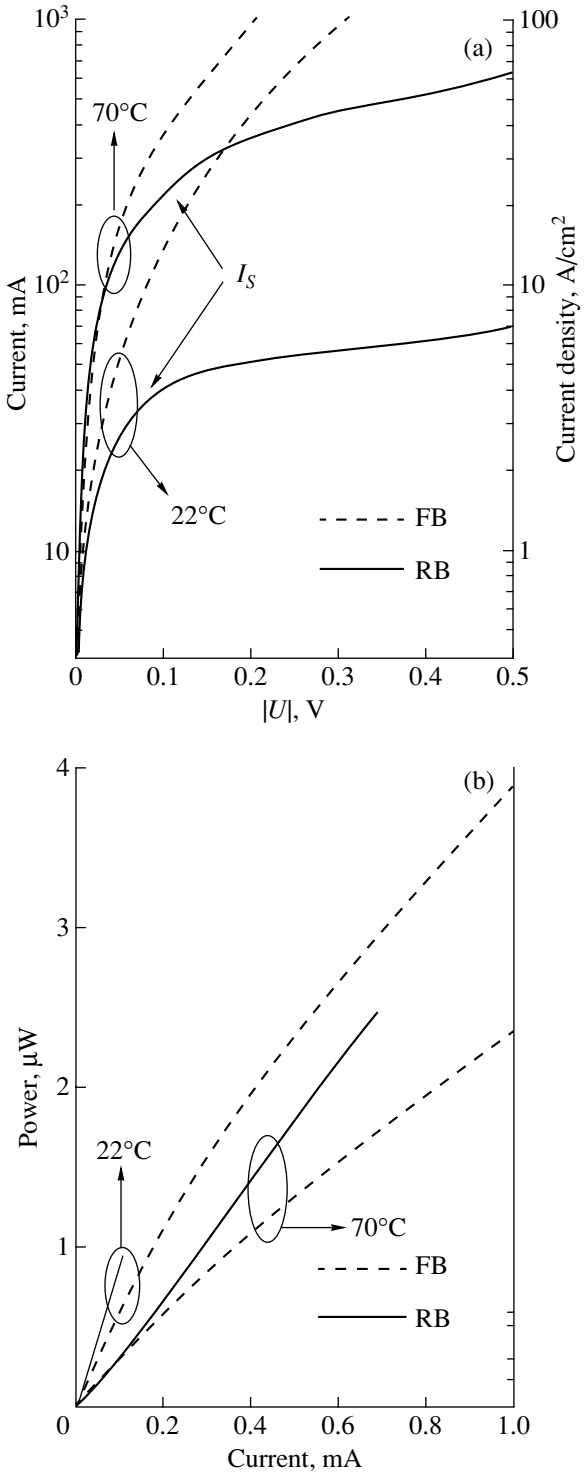

Fig. 2. (a) Current–voltage characteristics and (b) the dependence of the luminescence power on the pump current at forward and reverse biases (FB and RB, respectively).

ples investigated in [10]. The radiation was extracted through wide-gap *n*-InAsSbP layers and the *n*-InAs substrate.

The optical excitation was performed by radiation of a GaAs LED ($\lambda \approx 0.87$ μm, $\eta_{ext} \approx 8\%$) mounted on a silicon substrate using the flip-chip technique. The narrow-gap (luminescent) *n*-InAsSb layer was optically matched to the excitation LED using chalcogenide glass with the refractive index $n = 2.4$, as with the diodes studied in [11].

The spectral measurements were performed using the lock-in detection of a pulse signal (at a frequency of $f = 2$ kHz and pulse width of $\tau = 15$ μs) from a cooled CdHgTe photodiode with the maximum spectral sensitivity at a wavelength of 9.4 μm. The power values were obtained by taking into account the directional pattern of the LED and the absorption of radiation by water vapor in the region of 6 μm.

3. RESULTS AND DISCUSSION

3.1. Injection Luminescence

The current–voltage characteristics (Fig. 2a) have a diode character with portions of reverse-current saturation (I_S) at the voltage $|U| > 0.05$–0.01 V. The saturation is not complete, which is, apparently, due to the nonuniformity of current spreading in the structure that has a point contact to the *n*-type layer and to the increase in the contribution of peripheral (distant from the contact) regions to the conductivity of the structure as the reverse bias increases [10]. This fact, confirmed by the absence of saturation for the negative luminescence power, indicates that the surface leakage is insignificant. As the temperature rises, the increase in the intrinsic carrier concentration leads to an increase in the sat-

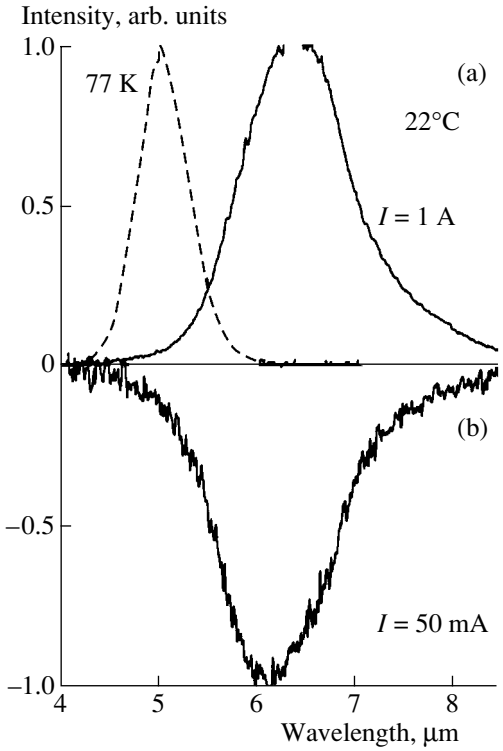

Fig. 3. Luminescence spectra at (a) forward and (b) reverse bias at T = 22°C (solid lines) and 77 K (dashed line).

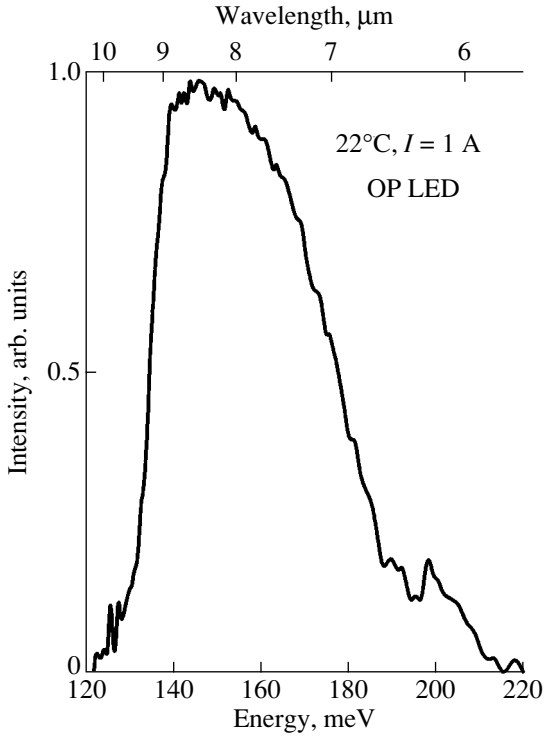

Fig. 4. The luminescence spectrum of an optically pumped LED at 22°C.

uration current and a decrease in the conversion efficiency (μW/A) (Fig. 2b). The dependences of the luminescence power on the current at forward and reverse biases have a sublinear or superlinear character due to an increase (decrease) in the rate of nonradiative Auger recombination as the minority carrier concentration increases (decreases).

The luminescence spectra (Fig. 3) at small forward and reverse currents $I = \pm 50$ mA have maxima at $\lambda = 6.15$ μm and are almost mirror reflections of each other. With an increase in the forward current, heating of the structure leads to a red shift of the spectrum. The value of overheating, estimated from the temperature coefficient of the variation in the band gap width for the closest analog (InAs), is no larger than 30°C at $I = 1$ A. The shape of the spectra is determined by the tails of the density of the states in the long-wavelength region and the absorption of short-wavelength radiation in the wide-gap layers of the structure. With a decrease in temperature to 77 K, the spectrum shifts to shorter wavelengths (the dashed line) following the temperature-induced narrowing of the band gap.

3.2. Photoluminescence

Figure 4 shows the spectrum of an optically pumped LED at room temperature based on an isotypic *n*-InAsSb structure. The spectrum has a characteristic dip in the region of 6.5 μm due to the absorption by water vapor and so drops from the long-wavelength side at $\lambda \approx 9.3$ μm, which is related to the drop of the spectral sensitivity of the PD used. The luminescence intensity in the spectral maximum at $\lambda = 8.5$ μm ($h\nu \approx 146$ meV) is somewhat lower than the value one might expect from the calculation of the band gap width for the given solid solution. This phenomenon is related to the Joule heating of the pump GaAs LED and, accordingly, the luminescent InAsSb layer adjacent to it. The maximum value of the luminescence intensity obtained is, as far as we know, the longest wavelength for the luminescence sources based on III–V materials and operating at interband transitions at room temperature.

Figure 5 shows the dependence of the efficiency ([μW/A]) of electrically and optically pumped LEDs at the linear portion the power–current characteristic (the data for the wavelengths 4.3, 4.6, and 5.5 μm are taken from [11]). As can be seen, the efficiency of optically pumped LEDs exceeds the value expected for LEDs with a *p*–*n* junction. The higher efficiency of LEDs based on *n*-type semiconductors is, apparently, due to the difference in the internal quantum yields of *n*- and *p*-type materials. An additional factor increasing the efficiency is the structural features of optically pumped LEDs, in which the regions of current flow and long-wavelength carrier recombination are spaced from each other and, therefore, may have significantly different temperatures during operation.

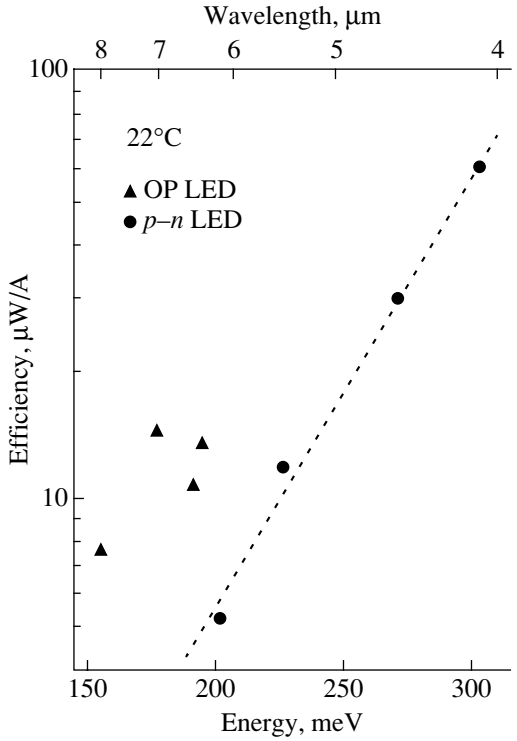

Fig. 5. The efficiency of an optically pumped LED and an LED with a *p–n* junction (OP LED and *p–n* LED, respectively) at 22°C.

4. CONCLUSIONS

Epitaxial multilayer $InAs_{1-x}Sb_x/\ldots/InAs_{1-x-y}Sb_xP_y/n$-InAs structures with an InSb content in the active (upper) layer as high as $x = 0.33$ were fabricated. The luminescence of these structures was observed in the wavelength range $\lambda \gtrsim 6$ μm with an efficiency ranging from 4 to 10 μW/A at forward and reverse bias, respectively. For the optically pumped structures, the maximum emission wavelength was 8–9 μm; in this case, it was as high as 10 μW/A.

REFERENCES

1. V. I. Ivanov-Omskiĭ, B. T. Kolomiets, and V. A. Smirnov, Dokl. Akad. Nauk SSSR **161**, 1308 (1965) [Sov. Phys. Dokl. **10**, 345 (1965)].
2. B. A. Matveev, M. A'daraliev, N. V. Zotova, *et al.*, Proc. SPIE **4285**, 109 (2001).
3. J. R. Lindle, W. W. Bewley, I. Vurgaftman, *et al.*, IEE Proc.: Optoelectron. **150**, 365 (2003).
4. T. Ashley, C. T. Elliott, N. T. Gordon, *et al.*, Appl. Phys. Lett. **64**, 2433 (1994).
5. P. J. P. Tang, H. Hardaway, J. Heber, *et al.*, Appl. Phys. Lett. **72**, 3473 (1998).
6. J. G. Crowder, H. R. Hardaway, and C. T. Elliott, Meas. Sci. Technol. **13**, 882 (2002).
7. B. A. Matveev, N. V. Zotova, S. A. Karandashev, *et al.*, IEE Proc.: Optoelectron. **149** (1), 33 (2002).
8. D. T. Cheung, A. M. Anfrews, E. R. Gertner, *et al.*, Appl. Phys. Lett. **30**, 587 (1977).
9. Z. M. Fang, K. Y. Ma, D. H. Jaw, *et al.*, J. Appl. Phys. **67**, 7034 (1990).
10. V. K. Malyutenko, O. Yu. Malyutenko, A. D. Podoltsev, *et al.*, Appl. Phys. Lett. **79**, 4228 (2001).
11. M. Aĭdaraliev, N. V. Zotova, S. A. Karandashev, *et al.*, Fiz. Tekh. Poluprovodn. (St. Petersburg) **36**, 881 (2002) [Semiconductors **36**, 828 (2002)].

Translated by Yu. Sin'kov

Semiconductors, Vol. 39, No. 2, 2005, pp. 218–220. Translated from Fizika i Tekhnika Poluprovodnikov, Vol. 39, No. 2, 2005, pp. 234–236.

SEMICONDUCTOR STRUCTURES, INTERFACES, AND SURFACES

Photovoltaic Properties of *n*-ZnO:Al/PbPc/*p*-Si Structures

G. A. Il'chuk*, S. E. Nikitin, Yu. A. Nikolaev**, V. Yu. Rud'***^, Yu. V. Rud'**, and E. I. Terukov****

**Lviv Polytechnic National University, Lviv, 79013 Ukraine*

***Ioffe Physicotechnical Institute, Russian Academy of Sciences, ul. Politekhnicheskaya 26, St. Petersburg, 194021 Russia*

****St. Petersburg State Technical University, ul. Politekhnicheskaya 29, St. Petersburg, 195251 Russia*

^e-mail: rudvas@spbstu.ru

Submitted June 3, 2004; accepted for publication June 9, 2004

Abstract—*n*-ZnO:Al/PbPc/*p*-Si photosensitive structures are fabricated for the first time. The steady-state current–voltage characteristics and spectral dependences of the relative quantum efficiency of the photoconversion of these structures are studied, and the mechanisms of charge transport and the photosensitivity processes are discussed. It is concluded that they are promising for application as multiband photoconverters of natural light.

The semiconductive properties of phthalocyanines, from various metals, have long been known [1, 2]. The first solar-radiation photoconverters based on these phthalocyanines (Pc) and featuring a quantum efficiency of about 3.6% have already been fabricated and studied [3]. Moreover, it has recently been established [4] that the heterocontact of a comparatively poorly studied class of organic semiconductors (for example, copper phthalocyanine) with inorganic semiconductors (e.g., crystalline silicon) can be used to fabricate the next-generation of photosensitive structures [4]. Taking into account the results reported in [1, 2], we may assume that a variation in the nature of the metals incorporated into a phthalocyanine structure would make it possible, in future, to control the photovoltaic properties of the structures under consideration. This study is a continuation of the efforts in this promising line of research in the field of contemporary electronics; thus, this paper reports the results of our pioneering studies of structures based on a lead phthalocyanine PbPc.

In order to fabricate the structures, we used *p*-Si wafers with a thickness of ~0.3 mm and an area of approximately 2 cm^2. The high quality of the wafers' surface with crystallographic orientation (111) was ensured first by mechanical treatment and then with chemical treatment. Thin ($d \approx 1$ μm) films of lead phthalocyanine PbPc were deposited onto the treated *p*-Si surface using a vacuum thermal sublimation of PbPc powder. The chosen conditions of sublimation made it possible to form the PbPc films so that they had a specular surface and good adhesion to the treated surface of the *p*-Si substrate. The substrate temperature during deposition was no higher than ~50°C. Fabrication of the structures was completed after the deposition of a thin *n*-ZnO:Al film onto the surface of the PbPc film already on the *p*-Si substrate. The thin ($d \approx 1$ μm) *n*-ZnO:Al films were deposited using magnetron sputtering of ZnO:Al targets in an argon atmosphere. Argon pressure during the film deposition made it possible to control the free-electron concentration in the ZnO film. The duration of the ZnO film deposition was varied from 2 to 4 hours; as a result, we could vary the film thickness. At argon pressures of approximately 0.5 Pa, the free-electron concentration in the ZnO films was as high as ~10^{20} cm^{-3} and nearly temperature-independent in the temperature range from 80 to 300 K. The quality of the surface of the *n*-ZnO:Al film corresponded to that of the substrate. As a result of the above-described fabrication procedure, we obtained *n*-ZnO:Al/PbPc/*p*-Si structures for the first time.

The steady-state current–voltage (*I–V*) characteristic of a typical *n*-ZnO:Al/PbPc/*p*-Si structure is shown in Fig. 1. It can be seen that the structures under consideration exhibit a pronounced rectification effect. The conducting mode for such structures is typically attained if a positive external bias is applied to the crystal of the *p*-Si substrate. The rectification factor for the structures, determined from the ratio between the forward and reverse currents, was typically equal to ≈10. The initial portion of the forward *I–V* characteristics for these structures follows the exponential law with the diode index $\beta \approx 6$–8, which suggests that the forward current has a tunneling–recombination origin. When the forward-bias voltages $U > 1$ V are applied, the current follows the linear law

$$I = \frac{U - U_0}{R_0}, \quad (1)$$

where the cutoff voltage $U_0 \approx 0.9$ V and the residual resistance $R_0 \approx 2 \times 10^6$ Ω at $T = 300$ K. The reverse current in the structures under consideration follows the power law $I \propto U^m$, where the exponent $m \approx 2$ in the tem-

perature range used; according to [5], this value of m indicates that currents limited by a space charge are involved in the mobility mode (the trap-free quadratic law) [5].

When the *n*-ZnO:Al/PbPc/*p*-Si structures are illuminated, a photovoltaic effect is observed. This effect is dominant if the wide-gap component of the structures (the *n*-ZnO:Al film) is illuminated. Irrespective of the location of the optical probe (with a diameter of ~0.4 mm) on the surface, the photon energy, the incident-radiation intensity, and the negative polarity of the photovoltage corresponds to the *n*-ZnO:Al film in all the structures under consideration. This observation is consistent with the rectification direction. Measurements showed that the highest voltage photosensitivity was ~100 V/W and the current photosensitivity was ~2 μA/W for the best of our *n*-ZnO:Al/PbPc/*p*-Si structures (the detection geometry illustrated in the inset in Fig. 2). We may assume that the low current photosensitivity of the structures is mainly caused by a high residual resistance. Evidently, in order to increase the photoconversion efficiency, one has to find ways of reducing the value of R_0 in these ZnO/PbPc/Si structures.

A typical spectral dependence of the relative quantum efficiency η of the photoconversion for an *n*-ZnO:Al/PbPc/*p*-Si structure exposed to nonpolarized light is shown in Fig. 2. It can be seen that, if the wide-gap side of these structures is illuminated, the photoconversion is observed in a wide spectral range (from 1 to 3 eV). The long-wavelength edge of the photosensitivity for the structures obeys the following law, which is characteristic of indirect band-to-band optical transitions [6]:

$$\eta = \frac{A'}{\hbar\omega}(\hbar\omega - E_g^{in})^2. \qquad (2)$$

Here, A' is a constant and E_g^{in} is the band gap. Extrapolation of the long-wavelength edge of the spectra $\eta(\hbar\omega)$ to zero $(\eta\hbar\omega)^{1/2} \longrightarrow 0$ yields $E_g^{in} \approx 1.10$ eV, which corresponds to the band gap of crystalline silicon [7, 8].

The short-wavelength falloff of the photosensitivity observed in the spectral dependences $\eta(\hbar\omega)$ at $\hbar\omega > 3$ eV is in satisfactory agreement with the onset of interband absorption in ZnO [7]. Therefore, this falloff should be related to an increase in the optical absorption of the ZnO film, which is accompanied by an increase in the distance between the layer where the electron–hole pairs are photogenerated and the active region of these structures; as a result, a short-wavelength edge appears in the $\eta(\hbar\omega)$ spectra. Consequently, the photosensitivity in the *n*-ZnO:Al/PbPc/*p*-Si structures manifests itself in a range limited by the band gaps of the two inorganic semiconductors (Si and ZnO) that are included in the structures under study. In this context, we can use an analogy with traditional heterojunctions that are based on the contact of two inorganic semiconductors to assume that the so-called window effect is observed in the new ZnO/PbPc/Si structures [9, 10]. However, in contrast to traditional semiconductors, the photosensitivity does not remain constant in the range limited by the Si and ZnO band gaps in the $\eta(\hbar\omega)$ spectra of the

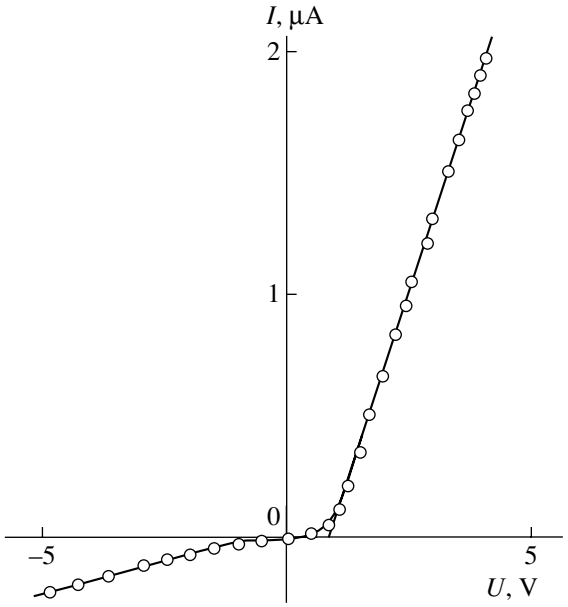

Fig. 1. The steady-state current–voltage characteristic of an *n*-ZnO:Al/PbPc/*p*-Si structure at $T = 300$ K. The conducting direction corresponds to the positive polarity of the external bias voltage applied to the KDB-0.03 (*p*-Si:B, $\rho = 0.03\ \Omega$ cm) crystalline substrate.

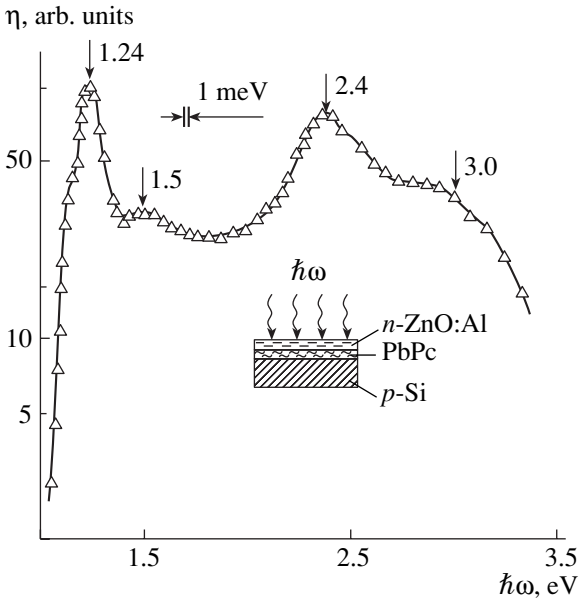

Fig. 2. Spectral dependence of the relative photoconversion quantum efficiency in an *n*-ZnO:Al/PbPc/*p*-Si structure at $T = 300$ K. The *n*-ZnO:Al film with the thickness $d \sim 1$ μm at the top of the structure was exposed to nonpolarized light. The inset illustrates the structure of the photoconverter under study and the geometry of the illumination.

n-ZnO:Al/PbPc/*p*-Si structures; on the contrary, the photosensitivity exhibits specific features that can easily be reproduced in all the structures under study and are indicated by arrows in Fig. 2.

Similar specific features have been observed before for the *n*-ZnO:Al/CuPc/*p*-Si structures [4]. These features can be related to the discrete character of the energy spectrum for the phthalocyanines of various metals [11], in which the replacement of one of these metals by another is accompanied by variations in the energy position of the transparency windows and intensity of the absorption bands that correspond to these features. It is this circumstance that gives rise to differences between the spectral positions of the maxima and minima of the photosensitivity in a photon-energy range limited by the band gaps of inorganic semiconductors in the *n*-ZnO:Al/PbPc/*p*-Si (Fig. 2) and *n*-ZnO:Al/CuPc/*p*-Si [4] structures.

When considering the $\eta(\hbar\omega)$ spectrum of the *n*-ZnO:Al/PbPc/*p*-Si structure, we can mention a new (relative to traditional heterojunctions [9, 10]) opportunity to attain the photosensitivity of the structures only in specific spectral regions; furthermore, the structures are almost insensitive to incident radiation outside these spectral regions. Indeed, it can be seen from Fig. 2 that there are two pronounced peaks at the photon energies $\hbar\omega_1 \cong 1.24$ eV and $\hbar\omega_2 \cong 2.4$ eV in the photosensitivity spectrum of the structure under consideration. The full widths of these bands at the half-heights of the absolute photosensitivity maxima are equal to $\delta_1 \approx 0.18$ eV and $\delta_2 \approx 0.69$ eV for the peaks $\hbar\omega_1$ and $\hbar\omega_2$, respectively. We may assume that further investigations into the spectral distribution of the photosensitivity of structures based on phthalocyanines of various metals and on various inorganic semiconductors would make it possible to ascertain the mechanisms for controlling the $\eta(\hbar\omega)$ spectra of these photoconverters.

In summary, we fabricated ZnO/PbPc/Si structures for the first time. We studied the photovoltaic properties of these structures and found that the structures can be used as multiband photoconverters with a controlled spectral contour of the highest photosensitivity.

ACKNOWLEDGMENTS

This study was supported by a program "New Concepts of Energy Conversion in Semiconductor Structures" of the Department of Physical Sciences of the Russian Academy of Sciences.

REFERENCES

1. A. T. Vartanyan, Zh. Fiz. Khim. **22**, 769 (1948).
2. A. T. Vartanyan, Zh. Fiz. Khim. **32**, 168 (1958).
3. P. Penmans and S. R. Forrest, Appl. Phys. Lett. **79**, 126 (2001).
4. G. A. Il'chuk, N. V. Klimova, O. I. Kon'kov, *et al.*, Fiz. Tekh. Poluprovodn. (St. Petersburg) **38**, 1056 (2004) [Semiconductors **38**, 1018 (2004)].
5. M. A. Lampert and P. Mark, *Current Injection in Solids* (Academic, New York, 1970; Mir, Moscow, 1973).
6. Yu. A. Ukhanov, *Optical Properties of Semiconductors* (Nauka, Moscow, 1977) [in Russian].
7. *Physicochemical Properties of Semiconductor Materials: Handbook*, Ed. by A. V. Novoselova and V. B. Lazarev (Nauka, Moscow, 1979) [in Russian].
8. K. V. Shalimova, *Physics of Semiconductors* (Énergiya, Moscow, 1976) [in Russian].
9. S. Sze, *Physics of Semiconductor Devices*, 2nd ed. (Wiley, New York, 1981; Mir, Moscow, 1984).
10. A. G. Milnes and D. L. Feucht, *Heterojunctions and Metal–Semiconductor Junctions* (Academic, New York, 1972; Mir, Moscow, 1975).
11. A. Stern and F. Prukhner, Z. Phys. Chem. A **178**, 420 (1937).

Translated by A. Spitsyn

Semiconductors, Vol. 39, No. 2, 2005, pp. 221–225. Translated from Fizika i Tekhnika Poluprovodnikov, Vol. 39, No. 2, 2005, pp. 237–241.

LOW-DIMENSIONAL SYSTEMS

Nonohmic Conductance and Mechanisms of Energy Relaxation in 2D Electron Gas in GaAs/InGaAs/GaAs Heterostructures

A. A. Sherstobitov*, G. M. Min'kov*^, O. E. Rut*, A. V. Germanenko*, and B. N. Zvonkov**

**Ural State University, Yekaterinburg, 620083 Russia*

^e-mail: Grigori.Minkov@usu.ru

***Lobachevskiĭ State University, Nizhni Novgorod, 603600 Russia*

Submitted October 14, 2003; accepted for publication May 17, 2004

Abstract—The effects of heating 2D electron gas in GaAs/InGaAs/GaAs structures at temperatures of 0.4–4 K and electron densities of $(1.5–6) \times 10^{15}$ m^{-2} are studied. For the entire range of temperatures and densities studied, the rate of energy relaxation agrees well with theoretical predictions of the energy relaxation via electron scattering at the piezoelectric and deformation potential of acoustic phonons. It is shown that the widely used analytical expressions for energy relaxation rate, which were obtained in low- and high-temperature limits, are applicable only when the relations between the Fermi quasi-momentum and the momentum of thermal phonons are strictly observed. It is shown that the dependence of the energy relaxation rate on the electron density is a nonmonotonic function. For example, at the lattice temperature of 1.4 K, it initially increases as the electron density decreases to $n = 2.5 \times 10^{15}$ m^{-2}, but then starts to decrease as the density decreases further. © *2005 Pleiades Publishing, Inc.*

1. INTRODUCTION

At low temperatures, the conductance of 2D electron gas increases as the electric field increases, and a significantly nonohmic conductance behavior is observed at the field strength of approximately several volts per centimeter. In the case of diffusion conduction, when $\sigma > e^2/h$, this increase is related to the heating of the electron gas. Studies of nonohmic conduction provide information on mechanisms of electron scattering. Additional interest in these studies has been generated by the fact that the study of nonohmic conduction makes it possible to experimentally determine the conditions (the degree of disordering and temperature) where a transition from diffusion conduction to conduction by hopping occurs. This possibility is based on the difference between the nonlinearity mechanisms in the diffusion and hopping modes. In the first case, the change of conductance in the electric field is related to the change in the effective electron temperature; in the second, additional mechanisms of nonlinearity appear, namely, the change of hopping probability in a strong electric field [1] and impact ionization of localized electrons.

During the last 20 years, multiple experimental studies have been devoted to electron heating of a 2D electron gas possessing high conductance in GaAs-based structures (see, e.g., [2–10] and the references therein). All the authors of these publications came to the conclusion that the main mechanism of energy relaxation at low temperatures was related to the interaction of acoustic phonons with the deformation and piezoelectric potentials; however, a significant quantitative difference exists between the data obtained in different studies. For example, in [8] and [9], the energy relaxation rate $P(T_L, T_e)$ at the lattice temperature T_L = 1.5 K and the electron gas temperature T_e = 2 K was determined in similar structures that had the electron density 5×10^{15} m^{-2}. It was found that the obtained values differed by a factor of 4. At lower lattice temperatures this difference was even larger. It remains unknown whether this discrepancy is related to additional mechanisms of relaxation in the structures examined in some studies, or to experimental errors.

In this study, we investigate, in detail, the dependence of the energy relaxation rate on the density of carriers in GaAs/InGaAs structures at $\sigma > e^2/h$, in the density range $(1.5–6) \times 10^{15}$ m^{-2} and temperature range 0.4–4 K.

2. SAMPLES AND EXPERIMENTAL RESULTS

The conductance of GaAs/InGaAs/GaAs structures with 2D electron gas was studied in the electric field up to E = 10 V/cm. The structures were grown by MOCVD on a semi-insulating GaAs substrate: a pure GaAs buffer layer of 200 nm thick, an InGaAs quantum well (QW) with the thickness d = 8 nm and a 20% In content, and a pure GaAs top layer of 200 nm thick. On the both sides of the QW, at a distance of 9 nm from it, δ-layers doped with Sn were grown.

In this study, we present a detailed analysis of the data obtained on four samples. All the samples had the form of Hall bridges of B = 0.5 in width, with the distance between the potential contacts L = 1 mm. In three of the samples, the density and conductance were varied with the aid of illumination, using the effect of persistent photoconductivity. For these samples, the fol-

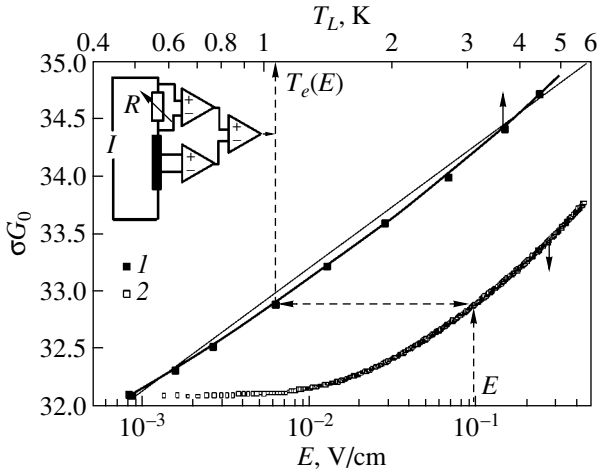

Fig. 1. Dependences of the conductance on (*1*) lattice temperature T_L in a weak electric field, and (*2*) on the electric field E at T_L = 0.47 K. Solid lines show different approximations of the $\sigma(T_L)$ temperature dependence, used in the treatment. The dashed line shows the method for the determination of $E(T_e)$ dependence, from which the dependence of power, $P(T_e, T_L)$, was calculated.

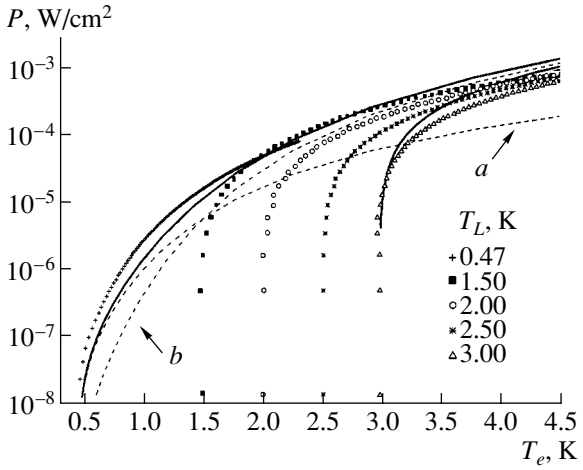

Fig. 2. The energy relaxation rate as function of the electron gas temperature for different lattice temperatures. For sample no. 3510, $n = 4.2 \times 10^{-15}$ m^{-2} and $\sigma(1.5\ \text{K}) = 33G_0$. Solid lines show theoretical dependences calculated in accordance with (17) for T_L = 0.47 and 1.4 K. Dashed lines show contributions of the scattering at (*a*) piezoelectric and (*b*) deformation potentials at T_L = 0.47 K.

lowing dark density and conductance values were found at a temperature of 1.5 K:

sample no. 3509: $n \approx 10^{15}$ m^{-2}, $\sigma = 10^{-3}G_0$;

sample no. 3508: $n \approx 3 \times 10^{15}$ m^{-2}, $\sigma = 20G_0$;

sample no. 3510: $n \approx 4 \times 10^{15}$ m^{-2}, $\sigma = 33G_0$,

where $G_0 = e^2/2\pi\hbar = 1.23 \times 10^{-5}\ \Omega^{-1}$. The electron density in the fourth sample, no. 3510G, was varied with the use of a gate electrode (Al). In the study of structures with a gate electrode in strong electric field, it is very important that the voltage drop along the channel should be much less than V_g, otherwise gradients of density; power; and, consequently, electron temperature arise along the channel. To reduce this effect, a thick (~10 μm) layer of organic insulator was first deposited onto sample no. 3510 and then onto the gate electrode. At the gate voltage $V_g = 0$, the parameters of sample no. 3510 were $n = 4 \times 10^{15}$ m^{-2} and $\sigma = 40G_0$. The measurements were performed in the dc mode in the temperature range T_L = 0.4–4 K. The dependence of the voltage V across the potential contacts on current I was measured with a continuous current sweep for each of the fixed lattice temperatures. Thus, the obtained values of conductance $\sigma(E, T_L) \equiv j/E$ (j is the current density) at $E \longrightarrow 0$ were used in the determination of the temperature dependence $\sigma(T_L)$.

At high conductance values ($\sigma > (20–30)G_0$), it varies in the electric field by only a few percent; therefore, to improve the precision, we used the compensation circuit shown in the inset in Fig. 1. This method allowed us to measure the conductance variation in the electric field and the temperature dependence of the conductance in a weak electric field with a relative accuracy of no worse than 0.05%.

Figure 1 shows dependences of the conductance on the lattice temperature $\sigma(T_L)$ at $E \longrightarrow 0$ and on the electric field at T_L = 0.47 K before the illumination for sample no. 3510. It can be seen that the temperature dependence of the conductance is nearly logarithmic for the entire range of T_L studied. This behavior of $\sigma(T_L)$ is defined by the temperature dependence of the quantum corrections to the conductance, i.e., corrections for interference and for electron–electron (*e–e*) interaction, both of which depend logarithmically on temperature. The value of these corrections is only defined by the temperature of the electrons, not of the lattice (a detailed analysis of quantum corrections to conductance in similar structures was made in [11]). In this case, as shown by the dashed line in Fig. 1, the dependence of the electron temperature T_e on E and, accordingly, on the applied power $P = j/E$ can be found from a comparison of the dependences of the conductance on the temperature and the electric field. After this treatment of the experimental data, we approximated the $\sigma(T_L)$ dependence at $E \longrightarrow 0$ with a smooth curve (see Fig. 1). Figure 2 shows, for one of the samples under study, the dependences of the power necessary to heat the electron gas to temperature T_e on T_e at different lattice temperatures T_L.

In steady-state conditions, this power is proportional to the rate of electron energy relaxation. The main mechanism of energy relaxation in the studied range of temperatures and electric fields is related to the interaction of electrons with acoustic phonons. Estimates show that, with our experimental conditions, the time taken for the establishment of equilibrium in the

electron system is several orders of magnitude less than the characteristic time for the electron–phonon interaction; therefore, the electron energy distribution function in the electric field remains the Fermi type, with the electron temperature $T_e > T_L$.

3. RESULTS OF THEORETICAL CALCULATIONS AND DISCUSSION OF THE EXPERIMENTAL DATA

The energy relaxation rate in 2D electron gas at low temperatures has been calculated in several studies (see, e.g., [12, 8]). The results of these studies do not differ strongly. Here, we use the results in [12], which are the simplest for numerical calculation.

The dependence of the energy relaxation rate on the electron and lattice temperatures, T_e and T_L, can be represented as the difference between two similar functions, one of which depends on T_e and the other on T_L:

$$P(T_e, T_L) = F(T_e) - F(T_L). \quad (1)$$

The main mechanism of electron energy relaxation in InGaAs and GaAs is related to scattering at the deformation and piezoelectric potentials of acoustic phonons. In this case, the function $F(T)$ has the form

$$F(T) = \frac{n}{\hbar E_F}\int dq|I(q)|^2\overline{aS(Q)^2(\hbar\omega)^3 N(\hbar\omega/k_B T)}, \quad (2)$$

where N is the phonon distribution function

$$N\left(\frac{\hbar\omega}{k_B T}\right) = \frac{1}{\exp\dfrac{\hbar\omega}{k_B T} - 1}, \quad (3)$$

the form factor is

$$I(q) = \int \rho(z)\exp(iqz)dz, \quad (4)$$

$\rho(z)$ is the squared wave function $\varphi(z)$, z is the normal to the QW plane, and q is the z component of the phonon wave vector. Estimates show that, for our structures, a good approximation in the calculation of the wave function is the model of a rectangular well with infinitely high walls. In this case, $\varphi(z)$ is given by

$$\varphi(z) = (2/d)^{1/2}\sin\pi z/d. \quad (5)$$

$S(Q)$ is the screening function

$$S(Q) = \frac{Q}{Q + pH(Q)}, \quad (6)$$

$$H(Q) = \iint \rho(z_1)\rho(z_2)\exp(-Q|z_1 - z_2|)dz_1 dz_2, \quad (7)$$

where $p = 2/a_B$ is the screening constant, a_B is the Bohr radius, and Q is the longitudinal component of the phonon wave vector.

The matrix element a depends on the type of interaction. In the case of scattering at the deformation potential, only the longitudinal component of a, which is

$$a_l^{DP}(q, Q) = b_0, \quad b_0 = \frac{m}{\hbar^2}\frac{\Xi^2}{2k_l}, \quad (8)$$

is of importance. Here, Ξ is the deformation potential constant and k_l is the elastic constant, which equals the density multiplied by the longitudinal velocity of sound s_l. For scattering at the piezoelectric potential, both components of the matrix element a,

$$a_l^{PZ}(q, Q) = b_0\frac{\alpha^2}{q^2 + Q^2}\frac{9q^2Q^4}{2(q^2 + Q^2)^3}, \quad (9)$$

$$a_t^{PZ}(q, Q) = b_0\frac{\alpha^2}{q^2 + Q^2}\frac{8q^4Q^2 + Q^6}{2(q^2 + Q^2)^3}, \quad (10)$$

are of importance. Here, $\alpha = eh_{14}/\Xi$, and h_{14} is the piezoelectric constant. The frequency ω in (2) equals

$$\omega = s\sqrt{q^2 + Q^2}, \quad (11)$$

where s is the corresponding velocity of sound.

For our case, when the velocity of sound (approximately 4000 m/s) is much less than the Fermi velocity of an electron (approximately 3×10^5 m/s), the magnitude Q is related to k_F and the scattering angle θ by the simple equation

$$Q = 2k_F\sin(\theta/2). \quad (12)$$

In Eq. (2), the averaging is performed over the angles of scattering θ, which means

$$\bar{\phi} = \frac{1}{\pi}\int_0^\pi \phi d\theta. \quad (13)$$

The total energy relaxation rate is determined as the sum of all the contributions:

$$F = F_l^{DP} + F_t^{PZ} + F_l^{PZ}, \quad (14)$$

where F_l^{DP}, F_t^{PZ}, and F_l^{PZ} are, respectively, the contributions of the deformation potential of the longitudinal acoustic phonons and the piezoelectric potential of the transverse and longitudinal acoustic phonons calculated in accordance with (2).

In several studies, the experiment was analyzed not with the use of Eq. (2) but using analytical relations obtained for two limiting cases: low temperatures, when $q_T < k_F$, and high temperatures, when $q_T \gg k_F$ (where q_T is the average quasi-momentum of acoustic phonons, $q_T = k_B T/hs$, and s is the corresponding velocity of sound). Then, in the limit of low temperatures, the function F^{PZ}, for scattering at the piezoelectric potential, is given by

$$F^{PZ} \propto 1/n^{1/2}T^5 \quad (15)$$

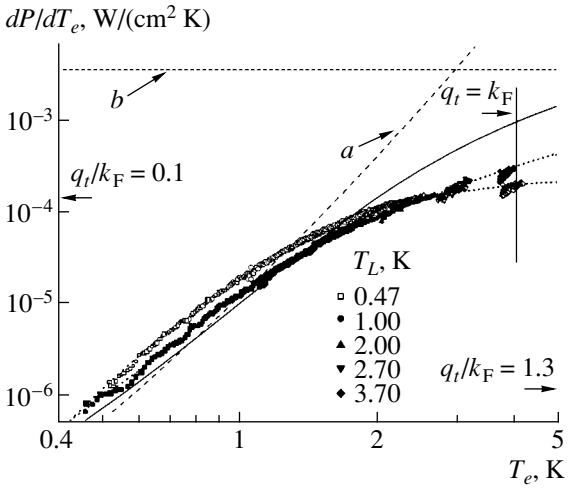

Fig. 3. Derivatives of the energy relaxation rate in respect to T_e at different lattice temperatures. For sample no. 3510, $n = 4.2 \times 10^{-15}$ m^{-2} and $\sigma(1.5\ \text{K}) = 33G_0$. The solid line shows the derivative of the theoretical dependence (14). Dashed lines show derivatives of the dependences (*a*) (18) and (*b*) (17). The full and open symbols correspond to different approximations of the $\sigma(T_L)$ dependences.

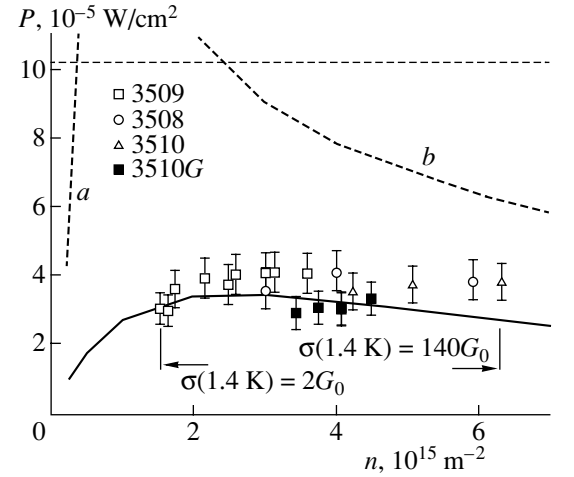

Fig. 4. The energy relaxation rate as function of 2D electron density at $T_L = 1.4$ K and $T_e = 1.8$ K. Solid lines show the theoretical dependence calculated in accordance with (14). Dashed lines show the analytical expressions (*a*) (17) and (*b*) (18).

and, for scattering at the deformation potential,

$$F^{\text{DP}} \sim 1/n^{1/2}T^7. \tag{16}$$

For a general case, F is given by

$$F = F^{\text{PZ}} + F^{\text{DP}}. \tag{17}$$

As is shown in [12], at high temperatures, when $q_T > k_F$, the deformation potential scattering is dominant, and F is given by

$$F \propto n^2T. \tag{18}$$

In the comparison of the theoretical dependence of the energy relaxation rate with the experimental data, we use the following values for constants [8]:

$$p = 0.2\ \text{nm}^{-1}, \quad \Xi = 11\ \text{eV}, \quad eh_{14} = 1.2\ \text{eV nm [13]},$$
$$s_l = 5000\ \text{m/s}, \quad s_t = 3000\ \text{m/s}.$$

The solid lines in Fig. 2 show the theoretical dependences of the energy relaxation rate calculated from (14) for the limiting (in the studied range) temperatures. The contributions to the energy relaxation rate made by scattering at the deformation and piezoelectric potentials for $T_L = 0.47$ K are also shown. It can be seen that, at $T_e < 1.5$ K, the main mechanism of energy relaxation is scattering at the piezoelectric potential of acoustic phonons, and also that the interaction with the deformation potential becomes significant at $T_e > 1.5$ K. The total energy relaxation rate satisfactorily describes the experimental data in the entire range of electron temperatures T_e.

The structure of Eq. (1), for the energy relaxation rate in the diffusion mode, makes a more detailed comparison of the experimental and theoretical data possible. Indeed, as follows from (1), the derivative dP/dT_e must be independent of the lattice temperature, i.e., the $dP/dT_e = f(T_e)$ dependences measured at different T_L must fall on a single curve $dF(T_L)/dT_L$.

Figure 3 shows the experimental dependences $dP/dT_e = f(T_e)$ for sample no. 3510 at the density $n = 4.2 \times 10^{15}$ m^{-2}. Indeed, it can be seen, that the curves $dP/dT_e = f(T_e)$ fall on almost the same dependence. At first glance, this seems astonishing because, evidently, the inaccuracy in the derivative of an experimental curve must be considerable. However, this is mainly the inaccuracy in the absolute magnitude, not in the $dP/dT_e = f(T_e)$ dependences obtained at different T_L. To illustrate this fact, we have shown, in the same figure, $dP/dT_e = f(T_e)$ dependences at different T_L, obtained with the use of another approximation of $\sigma(T_L)$ (see Fig. 1).

In Fig. 3, to compare the experimental and theoretical dependences of $dP/dT_e = f(T_e)$, we present the derivatives dP/dT_e, calculated from (14), (17), and (18) with the above mentioned parameters. It can be seen that the general relation (14) satisfactorily describes the experimental data in the whole temperature range. It is noteworthy that the use of analytical expressions (17) and (18), obtained in low-temperature and high-temperature approximations, demands a relatively strict fulfillment of the inequalities $q_t < k_F$ and $q_1 > k_F$. The low-temperature approximation becomes applicable at $T_L < 0.9$ K, which corresponds to $q_t/k_F \approx 0.2$, and the high-temperature approximation at $T_L > 15$–20 K, which corresponds to $q_t/k_F \approx 2.5$–3. Similar matching is observed in the entire range of densities studied, $1.5 \times 10^{15} < n < 6.2 \times 10^{15}$ m^{-2}, and the conductances, $2G_0 < \sigma < 140G_0$.

As can be seen from (17) and (18), the theory predicts that, in addition to the constants of electron–

phonon interaction and values of T_L and T_e, the only other parameter affecting the energy relaxation rate is the carrier density. Let us analyze this dependence at $T_L = 1.4$ K and $T_e = 1.9$ K. As can be seen in Fig. 4, in which the four samples under study are shown, all the points fall on a smooth curve, within the experimental error. Figure 4 also shows the theoretical dependences calculated using general expression (14) and those corresponding to low- and high-temperature limits, calculated using (17) and (18). Expression (14) satisfactorily describes the experimental data in the entire range of densities n. The energy relaxation rate increases slightly as n decreases to $1.5 \times 10^{15} < n < 7 \times 10^{15}$ m^{-2} and then decreases as n decreases further. Moreover, as can be seen in Fig. 4, frequently used analytic expressions for the limiting cases ($q_t \ll k_F$, $q_t \gg k_F$), which predict rather strong dependences on concentration, $P(n)$: $P \propto 1/n^{1/2}$ at $q_t/k_F \gg 1$ and $P \propto n^2$ at $q_t/k_F \ll 1$, give only asymptotic approximations of the result obtained in the calculation from expression (14) at high and low densities, respectively.

4. CONCLUSION

This study of the effects of heating electron gas in the diffusion region of the conduction has shown that the experimental dependences of the energy relaxation rate $P(T_e, T_L)$ are satisfactorily described by the theory of energy relaxation for the scattering at the deformation and piezoelectric potentials of acoustic phonons. At $T_L < 1.5$ K, the main mechanism of energy relaxation is scattering at the piezoelectric potential of acoustic phonons, while the interaction with the deformation potential becomes significant at $T_e > 1.5$ K. It is shown that the energy relaxation rate increases as the electron density decreases to $n = 2.5 \times 10^{15}$ m^{-2}, and then decreases as n decreases further, which is related to variation in the ratio between q_t and k_F.

ACKNOWLEDGMENTS

The study was supported by the Russian Foundation for Basic Research (project nos. 03-02-16150, 03-02-06025, and 01-02-16441), the programs "Physics of Solid-State Nanostructures" and "Universities of Russia, Fundamental Studies" (project no. UR.06.01.002), INTAS (grant 1B290), U.S. Civil Research & Development Foundation (CRDF) (grant no. REC-005), and by a grant of the Russian Ministry of Education and Science for post-graduate students.

REFERENCES

1. S. Marianer and B. I. Shklovskii, Phys. Rev. B **46**, 13100 (1992).
2. E. Chow, H. P. Wei, S. M. Girvin, *et al.*, Phys. Rev. B **56**, K1676 (1997).
3. N. J. Appleyard, J. T. Nicholls, M. Y. Simmons, *et al.*, Phys. Rev. Lett. **81**, 3491 (1998).
4. A. K. M. Wennberg, S. N. Ytterboe, C. M. Gould, *et al.*, Phys. Rev. B **34**, 4409 (1986).
5. D. R. Leadley, R. J. Nicholas, J. J. Harris, and C. T. Foxon, Semicond. Sci. Technol. **4**, 879 (1989).
6. R. Fletcher, Y. Feng, C. T. Foxon, and J. J. Harris, Phys. Rev. B **61**, 2028 (2000).
7. V. E. Gershenson, Yu. B. Khavin, D. Reuter, *et al.*, Phys. Rev. Lett. **85**, 1718 (2000).
8. Y. Ma, R. Fletcher, E. Zaremba, *et al.*, Phys. Rev. B **43**, 9033 (1991).
9. I. G. Savel'ev, T. A. Polyanskaya, and Yu. V. Shmartsev, Fiz. Tekh. Poluprovodn. (Leningrad) **21**, 2096 (1987) [Sov. Phys. Semicond. **21**, 1271 (1987)].
10. V. Chabasseur-Molyneus, A. S. Dzurak, A. Kozorezov, *et al.*, Phys. Rev. B **51**, 13793 (1995).
11. G. M. Minkov, O. E. Rut, A. V. Germanenko, *et al.*, Phys. Rev. B **64**, 235327 (2001).
12. P. J. Price, J. Appl. Phys. **53**, 6863 (1982).
13. A. Kabasi and D. Chattopadhyay, Phys. Rev. B **43**, 14638 (1991).

Translated by D. Mashovets

Semiconductors, Vol. 39, No. 2, 2005, pp. 226–230. Translated from Fizika i Tekhnika Poluprovodnikov, Vol. 39, No. 2, 2005, pp. 242–246.

LOW-DIMENSIONAL SYSTEMS

Special Features of the Electron–Electron Interaction in the Potential of a Heavily Doped $Al_xGa_{1-x}As$:Si/GaAs Heterojunction

V. I. Kadushkin^

Esenin State Pedagogical University, ul. Svobody 46, Ryazan', 390000 Russia

^e-mail: kadush@rspu.ryazan.ru

Submitted April 27, 2004; accepted for publication May 20, 2004

Abstract—A temperature shift of the poles in the Dingle plots was observed at temperatures ranging from 1.65 to 10.9 K. This shift indicates that the mechanisms of intrasubband and intersubband relaxation are transformed, which is directly confirmed by the temperature dependences of corresponding relaxation times.

1. INTRODUCTION

The Dingle plots [1], i.e., the dependences of the amplitudes of the Shubnikov–de Haas oscillations δ on the reciprocal magnetic field $1/B$, have a long history [2]. However, they still represent [3] an example of an informative method for studying the properties and measuring the parameters of a degenerate three-dimensional (3D) and two-dimensional (2D) electron gas in semiconductor compounds and systems [4].

The Dingle temperature T_D is a factor introduced to eliminate divergences in the density-of-state function under resonance conditions in which the Nth Landau level intersects the Fermi level given by

$$\xi_F = \hbar\omega\left(N + \frac{1}{2}\right), \quad (1)$$

where $\omega = eB/m^*$ is the cyclotron frequency. The quantity T_D is formally related to the time taken for an athermal collision-related broadening τ_q of the Landau levels to occur:

$$T_D = \hbar/2\pi k\tau_q. \quad (2)$$

Measurements of the temperature dependences of the amplitudes of the Shubnikov–de Haas oscillations (for example, $\delta(1/B)_{T = \text{const}}$) make it possible to use the dependence $\tau_q(T)$ to conclude what the dominant mechanism is for the collision-related broadening of the Landau levels. This method was also found to be productive for gaining insight into the origin of the amplitude–frequency modulation of the oscillations in the magnetoresistance when several subbands of dimensional quantization are filled with 2D electron gas [3, 5–8].

It has previously been shown [9, 10] that the Dingle plots (i.e., the dependences $\delta(1/B)_{T = \text{const}}$) intersect at a single point on the amplitude scale $\delta(1/B = 0)$ (the pole) if a single collisional mechanism is prevalent. This situation served as a basis for modifying the method [9] for processing experimental data involving oscillations of magnetoresistance [4].

Analysis of the published experimental data shows that the situation is ambiguous. For example, Coleridge [11] found that the position of the pole $\delta(1/B = 0)$ was temperature-independent from 1.04 to 3.40 K; however, it was also found [11] that the poles' positions for the oscillation amplitudes of the main (m) and the second excited (p) subbands of dimensional quantization differed radically (with respect to amplitudes). The latter finding is confirmed by an analysis of the experimental data concerned with semiconductor nanostructures that differed in vertical architecture, chemical composition of the layers, and concentration of 2D electrons [12, 13].

Shifts of the poles $\delta(1/B = 0)$ as a result of variations in the sample temperature were also revealed by analyzing the data obtained from experiments with a bulk n-InSb semiconductor [14, 15].

It is worth noting that, while discussing the broadening time τ_q determined from the Dingle plots (i.e., from the dependence $\delta(1/B)_{T = \text{const}}$), the authors of [5–8] separate, in τ_q, the components related to the intrasubband and intersubband transitions in a 2D electron gas and assume that the origin of the effect is the electron–electron (e–e) collisions. Recently [16, 17], a scheme and channels for the propagation of the external (with respect to the 2D electron gas) perturbation potential in an electronic subsystem, together with the reflection of this perturbation in the form of an experimentally measured relaxation time for collisional broadening, have been considered. It was specifically stated [16, 17] that the destruction of cyclotron orbits (attenuation of the oscillations' amplitudes) is caused by the ionized donors N_D^+ and acceptors N_A^- of residual impurities,

1063-7826/05/3902-0226$26.00 © 2005 Pleiades Publishing, Inc.

growth islands with a height Δ and extent Λ, variations in the mole fraction x of one of the components of the compounds, and so on. Electrons moving laterally in an external electric field "scan" the external potential $V(\mathbf{r}, t)$ and sense it as the spectrum $V_{tot}(\mathbf{q}, \omega)$. Temporal characteristics of the quantization destruction are governed by the totality of the channels for the extension of an external perturbation to the entire 2D electron system from the component that senses this perturbation most effectively. Thus, the external perturbation causing the quantization destruction manifests itself as e–e, intrasubband, and intersubband relaxation. However, it is difficult to unambiguously state that $\tau_q \equiv \tau_{ee}$, where τ_{ee} is the relaxation time of the e–e interaction, since there undoubtedly exists a reasonably effective electron–phonon (e–ph) interaction [6].

In this paper, we discuss experiments with a degenerate 2D electron gas in a separate heterojunction in which two subbands (m and p) of dimensional quantization with the Fermi energies E_m and E_p measured from the bottom of corresponding subband are filled. Direct proofs of the competition between, as well as a change of, the mechanisms of electron–electron interactions as a result of the effects of the temperature and magnetic field on the 2D electron system are obtained. It is ascertained that the effect of increasing temperature is opposite to the effect of increasing the magnetic field.

2. EXPERIMENT AND RESULTS

1. Oscillations of the transverse magnetoresistance and the Hall effect were measured for a number of $Al_{0.28}Ga_{0.72}As$:Si/GaAs heterostructures grown by molecular-beam epitaxy. The structures, which differed only in relation to the doping level, were grown in a single technological run and contained 2D electrons in concentrations ranging from 6×10^{11} to 2×10^{12} cm^{-2} in a quantum well of a separate heterojunction. The samples fabricated using photolithography had the shape of a double Hall bridge with a length and width of 6 and 0.3 mm, respectively. Contacts (In or the GeAu eutectic) to the 2D channel were alloyed in a hydrogen atmosphere or in free space. The measurements were performed at temperatures ranging from 1.65 to 20 K and in magnetic fields as high as 7.4 T. The magnetic-field uniformity over the sample length amounted to 10^{-4} T; furthermore, the broadening of the Landau levels introduced by the field nonuniformity was much smaller than that caused by collisions, temperature, and nonuniform distribution of the doping impurity over the bulk of the ternary compound [14]. The sample temperature was measured using an FeCu–Cu thermocouple and was constantly maintained to within 0.1 K in the temperature range 1 to 20 K. The currents through the samples were chosen in order to eliminate any heating of the 2D electron gas. The results of the oscillation-curve measurements were reproducible on the time scale, as was established in experiments with thermal cycling.

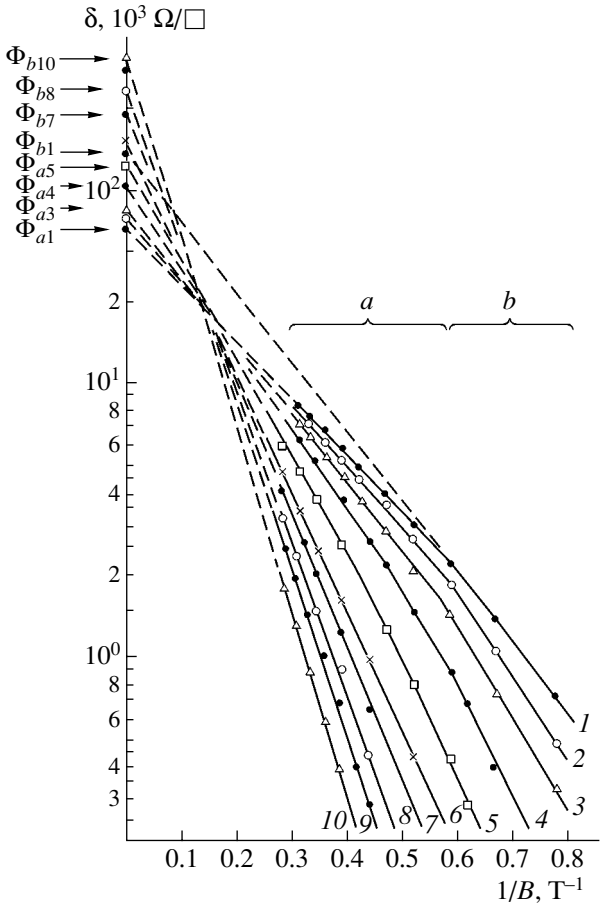

Fig. 1. Magnetic-field dependences of the amplitude of the Shubnikov–de Haas oscillations ρ_{xx}. These dependences illustrate the shift of the poles in the Dingle plots if the extrapolation to $1/B = 0$ is used. A sample of an $Al_{0.28}Ga_{0.72}As$:Si/GaAs heterostructure with the concentrations $n_m = 1.08 \times 10^{12}$ cm^{-2} and $n_p = 1.5 \times 10^{11}$ cm^{-2} was studied. T = (*1*) 1.65, (*2*) 3.03, (*3*) 4.2, (*4*) 5.5, (*5*) 6.8, (*6*) 7.7, (*7*) 8.6, (*8*) 9.0, (*9*) 10.0, and (*10*) 10.9 K.

The parameters of the 2D electrons were determined from measurements of the magnetoresistance oscillations, the Hall effect, and the electrical conductivity. The oscillations were analyzed graphically by the Sladek method [2] and using the Fourier spectra. The magnetic-field and temperature dependences of the oscillation components over the m and p subbands of dimensional quantization for the difference frequency of the oscillations were determined; i.e.,

$$F_{m,p} = \frac{2\pi\hbar}{e} n_{m,p}, \quad F_m - F_p = \frac{2\pi\hbar}{e}(n_m - n_p).$$

2. The magnetic-field dependences of the oscillation amplitudes (the Dingle plots) $\delta(1/B)$ for several temperatures and the extrapolation of these dependences to $1/B = 0$ for characteristic portions of the dependences (a and b) for sample 15 are shown in Fig. 1 (the results

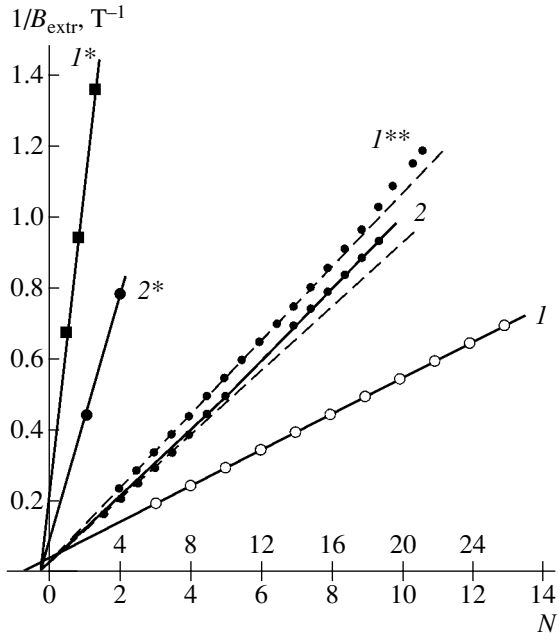

Fig. 2. Positions of the extrema in the magnetoresistance oscillations on the scale $1/B$ for the subbands of dimensional quantization m and p in relation to the Landau level number N at $T = 4.2$ K. For sample 8 (curves *1*, *1**, *1***), $n_m = 9.7 \times 10^{11}$ cm^{-2} and $n_p = 0.61 \times 10^{11}$ cm^{-2}. For sample 15 (curves *2*, *2**), $n_m = 10.8 \times 10^{11}$ cm^{-2} and $n_p = 1.5 \times 10^{11}$ cm^{-2}. The upper scale on the N axis corresponds to curve *1*** and the lower scale corresponds to all other curves.

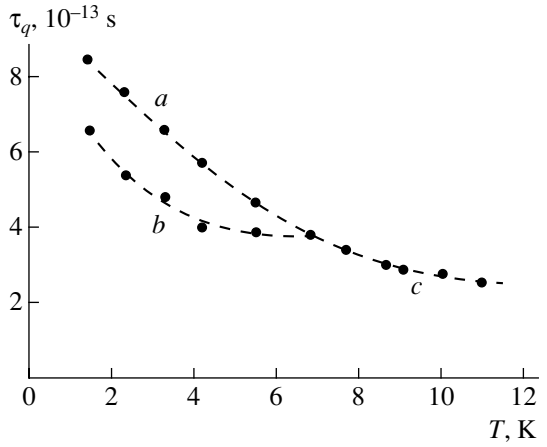

Fig. 3. An example of transformation of the intrasubband (region *a*) and intersubband (region *b*) times for the electron–electron interaction τ_q^a and τ_q^b as the temperature increases into the dependence $\tau_q^c(T)$ in region *c*.

of the Hall measurements at $T = 4.2$ K were $n_s^H = 12.0 \times 10^{11}$ cm^{-2} and $\mu^H = 39.5 \times 10^4$ cm^2/(V s)). The main feature of the experiment consists in the establishment of the family of poles Φ_a and Φ_b for the dependences $\delta(1/B)_{T = \text{const}}$. These poles shift to larger amplitudes independently of each other as the temperature increases. It can be seen by the example of Φ_a (curve *5*) and Φ_b (curve *1*) that the shift of the poles $\Phi_a(T)$ is overbalanced by the system of poles $\Phi_b(T)$. According to Coleridge [5], the poles $\Phi_{a,b}$ of the dependences $\delta(1/B)_{T = \text{const}}$ are related to the probability of electron–electron intrasubband and/or intersubband interactions of the 2D electrons in subbands m and p.

The filling of the m and p subbands also manifests itself in the results of an analysis of the magnetoresistance oscillations. For samples 8 and 15, these results are shown in Fig. 2 (for sample 8, the Hall measurements at $T = 4.2$ K yield $n_s^H = 12.2 \times 10^{11}$ cm^{-2} and $\mu^H = 5.68 \times 10^4$ cm^2/(V s) (the corresponding data for sample 15 were mentioned above)). Dependences of the positions of extrema on a scale of reciprocal magnetic fields ($1/B_{extr}$) on the quantum number N make it possible to determine the electron concentration in subband m (dependences *1* and *2*) and subband p (dependences *1** and *2**). Oscillations at the difference frequency of the dependence $1/B_{extr}$ on N are represented by experimental points that deviate from approximations *2* and *1*** in the region of large quantum numbers ($N > 5$ and $N > 15$ for curves *2* and *1***, respectively).

The Dingle plots $\delta(1/B)_{T = \text{const}}$ of types *1–10* in Fig. 1 were used to determine the dependence $T_D(T)$. Formula (2) was then used to estimate the values of τ_q in relation to temperature for regions *a* and *b* of the magnetic field (Fig. 1). The results of these estimations are shown in Fig. 3. In general, the dependences $\tau_q(T)$ were found to be nonmonotonic. The physical significance of the nonmonotonic behavior of $\tau_q(T)$ has previously been discussed [16, 17] in relation to the hypothesis that there is competition between the intrasubband and intersubband e–e relaxation in a two-subband energy model of the conduction band.

3. DISCUSSION

In region *b* of the magnetic fields (Fig. 1), a certain number of magnetic Landau subbands are found below the Fermi level in both the m and p subbands of dimensional quantization. If the energy gap $\hbar\omega$ between the Landau levels is small and the magnetic fields are moderate, electrons in the m and p subbands interact with each other according to the interband-relaxation time τ_q^{mp}. However, the 2D electrons of both subbands are scattered independently, for example, by remote impurities [5, 13] with the characteristic relaxation times τ_q^m and τ_q^p, respectively. Consequently, the electrons have three independent channels for small-angle scattering with an integrated characteristic time $\tau_q^b = f(\tau_q^m, \tau_q^p, \tau_q^{mp})$ in a magnetic field that belongs to region *b*. As the magnetic field increases (in region *a*), the Landau magnetic

levels shift to beyond the Fermi level. The electrons of subband p are localized at states with $N_p = 0$, 1, and 2, whereas there are Landau sublevels with $N_m \approx 10$ (for $n_m \approx 9 \times 10^{11}$ cm^{-2}) below the Fermi level for the electrons of subband m. In this situation, the efficiency of the intersubband interaction is reduced. One of the plausible causes of this circumstance may be the spatial localization of the electrons in each subband due to the wave functions of the 2D electrons being contracted in the heterojunction plane by a magnetic field. At the same time, one should take into account the spatial separation of the electrons in each subband in a direction perpendicular to the heterojunction. Using both the results of the oscillation analysis and the parameters, such as the doping level $N_{Si} \approx 4.7 \times 10^{17}$ cm^{-2}, the concentration of background impurities $N_A \lesssim 5 \times 10^{15}$ cm^{-3}, and the energy-band offset $\Delta E_C/\Delta E_g = 0.6$, the energy-band diagram $E_C(z)$ of the heterojunction at $T = 4.2$ K for the heterostructure under study was calculated. It was found out that the coordinates for the centroids of the wave functions in the subbands $|\psi_m|^2$ and $|\psi_p|^2$ $\langle z\rangle_m$ and $\langle z\rangle_p$ are separated by ~150 Å [16].

Taking into account the magnetic-field-induced suppression of the channel of intersubband scattering with the characteristic time τ_q^{mp} in region a ($\tau_q^{mp} > \tau_q^m, \tau_q^p$) and the independence of the m and p recombination channels from each other (the characteristic times τ_q^m and τ_q^p), so that $\tau_q^a = f(\tau_q^m, \tau_q^p)$, and using the Matthiessen rule

$$\frac{1}{\tau_q^b} = \frac{1}{\tau_q^a} + \frac{1}{\tau_q^{mp}}, \tag{3}$$

one can obtain the following formula relating τ_q^a to τ_q^b:

$$\tau_q^a = \tau_q^b\left(\frac{\tau_q^{mp}}{\tau_q^{mp} - \tau_q^b}\right). \tag{4}$$

The superscripts in τ_q^a and τ_q^b denote the regions a and b in Fig. 3. Taking into account that $\tau_q^{mp} > \tau_q^b$, we can use (4) to find that $\tau_q^a > \tau_q^b$. This situation corresponds to the experimental data shown in Fig. 3. If the data shown in Fig. 3 are compared with previously reported data [11–13], it is clear that the quantity τ_q^b is governed by the electron–electron interaction in the main (m) subband of dimensional quantization, whereas the quantity τ_q^a is controlled by the electron–electron interaction in subband p. Thus, the relation between the quantities τ_q^a and τ_q^b is consistent with the fact that τ_q^a depends on the quantities τ_q^m and τ_q^p, whereas τ_q^b depends parametrically on three quantities: τ_q^m, τ_q^p, and τ_q^{mp}.

In the samples under study, the position of the Fermi level is in the upper subband $E_p \approx 1$–2 meV; as a result, the degeneracy in this subband is partially removed and the efficiency of the intersubband electron–electron interaction is restored at measurement temperatures (Fig. 3) in the region $T > 4$ K. Thus, an increase in temperature exerts an effect on the electron–electron relaxation that is the opposite of the effect of an increase in the magnetic field, which is confirmed by the data shown in Figs. 1 and 3.

It follows from Fig. 1 that as temperature increases, region b in the dependences $\delta(1/B)_{T = \text{const}}$ extends at the expense of region a. This behavior was previously observed [16] as a shift of the boundary (conditional) between the regions a and b to larger values of B as the temperature increased. Consequently, as temperature increases, the curves a and b in Fig. 3 transform into curve c. The characteristic time τ_q^c is the same as τ_q^b with respect to the relaxation mechanism. However, it is difficult to separate the components τ_q^a, τ_q^b, and τ_q^m in τ_q^p and τ_q^{mp}.

4. CONCLUSION

Qualitative analysis the Shubnikov–de Haas oscillations in a two-band system of 2D electrons shows that there is competition in the channels of the intrasubband and intersubband electron–electron relaxation. The physical significance of the poles $\Phi_{a,b}$ for the dependences $\delta(1/B \longrightarrow 0)_{T = \text{const}}$ is difficult to perceive and, apparently, does not provide important information. Nevertheless, the tendency of the poles to shift provides an unambiguous insight into the dynamics of electron–electron (and, it would appear, electron–phonon) interactions in a system of 2D electrons in a situation where both the energy-spectrum structure and the spatial distribution of the electron density vary under the effect of a strong magnetic field.

The attempts to make the results of the theoretical calculations of $\tau_q(T)$ consistent with the experimental data (Fig. 3) (similarly to [17]) failed. Although the required expressions for τ_q^m, τ_q^p, and τ_q^{mp} were already derived [17], satisfactory agreement between experimental and theoretical values of τ_q (τ_q^{exp} and τ_q^{th}) is attained only if one uses adjustable parameters that do not correspond to the actual energy-band diagram $E_C(z)$ of the heterojunction. It would seem that the characteristic times of inelastic and elastic electron–phonon relaxation via the piezoelectric $\tau_{e\text{-}ph}^{PA}$ and deformation $\tau_{e\text{-}ph}^{DA}$ potentials of acoustic phonons should be included

in τ_q^{th} in a theoretical calculation in addition to the characteristic times of the intraband and interband electron–electron interactions. This mechanism was qualitatively justified by Kadushkin [18]. At the same time, one cannot exclude a combined effect (suppression and/or stimulation) of the temperature and magnetic field on the activity of the primary (with respect to the electron–electron and electron–phonon interactions) sources of the electron-system perturbations: donors N_D^+ and acceptors N_A^- that are far removed from the heteroboundary (including those introduced by an uncontrolled residual impurity), growth islands, and fluctuations of the mole fraction x of Al in the $Al_xGa_{1-x}As$ compound doped with Si.

ACKNOWLEDGMENTS

This study was supported by a program "The Physics of Condensed Matter" of the Russian Academy of Sciences (grant no. 4.15.99), the Ministry of Education of the Russian Federation (grant nos. E-00-3.4-75 and 02-3.4-319), and State contract no. 40.012.1.1.1153 for the Ministry of Industry, Science, and Technology of the Russian Federation.

REFERENCES

1. R. B. Dingle, Proc. R. Soc. London, Ser. A **211**, 517 (1952).
2. R. J. Sladek, Phys. Rev. **110**, 817 (1958).
3. N. S. Averkiev, L. E. Golub, S. A. Tarasenko, and M. Willander, J. Phys.: Condens. Matter **13**, 2517 (2001).
4. D. Shoenberg, *Magnetic Oscillations in Metals* (Cambridge Univ. Press, Cambridge, 1984; Mir, Moscow, 1986).
5. P. Coleridge, Phys. Rev. B **44**, 3793 (1991).
6. D. R. Leadley, R. Fletcher, R. J. Nicholas, *et al.*, Phys. Rev. B **46**, 12439 (1992).
7. R. M. Kusters, F. A. Wittekamp, J. Singleton, *et al.*, Phys. Rev. B **46**, 10207 (1992).
8. R. Fletcher, E. Zaremba, M. D'Iorio, *et al.*, Phys. Rev. B **41**, 10649 (1990).
9. D. McK. Paul and M. Springford, J. Low Temp. Phys. **27**, 561 (1977).
10. R. C. Mani and J. R. Anderson, Phys. Rev. B **37**, 4299 (1988).
11. P. T. Coleridge, Semicond. Sci. Technol. **5**, 961 (1990).
12. S. Yamada and T. Makimoto, Appl. Phys. Lett. **57**, 1022 (1990).
13. F. F. Fang, T. P. Smith III, and S. L. Wright, Surf. Sci. **196**, 310 (1988).
14. V. I. Kadushkin, Fiz. Tekh. Poluprovodn. (Leningrad) **15**, 230 (1981) [Sov. Phys. Semicond. **15**, 134 (1981)]; Fiz. Tekh. Poluprovodn. (Leningrad) **25**, 459 (1991) [Sov. Phys. Semicond. **25**, 277 (1991)]; Fiz. Tekh. Poluprovodn. (St. Petersburg) **26**, 1323 (1992) [Sov. Phys. Semicond. **26**, 739 (1992)].
15. V. I. Kadushkin, Doctoral Dissertation (Moscow Inst. of Engineering Physics, Moscow, 1995).
16. V. I. Kadushkin and F. M. Tsakhaev, Phys. Low-Dimens. Semicond. Struct., No. 1–2, 93 (2000).
17. V. I. Kadushkin and A. B. Dubois, Phys. Low-Dimens. Semicond. Struct., No. 7–8, 1 (2003).
18. V. I. Kadushkin, Fiz. Tekh. Poluprovodn. (St. Petersburg) **38**, 412 (2004) [Semiconductors **38**, 397 (2004)].

Translated by A. Spitsyn

Semiconductors, Vol. 39, No. 2, 2005, pp. 231–234. Translated from Fizika i Tekhnika Poluprovodnikov, Vol. 39, No. 2, 2005, pp. 247–250.

LOW-DIMENSIONAL SYSTEMS

The Effect of Thickness Fluctuations on the Static Electrical Conductivity of a Semiconductor Quantum Wire

M. A. Ruvinskiĭ^ and B. M. Ruvinskiĭ

Stefanyk Precarpathian University, Ivano-Frankivsk, 76000 Ukraine

^e-mail: ruvinsky@il.if.ua

Submitted May 24, 2004; accepted for publication May 24, 2004

Abstract—Expressions for the relaxation time, electron mobility, and static electrical conductivity along a semiconductor quantum wire are derived in relation to a random field of Gaussian fluctuations in the wire's thickness. In the case of nondegenerate statistics for charge carriers at relatively low temperatures (T), electron mobility is given by $u_n \propto T^{1/2}$. In the limiting case of a strong magnetic field H directed along the wire, the factor $H^{-1/2}$ appears in the mobility expression. It is shown that the considered mechanism of charge-carrier relaxation is important for the electrical conductivity of a fairly thin and pure quantum wire at low temperatures. © *2005 Pleiades Publishing, Inc.*

1. Quantization of the electron energy spectrum appreciably restricts the transverse motion of electrons and holes in thin semiconductor wires. These quantum-dimensional restrictions also manifest themselves in the electrical conductivity controlled by a type of mechanism for charge-carrier scattering in quasi-one-dimensional systems, which are of interest for nanoelectronics. Contemporary technologies [1] do not exclude that a random field caused by fluctuations in the thickness of a semiconductor quantum wire can exist. The purpose of this study is to determine the magnitude of the effect of these fluctuations on electrical conductivity and compare this effect to those of other scattering mechanisms reported in previous publications [2–7]. Furthermore, we consider the effect of a quantizing magnetic field that results in additional restrictions being imposed on the transverse motion of the charge carriers.

2. Let us consider a model of a semiconductor quantum wire with transverse sizes that are restricted in thickness d (in the direction of coordinate axis z) by a potential well $V(z)$ with infinitely high walls, and sizes are restricted in width (in the y direction) by a parabolic potential βy^2 ($\beta > 0$). A constant magnetic field **H** is directed along the wire (along the x axis); the components of the magnetic-field vector potential are $A_x = A_y = 0$ and $A_z = Hy$.

In a single-electron approximation [6], the Hamiltonian operator of the system is given by

$$\hat{H} = -\frac{\hbar^2}{2m_\perp}\Delta_\perp + \frac{1}{2m_z}\left(-i\hbar\frac{\partial}{\partial z} + \frac{e}{c}A_z\right)^2 + V(z) + \beta y^2 + U(\mathbf{r}_\perp), \quad (1)$$

where $\Delta_\perp = \partial^2/\partial x^2 + \partial^2/\partial y^2$, $m_\perp = m_x = m_y = m$ and m_z are the effective masses of the conduction electrons in corresponding directions; e is the elementary charge;

$$V(z) = \begin{cases} 0, & -d/2 \le z \le d/2, \\ \infty, & z < -d/2, \quad z > d/2; \end{cases} \quad (2)$$

$$U(\mathbf{r}_\perp) = \alpha[\xi_1(\mathbf{r}_\perp) - \xi_2(\mathbf{r}_\perp)] \quad (3)$$

is the potential energy of an electron in a random field, caused by fluctuations of the wire thickness; $\alpha = \partial E_c/\partial d$; E_c is the bottom of the conduction band; and $\xi_{1,2}(\mathbf{r}_\perp)$ are random functions that specify the amplitudes of the oscillations at different wire surfaces perpendicular to the z axis. We consider interaction (3) of a charge carrier with a random field as a perturbation that gives rise to quantum transitions in the translational motion along the wire (in the direction of the z axis). We restrict the discussion to the contribution of the lower quantum-dimensional energy level of the transverse electron motion to the electrical conductivity. Taking into account the electron states that have certain parity along the z axis, we can write the wave function of the unperturbed problem as

$$\Psi_{k_x}(\mathbf{r}) = \sqrt{\frac{2}{\pi^{1/2}Ldy_0}}\exp\left(ik_x x - \frac{y^2}{2y_0^2}\right)\cos\frac{\pi}{d}z, \quad (4)$$

where L is the quantum-wire length ($L \gg d$) and

$$y_0 = \hbar^{1/2}\left[2m\left(\beta + \frac{e^2H^2}{2m_z c^2}\right)\right]^{-1/4}. \quad (5)$$

1063-7826/05/3902-0231$26.00

The electron energy in state (4) is given by

$$E(k_x) = \frac{\hbar^2 k_x^2}{2m} + \frac{\pi^2\hbar^2}{2m_z d^2} + \hbar\left[\frac{1}{2m}\left(\beta + \frac{e^2H^2}{2m_z c^2}\right)\right]^{1/2}. \quad (6)$$

The reciprocal relaxation time of an electron along the quantum wire in the case of scattering by fluctuation field (3) can be written as

$$\frac{1}{\tau_n(k_x)} = \frac{2\pi}{\hbar} \times \sum_{k_x'} \langle\langle |\langle k_x'|U|k_x\rangle|^2 \rangle\rangle \left(1 - \frac{k_x'}{k_x}\right)\delta[E(k_x) - E(k_x')], \quad (7)$$

where the double brackets $\langle\langle\ldots\rangle\rangle$ signify the averaging over the random field. We assume that fluctuations on different wire surfaces are statistically independent, whereas the fluctuations on a single surface are assumed to be Gaussian; i.e.,

$$\langle\langle \xi_i(\mathbf{r}_{\perp 1})\xi_j(\mathbf{r}_{\perp 2})\rangle\rangle = \delta_{ij}\Delta_i^2 \exp\left[-\frac{(\mathbf{r}_{\perp 1} - \mathbf{r}_{\perp 2})^2}{2\Lambda_i^2}\right], \quad (8)$$

$$\langle\langle \xi_i(\mathbf{r}_\perp)\rangle\rangle = 0, \quad i, j = 1, 2.$$

After calculations using formula (7), and taking into account expressions (3) and (8), we obtain the final result for the relaxation time:

$$\frac{1}{\tau_n(k_x)} = \frac{\alpha^2 m\sqrt{2\pi}}{\hbar^3|k_x|}\sum_{i=1}^{2}\frac{(\Delta_i\Lambda_i)^2}{\sqrt{y_0^2 + \Lambda_i^2}}\exp(-2\Lambda_i^2 k_x^2). \quad (9)$$

3. We use the kinetic Boltzmann equation in the relaxation-time approximation to obtain the following expression for electron conductivity:

$$\sigma_n = \frac{2\hbar^2 e^2}{m^2}\int_0^\infty\left(-\frac{\partial f_0}{\partial\varepsilon}\right)k_x^2\tau_n(|k_x|)dk_x. \quad (10)$$

Here, $f_0 = \{\exp[(\varepsilon_{k_x} - \mu)/k_BT] + 1\}^{-1}$ is the Fermi–Dirac distribution function, $\varepsilon_{k_x} = (\hbar k_x)^2/2m$ is the kinetic energy of the electron motion with effective mass m along the quantum wire, μ is the chemical potential measured from the quantum-dimensional level of the electron motion transverse to the wire, and $2\Sigma_{k_x} f_0(k_x) = N$ is the total number of electrons in the quantum wire.

If the state of the semiconductor quantum wire is nondegenerate, we substitute (9) into (10) and obtain

$$\sigma_n = \frac{\pi e^2\hbar^3 n}{m^2 k_B T(2\pi m k_B T)^{1/2}}\frac{\Phi(-x, 2, a(T))}{4A_1(\Lambda_2^2 - \Lambda_1^2)^2}, \quad (11)$$

where

$$x = \frac{A_2}{A_1}, \quad A_i = \frac{\alpha^2 m\sqrt{2\pi}}{\hbar^3}\frac{(\Delta_i\Lambda_i)^2}{\sqrt{y_0^2 + \Lambda_i^2}} \quad (i = 1, 2); \quad (12)$$

$$a(T) = \frac{\gamma(T) - 2\Lambda_1^2}{2(\Lambda_2^2 - \Lambda_1^2)}, \quad \gamma(T) = \frac{\hbar^2}{2mk_BT}; \quad (13)$$

$$\Phi(-x, 2, a) = \sum_{s=0}^{\infty}\frac{(-1)^s x^s}{(s + a)^2}. \quad (14)$$

Here, $a > 0$, $x \le 1$ [8], and $n = N/L$ are the number of electrons per unit length of the quantum wire.

For $\Lambda_1 = \Lambda_2 = \Lambda$ and arbitrary values of x, we have

$$\sigma_n = \frac{\pi e^2\hbar^3 n}{m^2 k_B T(2\pi m k_B T)^{1/2}}\frac{(A_1 + A_2)^{-1}}{[\gamma(T) - 2\Lambda^2]^2}. \quad (15)$$

Formulas (11)–(15) are valid if $\gamma(T) > 2\Lambda_i^2$ and $[\gamma(T) - 2\Lambda_i^2](\pi/l)^2 \gg 1$, where l is the lattice constant along the wire axis. The first condition is related to the fact that the relaxation time given by (9) increases exponentially as the electron energy increases, whereas the Maxwell distribution decreases exponentially. Therefore, it is important for the scattering by Gaussian fluctuations to be efficient so that the thermal de Broglie wavelength of the charge carrier exceeds the correlation radius Λ_i. The second condition is related to the choice of an infinite upper limit in the integral in (10) and is typically satisfied in the situation under consideration.

At low temperatures, in which case

$$\gamma(T) \gg 2\Lambda^2, \text{ or } k_BT \ll (\hbar^2/4m\Lambda^2), \quad (16)$$

the electron mobility along the quantum wire is given by

$$u_n = \frac{2\sqrt{2\pi}e}{\hbar(A_1 + A_2)\sqrt{m}}(k_BT)^{1/2} \quad (17)$$

and the mechanism of scattering by the thickness fluctuations becomes important for a nondegenerate semiconductor quantum wire at low temperatures ($u_n \propto T^{1/2}$). This temperature dependence of the mobility resembles that in the case of so-called dipole scattering [7] in three-dimensional semiconductors.

At relatively high temperatures, such that

$$k_BT \ge \hbar^2/4m\Lambda^2, \quad (18)$$

or at large radii of fluctuations Λ, the charge-carrier mobility increases drastically; as a result, the mechanism under consideration becomes inefficient compared to scattering by longitudinal acoustic (LA) phonons [3].

The dependences of σ_n and u_n on the longitudinal magnetic field H are related to a contraction of the elec-

tron wave function transverse to the quantum wire (along the y axis) and are specified by the factor

$$A_i(H) \propto [y_0^2(H) + \Lambda_i^2]^{-1/2} \quad (19)$$

(see formulas (12) and (5)). At $y_0^2(H) \gg \Lambda_i^2$ and extremely high magnetic field, $e^2H^2/2m_zc^2 \gg \beta$, which gives rise to the factor $H^{-1/2}$ in the expressions for σ_n and u_n.

Poklonskiĭ *et al.* [3] studied the temperature dependence of the static electrical conductivity of a semiconductor quantum wire in an insulator. They found that this conductivity was caused by an interaction of nondegenerate electrons with LA phonons in the matrix material (if the spreading of the electron wave function in the transverse direction in the absence of a magnetic field is disregarded). In contrast to the relaxation mechanism considered by us, Poklonskiĭ *et al.* [3] obtained the temperature dependence of the electron mobility as $u_n \propto T^{-5/2}$.

The nondegenerate statistics occur at temperatures $T > \pi(\hbar n)^2/2k_Bm$. These temperatures correspond to $T >$ 5.3 K for GaAs with the one-dimensional electron concentration $n = 1.6 \times 10^5$ cm^{-1} and the charge-carrier effective mass $m = 0.067m_0$ [9].

In Fig. 1, we show estimates of the electron mobility $u_n = \sigma_n/en$ (at $H = 0$) in a nondegenerate and relatively pure semiconductor quantum wire when electron scattering by LA phonons [3] (curve *1*) and fluctuations of the quantum-wire thickness according to (15) occurs (curves *2*, *3*) for the following GaAs parameters [9]: the mass density $\rho = 5.3 \times 10^3$ kg/m^3, the longitudinal velocity of sound $v = 5.2 \times 10^3$ m/s, the deformation-potential constant $C = 2.2 \times 10^{-18}$ J [10], the wire thickness $d = 5 \times 10^{-9}$ or 7×10^{-9} m, $\alpha = -\pi^2\hbar^2/md^3$ [11], $\Delta_1 = \Delta_2 = 3 \times 10^{-10}$ m, and $y_0 = \Lambda = 1 \times 10^{-8}$ m.

It follows from Fig. 1 that the mechanism of charge-carrier relaxation at the roughness of the boundaries can be indeed more important than scattering by acoustic phonons at the wire thickness $d \lesssim 7 \times 10^{-9}$ m in the low-temperature region such that $k_BT < \hbar^2/4m\Lambda^2$.

For a nondegenerate system, as well as in the limiting case of low temperatures ($k_BT/\mu \ll 1$), the electrical conductivity along the quantum-wire axis is given by

$$\sigma_n \approx \frac{4e^2}{\hbar^2}\mu[A_1\exp(-2k_F^2\Lambda_1^2) + A_2\exp(-2k_F^2\Lambda_2^2)]^{-1}, \quad (20)$$

where $k_F^2 = (2m/\hbar^2)\mu$. The temperature dependence of σ_n is governed by the chemical potential μ of a one-dimensional electron gas; therefore,

$$\mu(T) \approx \mu_0\left[1 + \frac{\pi^2}{12}\left(\frac{k_BT}{\mu_0}\right)^2\right], \quad (21)$$

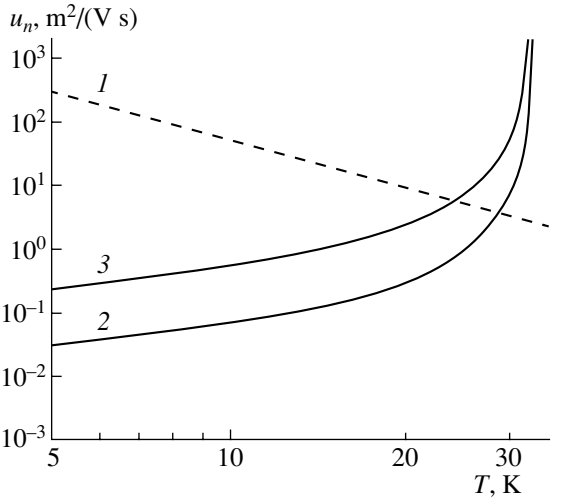

Fig. 1. The electron mobility along a nondegenerate quantum GaAs wire ($H = 0$): (*1*) scattering by LA phonons and (*2*, *3*) scattering by fluctuations in the quantum-wire thickness d with d = (*2*) 5×10^{-9} and (*3*) 7×10^{-9} m.

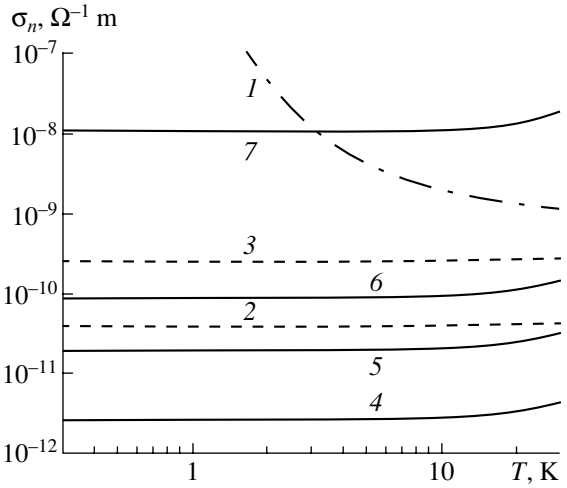

Fig. 2. Electrical conductivity along a degenerate GaAs quantum wire ($H = 0$): (*1*) acoustopiezoelectric scattering; (*2*, *3*) scattering by impurities at μ_{imp} = (*2*) 7.5 and (*3*) 50 m^2/(V s); and (*4*–*7*) scattering by fluctuations in the quantum-wire thickness d at d = (*4*) 5×10^{-9}, (*5*) 7×10^{-9}, (*6*) 9×10^{-9}, and (*7*) 2×10^{-8} m.

$$\mu_0 = \frac{\hbar^2}{8m}(\pi n)^2. \quad (22)$$

In Fig. 2, we show the calculated temperature dependences of electrical conductivity along a degenerate quantum wire based on GaAs in the limiting case of low temperatures for mechanisms of acoustopiezoelectric scattering [4] ($\sigma_{n,\,ph}$, curve *1*), scattering by impurity atoms [4] (σ_{imp}, curves *2* and *3* for the values of the low-temperature mobility in the absence of a magnetic field and the confinement potential μ_{imp} = 7.5 and

50 $m^2/(V\ s)$, respectively), and the considered relaxation mechanism according to formulas (20)–(22) for the wire thickness' $d = 5 \times 10^{-9}$, 7×10^{-9}, 9×10^{-9}, and 2×10^{-8} m (curves *4–7*). This is at the aforementioned values of the parameters for GaAs where the piezoelectric-interaction constant $P = 5.4 \times 10^{-20}$ J^2/m^2 [9] and $k_{F0} = \sqrt{2m\mu_0}/\hbar = 1 \times 10^8$ m^{-1}. In this case, $\sigma_{n,\,ph} \propto [k_F/(4k_F^2C^2 + P)]\exp(2\hbar k_F v/k_B T)$ and $\sigma_{imp} \propto \mu_{imp} k_F^2$ [4]. Optical phonons make a contribution comparable to that of acoustic phonons at $T \gtrsim 50$ K [4]. We do not consider here the localization-type effects [2] that arise in quasi-one-dimensional systems under conditions of a high-degree disorder (or at a high impurity concentration) and that cannot be accounted for in the slight-scattering theory. The temperature dependences of electrical conductivity that are reported in this paper differ significantly from those based on localization theory [2] (in particular, a transition at some temperature T_0 from a power-law dependence at $T > T_0$ to an exponential dependence at $T < T_0$ is characteristic of this theory).

The results obtained (Figs. 1, 2) indicate that the mechanism of charge-carrier scattering by Gaussian fluctuations in the thickness of a semiconductor quantum wire makes an important contribution to its electrical conductivity.

REFERENCES

1. *Nanotechnology*, Ed. by G. Tim (Springer, New York, 1999).
2. Y. Imry, *Introduction to Mesoscopic Physics* (Oxford Univ. Press, Oxford, 2002).
3. N. A. Poklonskiĭ, E. F. Kislyakov, and S. A. Vyrko, Fiz. Tekh. Poluprovodn. (St. Petersburg) **37**, 735 (2003) [Semiconductors **37**, 710 (2003)].
4. H. Bruus, K. Flensberg, and H. Smith, Phys. Rev. B **48**, 11144 (1993).
5. H. Smith and H. Højgaard, *Transport Phenomena* (Oxford Univ. Press, Oxford, 1989).
6. A. I. Anselm, *Introduction to Semiconductor Theory* (Nauka, Moscow, 1978; Prentice Hall, Englewood Cliffs, 1981).
7. B. K. Ridley, *Quantum Processes in Semiconductors*, 4th ed. (Oxford Univ. Press, Oxford, 1999; Mir, Moscow, 1986).
8. A. P. Prudnikov, Yu. A. Brychkov, and O. I. Marichev, *Integrals and Series*, Vol. 1: *Elementary Functions* (Nauka, Moscow, 1981; Gordon and Breach, New York, 1986).
9. J. S. Blakemore, J. Appl. Phys. **53**, R123 (1982).
10. E. E. Mendez, P. J. Price, and M. Heiblum, Appl. Phys. Lett. **45**, 294 (1984).
11. P. K. Basu and P. Ray, Phys. Rev. B **44**, 1844 (1991).

Translated by A. Spitsyn

Semiconductors, Vol. 39, No. 2, 2005, pp. 235–242. Translated from Fizika i Tekhnika Poluprovodnikov, Vol. 39, No. 2, 2005, pp. 251–257.

LOW-DIMENSIONAL SYSTEMS

Selective Electron Transfer between Quantum Dots Induced by a Resonance Pulse

L. A. Openov*^ and A. V. Tsukanov^^**

**Moscow Institute of Engineering Physics, Moscow, 115409 Russia*

^e-mail: opn@supercon.mephi.ru

***Institute of Physics and Technology, Russian Academy of Sciences, Moscow, 117218 Russia*

^^e-mail: tsukanov@ftian.oivta.ru

Submitted April 22, 2004; accepted for publication May 24, 2004

Abstract—A theoretical study of the effect of a resonance electromagnetic pulse on the coherent electron dynamics in a system of tunneling-coupled quantum dots (QDs) arranged in a closed-ring configuration is carried out. It is shown that selective electron transfer between two arbitrary QDs is possible. The transfer probability is calculated as a function of the parameters that characterize the QDs and the electromagnetic pulse. It is shown that this probability can be close to unity. Factors leading to a reduction of the transfer probability in a realistic system are considered. The results obtained can be used for the development of new types of nanoelectronic devices for performing operations with quantum bits. *© 2005 Pleiades Publishing, Inc.*

1. INTRODUCTION

The rapid development of nanotechnologies and the inevitable trend towards the miniaturization of the basic elements of modern microelectronics has resulted in the appearance of a new area of research, physics of low-dimensional structures, with nanoelectronics as one of its branches. In recent years, significant progress has been achieved in fabricating various types of nanostructures and studying their properties [1, 2]. Considerable attention has been attracted to quantum dots (QDs), sometimes referred to as "artificial atoms" [3], which combine properties of real atoms with properties controlled via the fabrication process. In particular, the possibility of using QDs for performing operations with quantum bits (qubits) is being actively discussed (see, e.g., [4–7]). Quantum information can be encoded either in the ground and/or excited states of electrons occupying discrete quantum-confinement levels in the QDs or in the electron-spin degrees of freedom. In future, fabrication of a quantum computer based on solid-state nanostructures seems possible. One of the problems being faced at the current stage of research is the development of methods for manipulating the state of electrons in nanostructures via controlled external actions.

Quantum effects, particularly quantum interference, have a major influence on the characteristics of many kinds of low-dimensional systems. One of the most striking examples is the coherent evolution of single-electron states in a system of two tunneling-coupled QDs under irradiation by a resonance laser pulse. As was shown previously [8, 9], the pulse parameters (frequency, duration, and intensity) can be chosen in such a way that an electron initially occupying the ground state in one of the QDs transfers to an excited state (which is delocalized, i.e., common to both QDs) and then transfers again to the ground state of another QD, where it remains after the end of the pulse. Thus, this excited state acts as a "transit" state. If logic variables 0 and 1 are assigned to the electron states localized in different QDs, the process of electron relocation between the dots corresponds to the quantum NOT logic operation [8–10].

Recently, an attempt has been made to generalize the results obtained in [8] to the case of two QDs to a system where there are a large number of QDs [11, 12]. It was shown that, in a linear chain of QDs it is, in general, rather difficult to perform the selective (addressable) transfer of an electron between two arbitrary QDs. This difficulty is related to the special features of electron excited states in a one-dimensional system with free boundary conditions; more specifically, the problem is caused by the fact that the probability amplitude of finding an electron in a given QD depends heavily on the position of the QD in the chain.

In this study, we show that resonance-pulse-induced selective electron transfer between any two QDs can be attained if the QDs are arranged in a ring-shaped configuration and local electrostatic potentials are applied to the QDs between which the electron is to be transferred. We derive an analytical expression for the transfer probability that takes into account possible differences in the parameters of the QDs and/or electrostatic potentials applied to them, as well as the effect of detuning the laser pulse out of resonance.

1063-7826/05/3902-0235$26.00

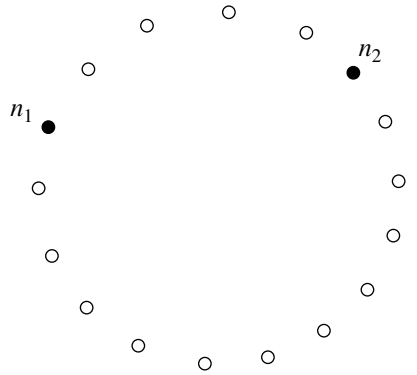

Fig. 1. A schematic layout of a quasi-one-dimensional system of quantum dots arranged in a closed ring. Identical local potentials are applied to the quantum dots n_1 and n_2, between which the electron is selectively transferred.

2. THE MODEL DESCRIPTION AND PROBLEM FORMULATION

Let us consider a system consisting of N identical QDs arranged in a closed-ring configuration (see Fig. 1). We assume that any QD has at least two quantum-confinement levels. One of these levels, with the energy ε_1, corresponds to the ground state $|1\rangle_n$ of the electron localized in a given QD (here, $n = 1, \ldots, N$ labels the number of the QD). If level ε_1 is close to the minimum of the electron potential energy in the region of the QD and the potential barrier separating the QDs is sufficiently high and wide, the ground-state wave functions $\langle \mathbf{r}|1\rangle_n$ are highly localized within the corresponding QDs and there is virtually no overlap between the wave functions of the neighboring QDs. Thus, we may assume, with good accuracy, that the lowest level of the system as a whole is N-fold degenerate with respect to the electron position. We can further assume that, in each QD, the excited level $|2\rangle_n$ (which is not necessarily the first excited level) with energy ε_2 lies close to the top of the potential barrier; consequently, there is a pronounced overlap between the wave functions $\langle \mathbf{r}|2\rangle_n$ of the neighboring QDs. Thus, due to the tunneling coupling between the QDs, this level splits into a subband containing N states, with each of them being extended over the entire system of QDs. Since, below, we make use of the resonance approximation (with respect to the external ac field), we disregard the possible existence of other quantum-confinement levels in the QDs, whose energies differ considerably from ε_1 and ε_2; we "omit" these levels in our enumeration and retain only those that are in resonance or close to resonance.

The Hamiltonian operator for an electron placed in the empty conduction band (in excess to those occupying the filled valence band) in such a QD system can be written as

$$\hat{H}_0 = \varepsilon_1 \sum_{n=1}^{N} \hat{a}^+_{1,n}\hat{a}_{1,n} + \varepsilon_2 \sum_{n=1}^{N} \hat{a}^+_{2,n}\hat{a}_{2,n} - V \sum_{n=1}^{N} (\hat{a}^+_{2,n+1}\hat{a}_{2,n} + \text{h.c.}); \quad (1)$$

here, $\hat{a}^+_{1,n}(\hat{a}_{1,n})$ and $\hat{a}^+_{2,n}(\hat{a}_{2,n})$ are the creation (annihilation) operators of an electron in the ground and excited states of nth QD, respectively; and V is the matrix element of the electron tunneling between the excited states of neighboring QDs (the value of this element can be calculated in each specific case). It should be noted that, since the QDs are arranged in a closed ring, $\hat{a}_{2,N+1} = \hat{a}_{2,1}$; in other words, the boundary conditions are periodic, in contrast to the case of a one-dimensional chain of QDs, where free boundary conditions are appropriate [11, 12]. The spin index is not explicitly included in Hamiltonian operator (1), as we are considering a single-electron problem.

We assume that, at the initial moment ($t = 0$), the electron is localized in the state $|1\rangle_{n_1}$, which is the ground state of the n_1th QD. As the overlap of the ground-state wave functions of the neighboring QDs is not large, the lifetime of an electron in this state, in the absence of external perturbation, is very long (this lifetime increases exponentially with the height and width of the potential barrier between the QDs). We assume that this time is much longer than all other characteristic times in the problem under study, i.e., it may be considered infinite. The goal now is to perform a selective transfer of an electron into the state $|1\rangle_{n_2}$, which is the ground state of the n_2th QD, i.e., to change the electron localization position in the system of QDs.

Let identical local electrostatic potentials be applied to each of the two QDs chosen. Then, the energies of the ground and excited electron states in these QDs are modified ($\varepsilon_1 \longrightarrow \varepsilon_1 + \tilde{U}$, $\varepsilon_2 \longrightarrow \varepsilon_2 + U$), and the Hamiltonian operator appears as

$$\hat{H} = \hat{H}_0 + \tilde{U}(\hat{a}^+_{1,n_1}\hat{a}_{1,n_1} + \hat{a}^+_{1,n_2}\hat{a}_{1,n_2}) + U(\hat{a}^+_{2,n_1}\hat{a}_{2,n_1} + \hat{a}^+_{2,n_2}\hat{a}_{2,n_2}). \quad (2)$$

Here, for the sake of simplicity, we disregard the change in the matrix element V of the electron tunneling from the n_1th and n_2th QDs to the neighboring QDs. This approximation is valid if the local potentials are small, i.e., $|U| \ll V$. In what follows, we assume, for clarity, that $\tilde{U} < 0$ and $U < 0$ (in general, $\tilde{U} \neq U$, although these quantities are of the same order of magnitude). To diagonalize Hamiltonian operator (2), we intro-

duce the operators $\hat{a}_k^+ = \sum_{n=1}^N C_{k,n}\hat{a}_{2,n}^+$ ($k = 1, \ldots, N$) and obtain

$$\hat{H} = \varepsilon_1 \sum_{n=1}^N \hat{a}_{1,n}^+ \hat{a}_{1,n} + \tilde{U}(\hat{a}_{1,n_1}^+ \hat{a}_{1,n_1} + \hat{a}_{1,n_2}^+ \hat{a}_{1,n_2}) + \sum_{k=1}^N E_k \hat{a}_k^+ \hat{a}_k. \quad (3)$$

Here, the energies E_k of the extended excited states and the coefficients $C_{k,n}$ are determined from the following system of equations:

$$E_k C_{k,n} = \varepsilon_1 C_{k,n} - V(C_{k,n-1} + C_{k,n+1}) + UC_{k,n}(\delta_{nn_1} + \delta_{nn_2}), \quad k = 1, \ldots, N, \quad (4)$$

where $C_{k,N+1} = C_{k,1}$. The coefficients $C_{k,n}$ represent the probability amplitude of finding the electron at the kth extended stationary level in the excited state $|2\rangle_n$, which is centered in the nth QD, and satisfy the normalization condition $\sum_{n=1}^N |C_{k,n}|^2 = 1$ for any $k = 1, \ldots, N$.

Expanding $C_{k,n}$ into the Fourier series

$$C_{k,n} = \frac{1}{N}\sum_{m=1}^N C_{k,m} \exp\left(i\frac{2\pi mn}{N}\right),$$

we obtain, from (4), the following relations between C_{k,n_1} and C_{k,n_2}:

$$C_{k,n_1} = A_k C_{k,n_1} + B_k C_{k,n_2}, \quad C_{k,n_2} = B_k^* C_{k,n_1} + A_k C_{k,n_2}. \quad (5)$$

Here,

$$A_k = -\frac{U}{N}\sum_{m=1}^N \frac{1}{E_k - \varepsilon_2 + 2V\cos(2\pi m/N)}, \quad B_k = -\frac{U}{N}\sum_{m=1}^N \frac{\exp[i2\pi(n_1 - n_2)m/N]}{E_k - \varepsilon_2 + 2V\cos(2\pi m/N)}. \quad (6)$$

It follows from (5) and (6) that $|C_{k,n_1}| = |C_{k,n_2}|$ for any level k in the subband of extended excited states. This relation between C_{k,n_1} and C_{k,n_2} will be important for the subsequent discussion. Note that, since the coefficients C_{k,n_1} and C_{k,n_2} can be chosen as real quantities, $C_{k,n_1} = \pm C_{k,n_2}$.

Now, let us assume that an alternating electric field $\mathbf{E}(t) = \mathbf{E}_0\cos(\Omega t)$ is applied to the QD system, and the frequency Ω is close to the difference between the energy E_{tr} of one of the levels $|\text{tr}\rangle$ (which will be referred to below as the transit level) from the subband of extended excited states and the energy $\varepsilon_1 + \tilde{U}$ of the ground state of electrons in QDs n_1 and n_2 (hereafter, we set Dirac's constant $\hbar = 1$). In the resonance approximation [8, 9], the Hamiltonian operator can be written as

$$\hat{H}(t) = \sum_{n=1}^N [\varepsilon_1 + \tilde{U}(\delta_{nn_1} + \delta_{nn_2})]\hat{a}_{1,n}^+ \hat{a}_{1,n} + E_{\text{tr}}\hat{a}_{\text{tr}}^+ \hat{a}_{\text{tr}} - (e/m^*c)\mathbf{A}(t)\sum_{n=1}^N (\mathbf{p}_n \hat{a}_{\text{tr}}^+ \hat{a}_{1,n} + \text{h.c.}) = \sum_{n=1}^N [\varepsilon_1 + \tilde{U}(\delta_{nn_1} + \delta_{nn_2})]\hat{a}_{1,n}^+ \hat{a}_{1,n} + E_{\text{tr}}\hat{a}_{\text{tr}}^+ \hat{a}_{\text{tr}} - \left\{\frac{1}{2}\exp(-i\Omega t)\sum_{n=1}^N \lambda_n \hat{a}_{\text{tr}}^+ \hat{a}_{1,n} + \text{h.c.}\right\}; \quad (7)$$

here, $\mathbf{p}_n = \langle \text{tr}|\hat{\mathbf{p}}|1\rangle_n$ are the matrix elements of the momentum operator, $\mathbf{A}(t)$ is the vector potential (we use the Lorentz gauge with zero scalar potential and ignore the term quadratic in the vector potential), and m^* is the electron effective mass. Taking into account the known relation between the vector potential and the strength of an electric field of frequency Ω and amplitude $\mathbf{E}_0$, we introduced the designation $\lambda_n = -(ie/m^*\Omega)\mathbf{E}_0\mathbf{p}_n$ into (7).

It is worth noting the relation between the values of λ_n and the coefficients $C_{\text{tr},n}$ in the expansion of the extended transit state $|\text{tr}\rangle = \sum_{n=1}^N C_{\text{tr},n}|2\rangle_n$ in states $|2\rangle_n$. From the definitions of λ_n and $\mathbf{p}_n$, we have

$$\lambda_n = -(ie/m^*\Omega)\mathbf{E}_0 \sum_{n'}^N C_{\text{tr},n'_n}^* \langle 2|\hat{\mathbf{p}}|1\rangle_n. \quad (8)$$

Since the wave functions $\langle \mathbf{r}|2\rangle_n$ of the QD excited states are centered around the corresponding QDs and the wave functions $\langle \mathbf{r}|1\rangle_n$ of the QD ground states are highly localized in the QDs, we may put ${}_{n'}\langle 2|\hat{\mathbf{p}}|1\rangle_n = {}_n\langle 2|\hat{\mathbf{p}}|1\rangle_n \delta_{nn'}$; thus, from (8), we obtain $\lambda_n = \lambda C_{\text{tr},n}$, where $\lambda = -(ie/m^*\Omega)\mathbf{E}_0\mathbf{p}$ and $\mathbf{p} = {}_n\langle 2|\hat{\mathbf{p}}|1\rangle_n$.

It should be noted that $\mathbf{p} \neq 0$ (i.e., $\lambda \neq 0$) only if a certain relation between the symmetries of the wave functions $\langle \mathbf{r}|1\rangle_n$ and $\langle \mathbf{r}|2\rangle_n$ is satisfied. For example, $\mathbf{p} = 0$ if both of these functions have an s-type symmetry, while $\mathbf{p} \neq 0$ if one of them has the s-type and the other has a p-type symmetry. Furthermore, the condition that λ be independent of n (necessary to ensure that $|\lambda_{n_1}| = |\lambda_{n_2}|$, which follows from the previously derived equality $|C_{\text{tr},n_1}| = |C_{\text{tr},n_2}|$ and, as we see below, is necessary for increasing the probability of the selective electron transfer between the QDs) requires that vector $\mathbf{p}$ (rather than just its magnitude) be independent of n. This can be the case if, for example, the functions $\langle \mathbf{r}|1\rangle_n$ have the

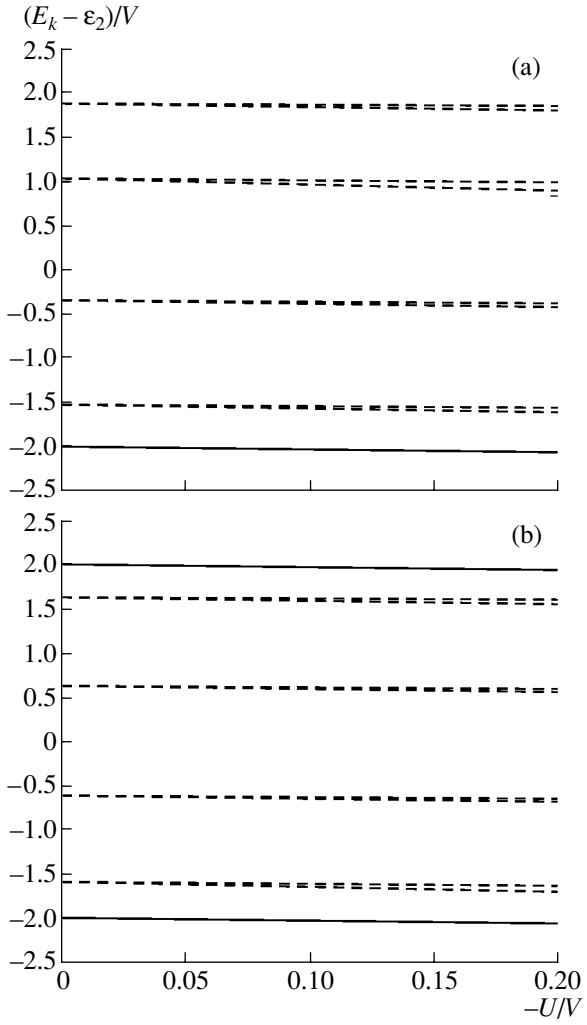

Fig. 2. Typical dependences of the energies E_k of the levels in the extended-state subband in a system of N quantum dots on the value of the shift U of the excited-state energy ε_2 in the dots n_1 and n_2: (a) $N = 9$, $n_1 = 1$, and $n_2 = 4$; (b) $N = 10$, $n_1 = 1$, and $n_2 = 5$. All the energies are measured in units of the matrix element V of the electron tunneling between the excited states of the neighboring quantum dots. The solid and dashed curves correspond to the levels that are nondegenerate and degenerate at $U = 0$, respectively.

s-type symmetry and the functions $\langle \mathbf{r}|2\rangle_n$ have a p_z-type symmetry (where the z axis is oriented perpendicularly to the plane of the QD ring, see Fig. 1); obviously, such a symmetry of the functions $\langle \mathbf{r}|2\rangle_n$ means that $\lambda \neq 0$ only if the vector $\mathbf{E}_0$ has a nonvanishing component along the z axis.

In the resonance approximation, the evolution of the electron state vector

$$|\Psi(t)\rangle = \sum_{n=1}^{N} B_n(t)\exp\{-i[\varepsilon_1 + \tilde{U}(\delta_{nn_1} + \delta_{nn_2})]t\}|1\rangle_n + B_{\text{tr}}(t)\exp(-iE_{\text{tr}}t)|\text{tr}\rangle \quad (9)$$

over time t is determined by the time-dependent Schrödinger equation

$$i\frac{\partial|\Psi(t)\rangle}{\partial t} = \hat{H}(t)|\Psi(t)\rangle \quad (10)$$

with Hamiltonian operator (7). According to the formulation of the problem stated above, the initial conditions have the form $B_n(0) = \delta_{nn_1}$ and $B_{\text{tr}}(0) = 0$. Our goal is to calculate $B_n(t)$ and $B_{\text{tr}}(t)$ as functions of t, thus obtaining $|\Psi(t)\rangle$. The quantities $p_n(t) = |B_n(t)|^2$ are the probabilities of finding the electron in the ground state of the nth QD at the instant t.

The lowest level in the excited-state subband was chosen as the transit level. This choice was motivated by the following considerations. First, the QD excited-state energy ε_2 is close to the top of the potential barrier and, thus, some of the upper levels of the subband may become pushed into the continuum of the energy spectrum. At the same time, the energy of the lowest subband level always becomes smaller than ε_2 and, thus, the corresponding wave function remains localized within the system of QDs (although it is delocalized between different QDs, in contrast to the QD ground-state wave functions). Second, the lowest level of the subband is not degenerate for $U = 0$ and remains nondegenerate for $U \neq 0$. At the same time, the higher levels in the subband are arranged in pairs of degenerate levels (excluding the highest one, but only for even N). For $U \neq 0$, the degeneracy is lifted (Fig. 2), but the spacing between the components of the appearing doublets is small. This means that tuning the laser pulse into resonance with the transit level is difficult if any other level than the lowest one is chosen.

3. RESULTS AND DISCUSSION

Let us define the resonance frequency as $\Omega_r = E_{\text{tr}} - (\varepsilon_1 - \tilde{U})$ and the detuning from the resonance as $\delta = \Omega - \Omega_r$. From (7), (9), and (10), we obtain the following set of differential equations for the coefficients $B_n(t)$ and $B_{\text{tr}}(t)$:

$$\dot{B}_n(t) = i\frac{1}{2}\lambda_n^* B_{\text{tr}}(t)\exp\{i[\delta - \tilde{U}(1 - \delta_{nn_1} - \delta_{nn_2})]t\},$$
$$n = 1, \ldots, N,$$
$$\dot{B}_{\text{tr}}(t) = i\frac{1}{2}\sum_{n=1}^{N}\lambda_n B_n(t) \times \exp\{-i[\delta - \tilde{U}(1 - \delta_{nn_1} - \delta_{nn_2})]t\}, \quad (11)$$

where dots above $B_n(t)$ and $B_{\text{tr}}(t)$ designate partial derivatives with respect to time. Here, we take into account that the states $|1\rangle_n$ and $|\text{tr}\rangle$ are eigenstates of the time-independent Schrödinger equation with eigenvalues of $\varepsilon_1 + \tilde{U}(\delta_{nn_1} + \delta_{nn_2})$ and E_{tr}, respectively.

As the shift $\tilde{U}$ of the energy levels in the QDs caused by the application of local potentials has a finite value, while the detuning δ is small (in an ideal case, $\delta = 0$), it may be assumed that $|\delta| \ll |\tilde{U}|$. In addition, we assume that $|\delta| \ll |\lambda|$ and $|\lambda| \ll |\tilde{U}|$, so that $|\delta| \ll |\lambda| \ll |\tilde{U}|$. Then, it follows from (11) that the characteristic time $\sim 1/|\lambda|$ of the variation in the coefficients $B_{n_1}(t)$, $B_{n_2}(t)$, and $B_{\text{tr}}(t)$ is much longer than the characteristic time $\sim 1/|\tilde{U}|$ of the variation in the coefficients $B_n(t)$ with $n \neq n_1, n_2$. This implies that $|B_{n \neq n_1, n_2}| \sim (|\lambda|/|\tilde{U}|)|B_{n = n_1, n_2}| \ll |B_{n = n_1, n_2}|$. Consequently, when performing summation in (11), we may disregard all the terms except those with $n = n_1$ and $n = n_2$ (more rigorous conditions for the validity of this approximation will be obtained below):

$$\begin{cases} \dot{B}_{n_1}(t) = i\dfrac{\lambda_{n_1}^*}{2} B_{\text{tr}}(t)\exp(i\delta t), \\ \dot{B}_{n_2}(t) = i\dfrac{\lambda_{n_2}^*}{2} B_{\text{tr}}(t)\exp(i\delta t), \\ \dot{B}_{\text{tr}}(t) = i\dfrac{\lambda_{n_1}}{2} B_{n_1}(t)\exp(-i\delta t) + i\dfrac{\lambda_{n_2}}{2} B_{n_2}(t)\exp(-i\delta t), \end{cases} \tag{12}$$

$$\dot{B}_{n \neq n_1, n_2}(t) = i\frac{\lambda_n^*}{2} B_{\text{tr}}(t)\exp[i(\delta - \tilde{U})t]. \tag{13}$$

Thus, the problem of the dynamics of an $(N + 1)$-level quantum system is reduced to a problem of the dynamics of a three-level system, because only states $|1\rangle_{n_1}$, $|1\rangle_{n_2}$, and $|\text{tr}\rangle$ are relevant under resonance or near-resonance conditions. We solved the latter problem for the case $\delta \neq 0$, $|\lambda_{n_1}| = |\lambda_{n_2}|$ [8] and for $\delta \neq 0$, $|\lambda_{n_1}| \neq |\lambda_{n_2}|$ [9]. Formulas for the probabilities $p_n(t)$ of finding the electron at each of the three levels were given in [8, 9] and can be immediately applied to the problem under study. It is found that, for $\delta = 0$, the probability of electron transfer between the QDs is [9]

$$p_{n_2}(t) = \left(\frac{2|\lambda_{n_1}| \cdot |\lambda_{n_2}|}{|\lambda_{n_1}|^2 + |\lambda_{n_2}|^2}\right)^2 \sin^4(\omega_R t), \tag{14}$$

where $\omega_R = \sqrt{|\lambda_{n_1}|^2 + |\lambda_{n_2}|^2}/4$; thus, selective electron transfer between the QDs takes place in a time period $T = \pi/2\omega_R$ if $|\lambda_{n_1}| = |\lambda_{n_2}|$. Deviation of δ from zero and $|\lambda_{n_1}|$ from $|\lambda_{n_2}|$ leads to a decrease in $p_{n_2}(t)$ by $[(|\lambda_{n_1}| - |\lambda_{n_2}|)^2 + (\pi^2/8)\delta^2]/|\lambda_{n_1}|^2$.

In this study, we also take into account the possibility that, due to the imperfection of the technology, the local potentials applied to the two selected QDs may differ from each other (or, which has the same effect, the shape and size of the QDs can be slightly different, which results in a difference between their energy levels and wave functions [9]). We assume that $U_{n_1} \neq U_{n_2}$ and $\tilde{U}_{n_1} \neq \tilde{U}_{n_2}$; then, Eqs. (12) and (13) take the form

$$\begin{cases} \dot{B}_{n_1}(t) = i\dfrac{\lambda_{n_1}^*}{2} B_{\text{tr}}(t)\exp(i\delta t), \\ \dot{B}_{n_2}(t) = i\dfrac{\lambda_{n_2}^*}{2} B_{\text{tr}}(t)\exp[i(\delta - \Delta\varepsilon)t], \\ \dot{B}_{\text{tr}}(t) = i\dfrac{\lambda_{n_1}}{2} B_{n_1}(t)\exp(-i\delta t) \\ \quad + i\dfrac{\lambda_{n_2}}{2} B_{n_2}(t)\exp[-i(\delta - \Delta\varepsilon)t], \end{cases} \tag{15}$$

$$\dot{B}_{n \neq n_1, n_2}(t) = i\frac{\lambda_n^*}{2} B_{\text{tr}}(t)\exp[i(\delta - \tilde{U}_{n_1})t]; \tag{16}$$

here, $\Omega_r = E_{\text{tr}} - (\varepsilon_1 + \tilde{U}_{n_1})$. Furthermore, we designated the difference between the ground-state energies of the n_1th and n_2th QDs as $\Delta\varepsilon = \tilde{U}_{n_1} - \tilde{U}_{n_2}$.

Let us introduce the new variables $B_{n_1}(t)$, $B_{n_2}(t)$, and $B_{\text{tr}}(t)$, which are related to $\tilde{B}_{n_1}(t)$, $\tilde{B}_{n_2}(t)$, and $\tilde{B}_{\text{tr}}(t)$ as

$$\begin{cases} B_{n_1}(t) = \tilde{B}_{n_1}(t)\exp\left(i\dfrac{\Delta\varepsilon}{2}t\right), \\ B_{n_2}(t) = \tilde{B}_{n_2}(t)\exp\left(-i\dfrac{\Delta\varepsilon}{2}t\right), \\ B_{\text{tr}}(t) = \tilde{B}_{\text{tr}}(t)\exp\left(-i\left(\delta - \dfrac{\Delta\varepsilon}{2}\right)t\right). \end{cases} \tag{17}$$

Substituting these quantities into (15), we obtain

$$\begin{cases} \dot{\tilde{B}}_{n_1}(t) + i\dfrac{\Delta\varepsilon}{2}\tilde{B}_{n_1}(t) = i\dfrac{\lambda_{n_1}^*}{2}\tilde{B}_{\text{tr}}(t), \\ \dot{\tilde{B}}_{n_2}(t) - i\dfrac{\Delta\varepsilon}{2}\tilde{B}_{n_2}(t) = i\dfrac{\lambda_{n_2}^*}{2}\tilde{B}_{\text{tr}}(t), \\ \dot{\tilde{B}}_{\text{tr}}(t) - i\left(\delta - \dfrac{\Delta\varepsilon}{2}\right)\tilde{B}_{\text{tr}}(t) = i\dfrac{\lambda_{n_1}}{2}\tilde{B}_{n_1}(t) + i\dfrac{\lambda_{n_2}}{2}\tilde{B}_{n_2}(t). \end{cases} \tag{18}$$

Using the third equation from (18), we express $\tilde{B}_{n_1}(t)$ in terms of $\tilde{B}_{n_2}(t)$, $\tilde{B}_{\text{tr}}(t)$, and $\dot{\tilde{B}}_{\text{tr}}(t)$; using the second equation, we express $\tilde{B}_{\text{tr}}(t)$ in terms of $\tilde{B}_{n_2}(t)$ and

$\dot{\tilde{B}}_{n_2}(t)$. Substituting these expressions into the first equation, we obtain for $\tilde{B}_{n_2}(t)$

$$\dddot{\tilde{B}}_{n_2}(t) - i(\delta - \Delta\varepsilon/2)\ddot{\tilde{B}}_{n_2}(t) + \left[\frac{|\lambda_{n_1}|^2 + |\lambda_{n_2}|^2}{4} + \left(\frac{\Delta\varepsilon}{2}\right)^2\right]\dot{\tilde{B}}_{n_2}(t) - \frac{\Delta\varepsilon}{2}\left[\frac{|\lambda_{n_1}|^2 - |\lambda_{n_2}|^2}{4} + \frac{(\delta - \Delta\varepsilon/2)\Delta\varepsilon}{2}\right]\tilde{B}_{n_2}(t) = 0. \quad (19)$$

Taking into account that $B_{n_1}(0) = 1$ and $B_{n_2}(0) = B_{\text{tr}}(0) = 0$, we use (17) and (18) to obtain the following initial conditions for Eq. (19): $\tilde{B}_{n_2}(0) = \dot{\tilde{B}}_{n_2}(0) = 0$ and $\ddot{\tilde{B}}_{n_2}(0) = -\lambda_{n_1}\lambda^*_{n_2}/4$.

Equation (19) can be solved exactly. However, the solution is very cumbersome, since it includes the roots of a third-order algebraic equation. Thus, we present the solution for the most interesting case of $|\delta|/|\lambda|$, $|\Delta\varepsilon|/|\lambda|$, and $|\Delta\lambda|/|\lambda| \ll 1$ (here, $\Delta\lambda = |\lambda_{n_1}| - |\lambda_{n_2}|$), which is accurate to terms of the second order (inclusive) in these small parameters:

$$B_{n_2}(t) = -\frac{\lambda_{n_1}\lambda^*_{n_2}}{|\lambda_{n_1}|^2 + |\lambda_{n_2}|^2 + (\Delta\varepsilon)^2}\exp\left(-i\frac{\Delta\varepsilon|\lambda_{n_2}|^2}{|\lambda_{n_1}|^2 + |\lambda_{n_2}|^2}t\right) \times\left\{1 - \left[\cos(2\omega_R t) - i\frac{\tilde{\delta}}{4\omega_R}\sin(2\omega_R t)\right]\exp\left(i\frac{\tilde{\delta}t}{2}\right)\right\}, \quad (20)$$

where

$$\tilde{\delta} = \delta - \frac{\Delta\varepsilon}{2} + \frac{3}{2}\Delta\varepsilon\frac{|\lambda_{n_2}|^2 - |\lambda_{n_1}|^2}{|\lambda_{n_1}|^2 + |\lambda_{n_2}|^2},$$

$$\omega_R = \frac{1}{4}\sqrt{|\lambda_{n_1}|^2 + |\lambda_{n_2}|^2 + \tilde{\delta}^2 + (\Delta\varepsilon)^2}.$$

For the probability of electron transfer between the QDs, we obtain

$$p_{n_2}(t) = |B_{n_2}(t)|^2 = \left(\frac{2|\lambda_{n_1}|\cdot|\lambda_{n_2}|}{|\lambda_{n_1}|^2 + |\lambda_{n_2}|^2}\right)^2 \times\left[\sin^4(\omega_R t) + \sin^2\left(\frac{\tilde{\delta}t}{4}\right)\cos(2\omega_R t) + \frac{\tilde{\delta}^2}{64\omega_R^2}\sin^2(2\omega_R t) - \frac{\tilde{\delta}}{8\omega_R}\sin\left(\frac{\tilde{\delta}t}{2}\right)\sin(2\omega_R t)\right]. \quad (21)$$

For $\Delta\varepsilon = 0$, this expression coincides with that previously derived by us for a nanostructure composed of two QDs [9]. An analysis shows that, for $|\delta|/|\lambda|$, $|\Delta\varepsilon|/|\lambda|$, and $|\Delta\lambda|/|\lambda| \ll 1$, the largest value

$$p_{n_2}^{\max} \approx 1 - [(\Delta\lambda)^2 + (\Delta\varepsilon)^2 + (\pi^2/8)(\delta - \Delta\varepsilon/2)^2]/|\lambda|^2 \quad (22)$$

is attained, similarly to the case $\Delta\varepsilon = 0$ [9], in a time period $T = \pi/2\omega_R$.

If the probabilities of finding the electron in the n_1th and n_2th QDs at the initial point in time have the arbitrary values $B_{n_1}(0) = \alpha$ and $B_{n_2}(0) = \beta$ (with the only limitation being that $|\alpha|^2 + |\beta|^2 = 1$, i.e., $B_{n\neq n_1, n_2}(0) = B_{\text{tr}}(0) = 0$), then, for an "ideal" structure ($\Delta\varepsilon = \Delta\lambda = 0$) under exact resonance conditions ($\delta = 0$), we obtain $B_{n_1}(T) = -\beta$ and $B_{n_2}(T) = -\alpha$. Thus, if the states of the electron localized in the two different QDs $|1\rangle_{n_1}$ and $|1\rangle_{n_2}$ are considered as the Boolean states $|0\rangle$ and $|1\rangle$, respectively, so that their linear combination represents a quantum bit (qubit), the effect of a resonance pulse of duration T is equivalent to the implementation of the unitary quantum NOT operation accompanied by a change of the net qubit phase by π:

$$\hat{U}_{\text{ideal}}(T)|\Psi(0)\rangle = \hat{U}_{\text{ideal}}(T)\begin{pmatrix}\alpha\\ \beta\end{pmatrix} = |\Psi(T)\rangle = \begin{pmatrix}\beta\\ \alpha\end{pmatrix}\exp(i\pi). \quad (23)$$

For nonvanishing values of δ, $\Delta\varepsilon$, and $\Delta\lambda$, the deviation of the fidelity in this operation $F = |\langle\hat{U}_{\text{ideal}}(T)\Psi(0)\,\hat{U}(T)\Psi(0)\rangle|^2 = |-\beta^* B_{n_1}(T) - \alpha^* B_{n_2}(T)|^2$ from unity is measured by small terms on the order of $|\delta|/|\lambda|$, $|\Delta\varepsilon|/|\lambda|$, and $|\Delta\lambda|/|\lambda|$.

Let us now discuss the validity of the approximation made above, when we disregarded the terms $B_{\text{tr}}(t)$ in Eq. (11) for $B_{n\neq n_1, n_2}(t)$, in more detail. Substituting expression $B_{\text{tr}}(t) = i(\lambda_{n_1}/4\omega_R)\sin(2\omega_R t)$, which follows from (18) for $\delta = \Delta\varepsilon = \Delta\lambda = 0$, into (16) and setting $\tilde{U}_{n_1} = \tilde{U}_{n_2} = \tilde{U}$, we find, for $|\tilde{U}| \gg |\lambda|$, that

$$B_{n\neq n_1, n_2}(t) \approx -i\frac{\lambda_{n_1}\lambda^*_n}{8\omega_R\tilde{U}}\sin(2\omega_R t)\exp(-i\tilde{U}t), \quad (24)$$

where the initial conditions $B_{n\neq n_1, n_2}(0) = 0$ were taken into account. Recalling that $\lambda_n = \lambda C_{\text{tr}, n}$ (where $C_{\text{tr}, n}$

are the coefficients in the expansion of the extended transit state $|\mathrm{tr}\rangle$ in the electron excited states $|2\rangle_n$ in different QDs) and taking into account that $|C_{\mathrm{tr},n_1}| \approx |C_{\mathrm{tr},n_2}|$ for $U_{n_1} \approx U_{n_2}$, we obtain

$$|C_{\mathrm{tr},n_1}|\frac{|\tilde{U}|}{|\lambda|} \gg \sum_{n\neq n_1,n_2}^{N} |C_{\mathrm{tr},n}|^2. \quad (25)$$

If the number of QDs in the system is relatively large ($N \gg 1$) and $|\tilde{U}| \ll V$, we have $|C_{\mathrm{tr},n_1}| \approx N^{-1/2}$ and $\sum_{n\neq n_1,n_2}^{N}|C_{\mathrm{tr},n}|^2 \approx 1$. Thus, condition (25) takes the form

$$|\tilde{U}|/|\lambda| \gg N^{1/2}. \quad (26)$$

This imposes a strict limitation on the possible difference between $\tilde{U}_{n_1}$ and $\tilde{U}_{n_2}$, which may result from the difference in the QD sizes [9] and/or in the values of the potentials applied to them. Indeed, to ensure that the probability of the selective electron transfer is close to unity, it is necessary that $|\Delta\varepsilon| = |\tilde{U}_{n_1} - \tilde{U}_{n_2}| \ll |\lambda|$ (see (22)). However, it then follows from (26) that, even for $N \sim 10$, the values of $\tilde{U}_{n_1}$ and $\tilde{U}_{n_2}$ must coincide with an accuracy of ~1%. This restriction, along with the necessity of the condition $|\Delta\lambda|/|\lambda| \ll 1$ (see (22)), means that the QDs must be nearly identical.

With the current technological level, fabricating a structure consisting of a large number of virtually identical QDs arranged in a regular configuration with respect to each other would appear rather problematic. In this context, it is worth mentioning another physical system where implementation of the effect studied in this paper is possible: a system of phosphorus donor atoms in silicon [13, 14]. The technique for a controlled implantation of P atoms into silicon [14] enables the formation of quite complicated configurations, in which, similarly to the QDs, P donors play the role of electron localization centers. All the "natural" atoms, in contrast to the "artificial" ones (QDs), are identical, and differences caused by the matrix distortion during the implantation can be minimized, for example, by an appropriate annealing. If, in a system of N donor atoms, $N - 1$ of them are ionized, the state of the remaining electron is described in terms of the single-particle model considered in this paper.

As the evolution of the electron states under the application of an external pulse takes place within a solid rather than in a free space, the inevitable interaction of the electron with its surroundings may result in the disruption of the unitary evolution. In particular, relaxation and dephasing processes originating from the interaction of electrons with acoustic phonons [15] are important. This imposes significant limitations on the parameters of the structure and the materials used for its fabrication. A detailed discussion of the decoherence effects in the structure under consideration is beyond the scope of this study.

4. CONCLUSION

In this paper, we considered a single-electron model of a nanostructure consisting of tunneling-coupled QDs and investigated the effect of a selective resonance transfer of the electron between two arbitrary QDs under the effect of a laser pulse. The probability amplitudes of finding the electron in the ground states of these two QDs at any instant of time are determined as functions of the parameters characterizing the structure and the laser pulse. It is shown that the probability of finding the electron in the ground state of the second QD can be close to unity. If logic values of 0 and 1 are assigned to the states of the electron localized in different QDs, the effect of the resonance pulse on an arbitrary linear combination of these states (a qubit) is equivalent to performing the quantum NOT operation accompanied by a change of the net phase by π.

We believe that a scheme of selective electron transfer utilizing an extended "transit" state, as proposed in this paper, is more advantageous than the scheme of sequential electron transfer between neighboring QDs discussed recently [16], as the operation is performed in a single step in the former case. All of the results obtained in this study can be equally applied to a description of the electron behavior in a system of P donor atoms in silicon, as well as in other systems of this kind, consisting of a large number of regularly arranged electron localization centers (e.g., atoms on the surface).

ACKNOWLEDGMENTS

We are grateful to K.A. Valiev for his interest in this study and S.A. Dubovis for his help at its initial stage.

REFERENCES

1. D. M. Eigler and E. K. Schweizer, Nature **344**, 524 (1990).
2. J. P. Dowling and G. J. Milburn, quant-ph/0206091 (2002).
3. L. Jacak, P. Hawrylak, and A. Wójs, *Quantum Dots* (Springer, Berlin, 1998).
4. A. Barenco, D. Deutsch, and A. Ekert, Phys. Rev. Lett. **74**, 4083 (1995).
5. D. Loss and D. DiVincenzo, Phys. Rev. A **57**, 120 (1998).
6. M. S. Sherwin, A. Imamoglu, and T. Montroy, Phys. Rev. A **60**, 3508 (1999).
7. X.-Q. Li and Y. Arakawa, Phys. Rev. A **63**, 012302 (2001).

8. L. A. Openov, Phys. Rev. B **60**, 8798 (1999).
9. A. V. Tsukanov and L. A. Openov, Fiz. Tekh. Poluprovodn. (St. Petersburg) **38**, 94 (2004) [Semiconductors **38**, 91 (2004)].
10. J. H. Oh, D. Ahn, and S. W. Hwang, Phys. Rev. A **62**, 052306 (2000).
11. A. A. Larionov, Quantum Comput. Comput. **3**, 46 (2002).
12. A. V. Tsukanov, Quantum Comput. Comput. **3**, 92 (2002).
13. L. C. L. Hollenberg, A. S. Dzurak, C. Wellard, *et al.*, Phys. Rev. B **69**, 113301 (2004).
14. A. S. Dzurak, L. C. L. Hollenberg, D. N. Jamieson, *et al.*, cond-mat/0306265 (2003).
15. L. Fedichkin and A. Fedorov, Phys. Rev. A **69**, 032311 (2004).
16. J. M. Villas-Boas, Sergio E. Ulloa, and Nelson Studart, cond-mat/0403447 (2004).

Translated by M. Skorikov

Semiconductors, Vol. 39, No. 2, 2005, pp. 243–248. Translated from Fizika i Tekhnika Poluprovodnikov, Vol. 39, No. 2, 2005, pp. 258–263.

LOW-DIMENSIONAL SYSTEMS

Optical Properties of Porous Nanosized GaAs

A. I. Belogorokhov*^, S. A. Gavrilov, I. A. Belogorokhov***, and A. A. Tikhomirov****

**State Research Institute for Rare-Metals Industry, Moscow, 119017 Russia*

^e-mail: belog@mig.phys.msu.su

***Moscow State Institute of Electronic Engineering (Technical University), Zelenograd, Moscow oblast, 103498 Russia*

****Moscow State University, Vorob'evy gory, Moscow, 119899 Russia*

Submitted March 30, 2004; accepted for publication June 3, 2004

Abstract—The optical properties of porous GaAs layers obtained by electrochemical etching of single-crystal *n*- and *p*-GaAs(100) wafers are studied. It is shown that the shape of the nanocrystals, their mean diameter, and their surface states depend on the conductivity type of the initial crystal. A shift of the peaks corresponding to the main optical phonons to lower frequencies in the Raman spectra is observed. Surface-phonon frequencies determined from the Raman spectra coincide with those determined from the reflection spectra in the infrared spectral region. The forms of the spectral dependences of the reflection coefficient in the phonon-resonance region in bulk GaAs differ from those in porous GaAs. This is caused by the appearance of additional oscillators related to spatially confined lattice vibrations in GaAs nanocrystals. Atomic-force microscopy is used to study the surface morphology of porous GaAs samples formed on the *n*-GaAs substrates, and a nanosized surface profile is observed. Estimations made for the mean diameter of GaAs nanocrystals based on data from the Raman scattering, infrared spectroscopy, photoluminescence, and atomic-force microscopy yield results that are in good agreement with each other. *© 2005 Pleiades Publishing, Inc.*

1. INTRODUCTION

GaAs structures with reduced dimensionality (such as, for example, quantum wires and quantum dots) are attracting increasing attention both as objects of basic research [1, 2] and as promising materials for the fabrication of devices with new operational capabilities that cannot be attained using traditional semiconducting materials [3]. For example, the use of porous GaAs (*por*-GaAs) as a substrate material for the growth of epitaxial GaN layers by molecular-beam epitaxy has made it possible to obtain continuous GaN layers that have a cubic modification [4]. Vapor-phase epitaxy from metal-organic compounds has also been used to obtain single-crystal GaAs, AlGaAs, and InGaAs layers on *por*-GaAs substrates [5].

An apparently promising approach is to obtain various porous semiconducting materials using electrochemical etching. This method has a number of advantages: it is fairly simple and inexpensive, and, in the case of a positive result, it would become possible to extend the spectral range of luminescence electronics and fabricate new types of light-emitting diodes. In addition, the use of porous materials as intermediate layers would allow the fabrication of new types of heterojunctions. Attempts undertaken in this line of research showed that the problem under investigation could be solved successfully [4, 6, 7]. However, until now, only few publications have been concerned with the production of nanosized porous GaAs [2, 5, 8]. Unfortunately, the data reported in these publications are sometimes contradictory, and data on the dynamics of the nanocrystal lattice that forms the porous GaAs layers are generally lacking.

2. EXPERIMENTAL

Porous GaAs structures were formed on single-crystal GaAs (100) substrates doped either with zinc (*p*-type conductivity, $N_{Zn} \approx (1–5) \times 10^{18}$ cm^{-3}) or with silicon (*n*-type conductivity, $N_{Si} \approx 10^{16}–10^{17}$ cm^{-3}) using electrochemical etching. The electrolyte composition was $HF : H_2O : HNO_3 = 39 : 59 : 2$. In some cases, diluted hydrochloric acid was added to the electrolyte. Electrochemical etching was performed in darkness for 5–15 min; the density of the constant current flowing through the electrolyte was 20–25 mA/cm^2.

The Raman spectra were obtained in the backscattering geometry, with the pump radiation produced by an Ar^+ laser at wavelengths of 488 and 514.5 nm. The experimental setup included a Jobin-Yvon T64000 double monochromator and a GaAs photomultiplier cooled to 77.3 K. An Olympus electron-diffraction microscope was used to study the microstructure of the samples. The laser beam was focused on the sample surface in the form of a spot with a diameter of 3 μm. As a result, the power density of laser radiation incident on the sample under study also increased. In order to avoid any irreversible thermal effects on the sample, or its degradation, we varied the pump power of the Ar^+ laser from 1 to 100 mW. A CCD camera combined with the microscope made it possible to visually observe (using a display) the state of the sample surface

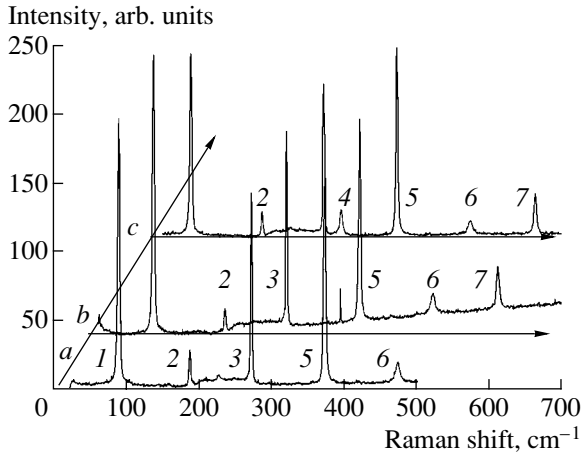

Fig. 1. The Raman spectra of the porous *n*-GaAs samples. The sample numbers are (*a*) 2, (*b*) 4-2, and (*c*) 4.

in the course of recording the Raman spectra. This method of measurement is known as micro-Raman.

Optical spectra in the infrared spectral region (FTIR) were measured at room temperature using an IFS-113v Fourier spectrometer (Bruker, Germany) in the frequency range ω = 10–700 cm^{-1} with a spectral resolution of no worse than 0.2 cm^{-1}. The obtained spectral dependences of the reflection coefficient $R(\omega)$ were processed using a combined approach based on the Kramers–Kronig relations, a dispersion analysis [9], and a genetic algorithm.

The surface microstructure and morphology were studied using a JEOL 840A scanning electron microscope (SEM) equipped with a LINK system for elemental analysis. The surface topography was studied using a Solver P47 atomic-force microscope (NT-MDT Corp.).

3. RAMAN SCATTERING

When interpreting the Raman spectra of *por*-GaAs samples, it is very important to have data on the chemical composition of the nanocrystals' surface. On the basis of the data obtained using X-ray photoelectron spectroscopy (XPS), we concluded that the [Ga] : [As] ratio in the samples under study was approximately equal to unity; i.e., the stoichiometry of the material was preserved. In addition, chlorine was detected on the surface; however, it was found in amounts of no larger than 3 at %. Ga_2O_3-, $GaCl_3$-, $AsCl_3$-, and As_2O_3-type chemical compounds can be formed on the surface of GaAs nanocrystals as a result of an electrochemical-treatment reaction. A comprehensive consideration of XPS data, laser mass analysis, and data on the surface morphology (according to the results obtained using scanning electron microscopy) suggested that, from the list of aforementioned compounds, only the As_2O_3 crystallites of diamond-like shape can be present on the surface of some of the studied *por*-GaAs samples.

High-intensity narrow peaks arranged almost equidistantly were observed in the Raman spectra of a number of porous structures formed on the *n*-type substrates. As an example, Fig. 1 shows the Raman spectra of three samples of porous *n*-GaAs. Peaks *3* and *4* correspond to the frequencies of the transverse (ω_{TO}) and longitudinal (ω_{LO}) optical GaAs phonons that are active in the Raman spectra of both crystalline and porous GaAs modifications. In the case of crystalline GaAs, these vibration modes should be located at frequencies of 268.5 cm^{-1} (TO) and 292.3 cm^{-1} (LO). In the case of *por*-GaAs, the phonon Raman lines are broadened and shifted to lower frequencies than those in crystalline GaAs. Lockwood *et al.* [1] studied the Raman spectra of the As_2O_3 and Ga_2O_3 chemical compounds in order to identify the remaining peaks: *1, 2*, and *5–7*. It was noticed [1] that As_2O_3 and Ga_2O_3 did not exhibit photoluminescent properties; at the same time, high-intensity peaks at 85, 183, 268, 369, 414, 471, and 560 cm^{-1} were observed in the Raman spectra of As_2O_3. In the case of Ga_2O_3, Raman peaks at 201, 418, and 769 cm^{-1} were observed. As can be seen from Fig. 1, resonance vibrations corresponding to As_2O_3 were observed in the Raman spectra of a number of porous *n*-GaAs samples we studied. We failed to detect traces of Ga_2O_3. It can also be seen from Fig. 1 that an increase in the intensity of background radiation at frequencies higher than 200 cm^{-1} was observed in the Raman spectrum of sample 4-2. This effect is related to the photoluminescence (PL) signal that appeared in this sample. No additional Raman peaks were observed in this case, which indicates that the physicochemical state of the nanocrystals' surface remained unchanged; thus, we may conclude that the effects of dimensional quantization play a decisive role in the appearance of the PL signal in the visible spectral region for the sample under consideration. In the fabrication of sample 4-2, the current density was 20% higher than that in the fabrication of sample 4. If we further increase the current that flows through the sample in the course of electrochemical etching, the electropolishing mode sets in rapidly, which, in turn, leads to a drastic decrease in the thickness of the porous film and, ultimately, to its complete disappearance.

The XPS data, and also the data from spectrometric and SEM analyses, show that As_2O_3 crystallites are not formed at the surface of pores in the *p*-GaAs samples, in contrast to what was observed for some samples of porous *n*-GaAs. At the same time, the total number of oxygen atoms involved in the formation of oxide bonds at the nanocrystals' surface was found to be almost the same in the porous *n*- and *p*-GaAs samples. It is worth noting that the PL intensity in the samples of porous *p*-GaAs is much lower than that in the samples of porous *n*-GaAs and the position of the PL peak is shifted to the red region of the spectrum. The structure of the porous *p*-GaAs layer is less homogeneous, and the nanocrystals' sizes range from 10 nm to several hundreds of nanometers. In the case of *n*-GaAs, the nanoc-

rystals' sizes are smaller and the variance of their mean diameter is determined from the PL peak position E_{max} using the approach described previously in [2]. The PL peak for the porous *n*-GaAs samples was located at photon energies of 1.85–2.52 eV, which corresponded to nanocrystal sizes ranging from 5 to 8 nm. In addition, similar estimates were obtained using the shift in frequency of the main optical phonons in the Raman spectra of *por*-GaAs and using AFM. For example, it can be seen from Fig. 2, where the Raman spectrum of porous *n*-GaAs free of As_2O_3 is shown, that the peak corresponding to the scattering of photons by longitudinal optical phonons in *por*-GaAs is shifted by $\Delta\omega \approx 1.6$ cm^{-1} to lower frequencies compared to the case of bulk GaAs. If the value of $\Delta\omega$ is known, we can estimate the mean diameter of the nanocrystals that form the porous *n*-GaAs layer in the sample under consideration. As a result, we obtained the value $d \approx 5.9$ mm for nanocrystals' diameter, which is consistent with the estimate obtained for the same sample using the PL data ($d \approx$ 6.3 nm, $E_{max} = 2.12$ eV).

In addition to the optical phonons confined in the nanocrystals' bulk, surface optical (SO) phonon modes were observed in the Raman spectra of the *por*-GaAs samples. In order to estimate the frequencies of the SO phonon modes, we performed calculations in the context of the approach outlined by Enderlein [10]. In particular, we used the following relations for determining the sought-for frequencies:

$$\omega_{SO}^2 = \omega_{TO}^2 + \omega_p^2 \frac{\varepsilon_\infty}{\varepsilon_\infty + \eta_m(r)}, \quad (1)$$

$$\eta_m(r) = -\frac{I_m'(r)K_m(r)}{I_m(r)K_m'(r)}. \quad (2)$$

Here, r is the nanocrystal radius, $I_m(r)$ is the cylindrical function, ω_p is the plasma frequency, and ε_∞ is the relative high-frequency dielectric constant. For the *por*-GaAs sample whose Raman spectrum is shown in Fig. 2, the frequency of the SO phonon mode was found to be equal to $\omega_{SO} = 284$ cm^{-1} (the SO mode is indicated by the arrow in the inset in Fig. 2). This value was obtained using a procedure in which the LO peak was decomposed into the constituent Gaussian functions. The following values of the GaAs parameters were used in the calculations: $\varepsilon_\infty = 11.2$, $\omega_{TO} = 268.5$ cm^{-1} [11], and $d \approx 6$ nm. The theoretical estimate of ω_{SO} virtually coincides with the obtained value.

4. INFRARED SPECTROSCOPY

Information about the topology of the *por*-GaAs samples can be obtained by analyzing the structure of the FTIR spectra. To this end, one can use the expression for the dielectric constant of a composite material [12]. In this situation, it is necessary to consider two plausible variants. In the first case, we are dealing with GaAs nanocrystals that are extended in the same direction,

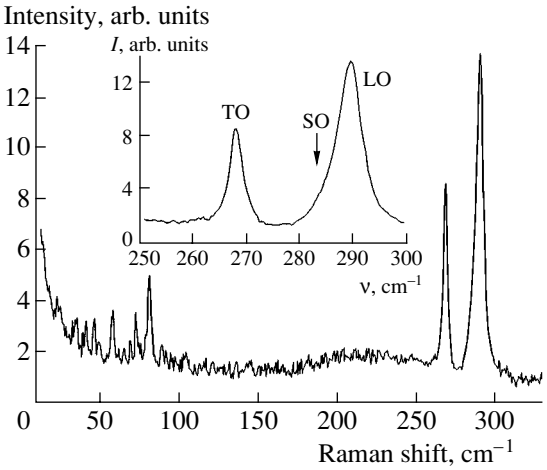

Fig. 2. The Raman spectra of a *por*-GaAs:Si sample. The spectral region where the TO and LO phonons manifest themselves is shown in the inset. The arrow indicates the location of the surface optical (SO) phonon mode.

have a radius r, and are surrounded by free space. We then have the following expression for the dielectric-constant tensor:

$$\varepsilon_{xx} = \varepsilon_{yy} = \frac{\varepsilon + 1 + C(\varepsilon - 1)}{\varepsilon + 1 - C(\varepsilon + 1)}. \quad (3)$$

Here, ε is the relative low-frequency dielectric constant. In the second case, where the porous layer consists of pores that have a radius r and thread through the crystalline GaAs matrix, the expression, which is similar to (3), is written as

$$\varepsilon_{xx} = \varepsilon_{yy} = \varepsilon\frac{2 + C(\varepsilon - 1)}{2 - C(\varepsilon + 1)}. \quad (4)$$

In both cases,

$$\varepsilon_{zz} = 1 + C(\varepsilon - 1). \quad (5)$$

The constant $C = \pi R^2 N$ specifies the fraction of crystalline GaAs in the porous-layer volume (the so-called filling factor). The frequency dependence of the tensor of dielectric function ε can be expressed as

$$\varepsilon(\omega) = \varepsilon_\infty\left(\frac{\omega^2 - \omega_{LO}^2}{\omega^2 - \omega_{TO}^2} - \frac{\omega_p^2}{\omega^2}\right). \quad (6)$$

The results of calculations performed using formulas (3)–(6), as well as the experimental reflection spectrum $R(\omega)$ for a sample of porous GaAs, are shown in Fig. 3. Comparing the theoretical and experimental data, we may conclude that the porous layer consists mainly of GaAs nanocrystals. For the sample under consideration, the filling factor, which is proportional to the sample's porosity, was found to be equal to $C = 0.75$. It is worth noting that a cylindrical configuration of the nanocrystals was assumed in the calculations; however, it is difficult to justify this assumption in the case under con-

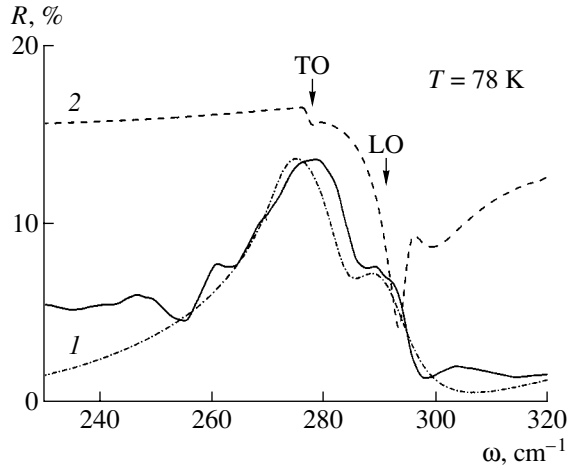

Fig. 3. The reflection spectrum of *por*-GaAs in the region of lattice vibrations (the solid line) at T = 78 K. Spectral dependences *1* and *2* represent the results of calculations for the case of (*1*) quantum wires and (*2*) extended pores.

sideration. Usually, crystallites of pyramidal shape are formed on the GaAs surface as a result of etching. Nevertheless, as can be seen from Fig. 3, satisfactory agreement between the experimental data and the results of the calculations is observed.

It can also be seen from Fig. 3 the dependence $R(\omega)$ is complex; the form of this dependence can be reproduced adequately if the effects from the localization of optical phonons in the bulk of GaAs nanocrystals are taken into account. In addition, using the approach described previously in [13], we can try to estimate the sizes of the nanocrystals that form the *por*-GaAs layer. According to our calculations, the mean nanocrystal diameter is equal to 6.2 nm, which is in good agreement with the estimates obtained from the Raman spectra ($d \approx 5.9$ nm) and from the PL data ($d \approx 6.3$ nm) for the sample under consideration. Moreover, the SO-phonon frequency determined from the IR reflection spectrum $\omega_{SO} = 283.7$ cm^{-1} is consistent with the frequency estimated from the experiments with the Raman scattering ($\omega_{SO} = 284.0$ cm^{-1}). In addition, we can use the results of a group-theory calculation [14] for GaAs nanocrystals to determine their mean radius from known frequencies of spatially confined optical-phonon modes. Nevertheless, we encounter a certain difficulty related to the fact that the highest vibrational-mode frequency obtained in [14] in the context of the empirical valence-force field model was found to be equal to 305 cm^{-1}, which exceeds the LO-phonon frequency in gallium arsenide (at the point Γ of the Brillouin zone). It was assumed in [14] that vibrational modes $|n, \mathbf{k}\rangle$ ($\mathbf{k} \neq 0$) of bulk GaAs control the vibrational properties of GaAs nanocrystals and have an energy lower than those of phonon modes at the center of the Brillouin zone (the point Γ). In particular, a linear combination of LO states $|\Delta_1, \mathbf{k}\rangle$ yields a single state A_1, a single doubly degenerate state E, and a single triply degenerate state T_2 for six directions $\langle 100 \rangle$ [14]. Thus, we have

$$6|\Delta_1, \mathbf{k}\rangle \Rightarrow A_1 + E + T_2. \quad (7)$$

Similarly, the following expression was obtained for TO modes along the $\langle 100 \rangle$ directions [14]:

$$6|\Delta_3 + \Delta_4, \mathbf{k}_\Delta\rangle \Rightarrow 2T_1 + 2T_2. \quad (8)$$

For the $\langle 111 \rangle$ directions, we have

$$4|\Lambda_1, \mathbf{k}_\Lambda\rangle \Rightarrow A_1 + T_2 \text{ (LO)}, \quad (9)$$

$$4|\Lambda_3, \mathbf{k}_\Lambda\rangle \Rightarrow E + T_1 + T_2 \text{ (TO)}. \quad (10)$$

It follows from above expressions that the vibration of the A_1 type is only affected by the bulk LO-phonon modes. Similarly, the T_1 vibration is controlled by the bulk transverse optical phonons. Therefore, the dimensional quantization profoundly affects the frequency of the A_1 vibration but hardly affects the T_1 vibration (an intermediate situation occurs for the T_2 vibration). The drawbacks of the model under consideration manifest themselves in an analysis of the vibrational properties of surface atoms. It is assumed that the atoms forming the surface of GaAs nanocrystals have the same charge as the atoms in the bulk of the nanocrystals. As a result, it seems that the nanocrystals can be considered as electrically neutral. It is worth noting that this issue is controversial since the total number of anions in a nanocrystal does not necessarily coincide with the total number of cations; consequently, the total charge at the surfaces of the nanocrystals can differ from zero. It is quite probable that the above assumption was the cause of the value of the theoretically calculated frequency of the A_1 mode being too large when compared with the frequency of a bulk LO phonon in GaAs. Nevertheless, we can extrapolate the values of the vibration frequencies reported in [14] and try to estimate the mean size of the nanocrystals that form the porous GaAs layer, whose reflection spectrum is shown in Fig. 3, on the basis of the model under consideration. The experimental and theoretical data agree most satisfactorily at the nanocrystal diameter $d \approx 62$ Å, which follows from the comparison of the results listed in the table. If we take into account that we had to extrapolate the results reported in [14], this agreement can be considered as quite adequate. Nevertheless, it should be emphasized that the number of vibrations present in the actual experimental optical spectrum exceeds that predicted in [14]. Here, we should recall that some of the E, T_1, and T_2

Experimental and theoretical [14] frequencies of the vibrational modes in the *por*-GaAs sample whose reflection spectrum is shown in Fig. 3. The frequencies are expressed in cm^{-1}

	A_1	A_2	E	T_1	T_2
The data from [14], r = 31 Å	289.3	275.3	285.1	282.3	287.0
Experimental results	288.8	275.1	280.8	278.1	283.5

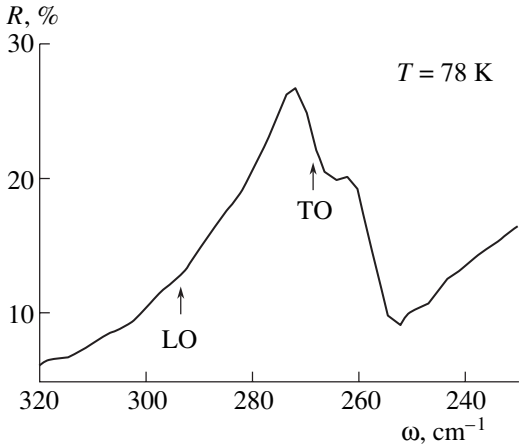

Fig. 4. The reflection spectrum $R(\omega)$ for a *por*-GaAs sample ($r \approx 25$–27 Å).

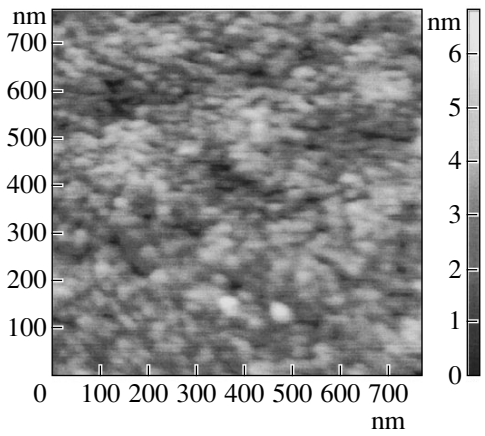

Fig. 5. An image of the surface profile for a porous *n*-GaAs sample. The image was obtained using AFM scanning.

modes are doubly or triply degenerate. The degeneracy can be removed owing to several factors, including those of a geometric nature; for example, the degeneracy disappears if the spherical geometry is replaced by a cylindrical geometry. Furthermore, the degeneracy of two transverse vibrations, which is characteristic of bulk isotropic semiconductors [11], is removed in a quantum wire. A nanocrystal 8 nm in size consists of 11855 atoms [14], and the particular geometric shape of a nanocrystal itself can be formed from these atoms. Therefore, we may expect that the vibrational properties of *por*-GaAs can be described in the case under consideration using the concept of GaAs nanocrystals that are extended in the same direction. This approach is partially confirmed both by the results reported by Ren *et al.* [14] and the data shown in Fig. 3 and calculated using formulas (3)–(6). In addition, *por*-GaAs with a columnar structure was observed previously in [6]. It is worth noting that, for the samples of porous GaAs, an attempt to describe the actual structure of the reflection spectrum using an approach based on the triangular geometry in the cross section of a quantum wire [15] failed to yield the desired results.

As the mean radius of the nanocrystals forming the porous GaAs layer decreases, the reflection spectrum is further transformed. This transformation manifests itself in the fact that the frequencies of vibrations corresponding to spatially confined phonon modes shift closer to the frequency of a transverse optical phonon. In this case, the reflectivity of the material in the region of wave numbers under consideration decreases. The above is illustrated in Fig. 4.

5. THE RESULTS OF AN AFM ANALYSIS

In Fig. 5, as an example, we show the results of an AFM analysis of the surface of a *por*-GaAs layer obtained under the same technological conditions as the sample whose Raman and FTIR spectra were shown in Figs. 2 and 3. Figure 5 shows a pattern of ordered arrangement for the GaAs nanocrystals whose mean diameter is 6.7 nm. Pyramidal nanocrystals are not observed, although the appearance of these nanocrystals should be expected if the surface of crystalline gallium arsenide is subjected to chemical etching [16]. Consequently, the assumption (made above when discussing the results of FTIR spectroscopy) that the GaAs nanocrystals have a nonpyramidal shape is confirmed experimentally. This observation can result from the fact that the process of electrochemical etching develops according to a different scenario. The obtained value $d \approx 6.7$ nm is in satisfactory agreement both with the results of the Raman and FTIR spectroscopy, and the PL data.

6. CONCLUSION

In this paper, we describe the process of obtaining porous GaAs layers using electrochemical etching and report the results from studying the optical and structural properties of these layers. We show that the morphology of the porous GaAs layer, the surface states, and the size of the nanocrystals that form the porous layer depend heavily on the conductivity type of the initial single-crystal GaAs. A shift of the main optical-phonon peaks and the appearance of both the vibrational modes localized in the bulk of nanocrystals and the surface phonons are observed in the optical and Raman spectra. We interpreted the complex structure of FTIR spectra for porous GaAs (*por*-GaAs). It is shown that the appearance of a photoluminescence (PL) signal in the visible region of the spectrum in the *por*-GaAs samples with *n*-type conductivity is caused by quantum-dimensional effects. We used AFM and XPS methods to study the *por*-GaAs morphology and chemical composition of nanocrystals. It is established that the stoichiometry of the nanocrystals' composition is preserved. We also found that the surface nanoprofile of *por*-GaAs samples obtained on *n*-GaAs substrates is homogeneous; this finding may be important with

respect to using these *por*-GaAs samples as substrates for obtaining epitaxial GaAs layers with improved structural properties. The Raman spectroscopy can be used to detect the As_2O_3 and Ga_2O_3 oxides on the surface of nanocrystals. The mean-diameter values of GaAs nanocrystals that form the *por*-GaAs layer, determined from the results of the Raman spectroscopy, FTIR spectroscopy, PL, and AFM, are in good agreement with each other.

ACKNOWLEDGMENTS

This study was supported by the Russian Foundation for Basic Research (project nos. 03-02-16938 and 02-03-32223) and the program "Integration" (project no. I-0964).

REFERENCES

1. D. J. Lockwood, P. Schmuki, H. J. Labbe, and J. W. Fraser, Physica E (Amsterdam) **4**, 102 (1999).
2. N. S. Averkiev, L. P. Kazakova, É. A. Lebedev, *et al.*, Fiz. Tekh. Poluprovodn. (St. Petersburg) **34**, 757 (2000) [Semiconductors **34**, 732 (2000)].
3. D. N. Goryachev and O. M. Sreseli, Fiz. Tekh. Poluprovodn. (St. Petersburg) **31**, 1383 (1997) [Semiconductors **31**, 1192 (1997)].
4. V. V. Mamutin, V. P. Ulin, V. V. Tret'yakov, *et al.*, Pis'ma Zh. Tekh. Fiz. **25** (1), 3 (1999) [Tech. Phys. Lett. **25**, 1 (1999)].
5. Yu. N. Buzynin, S. A. Gusev, V. M. Danil'tsev, *et al.*, Pis'ma Zh. Tekh. Fiz. **26** (7), 64 (2000) [Tech. Phys. Lett. **26**, 298 (2000)].
6. A. I. Belogorokhov, V. A. Karavanskiĭ, A. N. Obraztsov, and V. Yu. Timoshenko, Pis'ma Zh. Éksp. Teor. Fiz. **60**, 262 (1994) [JETP Lett. **60**, 274 (1994)].
7. A. I. Belogorokhov, Yu. A. Pusep, and L. I. Belogorokhova, J. Phys.: Condens. Matter **12**, 3897 (2000).
8. Yu. N. Buzynin, S. A. Gusev, Yu. N. Drozdov, and A. V. Murel', Zh. Tekh. Fiz. **70** (5), 128 (2000) [Tech. Phys. **45**, 650 (2000)].
9. E. A. Vinogradov and I. I. Khammadov, *Spectroscopy of Volume and Surface Phonons of Crystals* (Fan, Tashkent, 1989) [in Russian].
10. R. Enderlein, Phys. Rev. B **47**, 2162 (1993).
11. J. I. Pankove, *Optical Processes in Semiconductors* (Prentice Hall, Englewood Cliffs, N.J., 1971; Mir, Moscow, 1973).
12. A. V. Ghainer and G. I. Surdutovich, Phys. Rev. A **50**, 714 (1994).
13. A. I. Belogorokhov and L. I. Belogorokhova, Fiz. Tverd. Tela (St. Petersburg) **43**, 1693 (2001) [Phys. Solid State **43**, 1765 (2001)].
14. S.-F. Ren, Z.-Q. Gu, and D. Lu, Solid State Commun. **113**, 273 (2000).
15. M. A. Stroscio, K. W. Kim, M. A. Littlejohn, and H. Chuang, Phys. Rev. B **42**, 1488 (1990).
16. *Etching of Semiconductors*, Ed. by S. N. Gorin (Mir, Moscow, 1965) [in Russian].

Translated by A. Spitsyn

Semiconductors, Vol. 39, No. 2, 2005, pp. 249–253. Translated from Fizika i Tekhnika Poluprovodnikov, Vol. 39, No. 2, 2005, pp. 264–268.

LOW-DIMENSIONAL SYSTEMS

Kinetics and Inhomogeneous Carrier Injection in InGaN Nanolayers

D. S. Sizov^, V. S. Sizov, E. E. Zavarin, V. V. Lundin, A. V. Fomin, A. F. Tsatsul'nikov, and N. N. Ledentsov

Ioffe Physicotechnical Institute, Russian Academy of Sciences, St. Petersburg, 194021 Russia

^e-mail: Dsizov@pop.ioffe.rssi.ru

Submitted June 21, 2004; accepted for publication June 30, 2004

Abstract—The electrical and optical properties of light-emitting devices with an active region containing several layers of InGaN/GaN quantum dots (QDs) separated by GaN spacers are studied. It is shown that the overgrowth of the QD layer with an InGaN layer that has a reduced In content at higher temperatures raises the confinement energy of carriers in QDs. Furthermore, inhomogeneous carrier injection, predominantly into regions with higher confinement energy, is observed. The electrical and optical properties of *p–n* junctions and the effect of the inhomogeneities on these properties are studied in detail. It is shown that the shifts of photoluminescence and electroluminescence lines, which are observed when changing the experimental conditions, are related to these properties of the inhomogeneities in the *p–n* junction. © *2005 Pleiades Publishing, Inc.*

1. INTRODUCTION

In spite of progress in the design of GaN-based lasers and LEDs for the visible range, no clear comprehension of the electronic and optical properties of ultrathin InGaN layers in the active region of GaN light-emitting devices has been achieved. In many cases, the large body of experimental data and their different interpretations seem contradictory. The wide diversity of experimental data can be accounted for by the strong influence of specific features of the epitaxial growth procedure on the properties of the structures [1], which results in the strong dependence of the emission and electrical parameters of structures on the technological modes. Several parameters of the material, such as its composition and inhomogeneity [2], the spatial scale of this inhomogeneity [3], and morphological features and defects in the epitaxial layers, are sensitive to the conditions of InGaN epitaxial growth. The inhomogeneous broadening of the emission peaks of a InGaN/GaN system [4–6] is attributed both to phase decomposition of the solid solution and to fluctuations in the thickness of InGaN layers. If the scale of the inhomogeneities is comparable with the de Broglie wavelength of electrons and holes, and the confinement energy of carriers is high enough, one can suggest the presence of quantum dots (QDs) in InGaN/GaN structures [7]. The formation of QDs of less than 10 nm in size during the deposition of ultrathin InGaN layers in a GaN matrix has been demonstrated experimentally [8, 9]. According to the data obtained in optical studies, the energy spectrum of an array of these QDs is strongly broadened owing to inhomogeneities in the QD size and composition [5, 8, 10]. However, emission is observed from the tail of states related to QDs with the highest confinement energy. As shown in our earlier study [11], at room temperature, the distribution of carriers over the QD array is nearly statistical due to thermal activation; therefore, carriers occupy QDs that have higher confinement energy.

In addition to QDs, larger scale inhomogeneities, with a typical size on the order of 1 μm, have been observed in a InGaN/GaN system [1, 5, 12]. Both types of inhomogeneities induce the broadening of the emission spectrum, but under more detailed study they demonstrate different properties. The presence of strong built-in piezo- and pyroelectric fields in heterostructures based on Group-III nitrides causes a strong distortion in the band diagram. In this case, inhomogeneities in the In content in the active region exert an effect on the elastic stress in a structure and give rise to local distortion in the height of the barrier for the injection of nonequilibrium carriers, which, in turn, results in the inhomogeneity of the current flow.

To obtain lasing under injection pumping, it is necessary to optimize the technological parameters and to obtain a high-density QD array possessing the utmost possible homogeneity. The statistical redistribution of carriers enables them to occupy the deepest levels of those related to this array. However, an inhomogeneous injection, as well as kinetic lags in the redistribution of carriers between QD levels, can affect the homogeneity of the population in the emitting levels, thus raising the threshold parameters of lasers. In this study, we investigate processes of carrier injection in structures with an InGaN active region; the effect of injection inhomogeneities on the emission spectra of the structures is discussed.

1063-7826/05/3902-0249$26.00 © 2005 Pleiades Publishing, Inc.

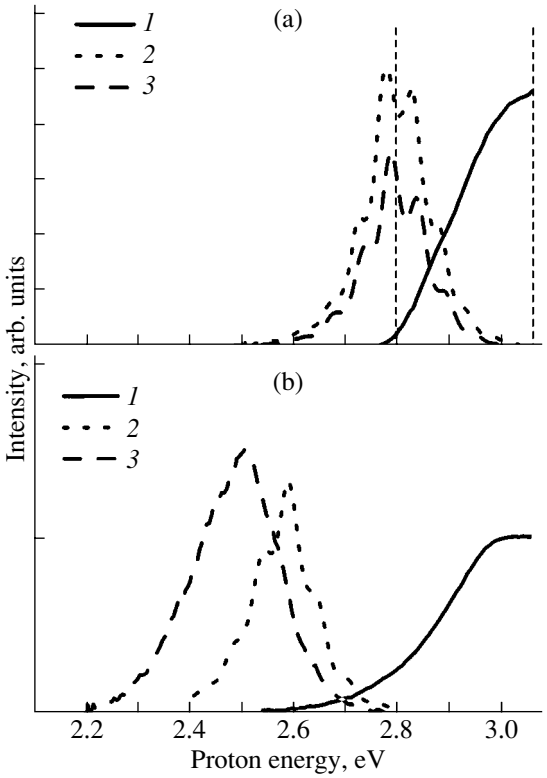

Fig. 1. (*1*) Photocurrent, (*2*) PL, and (*3*) EL spectra at T = 300 K for the structure with (a) high homogeneity of the active region and weak confinement of carriers, and (b) increased inhomogeneity of the active region (this structure contains QDs with strong confinement of carriers).

2. EXPERIMENTAL

The structures for the study were MOCVD-grown on (0001) sapphire substrates in an AIX 2000-HT system. After the deposition of an *n*-type GaN:Si buffer layer, an active region consisting of several InGaN layers was grown. In structure *A*, the QD layer was grown by deposition of an InGaN layer with an average thickness of 3 nm. However, in structure *B*, this layer was overgrown at a higher temperature with a InGaN layer that had a low In content, which leads to the formation of QDs with higher confinement energy. GaN barriers, of 10 nm in thickness, were doped with Si. The active region of the structures was overgrown with 20-nm-thick $Al_{0.15}Ga_{0.85}N$ and 250-nm-thick *p*-GaN:Mg layers.

A semitransparent Ni/Au contact was deposited onto the structure's surface in order to study photoluminescence (PL) under external bias. PL was excited by an He–Cd laser with a pumping density of 100 W cm^{-2} and measured using a lock-in amplifier, which allowed us to exclude the effect of steady-state electroluminescence (EL) emission at a positive bias. The photocurrent was excited with a xenon lamp.

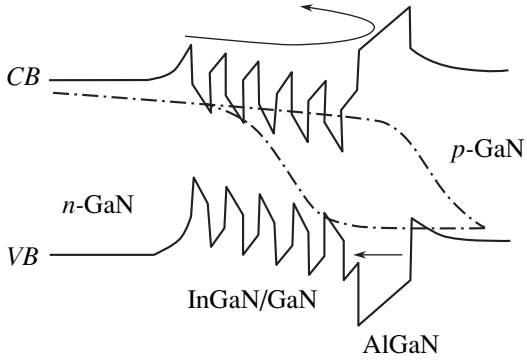

Fig. 2. The band diagram of the studied light-emitting structures at a positive bias. Arrows indicate the directions of motion for the nonequilibruim carriers.

3. RESULTS AND DISCUSSION

Figure 1 shows EL, PL, and photocurrent spectra for the two structures under study. A comparison of EL and photocurrent spectra shows that the emission of the structures is excited from the density-of-states tail, i.e., from the regions in which the carrier localization is stronger than that on average in the layer. This behavior is typical of QD structures, and the energy spacing between the emission peak and the peak in the density of states, which can be estimated from the photocurrent spectrum (the Stokes shift [10]), increases as the carrier localization in the QD levels becomes more effective. In contrast to structure *A*, the growth mode used for structure *B* was favorable for the formation of InGaN regions locally enriched with indium. This leads to the formation of QDs that have higher energy carrier confinement and a stronger spread of the QD size and composition, which is confirmed by the larger Stokes shift in structure *B*. Furthermore, in contrast to the situation in structure *A*, where this shift is very small, it can be seen that the PL peak in structure *B* is blue-shifted in respect to the EL peak.

To disclose the cause of the difference between the positions of the PL and EL peaks in structure *B*, we consider the process of carrier injection into the active region in detail. Figure 2 shows the band diagrams of the structures under study. Since the barriers in the active region were doped with a donor impurity, it can be assumed that, at zero bias, the Fermi level lies near the local levels of the active region. The applied bias slightly shifts the band diagram of the active region in respect to the Fermi level for the electrons, whereas the quasi-Fermi level for the holes shifts downwards. When it crosses the top of the AlGaN valence band, which plays the role of the injection barrier, holes are injected into the active region. There is published evidence that a considerable contribution is made by the tunneling injection in the *p*–*n* junction [13, 14], which is due to the very low density of extrinsic carriers in wide-bandgap semiconductors. The experimental data related to this effect will be discussed in detail below. Here it is

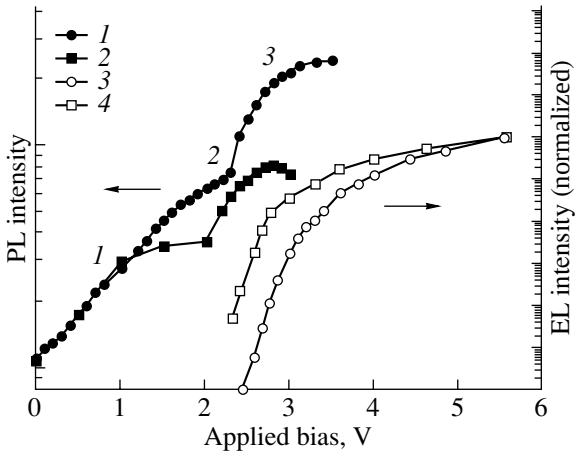

Fig. 3. The intensity of (*1, 2*) PL and (*3, 4*) EL as a function of the applied external bias. Curves *1* and *3* show the structure with high homogeneity of the active region, and *2* and *4* show the structure with increased inhomogeneity of the active region. The PL intensity is normalized to unity at a zero bias.

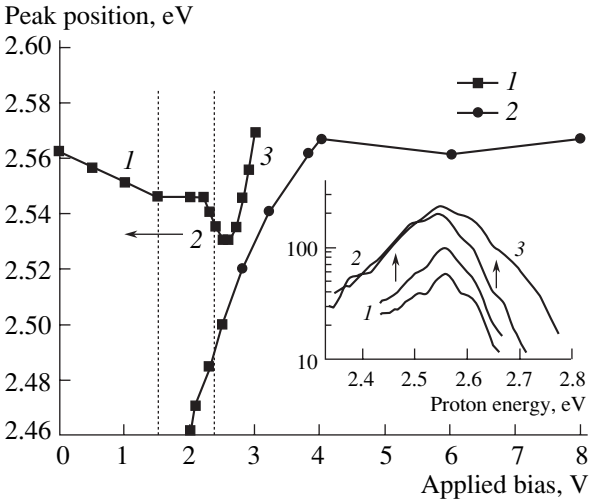

Fig. 4. Positions of (*1*) PL and (*2*) EL peaks as functions of the external bias for the structure with increased inhomogeneity of the active region. The inset shows the modification of the PL spectrum plotted in the logarithmic scale. The numbers in the frames indicate characteristic portions of curve *1* and the corresponding spectra.

necessary to note that small fluctuations in the composition and elastic stress fields in the active region can induce significant local distortions in the band diagram of a structure. Moreover, this factor will induce fluctuations in the height of the injection barrier. If these fluctuations exceed the characteristic energy k_BT (where k_B is the Boltzmann constant), and the Fermi level position away from the *p–n* junction is uniform, the number of carriers capable of crossing the barrier in regions with a lower barrier height will be many times larger; this will result in the injection of carriers only in some of the local regions of a structure.

Figure 3 shows the PL and EL intensity for the structures under study as functions of the applied bias. The curve describing the dependence for PL can be divided into three portions. The first corresponds to a steady increase in intensity as the external bias increases. We suggest the following interpretation for this dependence: a positive bias reduces the field of the *p–n* junction and depresses the separation of nonequilibrium carriers, resulting in an enhanced emission intensity.

The second portion, at biases exceeding 1.5 V, is characterized by a slower rise of the PL intensity as the bias increases, while the intensity rise in structure *B* ceases completely. We believe that, at this bias, the separating field varies only slightly. As the applied bias further increases (the third portion), the PL intensity increases again. If we compare these dependences with the EL intensity dependences on bias, we can see that the third portion corresponds to the onset of the emission induced by electrical injection. Without going into too much detail about the mechanism of this injection, we can say that, at these biases, there occurs an injection of holes (excited in the *p*-type layer by the pumping laser) into the active region. Therefore, the third portion corresponds to the emission with a predominant recombination of carriers that did not originate the active region, but found their way into the active region by overcoming the injection barrier. It is noteworthy that in structure *A*, which is characterized by a more homogeneous active region and weaker localization of carriers, the third portion begins at a higher bias (2.3 V) than structure *B* (2 V). This fact can be attributed to the lower injection barrier in the structure with more strongly localized levels in InGaN. Furthermore, this difference in the bias, which is necessary for the emission onset, can be accounted for by the occurrence of tunneling injection. The probability of tunneling injection to deeper levels is higher because a larger amount of resonant holes in the *p*-type region correspond to these levels. To reveal the effect of the injection and recombination inhomogeneities on the spectral characteristics of emission, we turn to Fig. 4, which shows the effect of positive bias on the PL spectra of structure *B*. At a positive bias, a red shift is observed in the first portion of the curve; in the second portion, it levels off. However, in the third portion, the red shift appears again and then gives way to a blue shift. It is noteworthy that structure *A* demonstrates a fundamentally different behavior (Fig. 5): a weaker, but steady, red shift at positive biases. The change of the peak's position under external bias is usually attributed to the Stark effect [15]. We believe that the possibility of an inhomogeneous injection of carriers must be taken into account in the estimations of this effect. As can be seen in Fig. 2, the PL intensity increases at a positive bias, which is related to the reduction in the separating field of the *p–n* junction. However, owing to the inhomogeneous distribution of indium during the deposition of the

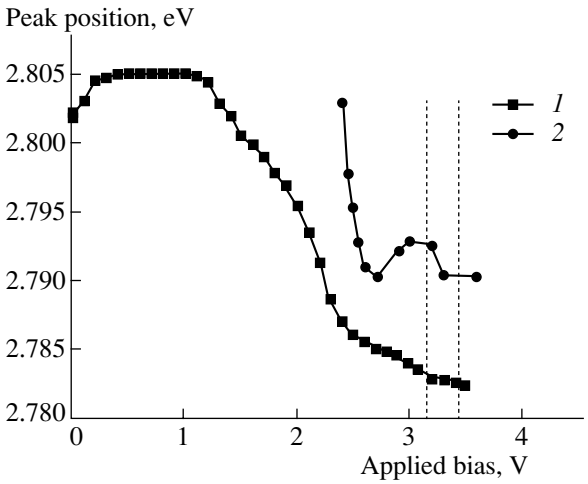

Fig. 5. Positions of (*1*) PL and (*2*) EL peaks as functions of the applied external bias for the structure with high homogeneity of the active region.

InGaN layer, a QD array with a strong spread of the size and confinement potential is formed. In addition, regions with a typical micrometer scale are formed, in which not only the average confinement energies of the carriers in QDs are different but also the effect of the positive bias on the electronic and optical properties of the *p–n* junction. As a result, the rise in positive bias leads to the increase of PL intensity in some selected areas, rather than homogeneously over the structure. At the same time, the intensity peak corresponds to the emission averaged over all the regions, which generally emit at different wavelengths. If the emission intensity increases in some of these regions with a particular wavelength, the averaged emission peak is shifted to the wavelength of the emission from these selected areas.

At a small bias, the EL spectral peak lies at the energy of 2.4 eV (Fig. 4) and is strongly blue-shifted as the bias (and the driving current) increases. This behavior can be accounted for by carriers filling the localized states. However, according to our estimates, the studied range for the injection current is much less than is necessary for the filling of the given density of these states, even at a quantum efficiency of about 100%. The density of the states can be determined from the photocurrent spectrum if it is assumed that the integral density of the states is close to the density of the states in a quantum well, 10^{14} cm^{-2}. The density of the states determined from the photocurrent spectrum at the point corresponding to the emission energy is only 1.5–2 orders of magnitude smaller than the maximum density of states. If QD levels with the transition energies near the emission peak are completely filled, the number of occupied levels (taking into account the width of the spectrum) will be about 10^{11}–10^{12} cm^{-2}. For a driving current of about 10^{-1} A and a lifetime at the QD levels on the order of 10^{-9} s [8], only a small fraction of the QDs will be occupied. Emission from different regions of a structure at different wavelengths was observed in [1, 12]. In this case, emission was observed at a low bias only from regions with the longest-wavelength position of the emission peak. We have observed a similar effect in the structures under study. Therefore, we believe that the blue shift of the EL peak when the applied bias is raised can be explained as follows: as the bias increases, carriers are injected not only into local regions with an increased average content of In and an emission wavelength exceeding the average of the structure, but also into regions with a lower average In content, which corresponds to shorter emission wavelength. The concentration of QDs with smaller confinement energy and higher optical-transition energy is significantly larger than that of QDs with larger confinement energy, as can be seen from the photocurrent spectra; however, higher bias voltage is necessary for the injection of carriers into these levels. In the case of a quasi-statistical distribution of carriers over the QD levels, thermal emission can stimulate a redistribution of the carriers to these levels that have a less pronounced confinement but significantly higher concentration. Nevertheless, the suppressed lateral transport of carriers between different QDs hinders this process by producing kinetic lags for this statistical redistribution. Therefore, at a small bias, only the emission from regions with local carrier injection is observed. These regions are characterized by the lower energy of their optical transitions.

The fact that small bias first affects those local regions of *p–n* junction in which the emission wavelength is longer than the average of the structure suggests that the rise of PL intensity at a small bias is due to the accumulation of carriers in the regions with a high average content of In and, consequently, with a lower energy of the electron-hole transition in a QD. This red-shifts the PL peak, making an additional contribution to the red shift along with the distortion of the band diagram (see the inset in Fig. 4). At the second part of the dependence of the emission peak position on the positive bias, both the shift of the PL peak and the rise of the emission intensity cease. As the bias further increases, in the third part of the dependence, the red shift appears again, which is also accompanied by a rise of the PL intensity. However, in the range of highest bias voltages, a sharp reverse shift of the PL peak, the so-called "blue jump," is observed. In this range of bias, the EL peak is blue-shifted, which corresponds to the injection of carriers into the regions that have a lower average energy of electron-hole transition. We believe that the PL peak is also shifted to the energy corresponding to the QD levels with the highest carrier population at temperatures higher than 100 K [16].

In structure *A*, no blue shift of the EL line is observed as the bias increases, but a slight red shift of the EL line occurs simultaneously with the shift of the PL line. We believe that the injection of carriers in this structure is homogeneous, in other words, the efficiency of the filling occurring at a given bias is the same

in regions with different carrier confinement energies. The spectral distribution of the emission from this structure is defined by the inhomogeneity of QD array in relation to its size and composition, and by the statistical distribution of carriers over the levels. The red shift of EL and PL is related to the distortion of the band structure (the Stark effect).

4. CONCLUSIONS

Depending on the growth mode, different types of InGaN QD arrays, characterized by different types of carrier injection, can be obtained in the active region of light-emitting structures. It is possible to fabricate an array of QDs in which the injection into the levels is homogeneous and the distribution of carriers over the QD levels is statistical. However, at other growth modes, QD arrays are formed in which the injection of carriers into the levels is inhomogeneous. This phenomenon occurs because of the predominant influence of the external bias of the *p–n* junction on those local parts of the active region that have a larger confinement energy. This may be due to tunneling (tunneling injection into the states with a confinement energy significantly larger than the average value for the case of a quasi-equilibrium population under optical pumping), or it may be due to the inhomogeneity of the *p–n* junction itself. In both cases, the spatial scale of the injection inhomogeneity must be significantly larger than the QD size. If it were not, the effect of the injection inhomogeneities would be insignificant owing to the statistical redistribution of carriers observed in this type of structure. In the case under study, we observe a kinetic lag in the redistribution. Therefore, in a general case, the position of the Fermi level is not the same in the plane of the active region parallel to the *p–n* junction plane.

REFERENCES

1. R. P. O'Donnell, S. Pereira, R. W. Martin, *et al.*, Phys. Status Solidi A **195**, 532 (2003).
2. T. Okumura and Y. Akagi, J. Cryst. Growth **223**, 43 (2001).
3. M. S. Jeong, J. Y. Kim, Y.-W. Kim, *et al.*, Appl. Phys. Lett. **79**, 976 (2001).
4. T. Mukai, M. Yamada, and S. Nakamura, Jpn. J. Appl. Phys. **38**, 3976 (1999).
5. S. Chichibu, T. Sota, K. Wada, and S. Nakamura, J. Vac. Sci. Technol. B **16**, 2204 (1998).
6. P. G. Eliseev, P. Perlin, J. Lee, and M. Osinski, Appl. Phys. Lett. **71**, 569 (1997).
7. N. N. Ledentsov, V. M. Ustinov, V. A. Shchukin, *et al.*, Fiz. Tekh. Poluprovodn. (St. Petersburg) **32**, 385 (1998) [Semiconductors **32**, 343 (1998)].
8. I. L. Krestnikov, N. N. Ledentsov, A. Hoffmann, *et al.*, Phys. Rev. B **66**, 155310 (2002).
9. A. V. Sakharov, W. V. Lundin, I. L. Krestnikov, *et al.*, in *Proceedings of 8th International Symposium on Nanostructures Physics and Technology* (St. Petersburg, 2000), p. 216.
10. R. W. Martin, P. G. Middelton, K. P. O'Donnell, and W. Van der Stricht, Appl. Phys. Lett. **74**, 263 (1999).
11. D. S. Sizov, V. S. Sizov, A. I. Besulkin, *et al.*, in *Proceedings of 12th International Symposium on Nanostructures Physics and Technology* (St. Petersburg, 2004).
12. P. Fisher, J. Christen, and S. Nakamura, Jpn. J. Appl. Phys. **39**, L129 (2000).
13. V. E. Kudryashov, K. G. Zolin, A. N. Turkin, *et al.*, Fiz. Tekh. Poluprovodn. (St. Petersburg) **31**, 1304 (1997) [Semiconductors **31**, 1123 (1997)].
14. H. C. Casey, Jr., J. Muth, S. Krishnankutty, and J. M. Zavada, Appl. Phys. Lett. **68**, 2867 (1996).
15. T. Takeuchi, C. Wetzel, S. Yamaguchi, *et al.*, Appl. Phys. Lett. **73**, 1691 (1998).
16. H. Kudo, T. Tanbe, H. Ishibashi, *et al.*, J. Appl. Phys. **89**, 5779 (2001).

Translated by D. Mashovets

Semiconductors, Vol. 39, No. 2, 2005, pp. 254–260. Translated from Fizika i Tekhnika Poluprovodnikov, Vol. 39, No. 2, 2005, pp. 269–275.

AMORPHOUS, VITREOUS, AND POROUS SEMICONDUCTORS

Electrical Characteristics of Insulator–Conductor and Insulator–Semiconductor Macrosystems

V. A. Sotskov^

Kabardino-Balkar State University, ul. Chernyshevskogo 173, Nalchik, 360004 Russia

^e-mail: sozkov_va@rambler.ru

Submitted April 5, 2004; accepted for publication May 13, 2004

Abstract—The volume resistivity and permittivity of a number of macroscopically disordered insulator–conductor and insulator–semiconductor systems are investigated as functions of the conducting-phase content. A qualitative model is proposed that explains the concentration dependences on the basis of the percolation theory in combination with a fractal concept. © *2005 Pleiades Publishing, Inc.*

1. INTRODUCTION

At present, investigation of the electrical properties of composites is becoming more and more important for materials science [1–3]. Macroscopically disordered insulator–conductor systems [3] are generally referred to as granular alloys. Granular metal–insulator alloys are systems composed of metal granules dispersed in a dielectric matrix. A metal–insulator transition occurs, at volume contents x of the metal, close to some critical value x_c, which is referred to as the percolation threshold. Granular alloys with a conducting-phase content close to x_c have a number of unique properties [3]. The search for materials with such properties and their application is one of the most interesting problems of technical physics. Significant changes in the conductivity, the temperature coefficient of the resistance, and other parameters in the vicinity of the percolation transition make it possible to obtain materials with different properties, within one process, that have small variations in the content of one component [1–3]. For example, the anomalous behavior of the real part of the permittivity ε' [4–7] may be of significant technical importance for the design of new types of capacitors in microelectronics. There are few experimental studies of the dependence of ε' on the conducting-phase content x ($\varepsilon' = f(x)$). In addition, real systems significantly differ from theoretical models in relation to a number of features, which must be carefully studied in an experimental context [1–7].

In this paper, we report the results of studying changes in the volume resistivity and permittivity of macroscopically disordered insulator–conductor and insulator–semiconductor systems as functions of the volume content of the conducting phase.

2. EXPERIMENTAL

As was shown in [8], the low-melting insulators paraffin and ceresin are most convenient for an investigation of the conductivity of macroscopically disordered systems (macrosystems). These insulators have quite a high resistivity, can be easily formed, and are passive to most metals and semiconductors [8–10]. Solid oil paraffin (P.1) with a resistivity of $\rho = 3 \times 10^{10}$ Ω m was used as a dielectric matrix.

A conducting phase (filler) was chosen according to the following considerations.

(i) Fillers must form a series of materials that have different resistances. This circumstance is decisive for the possibility of forming conducting chains and deriving information on the alignment and interaction of fractals.

(ii) One part of the filler particles must be uniform in their properties and have no oxide or other shells. The other part, in contrast, must have a complex structure and oxides with different resistances on the surface of particles. Such conditions cause the contact resistance between particles to change. The difference in the contact resistance significantly increases the spread of the potential barriers' heights. The conductivity of such a system is determined by the potential barriers with a height close to the percolation threshold [11], i.e., by the highest barriers. In this case, the nonlinearity of the current–voltage characteristics should increase, which provides additional possibilities for analysis.

Graphite, iron, and aluminum particles were used as conducting fillers. We intended to form a series of paraffin–conductor systems, in which the conductors would have different contact resistances due to the presence of oxides on the surfaces of metal particles. For this purpose, we chose the following composites: thermal graphite (dry colloidal graphite C-1) with an average particle size of 4 μm; pure-grade iron with a particle size of 6 μm; and pure-grade aluminum with a particle size, after sifting, of 10 μm.

The resistance of oxide films on the surface of Al and Fe granules was estimated from the following considerations. As is well known, an oxide film on the sur-

face of Fe has the chemical composition $Fe_2O_3 \cdot nH_2O$ [12] and may have different resistivity values. The resistivity ρ of the iron oxide was determined experimentally for a pure-grade Fe_2O_3 powder, kept in the same conditions as an Fe powder, which had resistivity $\rho \approx 10^5$ Ω m. This value was assumed to be the resistivity of the films on the surfaces of the iron particles. A thin, but fairly dense, high-resistivity film is formed on the surface of Al in air, which is widely used in practice [10]. The resistivity of the reagent-grade powder aluminum oxide was determined experimentally as $\rho = 3 \times 10^9$ Ω m. This value was assumed to be the oxide shell resistivity. The use of graphite as a conducting component [8] has a number of advantages over metal from the point of view of minimizing the contact resistance. Carbon oxides are gases, and, independent of the graphite origin, the formation of oxide films on graphite particles can be disregarded. The use of semiconductors as fillers can be regarded as a variant of using homogeneous conductors without oxide shells. The following semiconducting oxides were used: Fe_2O_3 in the form of approximately spherical particles 25 μm in diameter and CuO particles of approximately the same shape and size.

Before preparing a melt, Fe and Fe_2O_3 samples were demagnetized in an electromagnetic field using a conventional technique. The agitator, as well as the other equipment in contact with the composites, was made of nonmagnetic materials. The sample-preparation technique followed is described in detail in [8]. A capacitor with electrolytic copper plates was used as the experimental sample. A mixture of paraffin and filler (a conductor or semiconductor) with a certain conducting-phase content was poured between the plates in advance. The set of samples with the same conducting-phase content had a spread of 3–5% in the electrical parameters: resistivity, capacitance, and *Q* factor. A shrinkage force significantly affects the value of the contact resistance between conducting particles [2, 10, 13]. Shrinkage of paraffin can be estimated as follows. Assuming that the linear coefficient of the thermal expansion of paraffin $\alpha = 130 \times 10^{-6}$ K^{-1} [14] and the volume expansion coefficient $\beta \approx 3\alpha$, one can estimate the paraffin shrinkage under experimental conditions at a change in temperature $\Delta T \approx T_{melt} - T_{meas} \approx 65$ K as

$$\frac{\Delta V}{V_0} = \Delta T\beta \approx 2.5\%. \quad (1)$$

This value of the paraffin shrinkage is smaller than the typical values for Contactol and other polymers, in which shrinkage forces can destroy the oxide shells of conducting granules [2, 12, 13]. Taking into account the high plasticity of paraffin [8, 14], we can suggest that shrinkage forces are weak in macrosystems with paraffin and that the contact resistances form a series similar to the series of resistivities for shells of conducting granules.

No less than five samples were prepared for each value of the conducting-phase content *x* in a composite and no less than 50 samples with *x* close to x_c. The technique used to measure the volume resistivity met the standard requirements. The measurements were performed using a two-electrode scheme and without illumination of the samples. The capacitance of the samples and the *Q* factor of the capacitor were determined conventionally, taking into account the capacitance of terminating wires, the edge capacitance, and other factors [15, 16]. Samples in the form of planar and cylindrical capacitors were used.

It must be taken into account that the permittivity ε is a complex quantity:

$$\varepsilon = \varepsilon' - j\varepsilon''. \quad (2)$$

The real part of the permittivity, ε', was determined as the ratio of the capacitances [10, 15, 16]:

$$\varepsilon' = \frac{C_x}{C_0}, \quad (3)$$

where C_0 is the capacitance of an empty capacitor (filled with air) [15] and C_x is the capacitance of a sample with a conducting-phase content *x*. The imaginary part of the permittivity was determined as follows [10, 15, 16]:

$$\varepsilon'' = \tan\delta\varepsilon' = \frac{\varepsilon'}{Q}, \quad (4)$$

where *Q* is the *Q* factor of the capacitor. The value of *Q* was measured by a conventional method for the parallel connection of the capacitor and resistance. The measurements of the capacitance and the *Q* factor were performed at a frequency of 1 kHz. The technique for determining the fractal dimension of the conducting-phase surface was described in detail in [17–19]. Images of the paraffin–graphite films were obtained on a Latimed microscope with magnifications of 50, 100, and 200 during transmission and reflection, with the necessary resolution for subsequent treatment using the method proposed in [17, 18].

3. EXPERIMENTAL RESULTS

3.1. Paraffin–Conductor Systems

Figure 1 shows the dependences $\rho = f(x)$ for the paraffin–graphite, paraffin–iron, and paraffin–aluminum systems. The behavior of the dependences in Fig. 1 confirms the suggestion about the existence of different contact resistances in paraffin–conductor systems. The dependence $\rho(x)$ for the paraffin–graphite system (curve *1*) was used to determine the percolation threshold x_c as the intersection point of the straight lines approximating the low-resistivity branch (*BC*) and the descending portion of the characteristic (*AB*). As can be seen from Fig. 1, curve *1* does not contain an initial portion at which the composite properties used were determined by the matrix properties. According to these

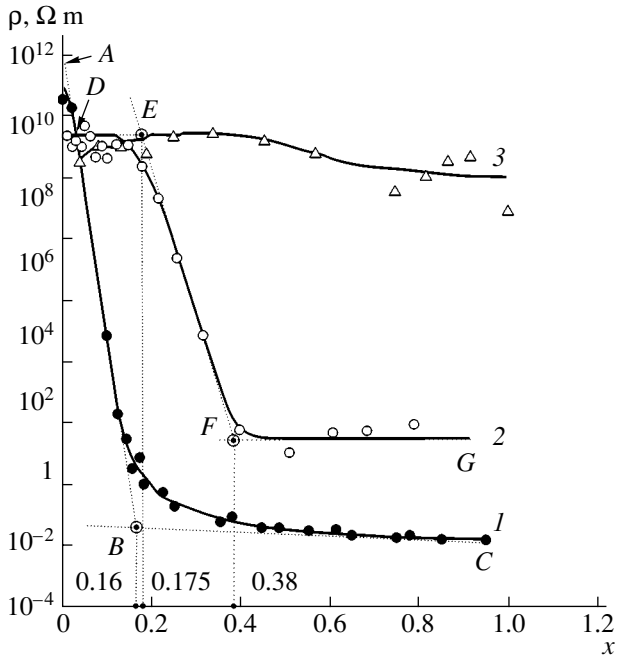

Fig. 1. Dependences of the volume resistivity ρ on the conducting-phase content x for the (*1*) paraffin–graphite, (*2*) paraffin–iron, and (*3*) paraffin–aluminum macrosystems.

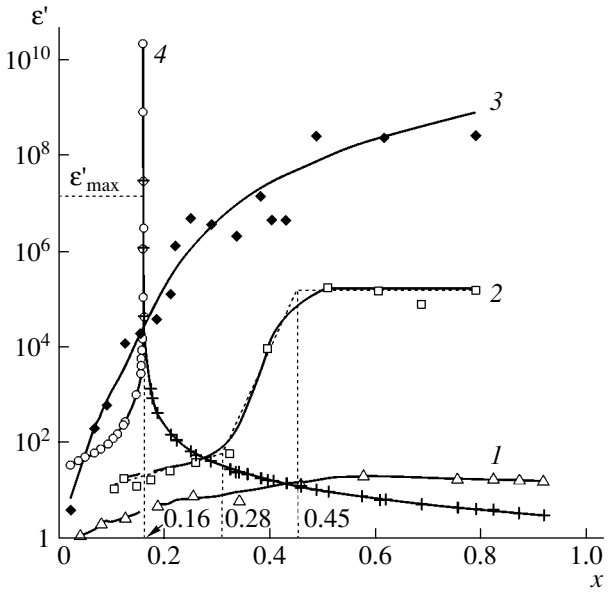

Fig. 2. Dependences of the real part of the permittivity ε' on the conducting-phase content x for the (*1*) paraffin–aluminum, (*2*) paraffin–iron, and (*3*) paraffin–graphite macrosystems. Theoretical curve *4* is plotted on the basis of the models proposed in [4–7] using the constants from [8].

plots, $x_c = 0.16$, which is consistent with the data in [8] and is in good agreement with the theory in [20, 21].

The plot of the dependence $\rho = f(x)$ for the paraffin–iron system (Fig. 1, curve *2*) consists of three portions: the high-resistivity portion *DE* ($0 \le x < 0.175$), where the resistivity weakly depends on the conducting-phase content and is determined by the matrix resistivity; EF, the portion of maximum change in ρ at $0.175 \le x < 0.38$; and the minimum-resistivity portion *FG*, where the dependence $\rho = f(x)$ is only weakly pronounced, since ρ is determined by the conductor resistivity in this range of x ($0.38 \le x < 1$). If we assume the scaling representation to be valid for the paraffin–iron system [4], we can write the following relations:

$$\sigma(x) = \sigma_M(x - x_c)^t \text{ and } \sigma(x) = \sigma_D(x_c - x)^{-q}, \quad (5)$$

where $\sigma(x)$ is the conductivity of the composite at a conducting-phase content x; σ_M and σ_D are the conductivities of the conducting phase and the dielectric matrix, respectively; and t and q are indices. Then, $q = t\left(\frac{1}{s} - 1\right)$, $s = \frac{1}{2}$ [4], and $t = 1.4$ [8]; hence, $q = 1.4$ and, considering both branches to be symmetric with respect to x_c, we can assume that the percolation threshold $x_c \approx 0.38$.

The dependences $\varepsilon' = f(x)$ are shown in Fig. 2. As can be seen, all the experimental dependences are rising curves with different changes in ε'. For example, for the paraffin–graphite system (curve *3*), the change in ε' in the range under study is approximately 4×10^7; for the paraffin–iron system (curve *2*), the change in ε' is smaller; and for the paraffin–aluminum system, the change in ε' is extremely small (curve *7*). It should be noted that the interval for maximum changes in ε' for the paraffin–iron composite is in the range $0.28 \le x < 0.45$, which radically differs from the range for the dependence $\rho = f(x)$. All the dependences $\varepsilon' = f(x)$ are similar to the dependences $\sigma = f(x)$.

The dependences of the imaginary part of the permittivity on the conducting-phase content x are shown in Fig. 3. All the plots are rising curves. The curves for the paraffin–iron (*2*) and paraffin–aluminum (*3*) systems tend to constant values. The curve for the paraffin–graphite composite (*1*) has a sharply increasing portion RQ.

3.2. Paraffin–Semiconductor Systems

Figure 4 shows the dependences $\rho = f(x)$ for two of the paraffin–semiconductor systems under consideration: paraffin–CuO (curve *2*) and paraffin–Fe_2O_3 (curve *3*). The dependence $\rho = f(x)$ for the paraffin–graphite macrosystem [8] is also shown in Fig. 4. The percolation threshold for curve *3* is $x_c \approx 0.29$.

The dependences $\varepsilon' = f(x)$ and $\varepsilon'' = f(x)$ for the paraffin–semiconductor systems are shown in Fig. 5.

4. DISCUSSION

4.1. Dependences $\rho = f(x)$

One of the most complete plots with respect to the presence of the portions considered in scaling representations [4] is the dependence for the paraffin–iron sys-

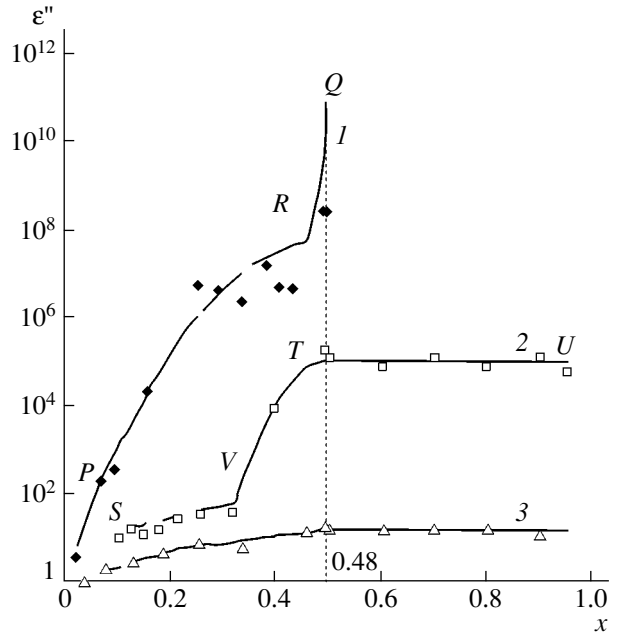

Fig. 3. Dependences of the imaginary part of the permittivity ε" on the conducting-phase content *x*. Curves *1–3* are the same as in Fig. 1.

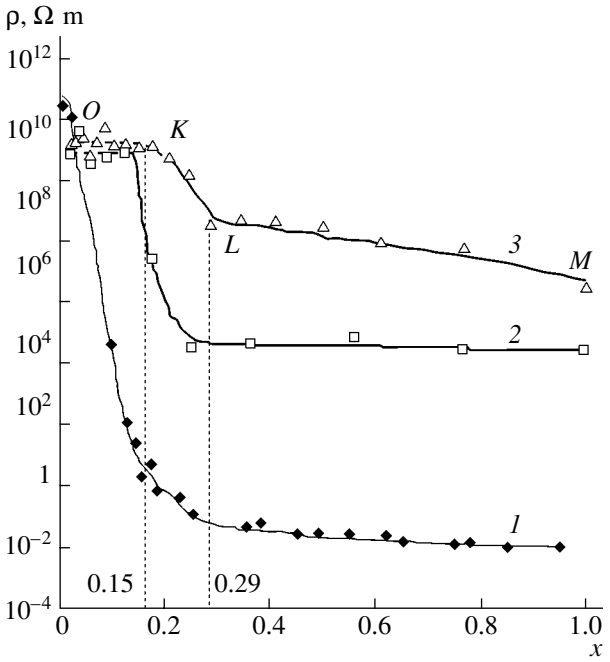

Fig. 4. Dependences of the volume resistivity ρ on the conducting-phase content *x* for the (*1*) paraffin–graphite, (*2*) paraffin–CuO, and (*3*) paraffin–Fe_2O_3 macrosystems.

tem (Fig. 1, curve *2*). Therefore, we will discuss the experimental results obtained for this system using the fractal concept, taking into consideration the results for other systems when necessary. The presence of three portions in the curve for the paraffin–iron system is consistent with percolation theory. The formation of a primary chain that closes the electrodes occurs at the *DE* portion (Fig. 1, curve *2*) since, according to percolation theory, the formation of a continuous cluster is possible even at $x \geq 0.15$ [20, 21]. Similar considerations are valid for the portion *OK* in the corresponding curve for the paraffin–Fe_2O_3 system (Fig. 4, curve *3*). However, no sharp transition of the resistivity of either a conductor or a semiconductor occurs when *x* increases. This is due both to contact phenomena and to the high resistance of the chain itself. In other words, a quasi-internal electrode is formed, which begins to serve as the continuous chain of an ideal conductor at $x \geq 0.15$ [20, 21] at the point *E* (Fig. 1, curve *2*). The only exception is the paraffin–graphite system (Figs. 1, 4; curves *1*). However, this exception only confirms the above considerations since the contact resistance in this system is minimal. As the filler content in the composite increases, formation of conglomerates begins, which, merging, form branched chains. Note that the development of such conducting chains depends on the resistance of the oxide shells on the conductor surface. As was noted above, the random spread of the barrier heights in a disordered system may significantly change the situation [11]. In the paraffin–semiconductor systems (Fig. 4, curves *2*, *3*) there is also a random spread of the barrier heights, which is due to the different areas and shapes of the contact between semiconducting particles; however, the barrier heights for the paraffin–iron system, as well as their spread, are larger. Indeed, the transition from matrix to filler properties

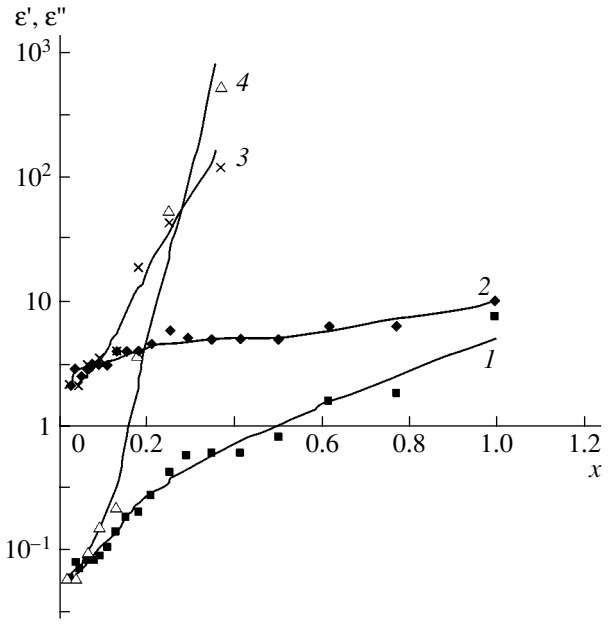

Fig. 5. Dependences of the real part of the permittivity ε' on the conducting-phase content *x* for the (*1*) paraffin–CuO and (*2*) paraffin–Fe_2O_3 systems, and the dependences of the imaginary part of the permittivity ε"(*x*) for the (*3*) paraffin–Fe_2O_3 and (*4*) paraffin–CuO systems.

occurs in the range $0.175 \le x < 0.38$ (Fig. 1, curve *2*, portion *EF*), whereas the transition in the paraffin–semiconductor system occurs in the range $0.15 \le x \le 0.29$ (Fig. 4, curve *3*, portion *KL*). The high finite filler content in the case of the paraffin–iron system is necessary for the development of a more branched structure, which can finally form a conducting chain parallel to a high potential barrier. If we assume that the ability of the Fe_2O_3 and CuO components to form branched chains is the same as for conductors [1, 2], the processes for both conductors and semiconductors occur similarly. The resistivity hardly changes at portion FG (Fig. 1, curve *2*).

By moving to interfractal interaction and using the terminology proposed by Feder [22], we can state that near point *E* (Fig. 1, curve *2*) fractals have few blue ends but many red ones (contacts with low and high resistances between different fractals, respectively). Gradually, at portion *EF*, the number of red ends decreases and the number of blue ends increases (Fig. 1, curve *2*); i.e., the fractals belonging to the left and right electrodes begin to merge. Equilibrium between the numbers of red and blue ends is attained at portion *FG*, which does not change with a further increase in the Fe content. For the paraffin–Fe_2O_3 system (Fig. 4, curve *3*, portion *LM*), the resistance gradually decreases for two reasons: the further development of the internal electrode and the stochastic change in the contact resistance owing to the increase in the contact area; however, this change is small. Despite the difference in the volume resistivities by approximately two orders of magnitude, the transition from the matrix to the semiconductor properties occurred at the same contents of the Fe_2O_3 and CuO semiconductors: $0.15 \le x \le 0.29$. This fact also indicates the dominance of topological processes in the conductivity of the system.

4.2. Dependences ε' = f(x)

The dependences $\varepsilon' = f(x)$ are rising curves (Figs. 2 and 5) for all the systems under consideration. During the experiments, no anomalies were found in the dependences of the real part of the permittivity on the content *x* in the vicinity of the percolation threshold [4–6] for the paraffin–conductor and paraffin–semiconductor macrosystems.

Let us consider some theoretical concepts of this problem. Curve *4* in Fig. 2 is the theoretical dependence for the paraffin–graphite system plotted on the basis of the models proposed in [4–7]. Some constants from [8] were used, as the systems under study were identical. Theoretically, the dependence $\varepsilon' = f(x)$ at a frequency $\omega = 0$ is given by the relation [4]

$$\varepsilon'(0, x) = \frac{\varepsilon'_0}{|x - x_c|^q}, \qquad (6)$$

where

$$\varepsilon'_0 = 2.1 \text{ [14]}; \quad q = t\left(\frac{1}{s} - 1\right) \text{ at } x_c = 0.16 \text{ [8]};$$

$$s = \frac{1}{2} \text{ [4] and } t = 1.4 \text{ [8]}.$$

Thus, $q = 1.4$. In Fig. 2, curve *4* is represented by two branches: a left branch at $x < x_c$ and a right branch at $x > x_c$. At $x = x_c$, the function has a discontinuity. The maximum value of ε'_{max} for a case in which

$$\frac{4\pi\sigma_D^0}{\varepsilon'_0} \gg \omega$$

can be calculated as [4]

$$\varepsilon'_{max} = \varepsilon'_0\left(\frac{\sigma_M}{\sigma_D}\right)^{1-s}$$

or

$$\varepsilon'_{max} = \varepsilon'_0\left(\frac{\rho_D}{\rho_M}\right)^{1-s},$$

where the resistivities of paraffin and graphite are $\rho_D = 3 \times 10^{10}\ \Omega$ m and $\rho_M = 4.1 \times 10^{-2}\ \Omega$ m, respectively [8]. In this case, $\varepsilon'_{max} \approx 5.8 \times 10^6$. Theoretical curve *4* in Fig. 2 has a small interval between the right and left branches. For example, an estimation at the level ε'_{max} yields the spacing between the left and right branches $\Delta x \approx 5 \times 10^{-5}$, and, in the region where the experimental and theoretical curves intersect ($\varepsilon' \approx 3 \times 10^4$), it yields $\Delta x \approx 1.2 \times 10^{-4}$. The initial components for the samples were weighted with an accuracy ensuring that they were in the range $\Delta x \approx 1.2 \times 10^{-4}$ at $x_c = 0.16$. We suggest that, in view of the stochastic processes occurring during the sample preparation (stirring, pouring, and cooling), none of the samples could enter the interval between the left and right branches at the level $\varepsilon' \approx 3 \times 10^4$ with respect to the conducting-phase content. This fact may account for the absence of a maximum in experimental curve *3* and a difference of two orders of magnitude for the experimental and theoretical values of ε' (Fig. 2, curves *3*, *4*) at $x = x_c$.

The experimental curve differs even more significantly from the theoretical one at $x > x_c$. It is of interest to find out the nature of the increase in ε' (and, therefore, the capacitance of the samples) at $x > x_c$. In [1], the increase in ε' was attributed to the increase in the contact surface between the metal and dielectric phases, and the decreasing thickness of the dielectric interlayers. Within the fractal model proposed, the increase in ε' is also attributed to the increase in the contact surface between the conducting phases belonging to different fractals and the decreasing thickness of the dielectric interlayers. In principle, the increase in ε' may be due to

an increase in both interfractal and intrafractal capacitances (which is, apparently, meant in [1]). These two types of capacitances can be distinguished by considering the kinetics of conducting-chain formation in fractals.

If the contact resistance of a filler is low, most of the branches in a fractal are conducting and the increase in ε' can mainly be attributed to the interfractal capacitance. In this case, the increase in ε' must be continuous. If the contact resistance is high, no significant difference should be observed in the rates of changes in the interfractal or intrafractal capacitances as x increases. In this case, fractal branches do not form conducting chains before the percolation threshold and, therefore, one might expect a slower increase in ε' before the percolation threshold. Indeed, in the paraffin–graphite (Fig. 2, curve *3*) and paraffin–semiconductor (Fig. 5, curves *1*, *2*) systems, ε' increases continuously and gradually as x increases. At the same time, for the paraffin–iron system, the portion of rapid increase in ε' (Fig. 2, curve *2*) arises only when the conducting-phase content becomes as high as ≈0.28, which is equal to the percolation threshold for this system. The best and worst conditions for the formation of conducting fractal chains are in the paraffin–graphite and paraffin–aluminum systems, respectively. Accordingly, the largest increase in ε' in the range of x under consideration is observed in the paraffin–graphite system, whereas the paraffin–aluminum system is characterized by the smallest change in ε'. On the whole, conducting chains are not formed in the paraffin–aluminum system (Fig. 1, curve *3*) and ε' increases little as x increases (Fig. 2, curve *1*). The plateau in the dependence $\varepsilon' = f(x)$ for the paraffin–iron system (Fig. 2, curve *2*) is in good agreement with the above model (Fig. 1, curve *2*, portion *FG*) using the terms proposed by Feder [22].

Analysis of the experimental results shows that it is the interfractal rather than intrafractal capacitance that makes the largest contribution to the increase in the capacitance as x increases. We suggest that fractals are formed simultaneously with an increase in x. When the fractals make contact with the electrodes, they make the electrode surface more developed, which is equivalent to the increase in the electrode area and the capacitance of the system. A fractal and an electrode can form both direct (electric contact) and capacitance bonds. In this model, the affiliation of a fractal to a particular electrode is determined from the fractal–electrode capacitance; i.e., the higher the capacitance, the stronger the capacitance bond.

In order to confirm this hypothesis as a whole, we experimentally estimated the fractal dimension of the conducting-phase surface as a function of the conducting-phase content. The experimental results for the two-dimensional space, after being recalculated for the three-dimensional (3D) space, are shown in Fig. 6. The method used in this study allowed us to perform the investigation only in the range $0.025 \le x \le 0.16$. At higher conducting-phase contents, the reliability of the results deteriorated; however, we can unambiguously state that the fractal dimension increases as the conducting-phase content increases and that it tends to 2.5 at $x \approx 0.16$. The data obtained indicate that the conducting-phase surface becomes more and more developed (increases in area), which confirms the above-stated hypothesis for the initial stage of fractal formation. Approximating these results to the entire range of variation in x, we can suggest that the dependence $\varepsilon' = f(x)$ is a steadily increasing function. As was mentioned above, the increase in ε' was attributed in [1] to the increase in the area of surface contact between the metal and dielectric phases and the decreasing thickness of dielectric interlayers at $x < x_c$, which corresponds to the model proposed. However, it is unclear why such an increase should cease at $x \approx x_c$ and be absent at $x > x_c$. Without casting doubt on the theoretical models [4–7], we can state that in real macrosystems the first chain is formed from a filler at $x \ge x_c$ but the conductivity of this chain differs from that of the filler. The reason for this is in the contact resistance, which can be rather high (when compared to the matrix resistance). This high contact resistance has many causes, some of which were mentioned above (for a detailed review of the data on contact resistances see [2, 13]).

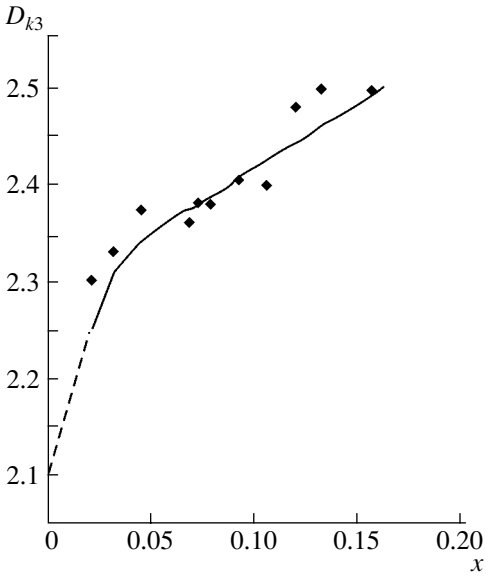

Fig. 6. The dependence of the fractal dimension of the surface of aggregates of filler particles D_{k3} on the volume fraction x of the filler for the paraffin–graphite system.

Thus, in our opinion, the increase in ε' in real macrosystems should also be continued at $x \ge x_c$. The experimental data of [5, 6], which are consistent with the theoretical model proposed in [4], were obtained for the metal–insulator transition in *n*-type Si [5] and for island films [6], which may have quite a different physical nature.

4.3. Dependences ε" = f(x)

Losses in insulators include conduction and relaxation losses [8, 10]. In the case under consideration, the relaxation losses are insignificant and make a noticeable contribution only at low conducting-phase contents [10]. The majority of the losses are due to the conduction. As a result, the dependence $\varepsilon'' = f(x)$ is determined, in many respects, by the function $\rho = f(x)$. The dependences $\varepsilon'' = f(x)$ were found to be rising for all the samples studied, with a limitation or sharp increase for conductors at $x \geq 0.48$ (Fig. 3, curves *1*, *2*). For the paraffin–graphite system (curve *1*), after the rising portion PR, a portion of rapid increase *RQ* begins at $x = 0.48$. We can suggest that, in this case, the resistivity of the composite is determined by the carbon framework ($\rho \approx 4 \times 10^{-3}$ Ω m), which corresponds to the values in the range $0.48 \lesssim x \lesssim 1$ for curve *1* in Fig. 1. For the paraffin–iron system (Fig. 3, curve *2*, portion *TU*), loss stabilization occurs at approximately the same values of $x \gtrsim 0.48$ but at higher resistivities ($\rho \approx 10$ Ω m) (portion FG in curve *2* of Fig. 1).

The experimental results indicate that the capacitance of the capacitor can be increased by introducing the conducting phase into it but at the cost of greater losses.

5. CONCLUSIONS

Based on the analysis of the data reported, we can draw the following conclusions.

(1) The concentration dependences were investigated for the following electrical parameters of the paraffin–conductor and paraffin–semiconductor systems: volume resistivity, electrical capacitance, *Q* factor, and permittivity. The percolation thresholds are determined for the paraffin–iron, paraffin–Fe_2O_3, and paraffin–CuO systems.

(2) It is found experimentally that the real part of the permittivity of the composites increases as the volume content of the conducting phase increases in the entire range of variations in *x*. The dielectric catastrophe in the vicinity of the percolation threshold was not found for the 3D macrosystems. Depending on the contact resistance of the particles of a used conductor, the capacitance and the real part of the permittivity may take relatively large values.

(3) It is shown experimentally that either a sharp increase in energy losses (for graphite) or their stabilization (for Fe) may occur at the conducting-phase content $x \approx 0.48$ in the composites. The character of the dependence $\varepsilon' = f(x)$ is mainly determined by the contact resistance of the conducting-phase particles. For semiconductors, the dependence $\varepsilon'' = f(x)$ is a steadily increasing function in the entire range of *x*.

(4) To explain the results obtained, a qualitative model is proposed, in which the change in electrical parameters as the conducting-phase content increases is regarded as growth of fractals. The increase in the capacitance and, respectively, the real part of the permittivity occurs due to the formation and growth of fractals and the increase in the surface area. The growth of fractals is interpreted as an increase in the equivalent area of the capacitor electrodes. The formation of conducting chains near fractals and, respectively, the kinetics of the entire process significantly depend on the contact resistance of the particles. The increase in the capacitance and the real part of the permittivity with an increase conducting-phase content is due to the increase in the interfractal capacitance.

REFERENCES

1. E. V. Kharitonov, *Dielectric Materials with Inhomogeneous Structure* (Radio i Svyaz', Moscow, 1983) [in Russian].
2. I. A. Chmutin, S. V. Letyagin, V. G. Shevchenko, and A. T. Ponomarenko, Vysokomol. Soedin. **36**, 699 (1994).
3. A. B. Khanikaev, A. B. Granovskiĭ, and J. P. Clerc, Fiz. Tverd. Tela (St. Petersburg) **44**, 1537 (2002) [Phys. Solid State **44**, 1611 (2002)].
4. A. L. Efros and B. I. Shklovskii, Phys. Status Solidi B **76**, 475 (1976).
5. V. E. Dubrov, M. E. Levinshtéin, and M. S. Shur, Zh. Éksp. Teor. Fiz. **70**, 2014 (1976) [Sov. Phys. JETP **43**, 1050 (1976)].
6. V. L. Bonch-Bruevich, Vestn. Mosk. Univ., No. 5, 550 (1975).
7. A. V. Néimark, Zh. Éksp. Teor. Fiz. **98**, 611 (1990) [Sov. Phys. JETP **71**, 341 (1990)].
8. V. A. Sotskov and S. V. Karpenko, Zh. Tekh. Fiz. **73** (1), 106 (2003) [Tech. Phys. **48**, 100 (2003)].
9. A. M. Petrov, Kh. V. Bal'yan, and A. T. Troshchenko, *Organic Chemistry* (Vysshaya Shkola, Moscow, 1963), p. 63 [in Russian].
10. V. V. Pasynkov, *Materials for Electronic Engineering* (Vysshaya Shkola, Moscow, 1980), p. 155 [in Russian].
11. B. I. Shklovskiĭ, Fiz. Tekh. Poluprovodn. (Leningrad) **13**, 93 (1979) [Sov. Phys. Semicond. **13**, 53 (1979)].
12. *Chemical Encyclopedic Dictionary* (Sovetskaya Éntsiklopediya, Moscow, 1983) [in Russian].
13. V. E. Gul' and L. Z. Shenfil', *Conducting Polymer Compositions* (Khimiya, Moscow, 1984), p. 72 [in Russian].
14. *Tables of Physical Data: Handbook*, Ed. by I. K. Kikoin (Atomizdat, Moscow, 1976) [in Russian].
15. A. R. Hippel, *Dielectric Materials and Applications* (Wiley, New York, 1954; Gosénergoizdat, Moscow, 1959).
16. V. P. Berzan *et al.*, in *Handbook on Capacitors*, Ed. by V. V. Ermuratskiĭ (Shtiintsa, Kishinev, 1982), p. 27 [in Russian].
17. G. V. Kozlov, Yu. G. Yanovskiĭ, and A. K. Mikitaev, Poverkhnost, No. 8, 43 (1999).
18. G. V. Kozlov, Yu. G. Yanovskiĭ, and A. K. Mikitaev, Mekh. Kompoz. Mater. **34**, 539 (1988).
19. G. N. Vstovskiĭ, A. G. Kolmakov, and F. Terent'ev, Metally, No. 4, 175 (1993).
20. J. M. Ziman, *Models of Disorder: the Theoretical Physics of Homogeneously Disordered Systems* (Cambridge Univ. Press, Cambridge, 1979; Mir, Moscow, 1982).
21. B. I. Shklovskiĭ and A. L. Éfros, *Electronic Properties of Doped Semiconductors* (Nauka, Moscow, 1979; Springer, New York, 1984).
22. J. Feder, *Fractals* (Plenum, New York, 1988; Mir, Moscow, 1991).

Translated by Yu. Sin'kov

Semiconductors, Vol. 39, No. 2, 2005, pp. 261–264. Translated from Fizika i Tekhnika Poluprovodnikov, Vol. 39, No. 2, 2005, pp. 276–280.

AMORPHOUS, VITREOUS, AND POROUS SEMICONDUCTORS

On the Injection Current Mechanism in Light-Emitting *p–i–n* Structures Based on *a*-$Si_{1-x}C_x$:H Hydrogenated Amorphous Alloys

A. A. Andreev

Ioffe Physicotechnical Institute, Russian Academy of Sciences, St. Petersburg, 194021 Russia
e-mail: arkand@gvg.ioffe.ru

Submitted April 29, 2004; accepted for publication May 17, 2004

Abstract—Current–voltage (*I–V*) characteristics of thin-film *p–i–n* and *pDiDn* structures in which the *i* layer is based on *a*-$Si_{1-x}C_x$:H hydrogenated amorphous alloys and the *p* and *n* layers are composed of doped *a*-Si:H were studied. To account for the specific features of these *I–V* characteristics, i.e., the small values of the constant *A* in the exponential dependence of the current on the voltage, $I \propto \exp(AV)$, a mechanism of tunneling injection from the *n* layer directly into the tail of localized states is suggested. The tunneling process has a multistep nature and is, in general terms, similar to the recombination current in heterojunctions. The high density of localized states in the energy gap of *a*-$Si_{1-x}C_x$:H near the band edge (~10^{20}–10^{21} cm^{-3}), as well as the density's dependence on the composition of this compound, make it possible to obtain a constant *A* close to the experimental value and to explain the decrease in *A*, which is observed as the content of carbon in the alloy increases. At high biases, there occurs a transition from monopolar to double injection and from the nonradiative to radiative recombination of nearly free electrons and holes. Structures with $x = 0.4$–0.6 exhibited a weak electroluminescence in the visible spectral range, with the emission peak being Stokes-shifted by ~$0.25E_g$ of the *i* layer. © *2005 Pleiades Publishing, Inc.*

1. INTRODUCTION

The system of *a*-$Si_{1-x}C_x$:H hydrogenated amorphous alloys has been the object of extensive studies because it possesses a number of unique properties. In this system, the energy gap E_g may vary from 1.7 eV ($x = 0$) to 3.5 eV ($x = 1$); moreover, alloys with $x < 0.6$ show a high photoconductivity, and those with $x \geq 0.4$ exhibit a photoluminescence in the visible spectral range at room temperature. At $x < 0.15$ the alloys can be doped and, consequently, *p–i–n* and other active multilayer structures, e.g., superlattices with specific properties, can be formed on the basis of a *a*-$Si_{1-x}C_x$ layer [1, 2]. To optimize *p–i–n* and other structures, e.g., *pDiDn* structures with a tunnel dielectric layer (*D*), which exhibit electroluminescence (EL) in the visible spectral range, it is necessary to elucidate the mechanism of current transport in these structures. The known studies of injection currents in light-emitting diodes based on amorphous semiconductors have been concerned with structures that have tunnel dielectric layers, i.e., *pDiDn* structures [3, 4]. The very fact that an insulator is present predetermines the choice of the Fowler–Nordheim tunneling emission as the main process governing the current–voltage (*I–V*) characteristic. Indeed, it is possible to satisfactorily describe experimental data in terms of this mechanism, but only in a narrow range of relatively high currents, from 10^{-4} to 10^{-1} A/cm^2, which corresponds to biases of $\gtrsim$(6–10) V. Our analysis of both published data and our own experimental *I–V* characteristics demonstrated that it is impossible to apply the Fowler–Nordheim relations at lower biases or to explain, in terms of this mechanism, the fact that the rate at which the current increases with voltage depends on the composition of the *i* layer, i.e., on *x*. The main difficulty is that, at the barrier parameters chosen for the range of biases in which agreement with the Fowler–Nordheim formula can be achieved, the tunneling currents fall dramatically and become negligible at biases of less than 5 V. This calculated result completely disagrees with the run of the experimental *I–V* characteristics. This means that the mechanism of current transport in light-emitting diodes based on silicon–carbon amorphous alloys remains unclear and, therefore, it is this mechanism that is the subject of this study. For a broader approach to the problem, it seemed justified to choose both types of structures, *p–i–n* and *pDiDn*, as objects of study in order to assess the role played by the complicating factor of the tunnel insulator.

2. EXPERIMENTAL PROCEDURE: FABRICATION OF *p–i–n* AND *pDiDn* STRUCTURES

The structures were fabricated by successive deposition of the constituent layers in a vacuum chamber for the decomposition of silane (SiH_4) and silane–methane mixtures ($SiH_4 + CH_4$) in a radio-frequency glow-dis-

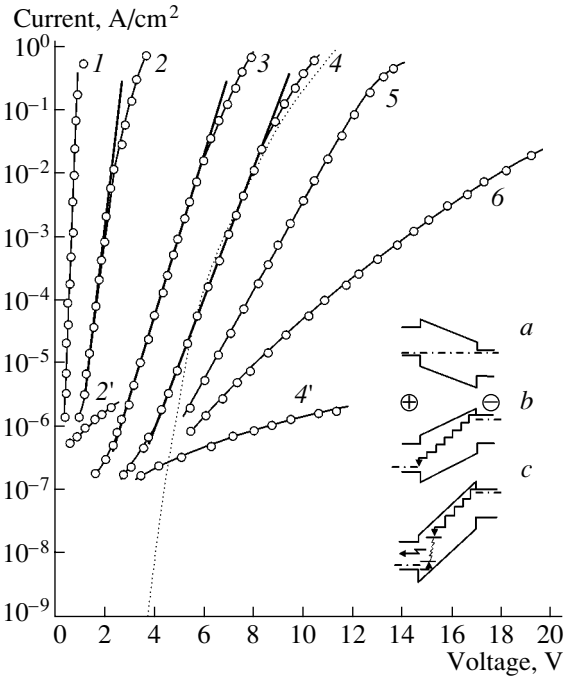

Forward current–voltage characteristics of (*1*–*5*) *p*–*i*–*n* structures and (*6*) a *pDiDn* structure with *a*-$Si_{1-x}C_x$:H layers. *x*: (*1*) 0, (*2*) 0.3, (*3*) 0.4, (*4*) 0.5, and (*5*, *6*) 0.6. E_g: (*1*) 1.7, (*2*) 2.1, (*3*) 2.45, (*4*) 2.5, and (*5*, *6*) 2.6 eV. (*2*', *4*') Reverse characteristics corresponding to forward characteristics *2* and *4*. Bold solid lines show the calculation in terms of the model of the tunneling recombination current, and the dotted line shows the calculation by Fowler–Nordheim at a barrier height of 0.3 eV, which gives the best agreement with the experiment. Inset: simplified (without the space charge region) schematic of the *p*–*i*–*n* structure at biases of (*a*) $V = 0$, (*b*) $V > 0$, and (*c*) $V >$ EL threshold.

charge plasma. As the material of the doped layers of both *p*- and *n*-types, we chose amorphous silicon *a*-Si:H obtained under conditions in which silane was strongly diluted with hydrogen (20% SiH_4 in H_2) at an increased power of the RF discharge and growth rates of <2.0 Å/s. The doping to obtain *p*- and *n*-type conduction was effected by the addition of up to 2% diborane (B_2H_6) or phosphine (PH_3), respectively. The layers deposited using this technique provided the highest value of the built-in potential V_{bi}. To obtain an *i* layer with a prescribed energy gap E_g, the composition of the silane–methane mixture was chosen empirically. As a criterion for evaluating E_g, we took the optical gap determined from the absorption spectra in terms of the Tauc law $\sqrt{\alpha h\nu} = \beta(h\nu - E_g)$ (α is the absorption coefficient; $h\nu$, the photon energy; and β, the coefficient). A transparent electrically conducting electrode was formed on the basis of the oxide $In_xSn_yO_z$ (ITO). The influence exerted by the microstructure of the oxide on the properties of the *p* layer was diminished by depositing a 50-Å-thick spacer heavily doped with phosphorus. The resulting abrupt *n*–*p* junction, which is of a tunneling type, created an ohmic contact between the structure and ITO. The second electrode was deposited by magnetron sputtering of an AlMg alloy. In the fabrication of a *pDiDn* structure, layers grown with a 10% SiH_4 + 90% CH_4 mixture served as dielectric layers. It would appear that the quality of such tunnel dielectric layers is not very high, but they still raise the intensity of EL to a certain extent. The layer thicknesses in the structure were 100 (*p* layer), 600 (*i* layer), 250 (*n*-layer), and 50 Å (*D*). The growth of the constituent layers and the structure as a whole was monitored with a laser interferometer. The quality of the *p*–*i*–*n* structures was determined by measuring the photovoltaic characteristics: built-in potential V_{bi} and collection efficiency. If V_{bi} is known, it is possible to roughly evaluate the density of defect states at the *p*/*i* and *n*/*i* interfaces of the structure. The collection efficiency furnishes information about the transport properties of nonequilibrium carriers, specifically, about the correspondence of the diffusion length to the thickness of the *i* layer. Measurements were made at a photon flux of $\sim 2 \times 10^{16}$ cm^{-2} s^{-1} and photon energy of $h\nu \approx 2.0$ eV. As is shown by the measurements, V_{bi} may be as high as 1.0–1.1 eV for structures with $x \leq 0.6$, and the collection efficiency falls dramatically as *x* increases: from ~0.8 for $x = 0.3$ to 0.2 for $x = 0.6$. This result suggests that the ambipolar diffusion length is comparable with the thickness of the structure. Consequently, the through (without charge accumulation) transport of carriers across the structure governs the current transport mechanism up to at least $x = 0.6$; moreover, the *i* layer is not the limiting element in the series circuit of *p*–*i* and -*i*–*n* junctions. The best confirmation of this conclusion is the diode effect observed in the fabricated structures, which is as high as 10^6 at biases exceeding 3 V.

3. RESULTS AND DISCUSSION

The dark *I*–*V* characteristics of *p*–*i*–*n* structures with different compositions for the *i* layer of *a*-$Si_{1-x}C_x$:H ($x = 0.3$ ($E_g = 2.1$ eV) and $x = 0.6$ ($E_g = 2.6$ eV)) and *pDiDn* structures with $x = 0.6$ are shown in the figure. For comparison, the figure also shows an *I*–*V* characteristic of a *p*–*i*–*n* structure based on *a*-Si:H. It can be seen that the experimental curves plotted in the coordinates $\log I = f(V)$ are, for the most part, satisfactorily fitted by straight lines. Consequently, the *I*–*V* characteristics are described by the exponential law $I = I_0 \exp(AV)$, where *A* is a constant. Deviations from the exponential behavior are observed at low and high biases, which may be due to shunting ohmic currents and to current limitation in the case of a double injection, respectively. The second result of fundamental importance, obtained by analysis of the curves, is that the slope of the *I*–*V* characteristics plotted in the semilog coordinates is considerably smaller than the maximum possible value predicted by the theory of overbarrier diffusion currents in *p*–*n* junctions. This is clearly seen when the slopes of

the *I–V* characteristics of *p–i–n* structures based on *a*-Si:H and *a*-$Si_{1-x}C_x$:H are compared. In the structure based on *a*-Si:H, $A \approx 20\ V^{-1}$. If *A* is understood in terms of the diffusion theory as $1/nkT$, this value corresponds to $n = 1.5$ at $T = 300$ K. For the structure based on *a*-$Si_{1-x}C_x$:H, the constant *A* varies with *x* from 5 to 1.5, which corresponds to $n = 6–20$. So large values of *n* cannot be understood in terms of the diffusion theory. However, other experimental observations have been made, according to which the constant *A* is considerably smaller than the theoretical lower limit. In the known cases, *A* decreases if the *i* region of the *p–i–n* junction receives additional light doping or the temperature is lowered [5]. In all the anomalous cases of a high value of *A*, there is good reason to attribute the rise in the constant *A* to the influence exerted by localized states near band edges on the carrier transport in the *p–n* junction.

As the density of localized states in the band tails (*N**) in an amorphous material is as high as $10^{20}–10^{21}$ cm^{-3} at the band edges, it is reasonable to assume that the role of these states will also be important in the *p–i–n* structure based on *a*-$Si_{1-x}C_x$:H. An additional factor making this role even more critical is the existence of band discontinuities at the *n*/*i* and *p*/*i* interfaces, i.e., between *a*-$Si_{1-x}C_x$:H and *a*-Si:H. According to [6, 7], these discontinuities are as large as 0.3 eV in the conduction band and 0.5 eV in the valence band. The height of the barriers formed by these discontinuities makes the thermally activated overbarrier transport of carriers from doped regions into the intrinsic *i* layer virtually impossible. Thus, the only remaining way to inject carriers is underbarrier tunneling. Owing to the high density of the states at the tunneling level, this process will, in all probability, involve localized states, because the presence of intermediate steps in a tunneling transition facilitates the tunneling. The multistep nature of the process also allows changes in the electron energy. Since the loss of energy is more probable, the motion of an electron qualitatively resembles a "downstairs motion." At a high density of the states in the energy gap and, accordingly, at their weak localization, a carrier tunnel-injected into the *p–i–n* structure will continue to drift in the field created by the positive bias. The final stage of this motion is recombination via acceptor states of the *p* layer. This process is illustrated in the inset in the figure (inset *b*). This scheme of tunneling, as well as the terminology "multistep tunneling recombination" and "tunneling recombination current," was first suggested by Riben and Fuecht [8] to describe forward currents in heterojunctions under conditions in which a diffusion current is suppressed by a barrier at the interface in the heterojunction. The process of multistep tunneling was analyzed theoretically in [8] in terms of a model of an excess current in tunnel diodes [9]. The theory takes into account the dependence of the width of the space charge region on the applied voltage and introduces, via this dependence, the density of the localized states in the energy gap into the final result. The current–voltage characteristic for the case of multistep tunneling injection, $I_{t/r}(V)$, is determined by the increasing exponential dependence on voltage, with the constant $A_{t/r}$ in the exponent containing the parameter of the material (the density of localized states *N**):

$$I_{t/r} = I_{0t/r}\exp(\beta T)\exp(A_{t/r}V), \qquad (1)$$

where $A_{t/r} = 4(m^*\varepsilon)^{1/2}/(1+\gamma)3\pi\hbar n^*$ and $\gamma \geq 1$.

The value of *N** is equal to a certain average density of the states in the tunneling range, and the parameter γ describes the excess of the density of the states in the tail of the valence band over that in the tail of the conduction band. The density of states *N* in amorphous semiconductors is not constant, but is distributed over energy *E* in accordance with the Urbach rule: $N = N_{be}\exp(-E/E_0)$, where N_{be} is the density at the band edge and E_0 is a constant equal to ~60 meV for *a*-Si:H and 150 meV for *a*-$Si_{1-x}C_x$:H at $x = 0.4–0.6$. A higher value of E_0 corresponds to a slower decay of the density of states *N* from the band edge into the energy gap. Thus, a certain average value *N**, which can be used to calculate the *I–V* characteristic, depends on the composition of the *i* layer and grows as *x* increases. As *N** determines the slope of the *I–V* characteristic, the observed decrease in the slope ratio of the dependence $\log I = f(V)$ can be explained in the most straightforward way. The increase in N_{Ef} (density of the states at the Fermi level pinned at the midgap of *a*-$Si_{1-x}C_x$ alloys) from 10^{17} cm^{-3} for $x = 0$ to 10^{19} cm^{-3} at $x = 0.6$ is also confirmed by ESR measurements [10]. At $N_{Ef} = 10^{19}$ cm^{-3} and $E_0 = 150$ meV, the density of the states at the band edge is as high as 10^{21} cm^{-3} ($E_g \approx 2.6$ eV).

On the assumption that the injecting *n–i* junction is current-limiting and, consequently, governs the *I*(*U*) characteristic, the substitution of $N^* = 8 \times 10^{20}$ cm^{-3} into (1) led to agreement between the calculated and experimental *I*(*U*) characteristics for an *i* layer with $x = 0.5$ at $\gamma = 3$. For $x = 0.3$, agreement between the slopes is observed at $N^* = 2 \times 10^{20}$ cm^{-3}, which also corresponds to the change in the density of the states with *x*. Additional confirmation of the mechanism of multistep tunneling injection is provided by temperature measurements. As temperature does not appear in the exponent in (1), the slope of the *I–V* characteristic should be temperature-independent. *I–V* characteristics were measured at temperatures ranging from 200 to 400 K. Below 300 K, an approximately parallel shift of the *I–V* characteristic to higher biases was observed as the temperature was increased, whereas, at $T > 300$ K, the slope increased as the temperature increased. Presumably, thermally activated tunneling from levels lying above the conduction band edge in the contact layer becomes important in this case, because the overbarrier transport still remains improbable at 400 K.

An additional decrease in the slope ratio of the $\log I = f(V)$ dependence, observed for *pDiDn* struc-

tures, is probably due to the introduction of *D* layers and the redistribution of voltage across the elements of the structure, rather than to a change of the injection mechanism for the Fowler–Nordheim tunneling, because the *I–V* characteristic remains exponential. This conclusion seems to be justified for one more reason: the wider-bandgap Si–C alloy used as the insulator does not differ significantly in the distribution of localized states the in band tails from the composition with $x = 0.6$.

As regards the analysis of reverse *I–V* characteristics, the following should be noted. A current transport mechanism similar to that considered above is also possible in this case. However, tunneling can occur under a reverse bias only from states, which are occupied by electrons, at the bottom of the conduction band of the *p* layer. Accordingly, the injection currents will be determined by the thermally equilibrium density of electrons in the conduction band of the *p* layer. However, this density is 8–10 orders of magnitude lower than that of the *n*-type layer of the injecting contact in the case of forward currents. For this reason, the tunneling currents should be negligible under a reverse bias. The experimentally observed reverse currents are, in all probability, due to strong-field effects, of the Frenkel–Pool type, in the *i* layer.

The above mechanism of injection under a forward bias is monopolar and cannot account for the observed EL because of the absence of nonequilibrium holes in the *i* layer. The assumption that electron–hole pairs are generated by impact-ionization mechanisms contradicts the EL characteristics, such as the uniform distribution of the emission intensity over the entire area of the structure; the absence of current instabilities or EL fatigue; the reproducibility of the EL threshold; and, finally, the bimolecular dependence of the emission intensity on current, $I_{EL} \propto I^{1.8}$, and its very weak temperature dependence. According to the results of the present study, the rise in the total emission intensity observed as the temperature is lowered is insignificant, with an activation energy $\Delta E = 0.028$ eV, which can be expected only for nearly free electrons and holes. In this context, it only remains to assume that the *p–i* junction also injects carriers, but of the opposite sign. The band discontinuity at the *p*/*i* interface creates a barrier that is a factor of 1.5–2 higher than that at the *n*/*i* interface. As a result, holes are injected from the *p* layer at higher biases, and it is this that predetermines the threshold nature of the EL. As the hole density increases, nonradiative recombination, via the acceptor centers of the *p* layer, of the electrons injected at the *n*/*i* interface (figure, inset *b*) changes for radiative electron–hole recombination (figure, inset *c*). Partial thermalization of the electrons during their transit across the base region of the *p–i–n* structure accounts for the Stokes shift of the EL. In the scheme suggested here, the current flowing through the structure is limited only by electrons, under all conditions; consequently, the injection of holes should have no effect on the shape of the *I–V* characteristics, which is actually the case. The emission peak in the experimental EL spectra is strongly broadened (FWHM 0.5 eV) and has extended wings. The position of the peak depends on the technological conditions of the process. The maximum energy of the EL peak was ~2.0 eV.

4. CONCLUSIONS

The *p–i–n* and *pDiDn* structures based on amorphous semiconductors, with doped *a*-Si:H forming the *p* and *n* layers and *a*-$Si_{1-x}C_x$:H forming the intrinsic *i* layer, were fabricated. Because of the band discontinuities at the *p*/*i* and *i*/*n* interfaces, the structures had the form of two in-series connected heterojunctions.

In *p–i–n* structures with *x* in the range 0.3–0.6, a photovoltaic effect is observed, with a built-in potential of ~1.0–1.1 eV and a collection efficiency of 0.8–0.2, depending on the composition. This result indicates that the quality of the active *p–i–n* structures is rather high for such complex materials.

The forward dark *I–V* characteristics are described by an exponential dependence. However, the constant in the exponent is considerably smaller than the value predicted by the diffusion theory and depends on the composition of the *i* layer. To explain such an *I–V* characteristic, a mechanism of tunneling recombination currents is suggested. This mechanism is typical of heterojunctions with a suppressed overbarrier current and high density of states at the interface.

At injection currents exceeding >100 mA/cm^2, a weak electroluminescence in the visible spectral range is observed. This electroluminescence has a broadened spectrum with a Stokes shift of ~$0.25E_g$. It is assumed that this electroluminescence results from the double injection and radiative recombination of nearly free electrons and holes.

REFERENCES

1. D. Kruangam, M. Deguchi, T. Toyama, *et al.*, IEEE Trans. Electron Devices **35**, 957 (1988).
2. G. Chen, F. Zhang, and Sh. Yan, J. Non-Cryst. Solids **137–138**, 1263 (1991).
3. S. M. Paashe, T. Toyama, H. Okamoto, and Y. Hamakawa, IEEE Trans. Electron Devices **36**, 2895 (1989).
4. A. B. Pevtsov, A. V. Zherzdev, N. A. Feoktistov, *et al.*, Int. J. Electron. **78**, 289 (1995).
5. A. Madan, W. Czubatyi, J. Yang, *et al.*, Appl. Phys. Lett. **40**, 234 (1982).
6. W. Guang-Pu, D. Kruangam, T. Endo, *et al.*, J. Non-Cryst. Solids **114**, 735 (1989).
7. L. Ley and H. Richter, J. Non-Cryst. Solids **114**, 238 (1989).
8. A. R. Riben and D. L. Feucht, Int. J. Electron. **20**, 583 (1966).
9. S. M. Sze, *Physics of Semiconductor Devices*, 2nd ed. (Wiley, New York, 1981; Mir, Moscow, 1984).
10. S. Liedtke, K. Jahn, F. Finger, and W. Fuhs, J. Non-Cryst. Solids **77–78**, 1429 (1985).

Translated by M. Tagirdzhanov

Semiconductors, Vol. 39, No. 2, 2005, pp. 265–268. Translated from Fizika i Tekhnika Poluprovodnikov, Vol. 39, No. 2, 2005, pp. 281–284.

PHYSICS OF SEMICONDUCTOR DEVICES

A Graded-Gap Photoelectric Detector for Ionizing Radiation

L. Dapkus, K. Požela, J. Požela, A. Šilėnas, V. Jucienė, and V. Jasutis

Institute of Semiconductor Physics, Vilnius, 01108 Lithuania

Submitted June 21, 2004; accepted for publication July 4, 2004

Abstract—A heterostructure consisting of a graded-gap *p*-$Al_xGa_{1-x}As$ layer on an *n*-GaAs substrate is studied in relation to its role as a photoelectric-response detector of X-ray photons and α particles. It is found that the current–power sensitivity of the detector is as high as 0.13 A/W and the voltage–power sensitivity exceeds 10^6 V/W. The effect of preliminary irradiation with 5.48-MeV α particles (^{241}Am) on the detector's sensitivity is studied. It is established that the detector's sensitivity is reduced by a factor of 1.5–2 after irradiation with α particles at a dose of 5×10^9 cm^{-2}. A further increase in the radiation dose to 4×10^{10} cm^{-2} does not affect the detector's sensitivity. © *2005 Pleiades Publishing, Inc.*

1. INTRODUCTION

Studies of the behavior of graded-gap ionizing-radiation detectors under irradiation with α particles show that the radiation resistance of detectors with an optical response is much higher than that of detectors with a current response [1]. It has been shown that the rate of recombination for nonequilibrium charge carriers in a graded-gap crystal increases by a factor on the order of 30 when irradiated with 5.48-MeV α particles (^{241}Am) at a dose $n_d = 10^9$ cm^{-2}. Correspondingly, the number of charge carriers collected by the graded-gap field of the crystal (i.e., the current response of the graded-gap detector) decreases.

Optical response (luminescence) through the wide-gap window of the detector at the same dose of α radiation decreases by a factor of only 1.5 owing to an increase in the radiative-recombination rate when irradiated with α particles [1].

However, the external quantum yield of the optical radiation is found to be very low (lower than 2%) due to the small angle of total internal reflection at the interface between $Al_xGa_{1-x}As$ and air. Therefore, in order to prevent radiation losses at the interface between $Al_xGa_{1-x}As$ and air, it is reasonable to collect the generated optical radiation within the crystal by placing the photodetector (the GaAs *p*–*n* junction) at the wide-gap side of the graded-gap structure. Such structures, with a photoelectric response at the *p*–*n* junction, have been used as ionizing-radiation detectors in a number of studies [2, 3].

In this paper, we report the results of studying ionizing-radiation (X-ray photons and α particles) detectors with a photoelectric response and consider the effect of irradiation with α particles on the characteristics of these detectors.

2. A GRADED-GAP IONIZING-RADIATION DETECTOR WITH A PHOTOELECTRIC RESPONSE

In Fig. 1, we show the structure of the detector schematically. It consists of a *p*-type graded-gap $Al_xGa_{1-x}As$ layer grown by liquid-phase epitaxy on an *n*-GaAs substrate. The Al content amounted to $x = 0.4$ at the substrate and to $x = 0$ on the surface of the graded-gap layer. We grew three types of detector structures that differed in the thickness L of their graded-gap layer: L = 18 μm (structure D18), 25 μm (D25), and 50 μm (D50).

The radiation to be detected was incident on the narrow-gap side of the graded-gap layer. X-ray photons with a characteristic line at 8 keV (the Cu anode) were used as the source of ionizing radiation. A ^{241}Am isotope served as the source of 5.48-MeV α particles.

The photoelectric response of the detector is represented by the photovoltage (or photocurrent) that appears at the $Al_xGa_{1-x}As$/GaAs *p*–*n* junction as a result of the absorption of the recombination radiation

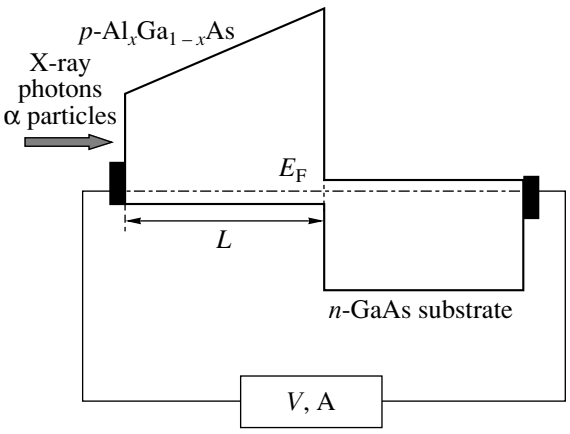

Fig. 1. The structure of the photoelectric detector and a schematic representation of the measurement method.

1063-7826/05/3902-0265$26.00 © 2005 Pleiades Publishing, Inc.

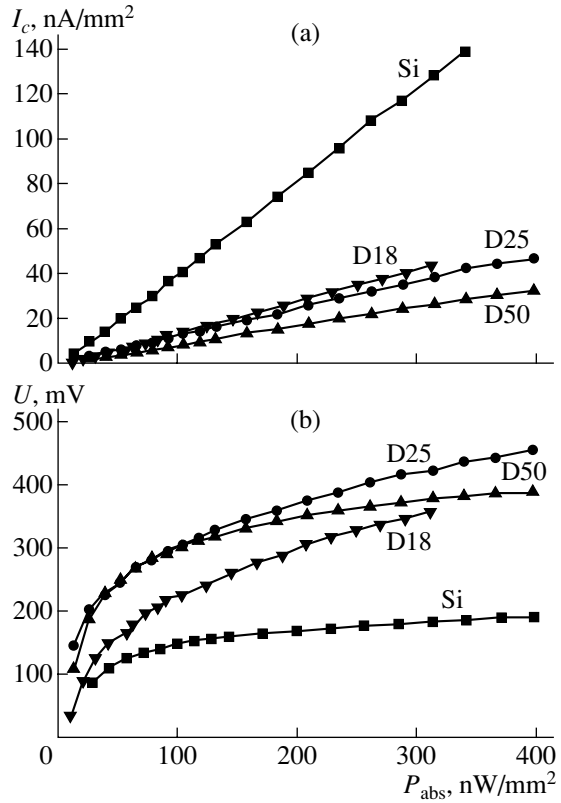

Fig. 2. The (a) current I_c and (b) voltage U response of photoelectric detectors D18, D25, and D50 in relation to the absorbed power P_{abs} of X-ray radiation. The characteristics of Si *p–i–n* detectors of X-ray radiation are also shown for comparison.

from the nonequilibrium electron–hole pairs generated in the graded-gap layer by external ionizing radiation. The magnitude of the photoelectric response depends on the rate at which the electron–hole pairs are generated by external ionizing radiation and on the internal quantum yield of the recombination radiation.

The rate at which the electron–hole pairs are generated depends on the absorbed-radiation power P_{abs} and also the minimal energy required for the generation of an electron–hole pair E_{th}. For GaAs, $E_{th} = 4$ eV.

The internal quantum yield is given by

$$\eta = \frac{1}{1 + \tau_r/\tau_{nr}}, \quad (1)$$

where τ_r and τ_{nr} are the characteristic times taken for the radiative and nonradiative recombination of electron–hole pairs, respectively.

One half of the recombination radiation reaches the wide-gap side of the *p–n* junction, while the other half, due to re-emission, is incident on the *p–n* junction. The effective quantum yield of the recombination radiation into the wide-gap portion of the graded-gap crystal can be estimated as

$$\eta_{eff} = \frac{1}{2}\eta\left(1 + \frac{1}{2}\eta + \frac{1}{4}\eta^2 + \ldots\right). \quad (2)$$

The short-circuit current of the GaAs *p–n* junction is equal to

$$I_{ph} = \frac{P_{abs}}{E_{th}}\eta_{eff}. \quad (3)$$

The photovoltage across the *p–n* junction is given by

$$U = \frac{kT}{q}\ln\frac{I_s + I_{ph}}{I_s}, \quad (4)$$

where I_s is the saturation current of the *p–n* junction, q is the elementary charge, and kT is the temperature expressed in energy units.

It should be noted that the shorter the radiative-recombination time, the larger the photocurrent I_{ph}. The response speed of the detector also depends on the above time. In the structures under consideration, $\tau_r \approx 10^{-9}$ s is attained by heavily doping the graded-gap crystals with Zn acceptors ($p \approx 10^{18}$ cm^{-3}), which are the radiative-recombination centers.

In Fig. 2, we show the experimental results of measuring the photoelectric response in relation to the absorbed power of X-ray radiation with the photon energy of 8 keV for three different detectors. As was mentioned above, these detectors have different values of the thickness L for the graded-gap layer: $L = 18$ μm (detector D18), 25 μm (D25), and 50 μm (D50).

The current sensitivity is $\beta_I = 0.13$ A/W for D18 and D25, and $\beta_I = 0.07$ A/W for D50. Correspondingly, the effective quantum yield is equal to $\eta_{eff} = 0.52$ for samples D18 and D25, and $\eta_{eff} = 0.27$ for sample D50.

The low effective quantum yield for the sample with a thick graded-gap layer (D50) can be attributed to the absorption of recombination radiation in the layer itself.

The largest current that can be attained at $\eta_{eff} = 1$ is $I_{max} = 0.25P_{abs}$. The voltage–power sensitivity of the detector exceeds 10^6 V/W at $P_{abs} \approx 50$ nW/mm^2. For comparison, Fig. 2 shows the experimental characteristics of a silicon *p–i–n* detector for X-ray radiation.

It is noteworthy that the current response of a silicon detector of X-ray radiation is larger, by a factor of 3, than that of a graded-gap $Al_xGa_{1-x}As$ detector as a result of a lower threshold energy E_{th}(Si) for the generation of an electron–hole pair.

The photovoltage appearing at the $Al_xGa_{1-x}As$/GaAs *p–n* junction is two times higher than that at a silicon *p–n* junction as a result of a lower saturation current j_s in $Al_xGa_{1-x}As$, which has a wider band gap compared to silicon (Fig. 2b).

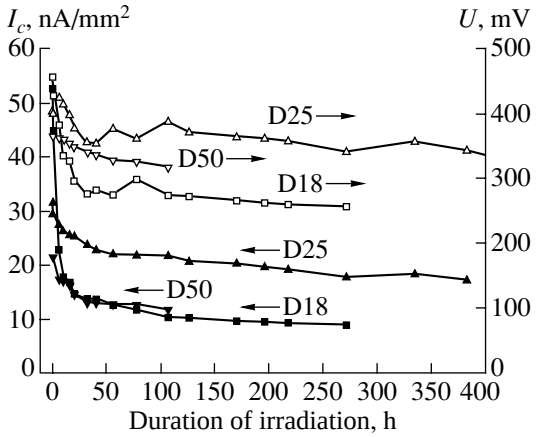

Fig. 3. The current I_c and voltage U response of photoelectric detectors D18, D25, and D50 at the power density of the incident X-ray radiation $P = 3.7 \times 10^{-5}$ W/cm^2 in relation to the duration of preliminary irradiation with α particles. One hour of irradiation corresponds to a dose of 10^8 cm^{-2} of α particles.

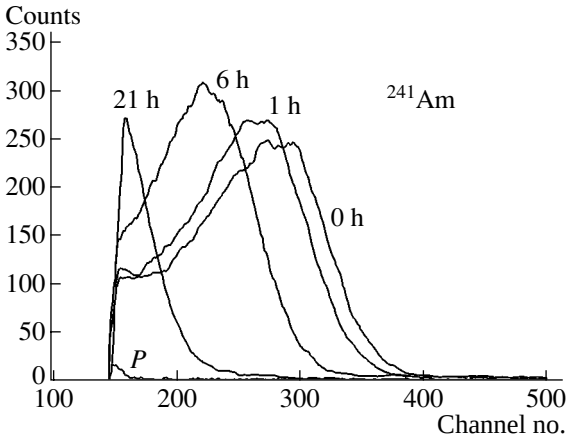

Fig. 4. The amplitude spectrum in the current response of a graded-gap photoelectric detector to irradiation with α particles for various doses of preliminary irradiation with α particles. The dose of irradiation is expressed in hours (see Fig. 3). The background signal, in the absence of a source of α particles, is denoted by *P*.

3. THE BEHAVIOR OF THE GRADED-GAP DETECTOR WITH A PHOTOELECTRIC RESPONSE UNDER IRRADIATION WITH ALPHA PARTICLES

The α-particle source (^{241}Am) was positioned directly on the surface of the narrow-gap side of the graded-gap layer. The 5.48-MeV α particles penetrated through the $Al_xGa_{1-x}As$ layer to a depth of about 21 μm. The α particles penetrated beyond the GaAs *p–n* junction in sample D18, whereas they stopped in the graded-gap $Al_xGa_{1-x}As$ layer before reaching the *p–n* junction.

In Fig. 3, we show the dependence of the photoelectric response of the X-ray detector on the duration of the irradiation with α particles. The irradiation dose amounted to 10^8 cm^{-2} per hour.

A decrease in the photocurrent I_{ph} and photovoltage U is observed as the dose of irradiation is increased. In the sample D18, the decrease in I_{ph} and U is especially pronounced at the initial stage of irradiation: after irradiation for 20 h, the current response decreases by a factor of 8 and the voltage response decreases by a factor of 2. Such a drastic decrease in the structure sensitivity at low radiation doses is probably related to the structural damage generated in the vicinity of the GaAs *p–n* junction. In samples D25 and D50, where the α particles do not reach the GaAs *p–n* junction, the decrease in the sensitivity as the dose increases is less pronounced. In sample D25, the sensitivity decreases by a factor of 1.5 after irradiation with α particles for 100 h. If the duration of the irradiation exceeds 100 h, the sensitivity of detectors D18 and D25 depends only slightly on the radiation dose. Thus, the effective quantum yield and, consequently, the ratio between the rates of the radiative and nonradiative recombination becomes independent of the radiation dose if the latter exceeds 10^{10} cm^{-2}. The defects produced by the α particles in the $Al_xGa_{1-x}As$ layer increase the radiative-recombination rate, so that an increase in the nonradiative-recombination rate is completely balanced by an increase in the radiative-recombination rate.

Thus, the detectors preliminarily irradiated with α particles are found to be highly radiation-resistant devices.

4. THE SPECTRUM OF ALPHA PARTICLES

In Fig. 4, we show the amplitude spectrum of the charge collected in graded-gap photoelectric-response detector D50 irradiated with 5.48-MeV α particles (^{241}Am) and also preliminarily irradiated with various doses of α particles.

The amplitude of collected charge is given by

$$Q(\varphi) = n_0\eta_{eff}\frac{\exp(-\gamma L)}{\gamma}(\exp(\gamma l_\alpha \cos\varphi) - 1), \quad (5)$$

where L is the thickness of the graded-gap layer, l_α is the track length for an α particle, φ is the angle of incidence for the α particles on the graded-gap layer, γ is the coefficient for the absorption of the recombination radiation in the wide-gap part of the graded-gap layer, and $n_0\eta_{eff}$ is the number of electron–hole pairs that are generated by an α particle and that recombine radiatively.

Because the sizes of the α-particle source and the detector are finite, the angle φ varies within a wide range, which broadens the peak in the spectrum that corresponds to the energy of an α particle.

The quantity η_{eff} depends on both the ratio τ_r/τ_{nr} and the dose of preliminary irradiation. During the experi-

ment, we observed a shift of the collected-charge amplitudes to smaller values as the dose of preliminary irradiation with α particles increased (see Fig. 4). This observation means that the rate of nonradiative recombination begins to exceed the rate of radiative recombination as the dose of preliminary irradiation with α particles increases. Similar behavior was also observed in the case of detecting X-ray photons (Fig. 3).

It is worth noting that, in the case of the graded-gap detector with the current response, the number of pulses at the peak of the spectrum does not decrease along with the amplitudes Q as the radiation dose increases.

However, after irradiation with α particles for more than 20 h (which corresponds to a radiation dose of 2×10^9 cm^{-2}), the graded-gap detector ceases to be a particle-energy spectrometer, since the peak corresponding to the energy of the α particles shifts to a region of pronounced background radiation (Fig. 4).

5. CONCLUSION

The graded-gap p-$Al_xGa_{1-x}As$ layer with n-GaAs contacting the wide-gap part of the layer forms a structure that acts as an ionizing-radiation detector with a photoelectric response. The recombination radiation of the electron–hole pairs generated by ionizing radiation in the graded-gap layer is detected by the p-$Al_xGa_{1-x}As$/n-GaAs photodiode.

The current sensitivity of the photoelectric detector that detects 8-keV X-ray photons amounts to 0.13 A/W of the absorbed power. The voltage sensitivity is higher than 10^6 V/W.

The current sensitivity is lower, by a factor of 3, and the voltage sensitivity is higher, by a factor of 2, than those of a silicon detector of X-ray radiation.

The current and voltage sensitivity of detectors that had a thickness of the graded-gap layer in excess of 25 μm and were irradiated with 5.48-MeV α particles is reduced by a factor of 1.5 as a result of irradiation with a dose of 5×10^9 cm^{-2} of α particles. A further increase in the radiation dose to 4×10^{10} cm^{-2} does not affect the sensitivity.

A decrease in the sensitivity is caused by an increase in the rate of nonradiative recombination in the graded-gap layer when irradiated with α particles. At radiation doses higher than 5×10^9 cm^{-2}, the ratio between the rates of radiative and nonradiative recombination remains unchanged. The effective quantum yield of the recombination radiation and the detector sensitivity are not affected by irradiation with α particles of doses higher than 5×10^9 cm^{-2}.

An increase in the radiative-recombination rate to values larger than 10^9 s^{-1} ensures the high operation speed of the photodetector.

ACKNOWLEDGMENTS

This study was supported by Lithuanian State Foundation for Science and Education (CERN-Vilnius-RD program).

REFERENCES

1. L. Dapkus, K. Požela, Yu. Požela, *et al.*, Fiz. Tekh. Poluprovodn. (St. Petersburg) **38**, 1147 (2004) [Semiconductors **38**, 1111 (2004)].
2. V. M. Andreev, V. N. Blinov, V. A. Nosenko, *et al.*, Fiz. Tekh. Poluprovodn. (Leningrad) **8**, 1227 (1974) [Sov. Phys. Semicond. **8**, 798 (1974)].
3. A. Silenas, J. Pozela, K. M. Smith, *et al.*, Nucl. Instrum. Methods Phys. Res. A **487**, 54 (2002).

Translated by A. Spitsyn

Semiconductors, Vol. 39, No. 2, 2005, pp. 269–272. Translated from Fizika i Tekhnika Poluprovodnikov, Vol. 39, No. 2, 2005, pp. 285–288.

PHYSICS OF SEMICONDUCTOR DEVICES

Ammonia Sensors Based on Pd–*n*-Si Diodes

V. I. Balyuba, V. Yu. Grisyk, T. A. Davydova, V. M. Kalygina^, S. S. Nazarov, and L. S. Khludkova

Kuznetsov Physicotechnical Institute, pl. Revolyutsiĭ 1, Tomsk, 634050 Russia

^e-mail: vmk@elefot.tsu.ru

Submitted June 9, 2004; accepted for publication June 23, 2004

Abstract—The influence of ammonia on the electrical characteristics of Pd–*n*-Si diode structures is studied. The kinetics of diode characteristics under exposure to ammonia is considered. It is shown that the response speed of ammonia sensors based on Pd–*n*-Si diodes can be controlled by applying additional potential pulses to the barrier electrode. © *2005 Pleiades Publishing, Inc.*

Previous studies of the influence of ammonia on the electrical characteristics of semiconductor structures were carried out with silicon MOS (metal oxide–semiconductor) capacitors and field-effect transistors. Their gate was grown by sputtering the films of metals characterized by catalytic properties (Pd, Pt, Ir, etc.) [1] or various combinations of thin layers of these metals [2]. In an ammonia atmosphere, a parallel shift along the voltage axis was observed in the capacitance–voltage (*C–V*) characteristics of MOS capacitors and in the dependence of the drain current on the gate voltage of the field-effect transistors. The response of structures to gas exposure was determined as a shift of the flat-band voltage in capacitors [2] and a threshold-voltage shift in transistors [1].

The experimental data were explained on the basis of the Lundström model, which was suggested in order to analyze the influence of hydrogen on MOS structures that had a palladium barrier electrode [3]. It was assumed that NH_3 molecules adsorbed on the surface of a catalytically active electrode dissociate and give rise to atomic hydrogen (H_a) [1]. The latter diffuses through a Pd film and is fixed at the Pd–SiO_2 interface in the form of dipoles. The dipole layer changes the electron work function of palladium, which causes band bending at the semiconductor surface, and, hence, a change in the electrical characteristics of semiconductor structures [1, 2].

However, estimations showed quantitative disagreement between the experimental data and the suggested model [4]. In fact, the response of MOS capacitors and field-effect transistors to NH_3/air, NH_3/Ar, NH_3/He, and other gas mixtures is stronger than would be expected from the effect of generated atomic hydrogen.

Due to the absence of an adequate model, further studies into the influence of ammonia on semiconductor structures are of particular interest.

In this paper, we consider the results of studying the influence of NH_3 on the electrical characteristics of Pd–*n*-Si structures. It is known that capacitors and diodes based on MIS (metal insulator–semiconductor) structures that have a Pd electrode are sensitive to many reductive gases, including ammonia, arsine, hydrogen, hydrogen sulfide, carbon oxide [5–12]. At identical concentrations and under other equal conditions, the largest change in the electrical characteristics of MIS diodes with a Pd electrode was observed under exposure to hydrogen [6, 11, 12].

The structures under study were grown on a basis of epitaxial Si layers with a layer resistivity of 5–7 Ω cm. Initially, in order to grow an SiO_2 protective layer, the epitaxial structures were subjected to oxidation in a wet oxygen flow at a temperature of 1100°C. A rear ohmic contact to the semiconductor was formed by aluminum deposition followed by 5-min annealing in free space at a temperature of 530°C. First, a platinum film was deposited onto the SiO_2 layer's surface using cathodic sputtering, and then a Π-shaped heating element was formed using photolithography. After that, windows were opened in the SiO_2 film and a palladium film was deposited by thermal evaporation in free space. Finally, a palladium electrode 2.4×10^{-3} cm^2 in area was formed using explosive photolithography. In the used technology, the palladium electrode became separated from the silicon by a tunneling-transparent layer of natural SiO_x oxide. After fabrication, diodes were annealed in an air medium for 10 min at a temperature of 300°C (which significantly exceeds the range of operating temperatures used in subsequent measurements). After annealing, the silicon structure was cut into individual crystals 1×1 mm^2 in size, and the obtained samples were soldered to a chip carrier.

Current–voltage (*I–V*) characteristics at dc voltage, as well as capacitance–voltage (*C–V*) and conductance–voltage (*G–V*) characteristics, were measured at a frequency of 1 MHz either in an air medium or in an ammonia–air mixture.

In contrast to previously studied diodes, the grown structures were not sensitive to hydrogen even at a content of 100%. Under exposure to ammonia, an increase in the forward and reverse currents, capacitance, and conductance was observed. The dependence of the

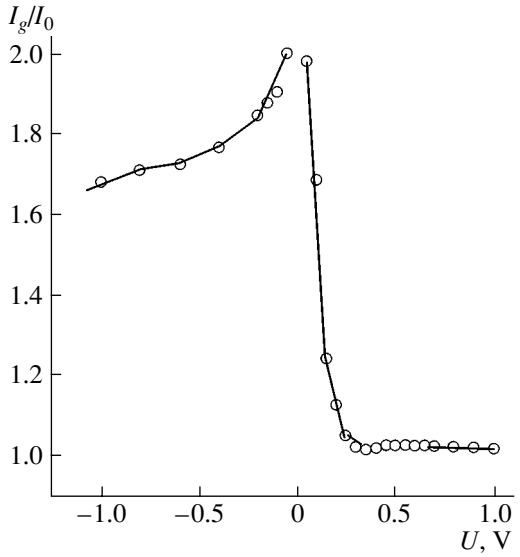

Fig. 1. Voltage dependence of the ratio of the current in a gas mixture (700 ppm NH_3)/air (I_g) to the current in an air medium (I_0).

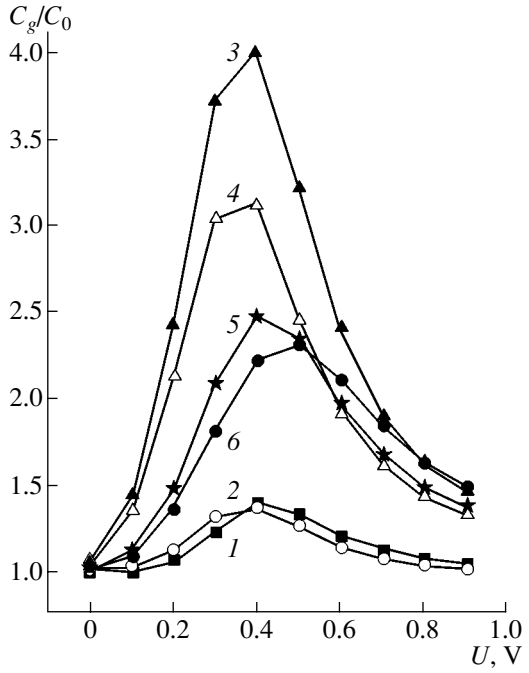

Fig. 2. Voltage dependence of the ratio of the capacitance in a gas mixture (700 ppm NH_3)/air (C_g) to the capacitance in an air medium (C_0) at temperatures of (*1*) 57, (*2*) 70, (*3*) 96, (*4*) 108, (*5*) 120, and (*6*) 127°C.

diode response to ammonia on the voltage is described by peaked curves. The strongest effect the changes in the electrical characteristics had was obtained for reverse and forward currents in the voltage range U = (–0.5)–(+0.15) V (see Fig. 1) in the capacitance and conductance at the ac signal for a diode bias U = 0.3–0.4 V (Fig. 2). At a fixed NH_3 content, the response of the capacitance (taken as the ratio C_g/C_0 of the capacitances in a gas and room-air medium) initially increases and then decreases as the temperature rises (Fig. 2).

The dependences of the capacitance and conductance on the ammonia content N for one of the diodes at T = 50°C and an operating voltage of 0.4 V are shown in Fig. 3.

One of the most important parameters of gas sensors is the response speed, which is characterized by the response time (τ_r) and the recovery time (τ_f). The response time is considered to be a time interval within which a measured value changes to the 0.9 level from the largest value. The recovery time is defined as a time interval within which a measured parameter is recovered to the 0.1 level from the largest value.

As a gas pulse is fed to a measurement chamber, steady-state values of the capacitance and conductance are established more rapidly at a fixed operating voltage (U_{op}) if a negative potential significantly exceeding U_{op} is applied to a barrier electrode for 5–10 s (Fig. 4).

As a rule, $\tau_f > \tau_r$; therefore, to determine the response speed of the sensors, it is of interest to study the kinetics of diode parameter recovery after exposure to a gas pulse. For most diodes, τ_r decreases as the operating temperature increases.

The recovery time depends heavily on the process conditions. For this reason, we studied the influence of

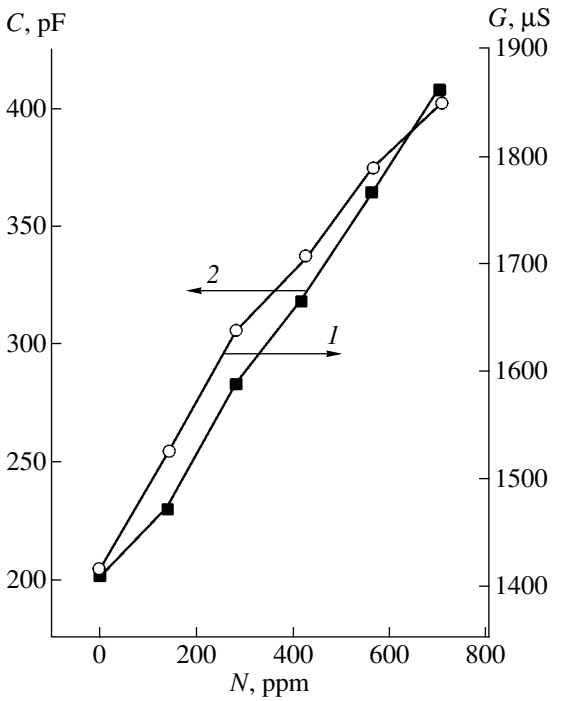

Fig. 3. Dependence of the (*1*) capacitance C and (*2*) conductance G on the ammonia content N at an operating voltage of 0.4 V and temperature of 50°C.

the potential at the palladium barrier electrode on changes in the diode conductance over time. Figure 5 shows the conductance falloff at the operating voltage

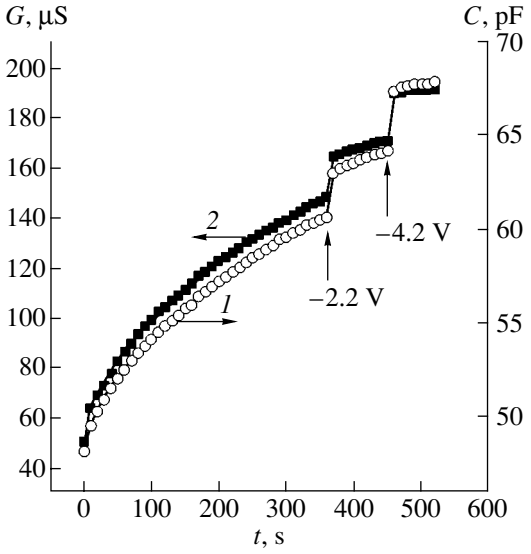

Fig. 4. Temporal variation in the (*1*) capacitance *C* and (*2*) conductance *G* after filling the measuring chamber with 700 ppm NH_3. The diode operating voltage is 0.2 V.

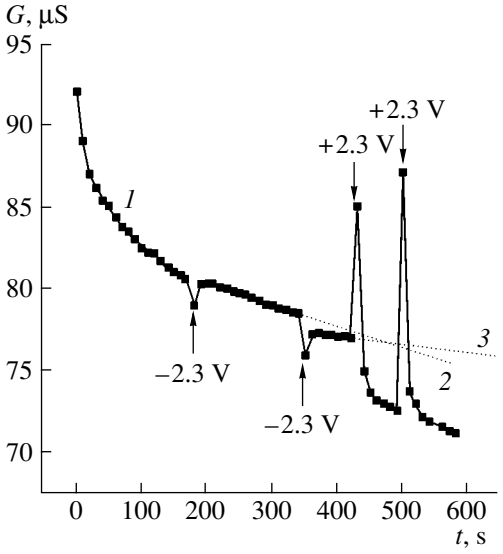

Fig. 5. Temporal variation in the conductance *G* after removing 700 ppm NH_3. The diode operating voltage is 0.3 V.

U_{op} = 0.3 V (curve *1*). After 170 s from falloff onset, the additional negative potential U_{ad} = –2.3 V was applied to the palladium electrode for 10 s, which slowed down the conductance falloff. After a further 170 s, the negative potential U_{ad} = –2.3 V was, as before, applied to the diode for 10 s, which slowed down the conductance decrease again. Dashed straight lines *2* and *3* in Fig. 5, plotted by extrapolating the experimental curve regions, show the expected *G* changes over longer time periods. However, if a positive potential is applied to the palladium electrode at any stage of the diode parameter recovery, the recovery process becomes faster. In Fig. 5, this effect is observed at U_{ad} = +2.3 V.

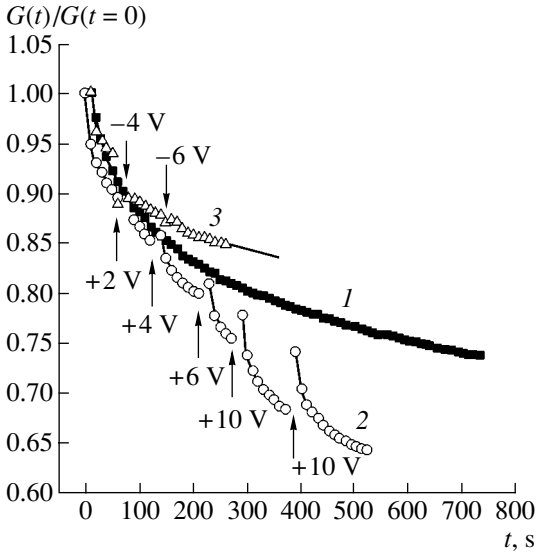

Fig. 6. Temporal variation in the conductance *G* normalized to *G* (*t* = 0) after removing 700 ppm NH_3. The operating voltage is 0.3 V. The additional voltage at the palladium electrode is (*1*) 0, (*2*) +(4–10), and (*3*) –(4–6) V.

The influence of the positive potential at the barrier electrode on the time dependences of the conductance is most pronounced for U_{ad} in the range 2–6 V. As U_{ad} further increases, the *G* relaxation rate becomes less noticeable.

In Fig. 6, we compare the conductance recovery curves without an additional potential at the Pd electrode (curve *1*) and with the multiple application of positive (curve *2*) and negative (curve *3*) potentials U_{ad}. These curves show that a positive potential at the Pd electrode ($U_{ad} \gg U_{op}$) makes the recovery process faster and increases the sensor response speed. A negative potential ($|U_{ad}| \gg U_{op}$) slows down the sensor parameter recovery to initial values, i.e., those before exposure to ammonia. Thus, by varying the potential sign and amplitude, one can control the response speed of sensors based on MIS diodes.

The absence of the effect of hydrogen on the Pd–*n*-Si structures under study is caused by the palladium silicides (Pd_2Si, PdSi) formed as a result of thermal annealing [13, 14]. It is known that palladium silicides have metallic conductivity but do not exhibit catalytic properties.

The mechanism of the diode response formation in an ammonia atmosphere can be conceived as follows: The mismatch between the lattice parameters of silicon and palladium silicide films causes stresses [13], whose relaxation in the barrier electrode result in the formation of microvoids and microcracks. Ammonia molecules adsorbed on the outer surface of the barrier electrode diffuse through the metal film and reach the interface

between Pd_2Si and the tunneling-thin SiO_x layer. The dipole moment of ammonia molecules is $\mu = 1.46$ D [15]; hence, by analogy with the hydrogen model, it is reasonable to consider that the generated dipole layer reduces the electron work function of the barrier electrode. As a result, the negative band bending at the *n*-Si surface decreases, which, in turn, increases the forward and reverse currents, capacitance, and conductance of the diodes.

The influence of the electric field on the recovery kinetics of the diode capacitance and conductance after a gas pulse is apparently caused by a change in the shape of the potential well, in which the ammonia molecule is trapped during adsorption at the interface between Pd_2Si and the tunneling-thin SiO_x layer [16]. At small electrode potentials corresponding to the operating voltages U_{op}, the potential barrier shape is almost unchanged. When there are large positive biases at the field electrode, the potential barrier is lowered, and the probability of the adsorbed molecule leaving the potential well sharply increases.

Thus, the studied Pd–*n*-Si structures can be used when developing ammonia sensors that are selective with respect to hydrogen.

REFERENCES

1. J. F. Ross, I. Robins, and B. C. Webb, Sens. Actuators **11**, 73 (1987).
2. A. Spetz, M. Armgarth, and I. Lundström, Sens. Actuators **11**, 349 (1987).
3. I. Lundström, Sens. Actuators **1**, 403 (1981).
4. I. Lundström, M. Armgarth, A. Spetz, and F. Winquist, Sens. Actuators **10**, 399 (1986).
5. W. Hornik, Sens. Actuators B **4**, 35 (1990).
6. M. Ogita, Dong-Bai Ye, K. Kawamura, and T. Yamamoto, Sens. Actuators **9**, 157 (1986).
7. T. Fare, A. Spetz, M. Armgarth, and I. Lundström, Sens. Actuators **14**, 157 (1988).
8. G. J. Maelay, K. W. Jelley, S. Nowrozi-Esfahani, and M. Formosa, Sens. Actuators **14**, 331 (1988).
9. W. Mokwa, K. Dobos, and G. Zimmer, Sens. Actuators **12**, 333 (1987).
10. M. Peschke, H. Lorenz, H. Riess, and I. Eisele, Sens. Actuators B **1**, 21 (1990).
11. V. I. Gaman, M. O. Duchenko, and V. M. Kalygina, Izv. Vyssh. Uchebn. Zaved., Fiz., No. 1, 69 (1998).
12. V. I. Gaman, V. I. Balyuba, T. A. Davydova, *et al.*, Izv. Vyssh. Uchebn. Zaved., Fiz., No. 11, 3 (2001).
13. C. Betty, Ch. Haydn, and R. Kenneth, in *Proceedings of Symposium on Thin Films: The Relationship of Structure to Properties, San Francisco, 1985* (Pittsburgh, 1985), p. 155.
14. G. A. Sarov, D. Kukurinkov, and A. Shopov, in *Proceedings of Anniversary Scientific and Technical Conference* (Botevgrad, 1987), Part 2, p. 158.
15. V. F. Kiselev, S. N. Kozlov, and A. V. Zoteev, *Fundamentals of the Physics of Solid Surface* (Mosk. Gos. Univ., Moscow, 1999) [in Russian].
16. L.-G. Petersson, H. M. Dannetun, J. Fogelberg, and I. Lundström, J. Appl. Phys. **58**, 404 (1985).

Translated by A. Kazantsev